Simulations of Longitudinal Beam Dynamics in Storage Rings

Dem Fachbereich Elektrotechnik und Informationstechnik
der Technischen Universität Darmstadt
zur Erlangung
der Würde eines Doktors der Naturwissenschaften (Dr. rer. nat.)
vorgelegte

Dissertation

von

Dipl.-Math. Christopher Burnton
geboren am 11. April 1966 in Wellington

Darmstadt 2000

Referent:	Prof. Dr.-Ing. Thomas Weiland
Korreferenten:	Prof. Dr. rer. nat. Dr. h.c. mult. Achim Richter
	Dr. rer. nat. Reinhard Brinkmann
Tag der Einreichung:	10. April 2000
Tag der mündlichen Prüfung:	8. November 2000

D 17
Darmstädter Dissertation

Contents

1 Introduction **3**

2 General Layout of the Dog-bone Damping Ring **7**
2.1 Introduction 7
2.2 Layout of the Dog-bone Damping Ring 10
2.3 Beam Optics and Vacuum System 12
2.4 Rf System 14

3 Longitudinal Dynamics in Electron Storage Rings **15**
3.1 Introduction 15
3.2 Basic Longitudinal Dynamics 16
3.3 Wake Fields 25
3.3.1 Wake Functions and Wake Potentials 25
3.3.2 Impedance 29
3.3.3 The Wake of a Single Cavity Mode 31
3.3.4 Accelerating Mode and Equivalent Circuit Model of the Rf System . 35
3.3.5 Beam Loading 36
3.4 Multibunch Instabilities 45
3.4.1 Robinson Instability (fundamental cavity mode) 45
3.4.2 Higher-Order Cavity Modes 51
3.5 The Vlasov Equation 51
3.6 The Haissinski Equation 54

4 Simulation Technique **60**
4.1 Single Bunch Tracking 60
4.2 Multibunch Simulation 65

5 Impedance Model **70**
5.1 Broad-band Impedance 70
5.1.1 A Broad-band Impedance Model 70
5.1.2 Sources of Inductive Impedance 72
5.1.3 Resistive Wall 74
5.1.4 Cavities 76
5.1.5 Fast Kickers 77
5.1.6 Summary of the contributions 79
5.2 Narrow-band Impedance 79
5.2.1 Cavities 79
5.2.2 Resistive Wall and Beam Position Monitors 81

6 Simulation Results **82**
6.1 Single Bunch Studies . . . 82
6.1.1 Convolution Error . . . 82
6.1.2 Tracking – General Remarks . . . 84
6.1.3 Tracking without Wake Fields . . . 85
6.1.4 Inductive Wake . . . 90
6.1.5 Resistive Wall . . . 94
6.1.6 Cavities . . . 97
6.1.7 Fast Kicker . . . 97
6.1.8 Total Wake . . . 100
6.2 Multibunch Tracking . . . 104
6.2.1 Simulations with Higher-Order Modes . . . 104
6.2.2 Simulations including the Fundamental Mode . . . 123

7 Comparison with other programs **138**
7.1 K. Oide and K. Yokoya's Code . . . 138
7.2 SLC Damping Ring . . . 140
7.3 Multibunch Tracking . . . 142

8 Summary and Conclusion **144**

A Formula Symbols **149**

B Fourier Transformation Relationships **151**

C Cavities **153**
C.1 The Impedance of a Single Cavity Mode . . . 153
C.2 Time Development of the Wake Function of a Cavity Mode with Repetitive Beam Loading . . . 155
C.3 Transient Behaviour of a Cavity driven by a Harmonic Current . . . 156
C.4 The Diffraction-Model Wake Potential of a Gaussian bunch . . . 158

D Potential-Well Distortion **160**
D.1 A Bunch Lengthening Estimate for a Potential Well Distorted by an Inductive Impedance. . . . 160
D.2 Derivation of the Resistive Impedance Potential-Well Solution . . . 162

E Multibunch Beam Signal **164**

F Approximate Invariant Amplitude of Motion **166**

G Glossary **168**

Bibliography **174**

Chapter 1

Introduction

High energy electron-positron colliders have proven in the past to be an excellent tool to study the fundamental constituents of matter and their interactions.
This year CERN's LEP e^+e^- collider reached a record beam energy of 100 GeV; however, due to synchrotron radiation losses, the energy range of circular e^+e^- accelerators cannot be significantly increased beyond the LEP energy ($\sim$ 200 GeV centre of mass).
Leptons, quarks, and their interactions have been successfully described by the so-called Standard Model; however, the Higgs particle, another constituent of the model, has not yet been observed. Higher centre-of-mass energies are needed to discover this particle and to look beyond this model for new phenomena.
Only a linear collider will be able to provide the possibility of exploring e^+e^- annihilations with centre-of-mass energies up to the TeV scale. Meanwhile, at CERN a new circular pp-collider LHC (Large Hadron Collider) is under construction, which is designed to reach a centre-of-mass energy of 12 – 14 TeV[1]. Nevertheless, studying e^+e^- collisions in the 300 to 1000 GeV range has a high potential for the future development of Particle Physics, and is in many respects complementary to the LHC [1].

In the following, a number of accelerator physics related terms like *luminosity*, *emittance* and expressions such as *transverse* or *longitudinal* are introduced without further direct explanation. They are to be found in the glossary in Appendix G.
A linear collider consists of two opposing main linear accelerators: one for electrons and one for positrons. At the end of each linac a special beam delivery system (BDS) collimates and focuses the beams to a very tiny spot size. The damping rings and the electron and positron source belong to the preaccelerator complex.
The only existing linear collider facility is the SLC at SLAC with a centre-of-mass energy of about 90 GeV and a spot size of down to 2000 $\times$ 600 nm [2] at the interaction point (IP). A next generation linear collider will have to provide spot sizes of something like 1000 $\times$ 20 nm to obtain the desired high luminosities ($> 10^{33}\,\mathrm{cm}^{-2}\,\mathrm{s}^{-1}$). The situation world-wide today is that at several High Energy Physics laboratories, designs for a future e^+e^- linear collider in the 0.5 to 1 TeV energy range are being studied.
A linear collider based on superconducting accelerating structures with an rf frequency of 1.3 GHz is being designed and technologically developed by the international TESLA

[1] The centre-of-mass energy at constituent level is about one tenth of this value.

collaboration. More than 30 institutes from China, Finland, France, Germany, Italy, Poland, Russia, and the USA are members of the collaboration.
Superconducting rf cavities are technically advantageous with respect to their high Q values and low rf-power losses in the resonator walls. These permit using large aperture structures operating at a relatively low frequency, with long pulse lengths and low peak rf-power requirements. The large aperture of the cavities has the beneficial consequence of substantially reduced transverse and longitudinal wake field effects.

Parameters		TESLA (ref.)	TESLA (new)
energy (c.o.m.)	GeV	500	500
luminosity $\mathcal{L}$	10^{34} cm^{-2} s^{-1}	0.68	3
site length	km	32.6	32.6
active length	km	20	23
acc. gradient	MV/m	25	21.7
quality factor Q_0	10^{10}	0.5	1
pulse length	μs	800	950
rep. rate $f_{\rm rep}$	Hz	5	5
number of bunches /pulse		1130	2820
bunch spacing	ns	708	337
bunch population	10^{10}	3.6	2
emittance $\gamma\epsilon_x/\gamma\epsilon_y$ (at IP)	10^{-6} m	14 / 0.25	10 / 0.03
bunch length σ_z	mm	0.7	0.4
beta at IP $\beta_{x/y}$	mm	25 / 0.7	15 / 0.4
spot size σ^*_x/σ^*_y	nm	845 / 19	553 / 5
beamstrahlung $\delta_{\rm B}$	%	2.5	2.8
disruption D_y		17	33
ac-power $P_{\rm ac}$ (2 linacs)	MW	95	95
efficiency (ac to beam) $\eta_{\rm AC\to b}$	%	17	23

Table 1.1: A comparison of the updated parameters at $E_{\rm cm} = 500\,$GeV with the original reference parameters [3].

The basic design parameters are listed in Table 1 for two options with luminosities of 6.8 and $30 \times 10^{33}\,$cm^{-2} s^{-1}. A complete description of the machine, including all sub-systems, is given in the Conceptual Design Report (CDR) [1]. The first parameter set "TESLA (ref.)" is the reference parameter list from the CDR, while the second "TESLA (new)" list represents an improvement towards higher luminosities [3].
The electrons and positrons are injected into damping rings to produce the low emittance beams which are required to reach the high luminosities. The 0.8 ms (approx. 240 km) long bunch trains are stored in the ring in a compressed mode, with the bunch spacing reduced by a factor of 14. Nevertheless, a large ring circumference of 17 km is still required. To avoid an additional ring tunnel of this size, a special damping ring design with long straight sections, called a dog-bone, has been chosen. The 8 km long straight sections are entirely placed in the main tunnel. Additional tunnels need only be built for the small loops at the ends. A sketch of the overall layout of the TESLA linear collider is given in Figure 1.1.

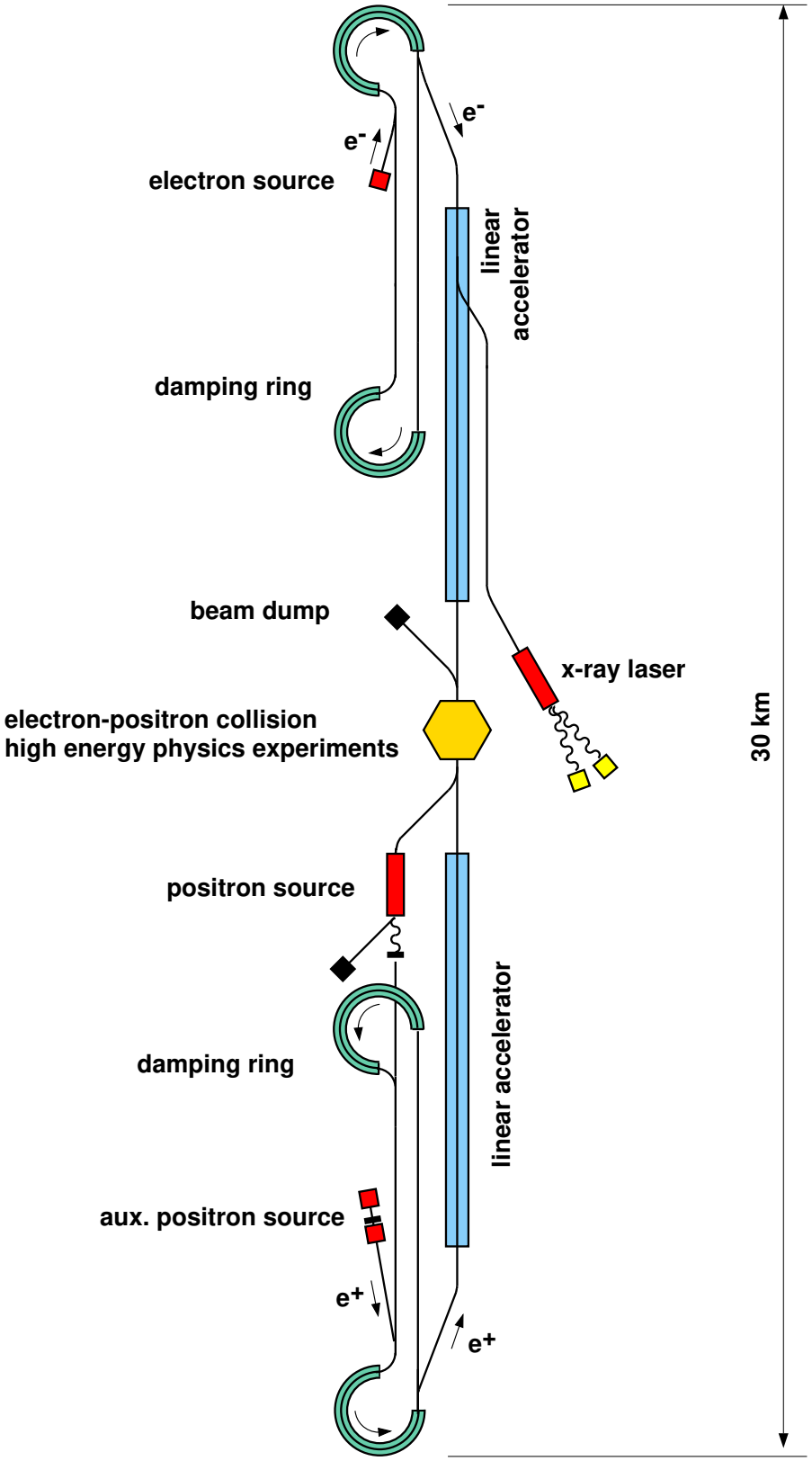

Figure 1.1: Overall layout of TESLA.

Longitudinal single and multibunch instabilities in the damping ring have to be avoided to guarantee the high quality bunch trains required for the operation of the linear collider. This thesis studied the longitudinal dynamics in the damping ring by analytical and numerical methods. It demonstrates that the design single bunch current is well below the instability threshold. Furthermore, the growth rate of longitudinal multibunch instabilities resulting from higher-order modes are smaller than the damping rate from synchrotron radiation. The detuning of the cavity resonance frequency for reasons of beam-loading optimization gives, however, rise to to an instability of the multibunch mode nearest in frequency. A feedback loop will be necessary to counteract the instability.
In Chapter 2, the sub-systems of the damping ring are introduced in detail, especially the parameters which determine the longitudinal dynamics.
The theory underlying the longitudinal dynamics in electron storage rings is summarized in Chapter 3. The concept of wake fields and impedances is explained. The analytical methods to treat collective effects are compiled and applied to the dog-bone damping ring.
The tracking techniques used for the computer simulations are described in Chapter 4. Single bunch and multibunch tracking are addressed separately due to different simulation methodologies. The former is characterized by using macroparticles and quasi-delta wake functions, the latter by a one-particle model (per bunch), higher-order cavity mode wake functions, and beam loading in the fundamental cavity mode. The higher-order mode studies were carried out as if there were no beam loading. When accounting for this effect (nearby-mode and transient beam-loading studies), the cavity voltage is decomposed into a generator and a beam component.
The impedance model of the dog-bone damping ring used in the simulations is presented in Chapter 5. It is followed by a presentation of simulation results in Chapter 6.
The computer code which was developed has also been applied to the SLAC damping ring, where longitudinal instabilities have been observed. The simulations concur with the experimental results. The details are presented in Chapter 7 of this thesis. Furthermore, the dog-bone tracking results are compared to those obtained by K. Yokoya's code [4].
The results and methods are summarized in the final chapter.
The appendix contains a list of the most common symbols and the conventions for the Fourier transformation relationships used in this thesis.

Chapter 2

General Layout of the Dog-bone Damping Ring

2.1 Introduction

The electron and positron injection system has to provide a total charge of about 4×10^{13} e^+ and e^- per beam pulse for the reference TESLA parameter set and even 5.6×10^{13} for the new parameter set.
Presumably the positrons will be produced by γ-conversion in a thin target. They are then preaccelerated in a conventional 200 MeV L-band (1.3 GHz) linac, followed by a 3 GeV superconducting accelerator. The necessary photons for the γ-conversion are created by sending the spent high-energy electron beam through a wiggler after the interaction point. The normalized transverse emittance (Glossary, page 171) of the resulting positron beam is several orders of magnitude larger than the design emittance for collider operation. The only conceivable way to achieve the required emittance is to store the beam temporarily (between linac pulses) in a damping ring.
Assuming a normalized transverse emittance of the positron beam injected into the ring of $\gamma\epsilon_\mathrm{i} = 0.01\,\mathrm{m}$ [1], the desired emittance reduction factors are $\epsilon_{\mathrm{f};x}/\epsilon_\mathrm{i} = 1.2 \times 10^{-3}$ and $\epsilon_{\mathrm{f};y}/\epsilon_\mathrm{i} = 2 \times 10^{-5}$ for the horizontal and vertical plane, respectively. These factors relate to the TESLA (ref.) parameters where an emittance dilution of 25 % between the extraction from the ring and the interaction point is included. The final emittance in the ring after a storage time equal to the linac cycle time $T_\mathrm{c} = 200\,\mathrm{ms}$ is given by

$$\epsilon_\mathrm{f} = \epsilon_\mathrm{eq} + (\epsilon_\mathrm{i} - \epsilon_\mathrm{eq}) \exp(-2T_\mathrm{c}/\tau), \tag{2.1}$$

with

e^+ emittance at injection	$\gamma\epsilon_{\mathrm{i};x,y}$	0.01 m
hor. equilibrium emittance	$\gamma\epsilon_{\mathrm{eq};x}$	1.2×10^{-5} m
hor. emittance at extraction	$\gamma\epsilon_{\mathrm{f};x}$	1.2×10^{-5} m
vert. equilibrium emittance	$\gamma\epsilon_{\mathrm{eq};y}$	1.0×10^{-7} m
vert. emittance at extraction	$\gamma\epsilon_{\mathrm{f};y}$	2.0×10^{-7} m
transverse damping time	$\tau_{x,y}$	35 ms.

In the case of the electron beam, a laser driven rf gun can be used to produce the required intensity. This would provide the e^- beam with an emittance significantly smaller than that of the e^+ beam. However, for optimum performance of the collider with a vertical emittance as small as possible, an electron damping ring will be required as well. This is especially the case for the upgraded (new) TESLA parameter set. In this thesis the positron damping ring has been considered since there are only minor differences between the electron and the positron version of the damping ring, with somewhat relaxed requirements for the e^- ring.
A bunch train has a length of almost 0.8 ms, or 240 km. Hence, the bunch train must be stored in the ring in a compressed mode, with a bunch spacing much smaller than in the linac. Furthermore, injection into and extraction from the damping ring has to be done bunch-by-bunch. The damping ring design circumference of 17 km represents a compromise between a reasonable upper limit for the circumference and a lower limit for the injection/extraction system bandwidth.
The luminosity of a linear collider can be increased by making σ_y^*, the vertical beam size at the IP, as small as possible. This is achieved by both a small vertical beta function (Glossary, page 169) at the IP and a small vertical emittance. The lower limit on the vertical beta function is given by the bunch length ("hourglass effect"): $\beta_y^* = \sigma_z$. A large aspect ratio $\sigma_x^*/\sigma_y^* \gg 1$ is chosen to satisfy the constraints on the fractional beam energy loss due to beamstrahlung (see [1]; Glossary, page 169). In order to keep the demands for the bunch compressor (Glossary, page 170) moderate, the damping ring should also satisfy constraints imposed by the longitudinal phase space:

equilibrium bunch length	σ_z	$4.5 \ldots 10\,\mathrm{mm}$
equilibrium momentum spread	σ_p/p	$\sim 0.1\,\%$
momentum acceptance	A_p	$> 0.5\,\%$.

The shorter bunch length of about 4.5 mm corresponds to the upgraded (new) TESLA parameter list with a bunch length of 0.4 mm at the IP.
Because the ring must safely accommodate the injected positron beam, lower limits must be set on the transverse acceptance (Glossary, page 168) of $\gamma A_{x,y} > 0.05\,\mathrm{m}$. The magnet lattice (Glossary, page 168) and the beam optics of the positron damping ring are discussed in reference [1] in detail.
One critical point with respect to the transverse dynamics results from an unusually large ratio of circumference over beam energy, causing a large space charge tune shift (Glossary, pages 172 and 173) [3].
In the next sections the general layout, the magnet lattice, the beam optics, and the rf system of the positron damping ring are discussed.

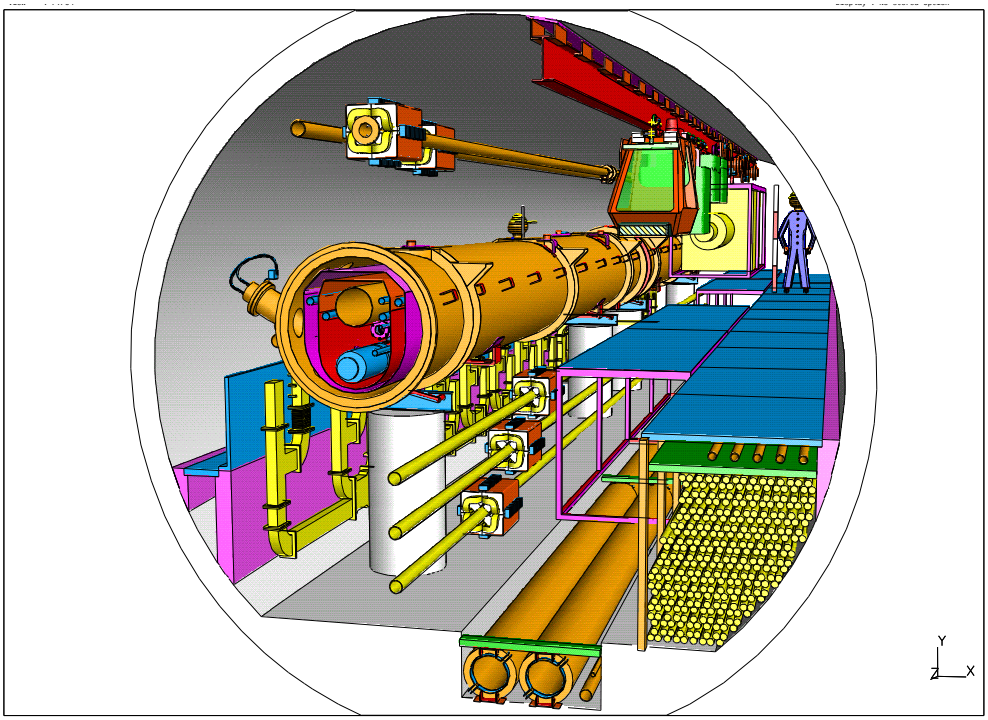

Figure 2.1: CAD view into the TESLA tunnel.

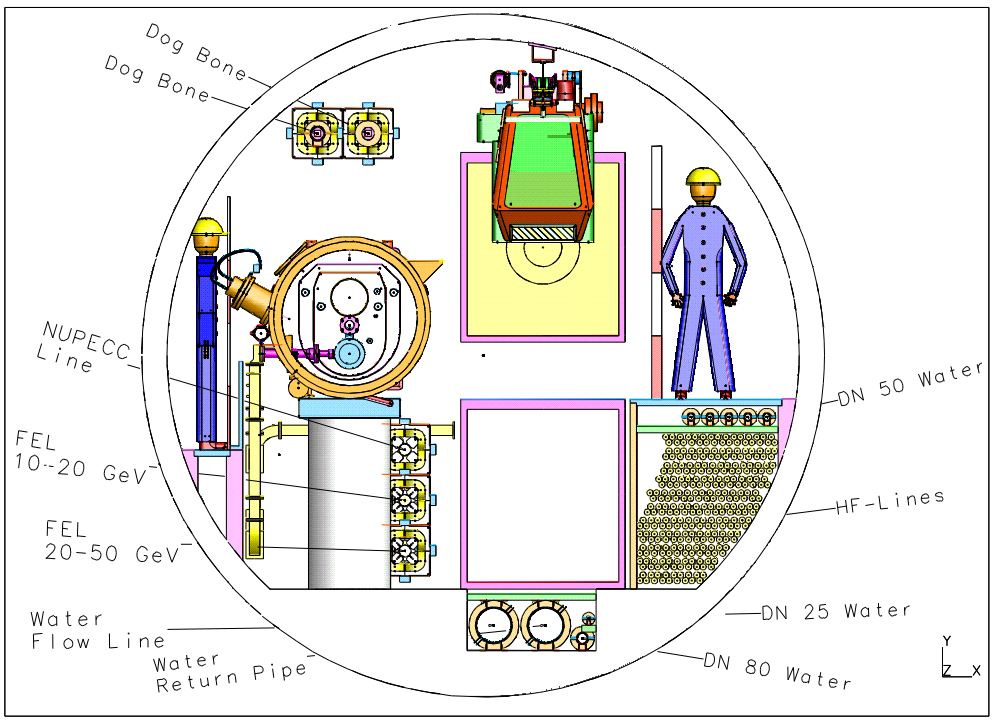

Figure 2.2: Cross-section of the TESLA tunnel. The straight section of damping ring is shown near the tunnel ceiling.

2.2 Layout of the Dog-bone Damping Ring

In order to avoid the need for a costly additional tunnel, the TESLA damping ring is designed so that about 95 % of the lattice can be installed in the linac tunnel (see Fig. 2.1 and 2.2). Additional tunnels are only required for the two "loops" at the ends of the 8 km long straight sections. Fig. 2.3 shows the location of the "loops" with respect to the linear collider for the DESY site option of the project. The arcs consist of a negative bending section with a bending angle of $\Phi_- = -11/48 \times 2\pi$, followed by a short straight section and a positive bending section with $\Phi_+ = 35/48 \times 2\pi$. The length of these short straight sections is adjusted so that the long straight sections in the linac tunnel are horizontally 0.8 m apart. The basic unit of the arcs is a FODO cell (Glossary, page 171) with a bending angle of $\pi/24$ and an average bending radius of 60 m.
In order to achieve a sufficiently small damping time, wiggler sections are included at the end of the long straight sections. The transverse damping time can be written as [5, p. 355]

$$\tau_{x,y} = \frac{2E_\mathrm{b}C}{U_0 c}\,, \tag{2.2}$$

where E_b is the beam energy and U_0 the energy loss per revolution. The latter is given by [5, p. 344]:

$$U_0 = \frac{C_\gamma E_\mathrm{b}^4}{2\pi}\oint G^2(s)ds = \frac{C_\gamma E_\mathrm{b}^4}{2\pi}\oint\left(\frac{ecB_{y0}(s)}{E_\mathrm{b}}\right)^2 ds = \frac{C_\gamma (ec)^2}{2\pi}E_\mathrm{b}^2\oint B_{y0}^2(s)ds, \tag{2.3}$$

where $G(s)$ is the curvature function and $C_\gamma = 8.85\times10^{-5}\,\mathrm{m(GeV)^{-3}}$. $B_{y0}(s)$ is the magnitude of the vertical component of the magnetic field on the ideal orbit. We find

$$\frac{U_0}{\mathrm{MeV}} = 1.26\cdot10^{-3}\times\frac{E_\mathrm{b}^2}{(\mathrm{GeV})^2}\oint\frac{B_{y0}^2(s)}{\mathrm{T}^2}ds\,. \tag{2.4}$$

For the beam energy, $E_\mathrm{b} = 3.2\,\mathrm{GeV}$ was chosen as the result of a parameter optimization, where the following factors were considered:

- The rf system. The required circumferential voltage V_rf grows with increasing E_b.
- The emittance contribution from the arcs. For a given beam optics, the normalized horizontal emittance scales approximately as $\gamma\epsilon_\mathrm{arc} \propto E_\mathrm{b}^6$, when the dominant contribution to the damping comes from the wigglers.
- The bunch compressor, which favours a low beam energy.
- The total length L_w of the wigglers. For a given field strength B_{y0}, L_w scales like E_b^{-1}, thus favouring a high beam energy.

Inserting a damping time of 35 ms into Eq. (2.2) results in a necessary energy loss per revolution of approximately 10.4 MeV. As an actual design parameter, an energy loss of $U_0 = 10.7\,\mathrm{MeV}$ is assumed, giving a damping time of 33.8 ms and determining the required damping integral (Eq. (2.4)), which comes predominantly from the wigglers.

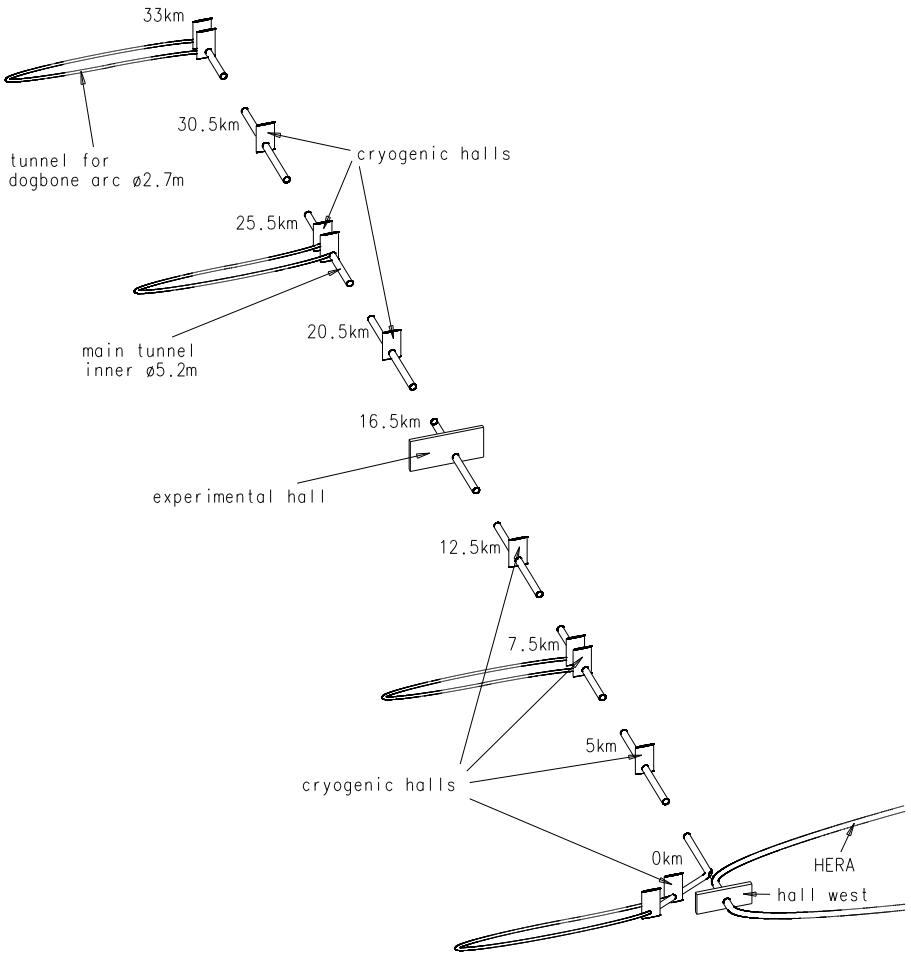

Figure 2.3: An overview of the possible TESLA site at DESY. The dog-bone arcs are not to scale.

The wiggler design described below has $B_{\rm w} = 1.5\,{\rm T}$, so that the length of each of the four wiggler sections is about 100 m. It is

$$\int_{\rm wiggler} B_{y0}^2(s)ds = 815\,{\rm T}^2{\rm m}. \tag{2.5}$$

The relative beam energy spread σ_E is determined from $E_{\rm b}$ and $B_{\rm w}$ as (see page 21 and Eq. (3.24)):

$$\sigma_E = \sqrt{\frac{\langle(\Delta E)^2\rangle}{E_{\rm b}^2}} \approx 0.468\cdot 10^{-3} \times \sqrt{\frac{E_{\rm b}}{\rm GeV}\frac{B_{\rm w}}{\rm T}} = 1.02\cdot 10^{-3}. \tag{2.6}$$

The roughly 8 km long straight sections are designed as simple periodic FODO channels. Injection and extraction take place at opposite ends of the straight section, so that the damping ring itself acts as part of the beamline required to transfer the positrons to the entrance of the main linac.

Circumference C	17 km
Beam energy E_b	3.20 GeV
Number of bunches N_b	1130
Bunch population N_e	3.63×10^{10}
Bunch spacing ΔT_b	50 ns
Stored current I_b	116 mA
Energy loss p. turn U_0	10.7 MV
Rf frequency f_rf	433 MHz
Rf voltage V_rf	25 MV
Energy spread σ_E	0.10 %
Momentum compaction factor α_c	3.4×10^{-4}
Bunch length σ_z	9.5 mm
Synchrotron tune ν_s	0.097
Energy acceptance $\Delta E_\mathrm{max}/E_\mathrm{b}$	1.5 %
Norm. hor. emittance $\gamma\epsilon_x$	1.10×10^{-5} m
Transverse damping time $\tau_{x,y}$	33.8 ms
Hor./vert. tune Q_x/Q_y	59.85 / 57.71
Hor./vert. chromaticity ξ_x/ξ_y	-68.6 / -73.3
Norm. acceptance $A_{x,y}$	0.06 m
Incoherent space charge ΔQ_y	-0.17

Table 2.2: Main design parameters of the positron damping ring. The top half are relevant in regards to the tracking simulations.

2.3 Beam Optics and Vacuum System

In this section the beam optics and the general layout of the vacuum system for the different parts of the ring are discussed. The main parameters for the beam optics are included in Table 2.2. A more detailed discussion can be found in [1].
The vertical equilibrium emittance in the damping ring is essentially determined by the quadrupole, sextupole, and beam position monitor (BPM) (Glossary, page 169) alignment tolerances and by the orbit correction procedures applied. The design value of the emittance can be achieved, assuming realistic alignment tolerances for the damping ring components; a smaller vertical emittance can be reached by applying sophisticated methods [1].

Straight Sections

The basic unit of the long straight sections is a 60° phase advance (Glossary, page 172) FODO cell of 100 m length. This choice of focusing strength is a compromise between keeping the β-functions within limits and avoiding an excessive contribution to the chromaticity (Glossary, page 170), which can only be compensated for in the relatively short arcs. A summary of the beam optics and magnet parameters is given in Table 2.3.

FODO cell length	100 m
cell phase advance	60°
total number of cells	152
chromaticity contribution $\xi_{x,y}$	27.9
average $\beta_{x,y}$	110 m
aperture radius	50 mm
quadrupole length	0.2 m
quadrupole gradient	1.05 Tm^{-1}

Table 2.3: Optics and magnet parameters for the straight sections.

The vacuum chambers will be made primarily from 100 mm diameter, 9.5 m long aluminium tubes. There are short pump unit sections between these tubes in order to reach the required average pressure of $\bar{p} = 10^{-9}$ mbar. The sections are connected by bellows.

Arcs

The FODO cell in the arcs has a length of 8.5 m. Each cell comprises two quadrupoles, two dipoles, two sextupoles, and two correction magnets. The design value of the phase advance is set to 90° per cell. The corresponding parameters are listed in Table 2.4. The quadrupoles and sextupoles are designed to allow for an increase in focusing strength, which provides sufficient flexibility for a smaller horizontal emittance and momentum compaction factor (Glossary, page 172) when desirable.
The vacuum chamber in each cell is split in the following way: two long chambers passing the dipole magnet and the correction coil and two short chambers through the quadrupole and sextupole magnets. Bellows are integrated on both sides of the quadrupole chambers. All chambers will have the same elliptical aperture of $50 \times 30\,\mathrm{mm}^2$ (major axis $\times$ minor axis).

FODO cell length	8.5 m
cell phase advance	90°
total number of cells	92
average $\beta_{x,y}$	8.3 m
half aperture (hor. $\times$ vert.)	25×15 mm
dipole length	3 m
dipole field	0.205 T
quadrupole length	0.2 m
quadrupole gradient	19.2 Tm^{-1}

Table 2.4: Optics and magnet parameters for the arc sections.

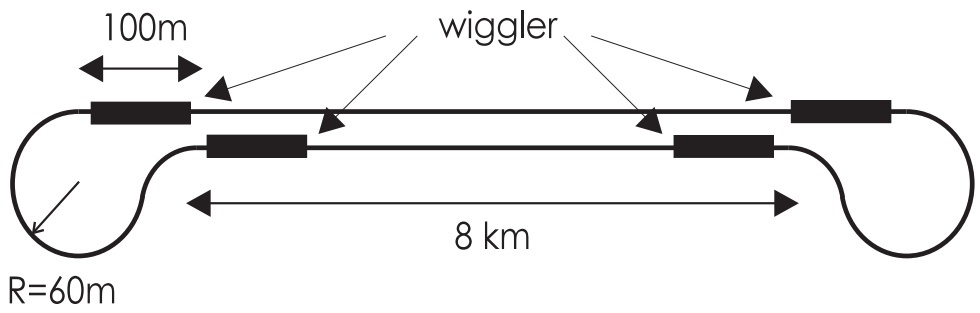

Figure 2.4: Wiggler sections in the "dog-bone"-shaped damping ring.

Wiggler Sections

The wiggler sections are shown schematically in Figure 2.4. The 388 m long wiggler section has been designed in such a way that the requirements for the damping integral and the horizontal emittance are safely achieved [1].
For a wiggler with an approximately rectangular field shape (the period length $\lambda_{\mathrm{w}} = 0.4\,\mathrm{m}$ is large compared to the gap height $g_{\mathrm{w}} = 25\,\mathrm{mm}$), the emittance is given by:

$$\gamma\epsilon_x = 2.22 \cdot 10^{-6}\,\mathrm{m} \times B_{\mathrm{w}}^3 \lambda_{\mathrm{w}}^2 \beta_{x,\mathrm{w}}\,, \tag{2.7}$$

where $\beta_{x,\mathrm{w}}$ denotes the horizontal beta function averaged over the wiggler length. A $\beta_{x,\mathrm{w}}$ of about 10 m is required, which is met by a FODO lattice with a cell length of about 10 m and a phase advance of 60° (the peak field B_{w} is 1.5 T). The same quadrupoles as in the arcs can be used here. Sufficient reserve for the focusing strength is provided, thus allowing to reduce $\beta_{x,\mathrm{w}}$ and, therefore, the horizontal emittance for the upgrade (new) TESLA parameter set.
The aluminium chamber through the wiggler magnets is water-cooled and has a vertical aperture of about 20 mm.

2.4 Rf System

The rf system has to provide a circumferential voltage of 25 MV and an average power of 1.24 MW to the beam (see Table 2.2). The choice of the rf frequency of $f_{\mathrm{rf}} = 433\,\mathrm{MHz}$, is motivated by having an integer fraction of the main linac frequency (1.3 GHz = 3 × 433 MHz) and by the availability of high power klystrons. The choice of accelerating cavities has to take into account multibunch effects due to higher-order cavity modes (HOMs). This thesis focuses on the concept of using 4-cell superconducting cavities very similar to the ones installed at HERA [6, 7] (but scaled in frequency from 500 MHz to 433 MHz). Other concepts are briefly addressed in [1].
A total of 8 cavities with 4-cells each are needed if a power limit per cavity of about 150 kW is assumed. The length of one 4-cell cavity is $4(\lambda_{\mathrm{rf}}/2) = 1.39\,\mathrm{m}$ and the required accelerating gradient amounts to 2.25 MV/m.

Chapter 3

Longitudinal Dynamics in Electron Storage Rings

3.1 Introduction

The motion of a single particle in a storage ring is determined by the external guide fields created by the magnets and the rf system, by the initial conditions, by synchrotron radiation, and by the interaction with its surroundings.
The many particles contained in a high intensity beam represent a sizeable charge and current which act as a source of electromagnetic fields, which are modified by the boundary conditions imposed by the beam surroundings (vacuum chambers, cavities, etc.) and act back on the beam. These fields are called *wake fields* and they can lead to a *frequency shift* (change of the betatron (Glossary, page 169) or synchrotron frequency (Glossary, page 173)), to an increase of a small disturbance of the beam (i.e. an instability) or a change of the particle distribution (e.g. bunch lengthening). These phenomena are called *collective effects* since they are caused by a collective action of the particles in the beam.

The concept of this chapter is as follows. To begin with, an insight into the longitudinal dynamics of particles in an electron storage ring is given; collective effects are not considered. The aim of the following section is to introduce the basic terminology and supply the necessary background information in connection with wake fields, so that the collective effects described in the remaining part are better understood. The section is split into five parts. The first is devoted to the time domain description of wake fields, the second to the frequency domain. The third specializes on the long-range behaviour of cavity wake fields and is complemented by Appendix C.1. In the fourth subsection, we introduce an equivalent circuit model for the accelerating mode. This leads to the topic of *beam loading* which is discussed in the fifth and last subsection. The effect of the long-range fields on the bunch train is the subject of Section 3.4, where a one-particle model is introduced by which multibunch instabilities may by estimated. The remaining two sections look at single bunch effects. First, the Vlasov equation is introduced, which describes the collective behaviour of a multiparticle system under the influence of electromagnetic forces. As an application, the distortion of the equilibrium shape of a beam bunch under the influence of longitudinal wake fields is studied and the Haissinski

equation [8] is derived.

3.2 Basic Longitudinal Dynamics

This section is based primarily on the presentations in [5, 9, 10, 11, 12, 13, 14].

Synchrotron Oscillation and Radiation Damping

A major rôle in the theory of longitudinal dynamics is played by the so-called *synchronous particle*. This is a fictitious particle which has exactly the *nominal energy* E_b, and follows the design orbit turn after turn with the *nominal revolution period* T_0. Therefore, it arrives at the cavities in such a manner that it always sees the same *synchronous phase* ϕ_s.
All other particles are related to the synchronous particle by their *energy deviation* $\varepsilon = E - E_\mathrm{b}$ and their *time displacement* τ. A particle ahead of the synchronous particle is depicted by a positive τ. These deviations are not constant, but change from turn to turn.
To begin with, a particle's time displacement depends on its energy deviation ε. A particle with a momentum deviation Δp is radially displaced by $\Delta x = D\Delta p/p$ with the dispersion D. As a result, the orbit length L, the revolution time, and the *revolution frequency* ω are changed. The relative change in path length with regard to the relative change in momentum of a particle is given by the momentum compaction factor α_c,

$$\frac{\Delta L}{L} = \alpha_\mathrm{c}\frac{\Delta p}{p}. \tag{3.1}$$

It is

$$\frac{\Delta T}{T_0} = \frac{\Delta L}{L} - \frac{\Delta v}{v} = \left(\alpha_\mathrm{c} - \frac{1}{\gamma^2}\right)\frac{\Delta p}{p} = \left(\alpha_\mathrm{c} - \frac{1}{\gamma^2}\right)\frac{1}{\beta^2}\frac{\Delta E}{E_\mathrm{b}} \tag{3.2}$$

with the relativistic factors β and γ and to first order

$$\frac{\Delta\omega}{\omega_0} = -\frac{\Delta T}{T_0},$$

where ω_0 is the nominal revolution frequency. Setting $\varepsilon = \Delta E$ and averaging over one turn, one has

$$\frac{d\tau}{dt} = \frac{\eta}{E_\mathrm{b}}\varepsilon, \tag{3.3}$$

where

$$\eta = \frac{1}{\beta^2}\left(\alpha_\mathrm{c} - \frac{1}{\gamma^2}\right) \tag{3.4}$$

is the *slippage factor*.
Throughout the rest of this section it will be assumed that $\beta = 1$ as the particles being studied are highly relativistic. Consequently, the corresponding factor in Eq. (3.4) will be

dropped in future references, as it is equal to one. In this connection, it is also justified to drop the term $1/\gamma^2$ in the definition of the slippage factor, and to use the momentum compaction factor in formulae instead.
As will be seen in the following, the time development of a particle's energy deviation depends on the current value as well as its time displacement.
The first term to be looked at is that of the synchrotron radiation. Let P_γ stand for the rate of loss of energy by radiation. It may be written as

$$P_\gamma = \frac{e^2 c^3}{2\pi} C_\gamma E^2 B_y^2 \quad \text{or as} \quad P_\gamma = \frac{c C_\gamma}{2\pi} \frac{E^4}{\rho^2} \tag{3.5}$$

using the local radius of curvature ρ and with

$$C_\gamma = \frac{4\pi}{3} \frac{r_0}{(mc^2)^3}$$

from page 10. The synchrotron radiation loss during one turn is

$$U_{\mathrm{rad}}(E) = \oint P_\gamma \, dt. \tag{3.6}$$

The synchronous particle radiates the energy

$$U_0 = \frac{(ec)^2 C_\gamma E_{\mathrm{b}}^2}{2\pi} \oint B_{y0}^2(s) ds. \tag{3.7}$$

Although, strictly speaking, the energy cannot remain at E_{b}, nor the trajectory remain on the design orbit, the deviations during one revolution can often be neglected.
A particle with an energy deviation $\varepsilon = E - E_{\mathrm{b}}$ suffers in linear approximation a radiation loss of

$$U_{\mathrm{rad}}(\varepsilon) = U_0 + \left(\frac{dU_{\mathrm{rad}}}{dE} \right)_0 \varepsilon = U_0 \left(1 + \frac{J_\varepsilon}{E_{\mathrm{b}}} \varepsilon \right), \tag{3.8}$$

where the damping partition number $J_\varepsilon = 2$ for the dog-bone ring. Higher energies are accompanied by an increase in energy loss due to synchrotron radiation, lower energies by a decrease in energy loss.
The second term to be studied is the energy gain in the cavities. The synchronous particle is characterized by the fact that the energy gain and U_0 cancel each other, whereby the synchronous phase ϕ_{s} is determined:

$$\sin \phi_{\mathrm{s}} = U_0 / (e V_{\mathrm{rf}}), \tag{3.9}$$

V_{rf} being the peak voltage, and assuming a sinusoidal voltage.
As will still be seen, the synchronous phase must be located in the second quadrant (90° – 180°) as the solution in the first quadrant (0° – 90°) does not lead to stable oscillations.
A particle at the cavities with the time deviation τ gains the energy

$$e V_{\mathrm{rf}} \sin(\phi_{\mathrm{s}} + \omega_{\mathrm{rf}} \tau) \tag{3.10}$$

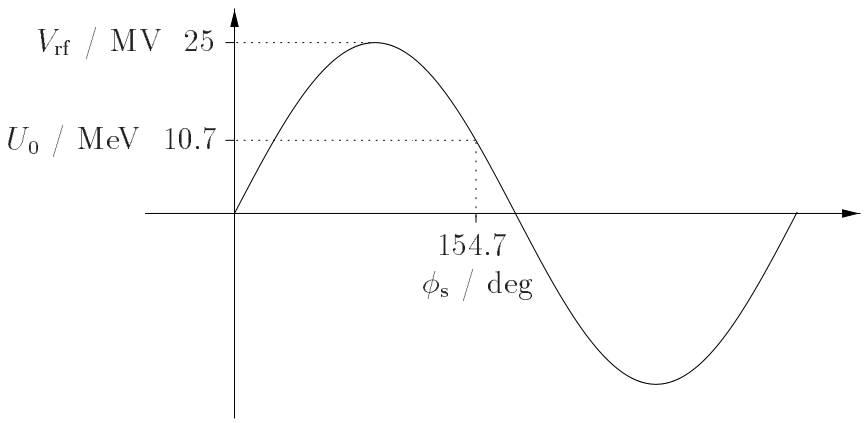

Figure 3.1: Rf voltage in the dog-bone damping ring.

and the energy change averaged over a complete turn is

$$\frac{d\varepsilon}{dt} = \frac{1}{T_0}\left(eV_{\rm rf}\sin(\phi_{\rm s}+\omega_{\rm rf}\tau) - U_0 - \left(\frac{dU_{\rm rad}}{dE}\right)_0 \varepsilon\right). \tag{3.11}$$

For small τ, Eq. (3.10) can be approximated by

$$eV_{\rm rf}\sin\phi_{\rm s} + \omega_{\rm rf}\tau eV_{\rm rf}\cos\phi_{\rm s} = U_0 + \omega_{\rm rf}\tau eV_{\rm rf}\cos\phi_{\rm s} \tag{3.12}$$

and Eq. (3.11) is replaced by

$$\frac{d\varepsilon}{dt} = \frac{\omega_0^2 h e V_{\rm rf}\cos\phi_{\rm s}}{2\pi}\tau - \frac{1}{T_0}\left(\frac{dU_{\rm rad}}{dE}\right)_0 \varepsilon, \tag{3.13}$$

where the *harmonic number* $h = \omega_{\rm rf}/\omega_0$ is the ratio of the rf to the revolution frequency. Introducing the *synchrotron frequency*

$$\omega_{\rm s0} = \sqrt{\frac{-h\alpha_{\rm c}\omega_0^2 eV_{\rm rf}\cos\phi_{\rm s}}{2\pi E_{\rm b}}} \tag{3.14}$$

and the *damping rate*

$$\alpha_\varepsilon = \frac{1}{2T_0}\left(\frac{dU_{\rm rad}}{dE}\right)_0, \tag{3.15}$$

which defines the rate of change of energy loss with energy to first order, Eqs. (3.3) and (3.13) can be combined into the following second-order differential equation

$$\frac{d^2\varepsilon}{dt^2} + 2\alpha_\varepsilon\frac{d\varepsilon}{dt} + \omega_{\rm s0}^2\varepsilon = 0. \tag{3.16}$$

The solution is

$$\varepsilon(t) = A\exp(-\alpha_\varepsilon t)\cos(\omega_{\rm s0}\sqrt{1-(\alpha_\varepsilon/\omega_{\rm s0})^2}t - \phi), \tag{3.17}$$

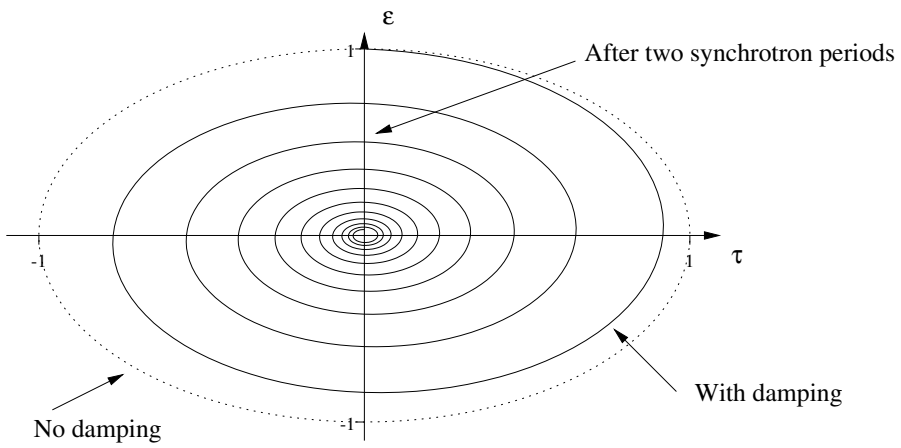

Figure 3.2: The longitudinal phase space, with and without damping. The coordinates have been normalized. The synchrotron frequency is that of the dog-bone damping ring, but the damping rate is ten times that of the damping ring.

where A and ϕ are constants.
As the damping rate in a storage ring is typically low ($\alpha_\varepsilon \ll \omega_{s0}$), the solution may be approximated by

$$\varepsilon(t) = A \exp(-\alpha_\varepsilon t) \cos(\omega_{s0} t - \phi). \tag{3.18}$$

Similarly one gets

$$\tau(t) = \frac{\alpha_c}{E_b \omega_{s0}} A \exp(-\alpha_\varepsilon t) \sin(\omega_{s0} t - \phi). \tag{3.19}$$

Equations (3.18) and (3.19) describe the longitudinal motion (time and energy deviation) of a single particle which sees no wake fields in the storage ring.

In order to ensure stable motion, the synchrotron frequency must be real, which means that $\alpha_c \cos\phi_s$ must be negative. $\frac{1}{2}\pi < \phi_s < \pi$ is required for stable synchrotron phase motion (phase focusing). That means that the synchronous phase is on the time-falling part of the rf-voltage wave. For example, a particle having too much energy, compared to the synchronous particle, will follow a longer path, and will receive, by comparison to the just obtained energy from the rf cavity, less on the next revolution. A particle that arrives too early, compared to the synchronous particle, will see more energy than the latter at the rf cavities, and will follow on the next revolution a longer path than that just accomplished. The time deviation growth due to the new turn will, therefore, be larger than on the previous one, eventually resulting – if not already the case – in a diminishing negative time deviation.
Neglecting the damping term α_ε, the electron will oscillate in time and energy with a fixed amplitude and synchronous frequency. The ratio of the synchronous frequency to the revolution frequency is called the *synchronous tune*, $\nu_{s0} = \omega_{s0}/\omega_0$.
If damping is included, the electron will spiral towards the orbit of a synchronous electron.

A short outline of how the damping rate and its inverse, the damping time T_ε, are determined is given in the following.
When the energy of a particle deviates from the nominal energy E_b, the energy loss changes because of several factors. First, the energy loss is itself a function of energy, and second, because the orbit deviates from the reference orbit, there may be a change in magnetic field and a change in path length. Taking these facts into account, one arrives at the solution (see [5, p. 346f])

$$\alpha_\varepsilon = \frac{U_0}{2T_0E_\mathrm{b}}(2+\mathcal{D}) \tag{3.20}$$

with

$$\mathcal{D} = \frac{\oint DG(G^2-2k)ds}{\oint G^2 ds}. \tag{3.21}$$

$\mathcal{D}$ is a property of the total guide-field configuration – obtained from integrations around the ring of expressions involving only the guide-field functions $D(s)$, the dispersion function, $G(s)$, the curvature function, and $k(s)$, the negative rate of change of the inverse radius with radial displacement:

$$k(s) = \frac{-ec}{E_\mathrm{b}}\left(\frac{\partial B_y}{\partial x}\right)_{0s}.$$

For separate function magnets (Glossary, page 172) and strong focusing (Glossary, page 173), as in the TESLA damping ring, $\mathcal{D}$ is approximately zero; it is $J_\varepsilon = 2+\mathcal{D}$ (see Eqs. (3.8), (3.15), and (3.20)).

Note that if the energy loss of a particle is generalized to accommodate the losses due to an impedance, then to first order (in a region where this applies) a term $-(\partial U/\partial t)\tau$ would need to be added in the numerator of Eq. (3.11). In Eq. (3.16) $\omega_{\mathrm{s}0}^2$ – where $\omega_{\mathrm{s}0}$ denotes the undisturbed synchrotron frequency – would be replaced by

$$\omega_{\mathrm{s}0}^2 - \frac{\omega_0}{2\pi}\frac{\alpha_\mathrm{c}}{E_\mathrm{b}}\frac{\partial U}{\partial t},$$

and the synchrotron frequency in Eq. (3.18) would be [10]

$$\omega_\mathrm{s} \approx \omega_{\mathrm{s}0} + \frac{1}{2}\frac{\omega_0}{2\pi}\frac{\alpha_\mathrm{c}}{\omega_{\mathrm{s}0}E_\mathrm{b}}\frac{\partial U}{\partial t}.$$

Quantum Excitation

Radiation damping is related to the average loss of energy due to synchrotron radiation, and so does not take into account that energy is lost in discrete "quanta" (photons) at random times and energies. This discontinuous energy change from the emission of a quantum disturbs the trajectory of the electron. The cumulative effect of many such

disturbances introduces a kind of "noise" into the various oscillation modes, causing their amplitudes to grow until the quantum excitation is, on average, balanced by the damping of the oscillations [5].
Summarizing:

- The damping effect is linearly proportional to the energy loss $\delta\varepsilon$, and so the total effect depends on the sum of these events, $\sum_i (\delta\varepsilon)_i$, and, therefore, on the total energy loss per turn U_0, independent of the energy distribution of the photons.
- The quantum effect leads to fluctuations in the radiation around its average, i.e. $(\Delta\varepsilon)^2 = \langle(\delta\varepsilon)^2\rangle - \langle\delta\varepsilon\rangle^2$, so the total effect is no longer simply related to the total energy loss per turn.

The combined effect of quantum excitation and radiation damping leads to a stable equilibrium. For basic approaches see refs. [5, 13].

Relative Energy Deviation, Synchrotron Radiation Integrals

The quantum emissions are independent of each other and, therefore, present a purely stochastic (Poisson) process, hereby yielding a Gaussian distribution of the energy deviation.
The relative energy deviation is given by:

$$\sigma_E = \frac{\sigma_\varepsilon}{E_\mathrm{b}} = \sqrt{C_\mathrm{q}\gamma^2 \left(\frac{I_3}{2I_2 + I_4}\right)}, \tag{3.22}$$

where the constant

$$C_\mathrm{q} = \frac{55}{32\sqrt{3}}\frac{\hbar}{mc} = 3.84 \times 10^{-13}\,\mathrm{m} \quad \text{(electrons)} \tag{3.23}$$

and the so-called synchrotron radiation integrals are

$$I_2 = \oint G^2 ds, \quad I_3 = \oint |G|^3 ds, \quad \text{and} \quad I_4 = \oint DG(G^2 - 2k) ds.$$

An absolute value in I_3 has been included, so that the correct value is obtained for elements with an opposite curvature to that of the main bending magnets (e.g. in insertion devices). Note that $I_4/I_2 = \mathcal{D}$ so that $J_\varepsilon = 2 + I_4/I_2$, which reduces to $J_\varepsilon = 2$ for the dog-bone ring. Besides the synchrotron radiation damping time T_ε one can express the damping times τ_x and τ_y with the help of the synchrotron radiation integrals (see [13]).
For an isomagnetic lattice, Eq. (3.22) simplifies to

$$\sigma_E^2 = \frac{C_\mathrm{q}\gamma^2}{J_\varepsilon \rho}. \tag{3.24}$$

The result of Eq. (2.6) is based upon this assumption (use $E = \gamma mc^2$ and $1/\rho = ecB_y/E$).

Bunch Length

The Gaussian distribution in energy results in a similar distribution in the time deviation τ, and hence a Gaussian bunch shape in the longitudinal direction with the standard deviation given by:

$$\sigma_t = \frac{\alpha_c}{\omega_{s0}}\sigma_E \quad \text{or equivalently} \quad \sigma_z = \frac{\alpha_c C}{2\pi\nu_{s0}}\sigma_E \tag{3.25}$$

with the synchrotron tune ν_{s0}.
Recall that in the absence of damping, an electron executes a harmonic oscillation which is represented in the longitudinal phase space by an ellipse. With the scaled time displacement

$$\widetilde{\tau} = \frac{\omega_{s0} E_b}{\alpha_c}\tau$$

the ellipses become circles. The distribution of particles in ε and $\widetilde{\tau}$ is given by a density $\Psi(\varepsilon,\widetilde{\tau})d\varepsilon d\widetilde{\tau}$ which describes the number of particles in the area $d\varepsilon d\widetilde{\tau}$. The projection of $\Psi(\varepsilon,\widetilde{\tau})$ on the ε axis is known to be Gaussian and must be the same for the $\widetilde{\tau}$ axis.
It should be noted that the energy spread and bunch length from equations (3.22) and (3.25) are their equilibrium values at low currents. As the intensity of the bunch increases, collective effects have to be included which modify these expressions; beam induced fields can distort the bunch shape even while the energy spread remains approximately Gaussian.
The rms emittance of the injected bunch is the area in phase space that the bunch occupies divided by π and is given by

$$\varepsilon_l = \sigma_t \sigma_\varepsilon$$

where σ_τ is the rms length of the bunch and σ_ε is the rms energy deviation of the bunch.

Hamiltonian, Rf Bucket

The longitudinal dynamics of a storage ring can also be studied by looking at the *Hamiltonian* of the system. This leads to the introduction of the terms *rf bucket* and *energy/momentum acceptance*. These are extremely important with regard to studying the motion of particles with comparatively large offsets from the nominal values. This can be, for example, the case when particles are injected into the system. Hence, the aim must be to determine the phase space area where stable motion is possible, the rf bucket, and the area where particles are eventually lost. The border line in phase space is given by the *separatrix*.
Note that the differential equation (3.16) and equations of motion (3.18) and (3.19) were obtained based on the premise that the amplitudes of the deviations were small enough that linear approximation of the rf voltage was possible. In the cases to be studied this may no longer be possible; therefore, one needs to return to the Eqs. (3.3) and (3.11).
Multiplying Eqs. (3.3) and (3.11), neglecting the damping term, that is

$$\dot{\varepsilon} = \frac{eV_{rf}\sin(\phi_s + \omega_{rf}\tau) - U_0}{T_0} \tag{3.26}$$

crosswise leads to

$$2\varepsilon\dot{\varepsilon} = \frac{2E_\mathrm{b}}{\alpha_\mathrm{c}T_0}\left(eV_\mathrm{rf}\sin(\phi_\mathrm{s}+\omega_\mathrm{rf}\tau)-U_0\right)\dot{\tau}. \tag{3.27}$$

Integrating once gives:

$$\varepsilon^2 + \frac{2E_\mathrm{b}}{\alpha_\mathrm{c}\omega_\mathrm{rf}T_0}\left(eV_\mathrm{rf}\cos(\phi_\mathrm{s}+\omega_\mathrm{rf}\tau)+\omega_\mathrm{rf}\tau U_0\right) = H' = \text{const.}$$

This expression is a constant of motion and must be directly related to the Hamiltonian. One easily finds that the Hamiltonian is

$$H = \frac{\alpha_\mathrm{c}}{2E_\mathrm{b}}\varepsilon^2 + \frac{1}{T_0\omega_\mathrm{rf}}\left(eV_\mathrm{rf}\cos(\phi_\mathrm{s}+\omega_\mathrm{rf}\tau)+\omega_\mathrm{rf}\tau U_0\right), \tag{3.28}$$

which satisfies the canonical equations

$$\frac{\partial H}{\partial\varepsilon} = \frac{\alpha_\mathrm{c}\varepsilon}{E_\mathrm{b}} = \dot{\tau}, \tag{3.29}$$

$$\frac{\partial H}{\partial\tau} = \frac{1}{T_0}(-eV_\mathrm{rf}\sin(\phi_\mathrm{s}+\omega_\mathrm{rf}\tau)+U_0) = -\dot{\varepsilon}. \tag{3.30}$$

The first term on the right-hand side of Eq. (3.28) is the normalized kinetic energy of the system, the second the potential energy $V(\tau)$. Figure 3.3 shows the potential.

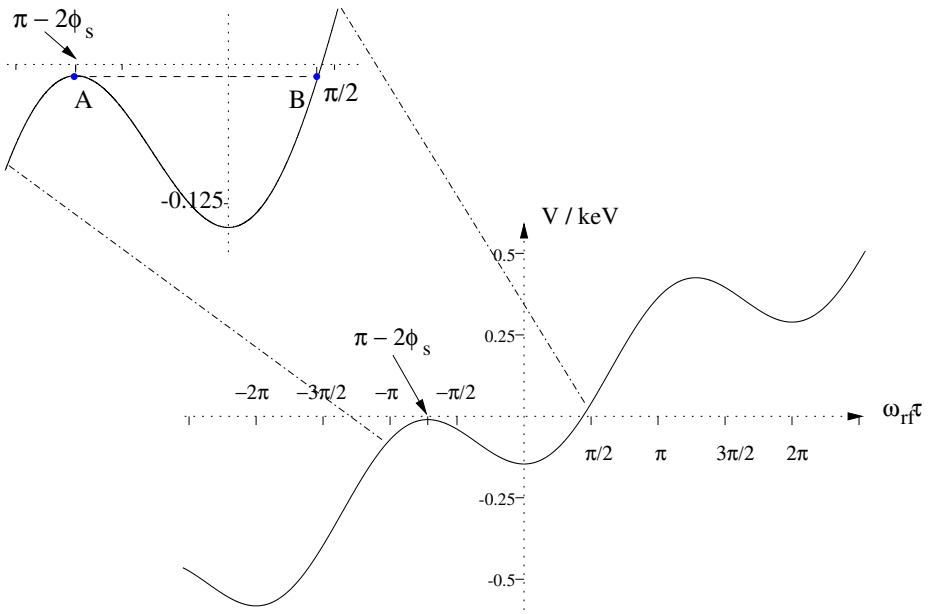

Figure 3.3: The normalized potential energy for the dog-bone ring parameters.

For small amplitudes, $\omega_\mathrm{rf}\tau \ll \pi$, the potential is nearly identical to that of an ideal harmonic oscillator. Growing amplitudes correspond to a more and more nonlinear area, where the potential becomes asymmetrical. The maximum stable phase area is determined

by the points A and B in the diagram. "A" marks a maximum of the potential function and can be determined by differentiating V:

$$\frac{dV}{d\tau} = \frac{1}{T_0\omega_{\mathrm{rf}}}\left(-\omega_{\mathrm{rf}} e V_{\mathrm{rf}} \sin(\phi_{\mathrm{s}} + \omega_{\mathrm{rf}}\tau) + \omega_{\mathrm{rf}} U_0\right) = 0,$$

corresponding to

$$V_{\mathrm{rf}} \sin(\phi_{\mathrm{s}} + \omega_{\mathrm{rf}}\tau) = V_{\mathrm{rf}} \sin(\phi_{\mathrm{s}}).$$

The trivial solution $\tau = 0$ is not of interest, whereas the maximum of the potential is reached for $\tau = \tau_{\max} = (\pi - 2\phi_{\mathrm{s}})/\omega_{\mathrm{rf}}$, i.e. $\phi_{\max} = \pi - 2\phi_{\mathrm{s}}$.
The Hamiltonian in this case can be expressed as

$$\begin{aligned} H &= \frac{1}{T_0\omega_{\mathrm{rf}}}\left(eV_{\mathrm{rf}} \cos(\phi_{\mathrm{s}} + \omega_{\mathrm{rf}}\tau_{\max}) + \omega_{\mathrm{rf}}\tau_{\max} U_0\right) \\ &= \frac{eV_{\mathrm{rf}}}{T_0\omega_{\mathrm{rf}}}\left(\cos(\pi - \phi_{\mathrm{s}}) + (\pi - 2\phi_{\mathrm{s}})\sin\phi_{\mathrm{s}}\right) \end{aligned} \tag{3.31}$$

whereby the separatrix is obtained:

$$\begin{aligned} \varepsilon &= \pm\sqrt{\frac{2E_{\mathrm{b}} eV_{\mathrm{rf}}}{\alpha_{\mathrm{c}} T_0\omega_{\mathrm{rf}}}\left(\cos(\pi - \phi_{\mathrm{s}}) + (\pi - 2\phi_{\mathrm{s}} - \omega_{\mathrm{rf}}\tau)\sin\phi_{\mathrm{s}} - \cos(\phi_{\mathrm{s}} + \omega_{\mathrm{rf}}\tau)\right)} \\ &= \pm\sqrt{\frac{-2eV_{\mathrm{rf}} E_{\mathrm{b}}}{\alpha_{\mathrm{c}} T_0\omega_{\mathrm{rf}}}\big(\cos\phi_{\mathrm{s}} + (2\phi_{\mathrm{s}} + \omega_{\mathrm{rf}}\tau - \pi)\sin\phi_{\mathrm{s}} + \cos(\phi_{\mathrm{s}} + \omega_{\mathrm{rf}}\tau)\big)}. \end{aligned} \tag{3.32}$$

The separatrix for the dog-bone ring is depicted by a solid line in Figure 3.4; the corresponding Hamiltonian is approximately $-10\,\mathrm{eV}$. The dashed lines represent phase trajectories corresponding to constant Hamiltonians. A particle that is injected onto one of these trajectories will remain on it as it moves in phase space (this is, of course, an approximation, since we are not considering disturbances). The values of the corresponding Hamiltonians are -100, -50, and $-25\,\mathrm{eV}$ (inner to outer rings). The dotted lines represent particles which will not be captured in the rf bucket; Hamiltonians: 100, 250, and 500 eV.
The bucket height is obtained by substituting 0 for τ in (3.32). It is

$$\varepsilon_{\max} = \sqrt{\frac{-2eV_{\mathrm{rf}} E_{\mathrm{b}}}{\alpha_{\mathrm{c}} T_0\omega_{\mathrm{rf}}}\big(2\cos\phi_{\mathrm{s}} + (2\phi_{\mathrm{s}} - \pi)\sin\phi_{\mathrm{s}}\big)}, \tag{3.33}$$

which can be transformed to

$$\left(\frac{\varepsilon_{\max}}{E_{\mathrm{b}}}\right)^2 = \frac{2U_0}{\alpha_{\mathrm{c}}\pi h E_{\mathrm{b}}}\left(\sqrt{q^2 - 1} - \arccos(1/q)\right). \tag{3.34}$$

This term is called the energy acceptance of the ring and is approx. 1.5 % for the TESLA damping ring. The overvoltage factor q is the ratio of maximum voltage to synchrotron radiation loss, $q = eV_{\mathrm{rf}}/U_0$. The bucket length is the maximum expansion in phase, depicted by the distance of the points A and B in Figure 3.3.

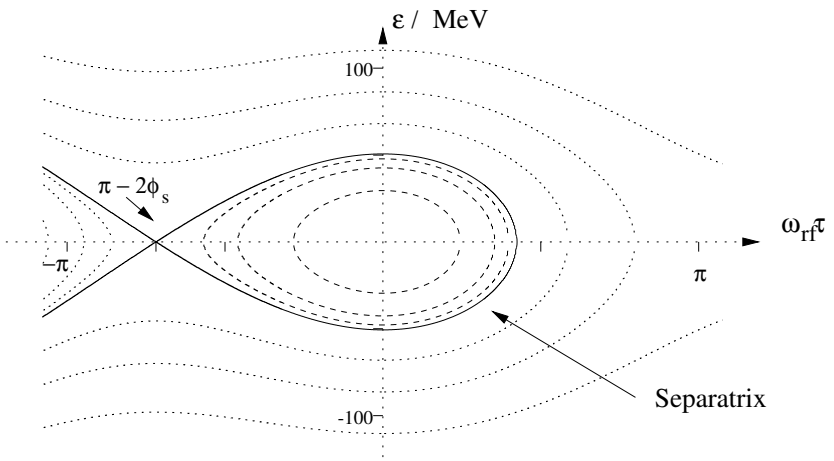

Figure 3.4: Longitudinal phase space diagram for the dog-bone damping ring rf bucket.

3.3 Wake Fields

A charged particle beam interacts electromagnetically with its vacuum chamber surroundings in an accelerator. The generated fields affect the dynamics of the charge itself, and may exert noticeable forces on any trailing particles. The fields are referred to as *wake fields* due to the fact that they are left mainly behind the travelling charge. In the ultra-relativistic limit ($\beta = 1$), causality requires there to be no field in front of the charge. The necessity to study the properties of these fields has been proven in machine operation. An outline is presented in the following.

3.3.1 Wake Functions and Wake Potentials

To begin with, two point charges travelling at the speed βc parallel to the chamber z-axis are considered. The leading (source) charge is denoted by q_1, the second by q (see Figure 3.5).
The electromagnetic fields generated by the leading charge must apply to the Maxwell equations with the appropriate boundary conditions. The Maxwell equations for sources in vacuum read:

$$\vec{\nabla} \times \vec{B} = \mu_0 \vec{j} + \frac{1}{c^2} \frac{\partial}{\partial t} \vec{E} \tag{3.35}$$

$$\vec{\nabla} \cdot \vec{B} = 0 \tag{3.36}$$

$$\vec{\nabla} \times \vec{E} = -\frac{\partial}{\partial t} \vec{B} \tag{3.37}$$

$$\vec{\nabla} \cdot \vec{E} = \frac{1}{\epsilon_0} \rho \tag{3.38}$$

For a point-like particle, the charge and current density are written as:

$$\rho(\vec{r}, z, t) = q_1 \delta^2(\vec{r} - \vec{r}_1) \delta(z - vt) \tag{3.39}$$

$$\vec{j}(\vec{r}, z, t) = \vec{v} \rho(\vec{r}, z, t), \tag{3.40}$$

where δ^2 denotes the Dirac delta function in two dimensions.

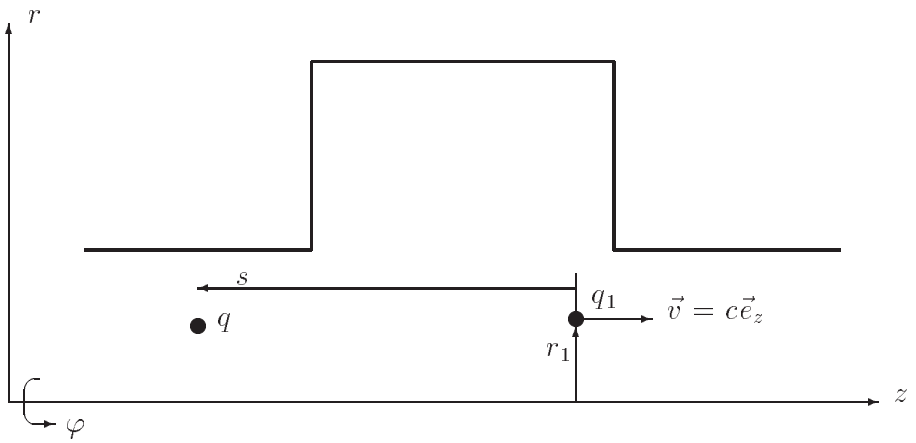

Figure 3.5: A charge q_1 traversing a cavity with offset $\vec{r}_1$ followed by a test charge q with offset $\vec{r}$.

The Lorentz force seen by the test charge q at position $(\vec{r}, z)$ is

$$\vec{F}(\vec{r}, z, \vec{r}_1, z_1, t) = q[\vec{E}(\vec{r}, z, \vec{r}_1, z_1, t) + \vec{v} \times \vec{B}(\vec{r}, z, \vec{r}_1, z_1, t)]. \tag{3.41}$$

Let s be a fixed distance between the leading and trailing charges; at any instant "t" they have the longitudinal coordinates $z_1(t) = vt$ and $z(t) = vt - s$, respectively. We now assume that the transverse coordinates of the two charges are constant whilst passing a structure where the fields are non-zero. This means that the ratio of the betatron oscillation wavelength to the structure length is required to be sufficiently large.
The net effect on the test charge is obtained by integration. This leads to the definition of the *wake function of a point source charge*, which is also referred to as the *delta wake function* (therefore, the subscript δ):

$$\vec{W}_\delta(\vec{r}, \vec{r}_1, s) = \frac{1}{q_1} \int_{-\infty}^{\infty} [\, \vec{E}(\vec{r}, z, \vec{r}_1, t) + \vec{v} \times \vec{B}(\vec{r}, z, \vec{r}_1, t) \,]_{t=(s+z)/v} \, dz \tag{3.42}$$

with $\vec{v} = \beta c \vec{e}_z$. $\vec{W}_\delta$ is sometimes called the *wake potential* of a point source charge (for example in [15, 16]).
In the limit of $\beta \approx 1$, the energy loss, and, as a result, the wake function, are not dependent on the absolute charge coordinates z, z_1, but only on the distance between them (i.e. $s = z_1 - z$).
Note that if both charges have the same radial coordinates $\vec{r} = \vec{r}_1$, the force on the test charge is calculated on the same path as that of the source charge, but just taking account of the time delay s/v.
The wake function describes the normalized shock response of the vacuum chamber environment to a δ-function charge [17] and is measured in V/C. Furthermore, it determines, as indicated above, the momentum kick delivered to the trailing test charge:

$$\Delta\vec{p} = \frac{q_1 q}{c} \vec{W}_\delta(\vec{r}, \vec{r}_1, s). \tag{3.43}$$

The *longitudinal component of the wake function* $W_{\delta,\parallel}$ classifies the work done by the longitudinal electromagnetic forces along the structure

$$W_{\delta,\parallel}(\vec{r},\vec{r}_1,s) = \frac{1}{q_1}\int_{-\infty}^{\infty} E_z(\vec{r},z,\vec{r}_1,(s+z)/\beta c)\,dz. \tag{3.44}$$

The magnetic field does not enter the energy balance because the product $\vec{e}_z \cdot (\vec{e}_z \times \vec{B})$ is zero (the particle trajectories were assumed to be parallel to the z-axis).
The *transverse component of the wake function* $\vec{W}_{\delta,\perp}$ describes the momentum transfer perpendicular to $\vec{e}_z$.

Loss Factor

The source charge itself loses energy – according to Eq. (3.44):

$$U_{11}(\vec{r}_1) = q_1\int_{-\infty}^{\infty} E_z(\vec{r}_1,z,\vec{r}_1,z/\beta c)\,dz.$$

The amount of energy lost by the source charge per unit charge squared is called the *loss factor* $k_{\delta,\parallel}$:

$$k_{\delta,\parallel}(\vec{r}_1) = \frac{-U_{11}(\vec{r}_1)}{q_1^2}. \tag{3.45}$$

It has the same units as the wake function, V/C.
In the ultrarelativistic limit ($\beta = 1$) it has been proven that [18]:

$$k_{\delta,\parallel}(\vec{r}_1) = \frac{-W_{\delta,\parallel}(\vec{r}_1,0^+)}{2}. \tag{3.46}$$

This is referred to as the *fundamental theorem of beam loading*. More details are to be found in [16, 19].

Panofsky-Wenzel Theorem and Other Properties

In the following, the dependency on the source charge has been omitted.
It is worth noting that knowledge of the longitudinal component of the wake function is sufficient, as the transverse component can be obtained from the former when the transverse electric field vanishes at the boundaries:

$$\frac{\partial}{\partial s}\vec{W}_{\delta,\perp}(\vec{r},s) = -\vec{\nabla}_\perp W_{\delta,\parallel}(\vec{r},s). \tag{3.47}$$

This is known as the *Panofsky-Wenzel theorem*, the proof of which is as follows. According to Faraday's law of induction, Eq. (3.37),

$$\vec{e}_z \times \frac{\partial}{\partial t}\vec{B} = \frac{\partial}{\partial z}\vec{E}_\perp - \vec{\nabla}_\perp E_z$$

so that

$$\begin{aligned}
\frac{\partial}{\partial s}\vec{W}_{\delta,\perp}(\vec{r},s) &= \frac{1}{q_1}\int_{-\infty}^{\infty}\frac{\partial}{\partial s}\vec{E}_\perp\big(\vec{r},z,\frac{z+s}{v}\big)+\vec{e}_z\times v\frac{\partial}{\partial s}\vec{B}_\perp\big(\vec{r},z,\frac{z+s}{v}\big)\,dz\\
&= \frac{1}{q_1}\int_{-\infty}^{\infty}\left(\frac{\partial}{\partial s}+\frac{\partial}{\partial z}\right)\vec{E}_\perp\big(\vec{r},z,\frac{z+s}{v}\big)-\vec{\nabla}_\perp E_z\big(\vec{r},z,\frac{z+s}{v}\big)\,dz\\
&= \frac{1}{q_1}\int_{-\infty}^{\infty}\left(\frac{d}{dz}\vec{E}_\perp\big(\vec{r},z,\frac{z+s}{v}\big)\right)-\vec{\nabla}_\perp E_z\big(\vec{r},z,\frac{z+s}{v}\big)\,dz\\
&= -\vec{\nabla}_\perp W_{\delta,\|}\big(\vec{r},z,\frac{z+s}{v}\big)+\frac{1}{q_1}\vec{E}_\perp\big(\vec{r},z,\frac{z+s}{v}\big)\Big|_{-\infty}^{\infty}.
\end{aligned}$$

Another important property of the longitudinal wake function is that in the ultrarelativistic limit it is a *harmonic function of the transverse coordinates* [16]:

$$\begin{aligned}
\vec{\nabla}_\perp^2 W_{\delta,\|}(\vec{r},s) &= \frac{1}{q_1}\int_{-\infty}^{\infty}\vec{\nabla}_\perp^2 E_z(\vec{r}_1,z,(s+z)/\beta c)\,dz &\text{(3.48a)}\\
&= 0+O(\gamma^{-2}). &\text{(3.48b)}
\end{aligned}$$

The proof hereof can, for example, also be found in [20].

Monopole Longitudinal Wake Function

As this thesis focuses on longitudinal dynamics, it is the longitudinal wake function which is of utmost interest. Now, generally it can be verified that during machine operation, with the help of orbit correction algorithms, the beam is only slightly displaced from the axis. Moreover, in a lot of cases of interest, where wake fields occur, it is in cylindrical symmetric structures – as in the case of the assumed rf cavity for the dog-bone. Accordingly, the longitudinal wake function can be expanded around the axis in a multipole series. Here, the property of being a harmonic function is very useful. If the beam path area includes the symmetry axis $r=0$ and extends to the beam pipe radius r_p, it can be shown that for particle offsets r_1, r_2 smaller than r_p, the wake function of a point charge can be expressed as [16, 21]:

$$W_{\delta,\|}(r_1,r_2,\phi_1,\phi_2,s)=\sum_{m=0}^{\infty}r_1^m r_2^m W_{\delta,\|}^m(s)\cos(m(\phi_2-\phi_1)). \tag{3.49}$$

The dominant term of the expansion is that produced by a charge on the axis, $W_{\delta,\|}^0$. Appropriately, it is called the monopole wake. The $m=1$ wake is called the dipole wake. The monopole wake function is the one which will be studied and used with respect to the longitudinal dynamics of the electrons in the storage ring; therefore, the radius dependencies of the above source and test charges are equal to zero, and they are omitted in the following. In principal, the wake functions throughout the remaining text should be labeled with an index "0", but this has been omitted for obvious reasons. Further details are to be found in [16, 19].

Arbitrary Charge Distributions

Similar to the wake functions, the *wake potentials* are defined as integrals over the forces exerted by the wake fields at the position of a test charge. These wake fields are generated by an arbitrary charge distribution.
We can obtain the wake potential of an arbitrary charge distribution by convolution of the line-charge density of the distribution with the delta wake function. Let λ be the normalized charge density (i.e. $\int \lambda(z)dz = 1$). Then the wake potential of the charge distribution (e.g. a bunch) is given by

$$W_{\lambda,\parallel}(s) = \int_{-\infty}^{\infty} \lambda(s-z) W_{\delta,\parallel}(z)\, dz; \tag{3.50}$$

the delta wake function serves as a Green's function.
The loss factor of the charge distribution is derived by applying the superposition principle, i.e. just the wake potential weighted by the normalized charge density:

$$k_{\lambda,\parallel} = -\int_{-\infty}^{\infty} \lambda(s) W_{\lambda,\parallel}(s)\, ds \tag{3.51a}$$

$$= -\int_{-\infty}^{\infty} \lambda(s) \int_{-\infty}^{\infty} \lambda(s-z) W_{\delta,\parallel}(z)\, dz\, ds. \tag{3.51b}$$

3.3.2 Impedance

Just as the longitudinal and transverse wake functions describe the time domain, the so-called longitudinal and transverse (coupling) impedances describe the frequency domain. The longitudinal relationships (with $\beta = 1$) are

$$Z_{\parallel}(\omega) = \frac{-1}{c} \int_{-\infty}^{\infty} W_{\delta,\parallel}(s) e^{-i\omega s/c}\, ds \tag{3.52}$$

and

$$W_{\delta,\parallel}(s) = \frac{-1}{2\pi} \int_{-\infty}^{\infty} Z_{\parallel}(\omega) e^{i\omega s/c}\, d\omega. \tag{3.53}$$

For the transverse impedance, it is often convenient to use a definition with an extra factor $-i$ [16]:

$$\vec{Z}_{\perp}(\vec{r},\omega) = \frac{i}{c} \int_{-\infty}^{\infty} \vec{W}_{\delta,\perp}(\vec{r},s) e^{-i\omega s/c}\, ds \tag{3.54}$$

because then the Panofsky-Wenzel theorem reads in the frequency domain

$$\frac{\omega}{c} \vec{Z}_{\perp}(\vec{r},\omega) = \vec{\nabla}_{\perp} Z_{\parallel}(\vec{r},\omega). \tag{3.55}$$

A direct consequence of the wake function being a real function is that the real part of the impedance is necessarily an even function of the frequency, whilst the imaginary part is an odd function:

$$\mathfrak{Re} Z_{\parallel}(\omega) = \mathfrak{Re} Z_{\parallel}(-\omega), \qquad \mathfrak{Im} Z_{\parallel}(\omega) = -\mathfrak{Im} Z_{\parallel}(-\omega).$$

Hence, the wake function in terms of the impedance is:

$$W_{\delta,\|}(s) = \frac{-1}{2\pi}\int_{-\infty}^{\infty} Z_{\|}(\omega)e^{i\omega s/c}d\omega$$
$$= \frac{-1}{2\pi}\int_{-\infty}^{\infty} \left(\mathfrak{Re}Z_{\|}(\omega)\cos(\omega s/c) - \mathfrak{Im}Z_{\|}(\omega)\sin(\omega s/c)\right) d\omega. \qquad (3.56)$$

Furthermore, in the ultrarelativistic case due to causality, the real and imaginary components are not independent of one another. Due to $W_{\delta,\|}(s) = 0$ for all $s < 0$ it follows that:

$$\int_{-\infty}^{\infty} \mathfrak{Re}Z_{\|}(\omega)\cos\left(\frac{\omega s}{c}\right) d\omega = -\int_{-\infty}^{\infty} \mathfrak{Im}Z_{\|}(\omega)\sin\left(\frac{\omega s}{c}\right) d\omega \qquad \text{for all } s > 0.$$

Eq. (3.56) can now be rewritten as:

$$W_{\delta,\|}(s) = \frac{-1}{\pi}\int_{-\infty}^{\infty} \mathfrak{Re}Z_{\|}(\omega)e^{i\omega s/c}d\omega. \qquad (3.57)$$

The loss factor of a charge distribution in terms of the impedance is as follows:

$$k_{\lambda,\|} = \frac{1}{2\pi}\int_{-\infty}^{\infty} |\tilde{\lambda}(\omega)|^2\, Z_{\|}(\omega)\, d\omega \qquad (3.58)$$
$$= \frac{1}{\pi}\int_{0}^{\infty} |\tilde{\lambda}(\omega)|^2\, \mathfrak{Re}Z_{\|}(\omega)\, d\omega.$$

Thus $k_{\lambda,\|}$ gives the real part of the impedance averaged over the square of the bunch spectrum (Eq. (3.51) and the convolution theorem are used in the derivation).

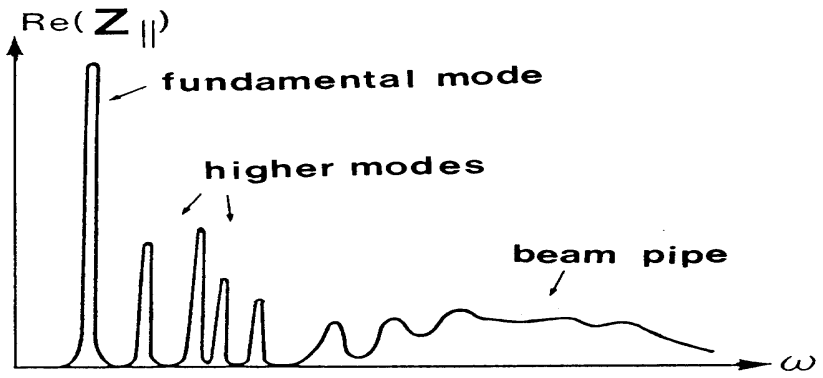

Figure 3.6: Real part of the impedance for a cavity with side pipes. The sharp peaks correspond to cavity modes, while above the cutoff frequency the continuous spectrum of beam pipe modes contribute to the broad-band impedance [16].

The phenomenon impedance is not merely another way of describing wake fields, but can be applied as an extremely useful tool when studying particle dynamics, since the impedance of a machine often contains a number of sharply defined frequencies corresponding to the modes of a cavity, or the long-range part of the wake function.

A typical impedance spectrum is shown in Figure 3.6. The beam pipe at the ends of a cavity is a waveguide with a cutoff frequency of approximately c/a, where a is the radial aperture. Below the cutoff frequency of the beam pipe, cavity modes are reflected by sharp peaks. Above the cutoff frequency, a continuous spectrum of beam pipe modes contribute to the impedance [16].

3.3.3 The Wake of a Single Cavity Mode

Single cavity modes can be described by the means of equivalent electric parallel circuits. The parameters of the circuit, C, L, and R are determined by the loss parameter, the resonance frequency ω_r, and the quality factor Q of the corresponding mode.
The quality factor of a resonant device is defined as:

$$Q = 2\pi \frac{\text{stored energy}}{\text{dissipated energy per cycle}} = \frac{\omega_\mathrm{r} U}{P_\mathrm{diss}}. \tag{3.59}$$

In the particular case of a cavity mode, the averaged stored energy U pertains to the particular mode:

$$U = \frac{\epsilon_0}{2} \int |\underline{\vec{E}}(\vec{r})|^2 d^3 r,$$

where $\vec{E}(\vec{r},t) = \mathfrak{Re}\underline{\vec{E}}(\vec{r}) \exp(i\omega_\mathrm{r} t)$ is the cavity field mode. P_diss is the dissipated power. The complex cavity voltage is given by $\underline{V} = \int \underline{E}_z(z) \exp(i\omega_\mathrm{r} z/c) dz$.
The loss factor of the mode, which is also called the *coupling parameter*, is [16]

$$k_{\delta,\parallel} = \frac{\underline{V}\,\underline{V}^*}{4U}. \tag{3.60}$$

We set the capacity of the equivalent circuit to relate to the loss factor as

$$\frac{1}{C} = 2k_{\delta,\parallel}, \tag{3.61}$$

the resonance frequency of the undamped LC circuit to be $\omega_\mathrm{r} = 1/\sqrt{LC}$, and the impedance R so that

$$Q = \omega_\mathrm{r} RC = \frac{R}{L\omega_\mathrm{r}}. \tag{3.62}$$

Then we have $U = C\underline{V}\,\underline{V}^*/2$ and $P_\mathrm{diss} = \underline{V}\,\underline{V}^*/(2R)$.
By inserting Q in its first form of Eq. (3.62) into Eq. (3.61), we obtain the following relationship for the loss factor:

$$k_{\delta,\parallel} = \frac{\omega_\mathrm{r} R}{2Q}. \tag{3.63}$$

Let us now establish the time dependence of the voltage in the equivalent circuit; in the end we want to obtain the voltage/wake function excited by a point charge.

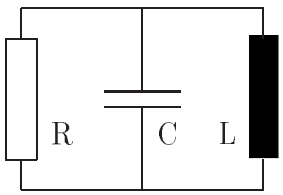

Impedance of the equivalent circuit:

$$\frac{1}{Z} = \frac{1}{R} + \frac{1}{i\omega L} + i\omega C$$

Figure 3.7: Equivalent circuit model for a cavity mode.

Inserting in Kirchhoff's rule

$$I = I_{\mathrm{R}} + I_{\mathrm{C}} + I_{\mathrm{L}} \tag{3.64}$$

the formulae

$$I_{\mathrm{R}}(t) = V(t)/R, \quad I_{\mathrm{C}}(t) = C\dot{V}(t), \quad \dot{I}_{\mathrm{L}}(t) = V(t)/L \tag{3.65}$$

(where it has been taken into account that the voltages in the components are equal) and differentiating once yields

$$\dot{I}(t) = \frac{\dot{V}(t)}{R} + C\ddot{V}(t) + \frac{V(t)}{L}. \tag{3.66}$$

Replacing the inductance L and the capacity C by the quantities Q and ω_{r} leads to the equivalent form

$$\frac{\omega_{\mathrm{r}} R}{Q}\dot{I} = \ddot{V} + 2\Gamma\dot{V} + \omega_{\mathrm{r}}^2 V \tag{3.67}$$

with

$$\Gamma = \frac{\omega_{\mathrm{r}}}{2Q}. \tag{3.68}$$

The solution of this differential equation may be obtained with the help of the Green's function of a damped harmonic oscillator:

$$V(t) = \frac{1}{\bar{\omega}_{\mathrm{r}}} \int_{-\infty}^{t} F(t') \exp[-\frac{\omega_{\mathrm{r}}}{2Q}(t-t')] \sin(\bar{\omega}_{\mathrm{r}}(t-t'))\, dt',$$

with the natural angular frequency

$$\bar{\omega}_{\mathrm{r}} = \sqrt{\omega_{\mathrm{r}}^2 - \Gamma^2} = \omega_{\mathrm{r}}\sqrt{1 - \frac{1}{4Q^2}} \tag{3.69}$$

and

$$F(t) = \frac{\omega_{\mathrm{r}} R}{Q}\dot{I}.$$

The solution for the impulsive excitation of a δ-point charge at the time $t_0 = 0$, i.e. $\dot{I} = -q\delta(t)$, leads to the wake function [22]

$$W_{\delta,\parallel}(t) = \frac{-1}{C} \exp(-\Gamma t) \left(\cos \bar{\omega}_\mathrm{r} t - \frac{\Gamma}{\bar{\omega}_\mathrm{r}} \sin \bar{\omega}_\mathrm{r} t \right) \Theta(t). \tag{3.70}$$

Θ is the step function:

$$\Theta(s) = \begin{cases} 0 & s < 0 \\ 1/2 & s = 0 \\ 1 & s > 0 \end{cases} .$$

For $Q \gg 1$, a simplified formula of the wake function can be used:

$$W_{\delta,\parallel}(t) \approx -2k_{\delta,\parallel} \exp(-\Gamma t) \cos \omega_\mathrm{r} t \ \Theta(t), \tag{3.71}$$

where we have applied Eq. (3.61).
Note that the above defined Γ acts as the attenuation coefficient of the wake function. The wake is depicted for three quality factors in Figure 3.8. Another possibility for obtaining the wake function is by calculating it as the Fourier transform of the circuit impedance (in both cases, see Appendix C.1 for details).

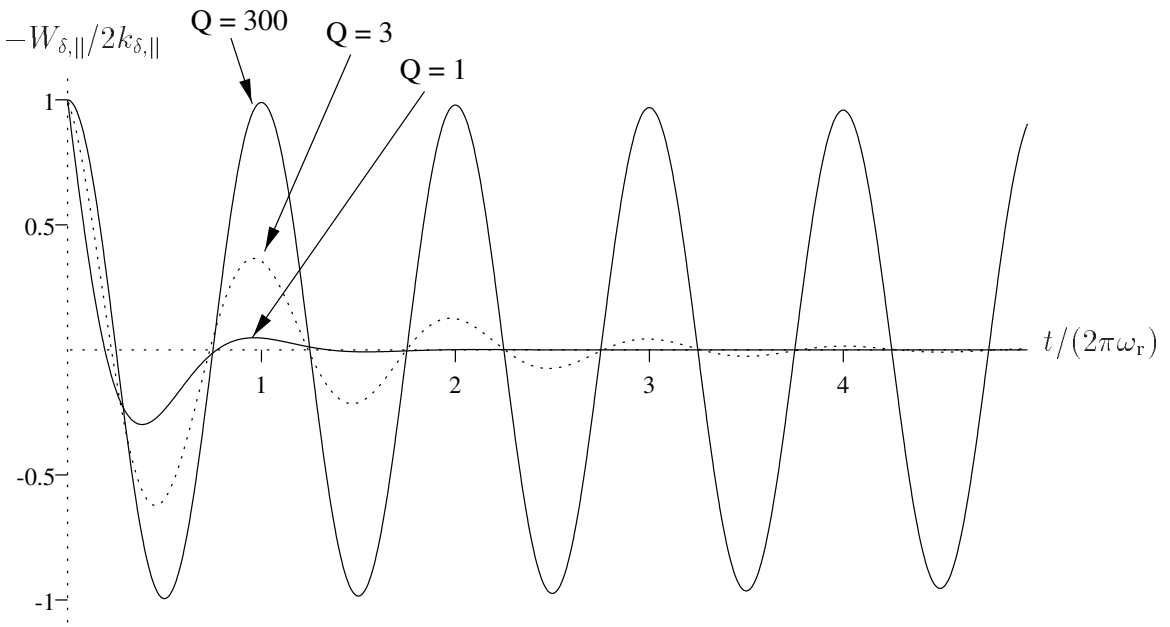

Figure 3.8: Wake function corresponding to a LRC circuit as a model for the δ-wake function of a cavity mode.

Bunch Form Factor

The voltage induced by an arbitrary charge distribution can be related to the charge induced by a point charge using a bunch form factor [18]; the same applies to the wake potential. The voltage at time t induced at time t' by a charge element $dq = q\lambda(t')dt'$ is

$$dV(t) = -2qk_{\delta,\|}\,\lambda(t')\cos(\omega_{\rm r}(t-t'))\,dt', \tag{3.72}$$

where the slow exponential decay (large quality factor) is omitted. The total voltage induced by the charge distribution can be set equal to that induced by a point charge, reduced by a factor $F_{\rm b}$ and located at time t_0 (or at phase $\omega_{\rm r}t_0 = \phi$),

$$V(t) = -2qk_{\delta,\|}\int_{-\infty}^{\infty}\lambda(t')\cos(\omega_{\rm r}(t-t'))\,dt' = -2qk_{\delta,\|}\,F_{\rm b}\cos(\omega_{\rm r}t-\phi). \tag{3.73}$$

Solving for $F_{\rm b}$ and ϕ,

$$F_{\rm b} = \sqrt{C_{\rm S}^2 + C_{\rm A}^2}, \qquad\qquad \tan\phi = \frac{C_{\rm A}}{C_{\rm S}}, \tag{3.74}$$

where $C_{\rm S}$ and $C_{\rm A}$ are the symmetric and antisymmetric integrals

$$C_{\rm S} = \int_{-\infty}^{\infty}\lambda(t')\cos\omega_{\rm r}t'\,dt'; \quad C_{\rm A} = \int_{-\infty}^{\infty}\lambda(t')\sin\omega_{\rm r}t'\,dt'. \tag{3.75}$$

The bunch factor for a Gaussian distribution is

$$F_{\rm b}({\rm Gaussian}) = e^{-\omega_{\rm r}^2\sigma_t^2/2}. \tag{3.76}$$

This means nothing other than in the case of a Gaussian charge distribution adding the factor $\exp(-\omega_{\rm r}^2\sigma_t^2/2)$ in Eq. (3.71).

If a charge distribution having a time-width which is not negligible compared to the rf period is accelerated across a cavity, the average energy gain per electron in the bunch is reduced by the same factor. If $e\widehat{V}\cos(\omega_{\rm r}t)$ is the energy gain by a point particle crossing the cavity, then the charge-weighted average energy gain is

$$eV_{\rm ave} = e\widehat{V}\int_{-\infty}^{\infty}\lambda(t')\cos(\omega_{\rm r}(t-t'))\,dt' = e\widehat{V}\,F_{\rm b}\cos(\omega_{\rm r}t-\phi), \tag{3.77}$$

where $F_{\rm b}$ and ϕ are again given by Eq. (3.74).
It is important to note that, for any charge distribution, both the average accelerating voltage and the net beam-induced voltage are reduced by exactly the same factor with respect to a point charge.
Recalling the discussion on page 29 about arbitrary charge distributions, it is

$$k_{\lambda,\|}({\rm Gaussian}) = e^{-\omega_{\rm r}^2\sigma_t^2}k_{\delta,\|}. \tag{3.78}$$

3.3.4 Accelerating Mode and Equivalent Circuit Model of the Rf System

From calculations with MAFIA [23] one obtains a loss parameter of $k_{\delta,||} = 0.306\,\mathrm{V/pC}$ for the π-mode of one 4-cell cavity. Figure 3.9 shows the accelerating (π) mode of the cavity. The quality factor of the superconducting cavity, Q_0, is of the order 10^9. We will use

$$Q_0 = 1 \times 10^9. \tag{3.79}$$

Q_0 is referred to as the unloaded quality factor.

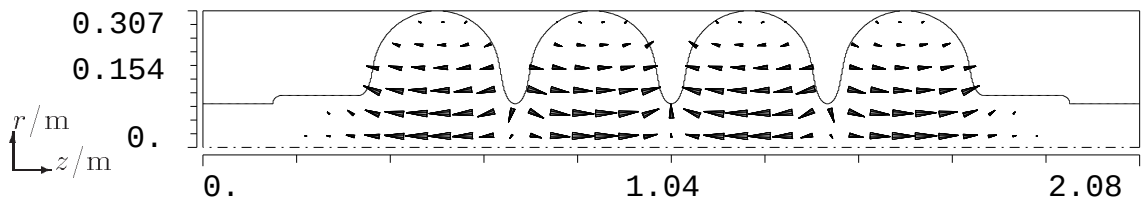

Figure 3.9: Plot of the electric field in a 4-cell cavity. The π-mode has been calculated with the computer code [23].

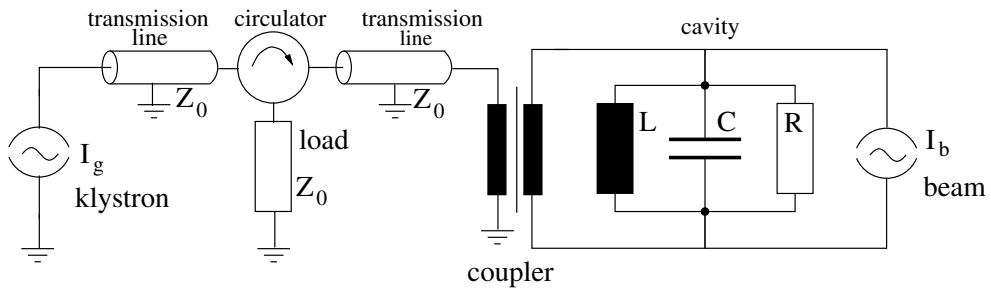

Figure 3.10: Network model of the rf system, based on equivalent circuits.

Now, the accelerating mode can be represented by an equivalent circuit model. The whole system, including klystron, circulator, transmission line, coupler, and cavity is schematically shown in Figure 3.10. The circulator directs the rf wave from the klystron to the cavity and deviates waves which are reflected at the cavity to a matched load. This is necessary to protect the klystron from reflected waves. The model can be further simplified to an equivalent current generator with an external impedance, the cavity, and the beam (see Figure 3.11).
The loaded cavity impedance seen by the beam is given by:

$$\frac{1}{R_\mathrm{L}} = \frac{1}{Z_\mathrm{EXT}} + \frac{1}{R} \tag{3.80}$$

The coupler is used to adjust the value of the loaded impedance. The loaded quality factor Q_{L} corresponds to the loaded impedance R_{L}. It is defined as

$$Q_{\mathrm{L}} = 2\pi \frac{\text{stored energy}}{\text{total loss per cycle}}. \tag{3.81}$$

The total loss per cycle includes the losses in the external devices.
The coupling parameter β_{c} characterizes the coupling of the transmission line to the cavity:

$$R_{\mathrm{L}} = \frac{R}{1+\beta_{\mathrm{c}}}, \qquad Q_{\mathrm{L}} = \frac{Q_0}{1+\beta_{\mathrm{c}}}. \tag{3.82}$$

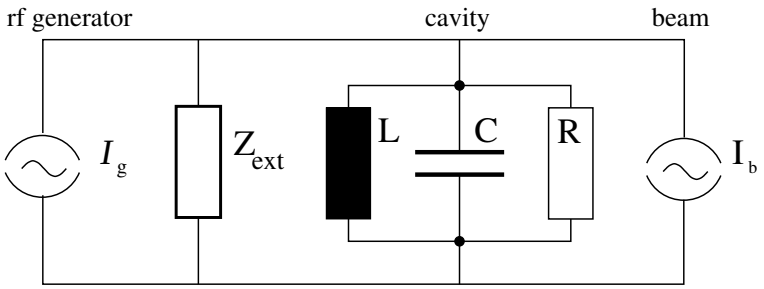

Figure 3.11: Simplified equivalent circuit model of the rf system.

The choice of the loaded quality factor is determined by the high beam loading. This is the topic of the next subsection.

3.3.5 Beam Loading

Having studied the wake of a cavity mode in the penultimate subsection and the equivalent circuit model of the rf system in the previous subsection, we now move on to the combined wake of a bunch train in the fundamental mode and its implications. An evaluation of this term after an infinitely long time, as well as its build-up (i.e. its transient behaviour) is given first for the case of a bunch train with equally spaced and charged bunches and then for the situation where the beam has a gap. Furthermore, the aspect of the filling of the dog-bone damping ring is examined (the beam is stored in a compressed mode).
It is assumed that the simplified form of the cavity mode wake function, Eq. (3.71), is valid (high quality factor). The subsection is based to a large extent on [18, 25].

Beam Loading by a Train of Equally Spaced Bunches

The easiest situation to study is that of an infinitely long bunch train with the bunch spacing ΔT_{b}. The beam current is then $I_{\mathrm{b}} = q_{\mathrm{b}}/\Delta T_{\mathrm{b}}$ (q_{b} being the bunch charge). The corresponding situation in a storage ring is that of a circulating beam without a gap. With N_{b} denoting the number of bunches, the bunch spacing is $\Delta T_{\mathrm{b}} = T_0/N_{\mathrm{b}}$.

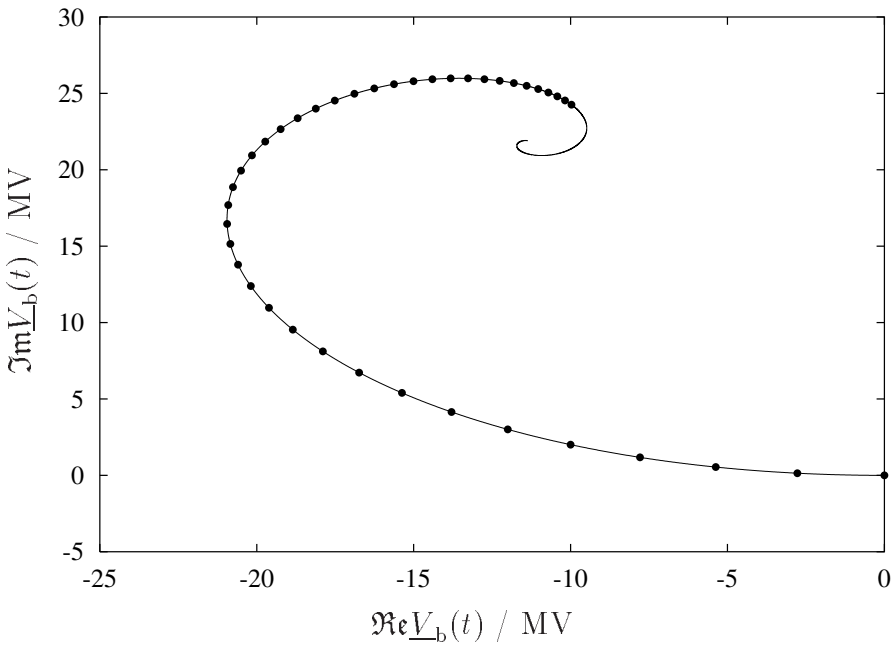

Figure 3.12: Transient build-up of the beam-induced voltage $\underline{V}_\mathrm{b}(t)$ for the TESLA damping ring cavities. $\underline{V}_\mathrm{b}(t)$ follows an equiangular spiral. A beam current of 0.116 A equally spread over 1170 bunches is assumed, i.e. there is no gap. The bunch spacing is approx. 50 ns, the coupling parameter has been selected to be $\beta_\mathrm{c} = 1.1\beta_{\mathrm{c}0}$. The decay factor τ_d is 5.2×10^{-4} and $\delta = -9.9 \times 10^{-4}$. The points indicate the values at each one-hundredth passage of the first 4000. Note, however, that the bunch train does not enter the dog-bone damping ring with the bunch spacing ΔT_b – the train is stored in a compressed mode.

In the following analysis, point-size bunches are considered. A summary of the necessary modifications if the time-width is non-negligible is given at the end.
A time reference is chosen so that the voltage

$$V_{\mathrm{b}0} = -2k_{\delta,\parallel}q_\mathrm{b} = -\omega_\mathrm{r}\left(\frac{R}{Q}\right) I_\mathrm{b}\Delta T_\mathrm{b} = -2I_\mathrm{b}R_\mathrm{L}\tau_\mathrm{d}; \quad \tau_\mathrm{d} = \Gamma\Delta T_\mathrm{b}, \quad \Gamma = \frac{\omega_\mathrm{r}}{2Q_\mathrm{L}} \tag{3.83}$$

induced by each of the bunches passing through the cavity, lies along the negative real axis. Between successive bunches, the induced cavity voltage slips in phase (relative to a phasor coordinate frame rotating as $e^{i\omega_\mathrm{rf}t}$, i.e. with the rf frequency) by an amount

$$\delta = (\omega_\mathrm{r} - \omega_\mathrm{rf})\Delta T_\mathrm{b} \tag{3.84}$$

and decays in length by a factor $e^{-\tau_\mathrm{d}}$. The process of the build-up of the net beam induced voltage is illustrated in Figure 3.12, shown after a large number of bunches have passed through the cavity. The net induced voltages just before and just after the bunch arrival time are denoted by $\underline{V}_\mathrm{b}^-$ and $\underline{V}_\mathrm{b}^+$, where the latter after n passages is given by

$$\begin{aligned}\underline{V}_\mathrm{b}^+(n) &= V_{\mathrm{b}0}(1 + e^{-\tau_\mathrm{d}}e^{i\delta} + e^{-2\tau_\mathrm{d}}e^{2i\delta} + \cdots + e^{-(n-1)\tau_\mathrm{d}}e^{i(n-1)\delta}) \\ &= V_{\mathrm{b}0}\frac{1 - e^{-n\tau_\mathrm{d}}e^{in\delta}}{1 - e^{-\tau_\mathrm{d}}e^{i\delta}}.\end{aligned} \tag{3.85}$$

In the limit of $n \to \infty$ the above expression becomes

$$\underline{V}^{+}_{\mathrm{b},\infty} = V_{\mathrm{b}0}\frac{1}{1-e^{-\tau_{\mathrm{d}}}e^{i\delta}} = V_{\mathrm{b}0}\frac{1-e^{-\tau_{\mathrm{d}}}e^{-i\delta}}{1-2e^{-\tau_{\mathrm{d}}}\cos\delta+e^{-2\tau_{\mathrm{d}}}}. \tag{3.86}$$

For $|\delta|, \tau_{\mathrm{d}} \ll 1$ the phasors $\underline{V}^{+}_{\mathrm{b},\infty}$ and $\underline{V}^{-}_{\mathrm{b},\infty}$ converge to $\underline{V}^{\infty}_{\mathrm{b}}$ which may be approximated as

$$\underline{V}^{\infty}_{\mathrm{b}} \approx V_{\mathrm{b}0}\frac{\tau_{\mathrm{d}}+i\delta}{\tau_{\mathrm{d}}^2+\delta^2} = \frac{V_{\mathrm{b}0}}{\tau_{\mathrm{d}}}\cos\psi e^{i\psi} = -V_{\mathrm{br}}\cos\psi e^{i\psi}, \tag{3.87}$$

where

$$\tan\psi = \frac{\delta}{\tau_{\mathrm{d}}} = \frac{1}{\Gamma}(\omega_{\mathrm{r}}-\omega_{\mathrm{rf}}) = \frac{2Q_{\mathrm{L}}}{\omega_{\mathrm{r}}}(\omega_{\mathrm{r}}-\omega_{\mathrm{rf}}). \tag{3.88}$$

ψ is the usual *tuning angle*, which gives the variation in the phase of the beam-induced cavity voltage as the cavity is tuned off-resonance.
$V_{\mathrm{br}} = -V_{\mathrm{b}0}/\tau_{\mathrm{d}} = 2I_{\mathrm{b}}R_{\mathrm{L}}$ is the magnitude of $\underline{V}^{\infty}_{\mathrm{b}}$ at resonance ($R^{\mathrm{a}}_{\mathrm{L}} = 2R_{\mathrm{L}}$ is the accelerator definition of the loaded shunt impedance; R_{L} is the circuit theory definition).
We now consider a generator current I_{g}, representing an external rf source driving the cavity. The rf power of the source is identified as the available power from the generator, $P_{\mathrm{g}} = I_{\mathrm{g}}^2R/8\beta_{\mathrm{c}}$ [18]. The voltage produced across the circuit is

$$\underline{V}_{\mathrm{g}} = V_{\mathrm{gr}}\cos\psi e^{i\psi}, \quad V_{\mathrm{gr}} = I_{\mathrm{g}}R_{\mathrm{L}}. \tag{3.89}$$

Let us continue by assuming that the generator current $\underline{I}_{\mathrm{g}}$, which is collinear with the generator-induced voltage at resonance, $\underline{V}_{\mathrm{gr}}$, lies at an angle θ with respect to the real axis (and with respect to the beam current $\underline{I}_{\mathrm{b}}$). Then we have $\underline{V}_{\mathrm{g}} = \underline{V}_{\mathrm{gr}}\cos\psi e^{i\psi}$ and $\underline{V}_{\mathrm{gr}} = \underline{I}_{\mathrm{g}}R_{\mathrm{L}}$.
The net cavity voltage, $\underline{V}_{\mathrm{c}}$, is obtained from the superposition of $\underline{V}_{\mathrm{g}}$ and $\underline{V}_{\mathrm{b}}$. $\underline{V}_{\mathrm{c}}$ must lie at the synchronous phase angle $\hat{\phi}_{\mathrm{s}} = \phi_{\mathrm{s}} - \pi/2$ with respect to the real axis, and its magnitude must be equal to V_{rf}; the projection of the cavity voltage on the real axis gives the accelerating component of the voltage. Note that

$$\mathfrak{Re}\, e^{i\hat{\phi}_{\mathrm{s}}} = \cos\hat{\phi}_{\mathrm{s}} = \sin(\hat{\phi}_{\mathrm{s}}+\pi/2) = \sin\phi_{\mathrm{s}}.$$

If the reflected voltage from the beam-loaded cavity is to look real (i.e. it has the same phase as the voltage reflected from the cavity at resonance without a beam), then the net cavity voltage $\underline{V}_{\mathrm{c}}$ must also be collinear with $\underline{V}_{\mathrm{gr}}$ (and, therefore, with $\underline{I}_{\mathrm{g}}$). This implies $\theta = \hat{\phi}_{\mathrm{s}}$ (θ we had defined as the angle of $\underline{V}_{\mathrm{gr}}$ with respect to the real axis). Using this condition, and by studying the various components in a phasor diagram, one finds that for a given coupling parameter β_{c}, the detuning angle must obey [25]

$$\tan\psi_0 = \frac{V_{\mathrm{br}}}{V_{\mathrm{rf}}}\cos\phi_{\mathrm{s}}. \tag{3.90}$$

ψ_0 is called the optimum tuning angle. Figure 3.13 shows the basic phasor diagram at optimum tuning.

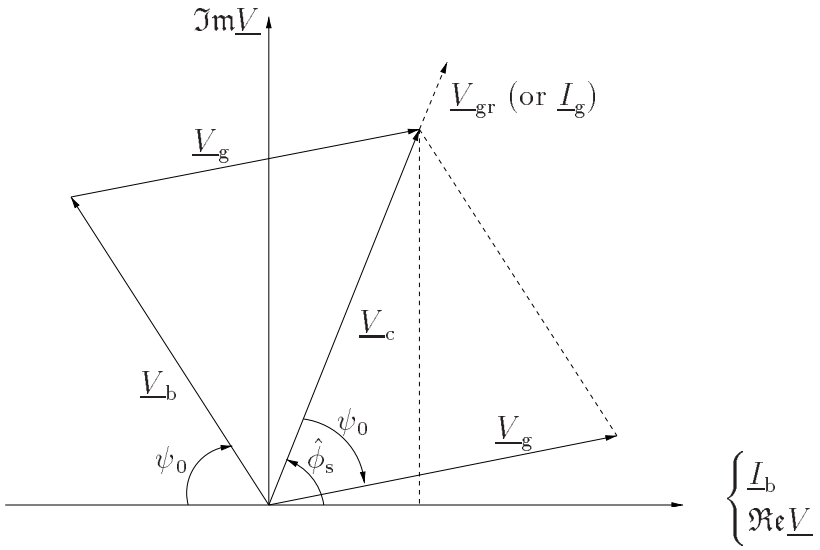

Figure 3.13: Diagram showing vector addition of generator and beam-loading voltages in an rf cavity at optimum tuning ($\underline{I}_{\mathrm{g}}$ collinear with $\underline{V}_{\mathrm{c}}$) for negative ψ_0. The projection of $\underline{V}_{\mathrm{c}}$ on the real axis gives the accelerating component of the voltage. $\hat{\phi}_{\mathrm{s}}$ is defined as $\phi_{\mathrm{s}} - \pi/2$.

$\psi = \psi_0$ is also the condition for minimum generator power [18]; for $\psi = \psi_0$ we have

$$P_{\mathrm{g}} = \frac{1+\beta_{\mathrm{c}}}{8\,\beta_{\mathrm{c}}}\,\frac{1}{R_{\mathrm{L}}}\left(V_{\mathrm{rf}} + 2\,I_{\mathrm{b}}\,R_{\mathrm{L}}\,\sin\phi_{\mathrm{s}}\right)^2 . \tag{3.91}$$

By differentiating the generator power with respect to β_{c}, one finds the value of the cavity coupling which minimizes the generator power:

$$\beta_{\mathrm{c0}} = 1 + \frac{P_{\mathrm{b}}}{P_{\mathrm{c}}} = 1 + \frac{2 I_{\mathrm{b}} R \sin\phi_{\mathrm{s}}}{V_{\mathrm{rf}}}. \tag{3.92}$$

At this value, the generator power is equal to the beam power $P_{\mathrm{b}} = V_{\mathrm{rf}}\,I_{\mathrm{b}}\sin\phi_{\mathrm{s}}$ and the dissipated cavity power $P_{\mathrm{c}} = V_{\mathrm{rf}}^2/(2\,R)$; the reflected power $P_{\mathrm{r}} = P_{\mathrm{g}} - P_{\mathrm{b}} - P_{\mathrm{c}}$ vanishes. In the extreme beam-loaded case, as for the superconducting cavities in the TESLA damping ring, where $P_{\mathrm{b}} \gg P_{\mathrm{c}}$, the following approximations hold:

$$\beta_{\mathrm{c0}} \approx \frac{P_{\mathrm{b}}}{P_{\mathrm{c}}} \tag{3.93}$$

$$\text{and} \quad \psi_0 \approx -(\phi_{\mathrm{s}} - \pi/2) \quad \text{for} \quad \beta_{\mathrm{c}} = \beta_{\mathrm{c0}} \tag{3.94}$$

since

$$\tan\psi_0 = \frac{V_{\mathrm{br}}}{V_{\mathrm{rf}}}\cos\phi_{\mathrm{s}} = \frac{P_{\mathrm{b}}}{P_{\mathrm{c}}(1+\beta_{\mathrm{c}})}\cot\phi_{\mathrm{s}} \approx \cot\phi_{\mathrm{s}} = -\tan(\phi_{\mathrm{s}} - \pi/2).$$

The optimum coupling factor for the TESLA damping ring parameters leads to a loaded quality factor Q_{L} of approximately 140 000. The detuning angle is approximately 65°,

which corresponds to a frequency change of about 3.2 kHz. The required forward power is $P_g = 1.24\,\mathrm{MW}$ or 155 kW per cavity. The klystron has to provide a power of 1.34 MW if typical losses of 8 % in the transmission system are included.
In practice, the cavity coupling is often adjusted to be slightly greater than that given by Eq. (3.92) in order to make the system somewhat less sensitive to beam-loading effects [25]. The reflected power at optimum cavity tuning is then

$$\frac{P_r}{P_c} = \frac{(\beta_c - \beta_{c0})^2}{4\beta_c}. \tag{3.95}$$

In the simulations, β_c was chosen to be larger than the optimal value by a factor of 1.1 to 1.4.
For superconducting cavities and for optimum cavity tuning, the detuning angle relates as $\tan\psi = \beta_{c0}/\beta_c \tan\psi_0$. The decay time is increased by the reciprocal factor (the resonance frequency ω_r and δ are not changed).

When taking into account the length of the bunches, V_{b0} and the other beam-loading voltages are reduced by the bunch form factor F_b. In the various formulae, this is achieved by multiplying the charge/beam current with F_b. In the multibunch simulations, the synchronous phase in the preceding equations has been replaced by the nominal average bunch phase (the nominal average bunch phase does not coincide with the synchronous phase since the rf voltage is not linear over the bunch; see Eq. (3.77)). Note that the optimal coupling factor is independent of the bunch length.

Beam Loading by a Circulating Beam with a Gap

The study moves to the situation where the bunch phases are fixed, corresponding to a linac where the timing of the bunches is set by an external generator (the injector).
The number of bunches in the train is denoted by N_b, whilst N_g is the corresponding number of empty buckets in the gap. N is defined as the maximum number of bunches possible at the specified bunch spacing, i.e. $N = T_0/\Delta T_b = N_b + N_g$. Furthermore, let

$$\underline{T}_t = e^{N_b(-\tau_d + i\delta)}, \quad \underline{T}_g = e^{(N_g+1)(-\tau_d+i\delta)}, \quad \text{and} \quad \underline{T}_0 = e^{N(-\tau_d+i\delta)}, \tag{3.96}$$

where the latter corresponds to the revolution time, $\underline{T}_g$ to the gap endurance, and the term $\underline{T}_t e^{-(-\tau_d+i\delta)}$ to the period between the beginning and end of the bunch train.
The voltage induced by a bunch is now:

$$V_{b0} = -2k_{\delta,\parallel} q_b \; = -\omega_r \left(\frac{R}{Q}\right) \frac{N I_b}{N_b} \Delta T_b. \tag{3.97}$$

At the beginning of the first gap, i.e. just after the bunch train has passed the cavity for the first time, the net induced voltage is

$$\underline{V}^-_{b,1} = V_{b0}\left(1 + e^{-\tau_d+i\delta} + \ldots + e^{(N_b-1)(-\tau_d+i\delta)}\right) = \frac{1-\underline{T}_t}{1-e^{-\tau_d+i\delta}} V_{b0}. \tag{3.98}$$

After m passages one finds

$$\underline{V}^-_{\mathrm{b},m} = \frac{1-\underline{T}_0^m}{1-\underline{T}_0}\underline{V}^-_{\mathrm{b},1} \tag{3.99}$$

resulting in a steady-state phasor after a sufficiently long time:

$$\underline{V}^-_{\mathrm{b}} = \frac{\underline{V}^-_{\mathrm{b},1}}{1-\underline{T}_0} = \frac{1-\underline{T}_{\mathrm{t}}}{(1-\underline{T}_0)(1-e^{-\tau_{\mathrm{d}}+i\delta})}V_{\mathrm{b}0}. \tag{3.100}$$

Correspondingly, there is a steady-state phasor at the end of the gap:

$$\underline{V}^+_{\mathrm{b}} = \underline{T}_{\mathrm{g}}\underline{V}^-_{\mathrm{b}}. \tag{3.101}$$

The next step in the analysis is to evaluate the average beam loading over the bunch train. Assuming that the steady-state voltages before and after the gap have been reached, $\underline{V}^+_{\mathrm{b,av}}$ is given by

$$\underline{V}^+_{\mathrm{b,av}} = \frac{1}{N_{\mathrm{b}}}\sum_{n=1}^{N_{\mathrm{b}}}\underline{V}^+_{\mathrm{b}}(n) + e^{(n-1)(-\tau_{\mathrm{d}}+i\delta)}\underline{V}^+_{\mathrm{b}} \tag{3.102}$$

with $\underline{V}^+_{\mathrm{b}}(n)$ as in Eq. (3.85); therefore,

$$\begin{aligned}
\underline{V}^+_{\mathrm{b,av}} =& \frac{1}{N_{\mathrm{b}}}\sum_{n=1}^{N_{\mathrm{b}}}\frac{1-e^{n(-\tau_{\mathrm{d}}+i\delta)}}{1-e^{-\tau_{\mathrm{d}}+i\delta}}V_{\mathrm{b}0} + e^{(n-1)(-\tau_{\mathrm{d}}+i\delta)}\frac{1-\underline{T}_{\mathrm{t}}}{1-e^{-\tau_{\mathrm{d}}+i\delta}}\frac{\underline{T}_{\mathrm{g}}}{1-\underline{T}_0}V_{\mathrm{b}0} \\
=& \frac{V_{\mathrm{b}0}}{N_{\mathrm{b}}(1-e^{-\tau_{\mathrm{d}}+i\delta})}\left\{N_{\mathrm{b}} - \frac{1-\underline{T}_{\mathrm{t}}}{1-e^{-\tau_{\mathrm{d}}+i\delta}}e^{-\tau_{\mathrm{d}}+i\delta} + \frac{(1-\underline{T}_{\mathrm{t}})^2}{1-e^{-\tau_{\mathrm{d}}+i\delta}}\frac{\underline{T}_{\mathrm{g}}}{1-\underline{T}_0}\right\} \\
=& \frac{V_{\mathrm{b}0}}{N_{\mathrm{b}}(1-e^{-\tau_{\mathrm{d}}+i\delta})}\left\{N_{\mathrm{b}} - \frac{1-\underline{T}_{\mathrm{t}}}{(1-e^{-\tau_{\mathrm{d}}+i\delta})(1-\underline{T}_0)}\left(e^{-\tau_{\mathrm{d}}+i\delta} - \underline{T}_{\mathrm{g}}\right)\right\}.
\end{aligned} \tag{3.103}$$

If the number of missing bunches in the gap is small enough that $N_{\mathrm{g}}\tau_{\mathrm{d}}$ and $N_{\mathrm{g}}|\delta| \ll 1$, then

$$\frac{e^{-\tau_{\mathrm{d}}+i\delta} - \underline{T}_{\mathrm{g}}}{1-e^{-\tau_{\mathrm{d}}+i\delta}} \approx N_{\mathrm{g}}.$$

Hence,

$$\begin{aligned}
\underline{V}^+_{\mathrm{b,av}} &\approx \frac{V_{\mathrm{b}0}}{1-e^{-\tau_{\mathrm{d}}+i\delta}}\left\{1 - \frac{N_{\mathrm{g}}(1-\underline{T}_{\mathrm{t}})}{N_{\mathrm{b}}(1-\underline{T}_0)}\right\} \\
&= \frac{V_{\mathrm{b}0}}{1-e^{-\tau_{\mathrm{d}}+i\delta}}\left\{1 - \frac{N_{\mathrm{g}}}{N_{\mathrm{b}}}\left(1 - \underline{T}_{\mathrm{t}}\frac{1-\underline{T}_{\mathrm{g}}e^{-(-\tau_{\mathrm{d}}+i\delta)}}{1-\underline{T}_0}\right)\right\}.
\end{aligned} \tag{3.104}$$

For beams with $N_{\mathrm{b}} \gg N_{\mathrm{g}}$ it is reasonable to neglect the last term. Then the average net induced voltage can be seen to be approximately equal to the steady-state beam loading phasor $\underline{V}^\infty_{\mathrm{b}}$ for a beam with the same current I_{b} and bunch spacing but without a gap. Note that it is $1 - N_{\mathrm{g}}/N_{\mathrm{b}} \approx N_{\mathrm{b}}/N$ for $N_{\mathrm{g}}/N_{\mathrm{b}} \ll 1$.

In reality the situation is more complex, as the bunch phases will adjust themselves on the order of the damping time to pick up a constant accelerating voltage. Hence, there will be a bunch phase shift across the gap.

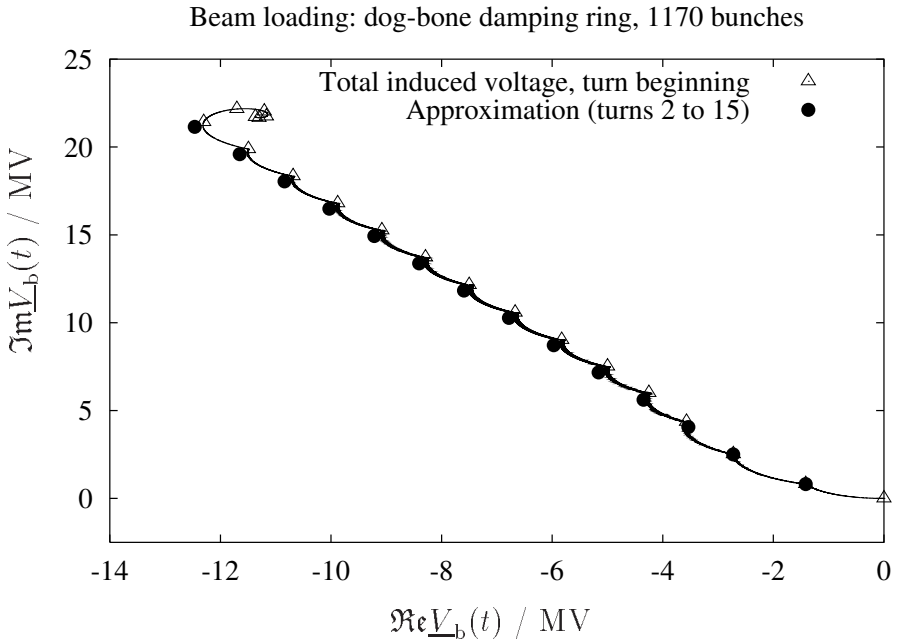

Figure 3.14: Initial transient build-up of the beam-induced voltage $\underline{V}_\mathrm{b}(t)$ in the dog-bone damping ring for a beam without a gap. The assumed filling of the ring is described in the text (page 43). The triangles mark the total induced voltage at the beginning of a turn, the circles the approximation as given by Eq. (3.107).

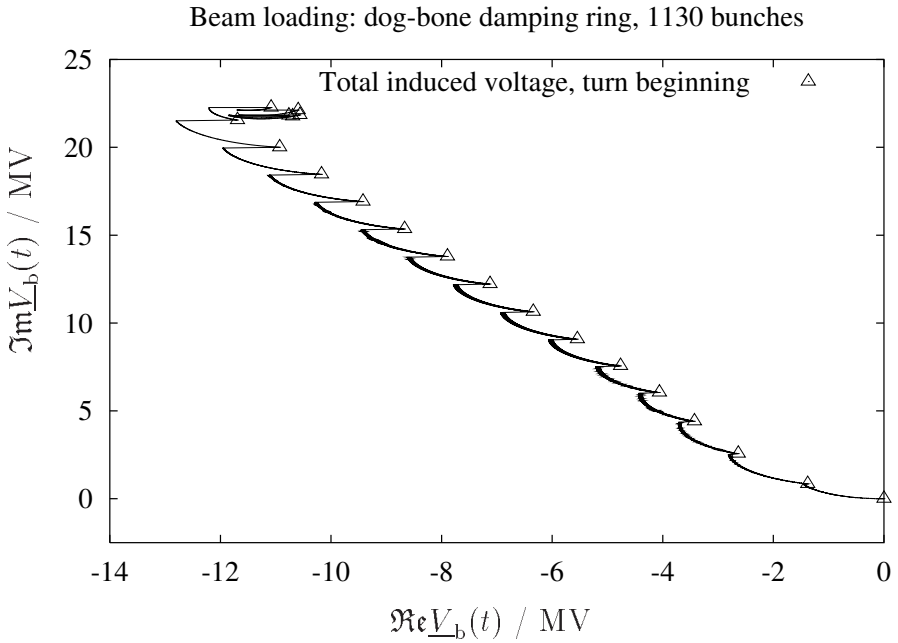

Figure 3.15: Initial transient build-up of the beam-induced voltage $\underline{V}_\mathrm{b}(t)$ in the dog-bone damping ring for a bunch train consisting of 1130 bunches. The change of the total induced voltage between the bunch train tail and head is clearly visible.

Initial Transient Beam Loading in the Dog-bone Damping Ring

The bunches in the dog-bone damping ring are stored in a compressed mode, with the bunch spacing reduced by a factor $m = 14$ (see page 3). To estimate what the initial transient beam loading might look like, it is assumed here that the bunches enter the ring as follows:

- bunches 1, 15, 29, 43, ... ,
- bunches 2, 16, 30, 44, ... ,
- and so forth.

The bunch numbering corresponds to the relative position when the ring is filled: bunch number 1 is the train head, bunch 1130 sits at the train tail, followed by the gap; for a beam without a gap, bunch 1170 occupies the last position at the train tail. It is furthermore assumed that all the bunches begin with and maintain the same phase (meaning that they are unaffected by the beam loading and that there are no synchrotron oscillations). The transient beam loading is depicted in the Figures 3.14 (1170 bunches) and 3.15 (1130 bunches). They suggest that the build-up during the filling is reasonably linear. An analytic approximation of the total induced voltage at the beginning of the turns 2 to 15 (14 turns are required to fill the damping ring) confirms this impression. The approximation is derived in the following for the case of 1170 bunches.
The induced voltage at the beginning of the second turn (bucket no 1) due to the beam loading from the first turn is (note that $83 \cdot 14 + 8 = 1170$):

$$\underline{V}_2 = V_{\mathrm{b}0} \sum_{j=0}^{n-1} e^{(jm+8)(-\tau_{\mathrm{d}}+i\delta)} = V_{\mathrm{b}0} \frac{1 - e^{mn(-\tau_{\mathrm{d}}+i\delta)}}{1 - e^{m(-\tau_{\mathrm{d}}+i\delta)}} e^{8(-\tau_{\mathrm{d}}+i\delta)} \tag{3.105}$$

where n is 84. The generalized formula of the total induced voltage at the beginning of the turns r, $2 \leq r \leq 9$, is

$$\begin{aligned}
\underline{V}_r =& V_{\mathrm{b}0} \frac{1 - e^{mn(-\tau_{\mathrm{d}}+i\delta)}}{1 - e^{m(-\tau_{\mathrm{d}}+i\delta)}} \sum_{j=0}^{r-2} e^{(8-j)(-\tau_{\mathrm{d}}+i\delta)} \sum_{k=0}^{r-2-j} \underline{T}_0^k \\
=& \frac{V_{\mathrm{b}0}}{1 - e^{m(-\tau_{\mathrm{d}}+i\delta)}} \frac{1 - e^{mn(-\tau_{\mathrm{d}}+i\delta)}}{1 - \underline{T}_0} \sum_{j=0}^{r-2} e^{(8-j)(-\tau_{\mathrm{d}}+i\delta)} (1 - \underline{T}_0^{r-1-j}) \\
=& \frac{V_{\mathrm{b}0} e^{8(-\tau_{\mathrm{d}}+i\delta)}}{1 - e^{m(-\tau_{\mathrm{d}}+i\delta)}} \frac{1 - e^{mn(-\tau_{\mathrm{d}}+i\delta)}}{1 - \underline{T}_0} \left(\frac{(1 - e^{-(r-1)(-\tau_{\mathrm{d}}+i\delta)})}{1 - e^{-(-\tau_{\mathrm{d}}+i\delta)}} - \sum_{j=1}^{r-1} \underline{T}_0^j e^{(j+1-r)(-\tau_{\mathrm{d}}+i\delta)} \right).
\end{aligned} \tag{3.106}$$

The prefactor of the above equation relates to the steady-state voltage (see Eq. (3.87)) as

$$\frac{V_{\mathrm{b}0}}{1 - e^{m(-\tau_{\mathrm{d}}+i\delta)}} e^{8(-\tau_{\mathrm{d}}+i\delta)} \approx \frac{1}{m} \underline{V}_{\mathrm{b}}^{\infty}$$

(note that $m\tau_\mathrm{d}$ and $m|\delta|$ are much smaller than one). Furthermore, the first term in the brackets of Eq. (3.106) is approximately $r-1$, and the sum in the brackets can be approximated by the two largest terms. This is due to $|\underline{T}_0^j| = \exp(-jN\tau_\mathrm{d}) = \exp(-j\Gamma T_0)$, and that the cavity filling time, the inverse of Γ, is approximately $2T_0$ for the dog-bone parameters. We obtain

$$\underline{V}_r \approx \frac{\underline{V}_\mathrm{b}^\infty}{m}\Big((r-1) - \underline{T}_0 - (1-\delta_{r,2})\underline{T}_0^2\Big). \tag{3.107}$$

Approximation (3.107) also applies to the turns r, $10 \le r \le 15$, due to

$$\begin{aligned}\underline{V}_r = {} & \frac{V_{\mathrm{b}0}e^{8(-\tau_\mathrm{d}+i\delta)}}{1-e^{m(-\tau_\mathrm{d}+i\delta)}}\frac{1-e^{mn(-\tau_\mathrm{d}+i\delta)}}{1-\underline{T}_0}\left(\frac{(1-e^{-8(-\tau_\mathrm{d}+i\delta)})}{1-e^{-(-\tau_\mathrm{d}+i\delta)}} - \sum_{j=0}^{7}\underline{T}_0^{r-1-j}e^{-j(-\tau_\mathrm{d}+i\delta)}\right) \\ & + \frac{V_{\mathrm{b}0}e^{m(-\tau_\mathrm{d}+i\delta)}}{1-e^{m(-\tau_\mathrm{d}+i\delta)}}\frac{1-e^{m(n-1)(-\tau_\mathrm{d}+i\delta)}}{1-\underline{T}_0}\left(\frac{(1-e^{(9-r)(-\tau_\mathrm{d}+i\delta)})}{1-e^{-(-\tau_\mathrm{d}+i\delta)}} - \sum_{j=1}^{r-9}\underline{T}_0^{j}e^{(j+9-r)(-\tau_\mathrm{d}+i\delta)}\right).\end{aligned}$$

Phase Stability in the Presence of Heavy Beam Loading

In the course of discussing phase oscillations in Section 3.2, the conclusion was drawn that the derivative of the rf voltage at the synchronous phase must be negative. When the beam-induced voltage component is large, the situation is more complicated. For simplicity, suppose that the synchrotron period is much greater than the cavity filling time; then cavity dynamical effects can be ignored and the cavity response is virtually instantaneous. As the arrival time of the bunches varies due to phase oscillations, the beam-induced voltage component moves with the bunches and, consequently, cannot contribute to phase stability. Hence, only the generator voltage component can provide a restoring force against phase perturbations. The derivative of $\mathfrak{Re}\underline{V}_\mathrm{g}$ with respect to t at $\hat{t}_\mathrm{s} = \hat{\phi}_\mathrm{s}/\omega_\mathrm{rf}$ leads to the condition

$$V_\mathrm{rf}\sin\hat{\phi}_\mathrm{s} + \frac{1}{2}V_\mathrm{br}\sin 2\psi > 0 \tag{3.108}$$

(this is also the case when the cavity tuning is not optimal). Expression (3.108) is called the *first Robinson stability criterion*. If the cavity tuning is adjusted to make the beam-loaded cavity voltage real, the above equation can be recast as

$$V_\mathrm{rf} > V_\mathrm{br}\cos\hat{\phi}_\mathrm{s} \tag{3.109}$$

or as a stability condition for the coupling coefficient:

$$\beta_\mathrm{c} > \beta_\mathrm{c0} - 2. \tag{3.110}$$

Eq. (3.110) demonstrates that the stability criterion is only barely satisfied for a matched superconducting cavity. Even a small phase perturbation of the bunches can result in an instability. To safeguard against such an occurrence, one can overcouple the cavity, or

alternatively, detune the cavity by an angle ξ ($0 \leq \xi \leq \hat{\phi}_\mathrm{s}$) from the optimum, where ξ is known as the tuning offset ($\psi \approx -\hat{\phi}_\mathrm{s} + \xi$) [26].
The effects of beam loading on the stability of the coherent and incoherent motion as well as the corresponding bucket shapes are discussed in [27] (premise: instantaneous cavity response). The subject of stability is continued in the next section.

3.4 Multibunch Instabilities

In this section, a one-particle model (per bunch) is developed to illustrate the longitudinal instabilities encountered by a bunched beam in a circular accelerator. Whereas the bunches are considered to be rigid and structureless in this model, they do execute longitudinal synchrotron oscillations and interact with their own wake fields as well as those of the other bunches. An important result is that of the so-called *Robinson instability growth rate*. In the derivation, the formalism for point-size bunches is used; the modifications for bunches with non-negligible time-widths is clear.

3.4.1 Robinson Instability (fundamental cavity mode)

The following derivation (see [17] – small modifications have been made) is based on the assumption that there are N_b equally spaced bunches of the same charge $N_\mathrm{e}e$. Furthermore, a one-particle model is used in which each bunch is represented by one macroparticle. The bunches are numbered $n = 0, 1, \ldots, N_\mathrm{b} - 1$, where the first bunch is denoted by the index 0, the second (meaning behind) by $n = 1$, and so forth.

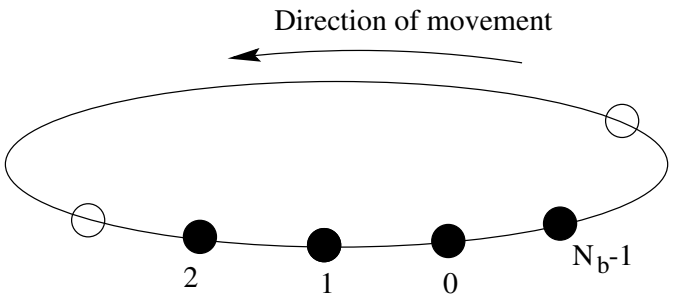

Figure 3.16: Snapshot of the bunches in the ring.

As in Section 3.2, the time displacement and the energy deviation of the bunches are studied, but now with respect to position (i.e. the s-coordinate). It is the spatial displacement of the bunches at the location of the source of the impedance which is of importance – these determine the wake seen by the bunches on their revolutions. In the following, a prime denotes a derivative with respect to s. Recalling equations (3.3) and (3.11), one has for relativistic particles ($s = ct$):

$$\tau_n' = \frac{\alpha_\mathrm{c}}{cE_\mathrm{b}}\varepsilon_n$$
$$\varepsilon_n' = \frac{eV_\mathrm{g}\sin(\phi_\mathrm{s} + \omega_\mathrm{rf}\tau) - U_0 - 2T_0\alpha_\varepsilon\varepsilon_n}{C},$$

where V_g is the steady-state voltage delivered by the generator; in the limit of no beam loading it is $V_\mathrm{rf}\sin(\phi_\mathrm{s}+\omega_\mathrm{rf}\tau)$. On the right-hand side of the second equation, the change of energy due to the wake fields,

$$N_\mathrm{e}e^2\sum_{k=0}^{\infty}\sum_{m=0}^{N_\mathrm{b}-1}W_{\delta,\|}\left[kC+\frac{n-m}{N_\mathrm{b}}C+c\tau_n(s)-c\tau_m\left(s-kC-\frac{n-m}{N_\mathrm{b}}C\right)\right], \tag{3.111}$$

must be added in the numerator. $W_{\delta,\|}$ is the longitudinal wake function accumulated over one turn of the storage ring. The summation over k and m is over the wake fields left behind by the N_b bunches on the previous revolutions.
In case the beam bunches have an oscillation amplitude much shorter than the wavelength of the fundamental cavity mode, the wake function can be expanded as:

$$\begin{aligned}&W_{\delta,\|}\left[kC+\frac{n-m}{N_\mathrm{b}}C+c\tau_n(s)-c\tau_m\left(s-kC-\frac{n-m}{N_\mathrm{b}}C\right)\right]\approx\\&\quad W_{\delta,\|}\left(kC+\frac{n-m}{N_\mathrm{b}}C\right)\\&\quad +W'_{\delta,\|}\left(kC+\frac{n-m}{N_\mathrm{b}}C\right)\left\{c\tau_n(s)-c\tau_m\left(s-kC-\frac{n-m}{N_\mathrm{b}}C\right)\right\}.\end{aligned} \tag{3.112}$$

The sum over the first term

$$N_\mathrm{e}e^2\sum_{k=0}^{\infty}\sum_{m=0}^{N_\mathrm{b}-1}W_{\delta,\|}\left(kT_0+\frac{n-m}{N_\mathrm{b}}T_0\right)=N_\mathrm{e}e^2\sum_{k=0}^{\infty}W_{\delta,\|}\left(\frac{k}{N_\mathrm{b}}T_0\right)$$

is just the steady-state beam-loading term encountered in Eq. (3.86). It does not play a rôle in the dynamics and is taken into account by the generator voltage; the difference is the required rf voltage $V_\mathrm{rf}\sin(\phi_\mathrm{s}+\omega_\mathrm{rf}\tau)$.
Returning to the above equation for the rate of energy change, linearizing the voltage term, and applying the above approximations, one arrives at

$$\begin{aligned}\varepsilon'_n=&-\frac{\omega_{\mathrm{s}0}^2E_\mathrm{b}}{c\alpha_\mathrm{c}}\tau_n-\frac{2\alpha_\varepsilon\varepsilon_n}{c}+\\&\frac{N_\mathrm{e}e^2c}{C}\sum_{k=0}^{\infty}\sum_{m=0}^{N_\mathrm{b}-1}W'_{\delta,\|}\left(kC+\frac{n-m}{N_\mathrm{b}}C\right)\left\{\tau_n(s)-\tau_m\left(s-kC-\frac{n-m}{N_\mathrm{b}}C\right)\right\}.\end{aligned}$$

Note that

$$\frac{\omega_\mathrm{rf}eV_\mathrm{rf}\cos\phi_\mathrm{s}}{T_0}=\frac{-\omega_{\mathrm{s}0}^2E_\mathrm{b}}{\alpha_\mathrm{c}}$$

has been used (compare with Eq. (3.14)). Combining the two first-order differential equations one obtains for $n=0,\ldots,N_\mathrm{b}-1$

$$\begin{aligned}\tau''_n(s)+\frac{2\alpha_\varepsilon}{c}\tau'_n(s)+\frac{\omega_{\mathrm{s}0}^2}{c^2}\tau_n(s)=&\frac{N_\mathrm{e}e^2\alpha_\mathrm{c}}{CE_\mathrm{b}}\sum_{k=0}^{\infty}\sum_{m=0}^{N_\mathrm{b}-1}W'_{\delta,\|}\left(kC+\frac{n-m}{N_\mathrm{b}}C\right)\\&\times\left\{\tau_n(s)-\tau_m\left(s-kC-\frac{n-m}{N_\mathrm{b}}C\right)\right\}.\end{aligned} \tag{3.113}$$

We have now a N_b-dimensional homogeneous second-order differential equation. The ansatz

$$\underline{\tau}_n(s) = \underline{\tau}_n e^{i\underline{\Omega}s/c} \tag{3.114}$$

leads to

$$\begin{aligned}(-\underline{\Omega}^2 + 2i\underline{\Omega}\alpha_\varepsilon + \omega_{\mathrm{s}0}^2)\underline{\tau}_n = \frac{cN_\mathrm{e}e^2\alpha_\mathrm{c}}{T_0E_\mathrm{b}} \sum_{k=0}^{\infty}\sum_{m=0}^{N_\mathrm{b}-1} W'_{\delta,\parallel}\left(kC + \frac{n-m}{N_\mathrm{b}}C\right) \\ \times\left\{\underline{\tau}_n - \underline{\tau}_m \exp\left(-i\Big(k+\frac{n-m}{N_\mathrm{b}}\Big)\underline{\Omega}T_0\right)\right\}.\end{aligned} \tag{3.115}$$

The first term in the curly brackets is the potential-well term. It can be absorbed into a redefinition of the synchrotron frequency as

$$\begin{aligned}\omega_\mathrm{s}^2 &= \omega_{\mathrm{s}0}^2 - \frac{cN_\mathrm{e}e^2\alpha_\mathrm{c}}{T_0E_\mathrm{b}} \sum_{k=0}^{\infty}\sum_{m=0}^{N_\mathrm{b}-1} W'_{\delta,\parallel}\left(kC + \frac{n-m}{N_\mathrm{b}}C\right) \\ &= \omega_{\mathrm{s}0}^2 - \frac{cN_\mathrm{e}e^2\alpha_\mathrm{c}}{T_0E_\mathrm{b}} \sum_{k=0}^{\infty}\sum_{m=0}^{N_\mathrm{b}-1} W'_{\delta,\parallel}\left(kC + \frac{m}{N_\mathrm{b}}C\right).\end{aligned} \tag{3.116}$$

The summation of k can be extended to $-\infty$, where the wake and its derivative vanish due to causality. Under the assumption that this incoherent synchrotron frequency shift $\Delta\omega_\mathrm{s} = \omega_\mathrm{s} - \omega_{\mathrm{s}0}$ is small, one gets

$$\begin{aligned}\Delta\omega_\mathrm{s} &\approx \frac{-cN_\mathrm{e}e^2\alpha_\mathrm{c}}{2T_0E_\mathrm{b}\omega_{\mathrm{s}0}} \sum_{k=-\infty}^{\infty} W'_{\delta,\parallel}\left(\frac{k}{N_\mathrm{b}}C\right) \\ &= \frac{-cN_\mathrm{e}e^2\alpha_\mathrm{c}}{2T_0E_\mathrm{b}\omega_{\mathrm{s}0}}\frac{N_\mathrm{b}}{cT_0} \sum_{p=-\infty}^{\infty} (i\omega)(-Z_\parallel(w))\big|_{w=2\pi pN_\mathrm{b}/T_0} \\ &= \frac{N_\mathrm{b}N_\mathrm{e}e^2\alpha_\mathrm{c}}{2T_0^2E_\mathrm{b}\omega_{\mathrm{s}0}} \sum_{p=-\infty}^{\infty} ipN_\mathrm{b}\omega_0\, Z_\parallel(pN_\mathrm{b}\omega_0) \\ &= \frac{-N_\mathrm{b}N_\mathrm{e}e^2\alpha_\mathrm{c}}{2T_0^2E_\mathrm{b}\omega_{\mathrm{s}0}} \sum_{p=-\infty}^{\infty} pN_\mathrm{b}\omega_0\, \mathfrak{Im}Z_\parallel(pN_\mathrm{b}\omega_0).\end{aligned} \tag{3.117}$$

In the first step, advantage is made of the Poisson sum formula (Eq. (B.8), page 151). The real part of the impedance vanishes in the last step because it is an even function of ω. Equation (3.115) can now be rewritten as:

$$\begin{aligned}(\underline{\Omega}^2 - 2i\underline{\Omega}\alpha_\varepsilon - \omega_\mathrm{s}^2)\underline{\tau}_n = \frac{cN_\mathrm{e}e^2\alpha_\mathrm{c}}{T_0E_\mathrm{b}} \sum_{k=-\infty}^{\infty}\sum_{m=0}^{N_\mathrm{b}-1} W'_{\delta,\parallel}\left(kC + \frac{n-m}{N_\mathrm{b}}C\right) \\ \times\,\underline{\tau}_m \exp\left(-i\Big(k+\frac{n-m}{N_\mathrm{b}}\Big)\underline{\Omega}T_0\right).\end{aligned} \tag{3.118}$$

Application of the Poisson sum formula gives:

$$
\begin{aligned}
&(\underline{\Omega}^2 - 2i\underline{\Omega}\alpha_\varepsilon - \omega_\mathrm{s}^2)\underline{\tau}_n \\
&= \frac{cN_\mathrm{e}e^2\alpha_\mathrm{c}}{T_0E_\mathrm{b}} \sum_{p=-\infty}^{\infty} \sum_{m=0}^{N_\mathrm{b}-1} \underline{\tau}_m \, \frac{i(\omega+\underline{\Omega})}{cT_0} \exp\left(i\omega\frac{n-m}{N_\mathrm{b}}T_0\right) (-Z_\parallel(\omega+\underline{\Omega}))\Big|_{\omega=2\pi p/T_0} \\
&= \frac{-iN_\mathrm{e}e^2\alpha_\mathrm{c}}{T_0^2E_\mathrm{b}} \sum_{p=-\infty}^{\infty} \sum_{m=0}^{N_\mathrm{b}-1} \underline{\tau}_m(p\omega_0+\underline{\Omega}) \exp\left(i2\pi p\frac{n-m}{N_\mathrm{b}}\right) Z_\parallel(p\omega_0+\underline{\Omega}). \qquad (3.119)
\end{aligned}
$$

There will be a total of N_b modes of the multibunch motion, each specified by an index μ which assumes the values 0, 1, ... , $N_\mathrm{b}-1$. The amplitudes of the N_b bunches as the whole beam is executing the μth multibunch mode are given by

$$
\underline{\tau}_n \propto e^{i2\pi\mu n/N_\mathrm{b}}. \qquad (3.120)
$$

The oscillation amplitudes τ_n of two modes are shown in Figure 3.17 for the case of $N_\mathrm{b} = 4$.

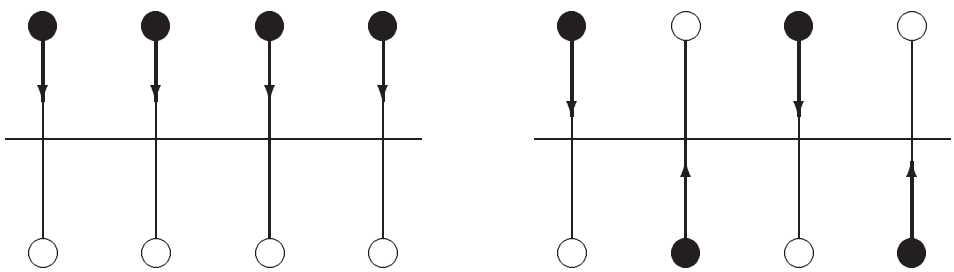

Figure 3.17: "0" and "π" oscillation modes.

Substituting Eq. (3.120) into Eq. (3.119) leads to the following equation for the mode frequencies

$$
\begin{aligned}
&\underline{\Omega}_{(\mu)}^2 - 2i\underline{\Omega}_{(\mu)}\alpha_\varepsilon - \omega_\mathrm{s}^2 \\
&= \frac{-iN_\mathrm{e}e^2\alpha_\mathrm{c}}{T_0^2E_\mathrm{b}} \sum_{p=-\infty}^{\infty} \sum_{m=0}^{N_\mathrm{b}-1} (p\omega_0+\underline{\Omega}_{(\mu)}) \exp\left(i2\pi(p-\mu)\frac{n-m}{N_\mathrm{b}}\right) Z_\parallel(p\omega_0+\underline{\Omega}_{(\mu)}) \\
&= \frac{-iN_\mathrm{b}N_\mathrm{e}e^2\alpha_\mathrm{c}}{T_0^2E_\mathrm{b}} \sum_{p=-\infty}^{\infty} ((pN_\mathrm{b}+\mu)\omega_0+\underline{\Omega}_{(\mu)}) Z_\parallel((pN_\mathrm{b}+\mu)\omega_0+\underline{\Omega}_{(\mu)}). \qquad (3.121)
\end{aligned}
$$

Given the impedance, Eq. (3.121) can in principle be solved for the $\underline{\Omega}_{(\mu)}$. Here a perturbative approach is taken and it is assumed that the $\underline{\Omega}_{(\mu)}$ do not deviate much from ω_s for modest beam intensities; thus, the $\underline{\Omega}_{(\mu)}$ are replaced by ω_s on the right-hand side of Eq. (3.121).

The real parts of the $\underline{\Omega}_{(\mu)}$ are the perturbed synchrotron oscillation frequencies of the collective beam motion. The coherent frequency shifts are

$$\mathfrak{Re}(\underline{\Omega}_{(\mu)} - \omega_\mathrm{s}) \approx \frac{N_\mathrm{b} N_\mathrm{e} e^2 \alpha_\mathrm{c}}{2T_0^2 E_\mathrm{b} \omega_\mathrm{s}} \sum_{p=-\infty}^{\infty} \omega_{pN_\mathrm{b},\mu} \mathfrak{Im} Z_\parallel(\omega_{pN_\mathrm{b},\mu}), \tag{3.122}$$

where $\omega_{pN_\mathrm{b},\mu} = (pN_\mathrm{b} + \mu)\omega_0 + \omega_\mathrm{s}$.

Robinson instability

The imaginary components of the $\underline{\Omega}_{(\mu)}$ satisfy

$$\mathfrak{Im}(\underline{\Omega}_{(\mu)} - \omega_\mathrm{s}) \approx \alpha_\varepsilon - \frac{N_\mathrm{b} N_\mathrm{e} e^2 \alpha_\mathrm{c}}{2T_0^2 E_\mathrm{b} \omega_\mathrm{s}} \sum_{p=-\infty}^{\infty} \omega_{pN_\mathrm{b},\mu} \mathfrak{Re} Z_\parallel(\omega_{pN_\mathrm{b},\mu}); \tag{3.123}$$

hence, the instability growth rate of the μth mode is

$$\begin{aligned} \tau_\mu^{-1} &= \frac{N_\mathrm{b} N_\mathrm{e} e^2 \alpha_\mathrm{c}}{2T_0^2 E_\mathrm{b} \omega_\mathrm{s}} \sum_{p=-\infty}^{\infty} (pN_\mathrm{b}\omega_0 + \mu\omega_0 + \omega_\mathrm{s}) \mathfrak{Re} Z_\parallel(pN_\mathrm{b}\omega_0 + \mu\omega_0 + \omega_\mathrm{s}) \\ &= \frac{\alpha_\mathrm{c} I_\mathrm{b} f_0}{2(E_\mathrm{b}/e)\nu_\mathrm{s}} \sum_{p=-\infty}^{\infty} (pN_\mathrm{b} + \mu + \nu_\mathrm{s}) \mathfrak{Re} Z_\parallel(\omega_0(pN_\mathrm{b} + \mu + \nu_\mathrm{s})) \end{aligned} \tag{3.124}$$

which finds its counterpart in the damping decrement α_ε. Modes with positive growth rates are "dangerous" as they relate to an exponential growth (see Eqs. (3.114) and (3.120)). Those with negative ones are damped; however, the former may in some cases be overcome by the synchrotron radiation damping rate if they are smaller.
It is instructive to investigate why the impedance is sampled at the frequencies in Equation (3.121). This is done in Appendix E.

Robinson criterion

The rf frequency $\omega_\mathrm{rf} = h\omega_0$ lies near the resonance frequency ω_r of the fundamental rf cavity mode, and the harmonic number is necessarily a multiple of N_b (equidistant bunches have been assumed in the derivation – no gap). Now, the impedance is sharply peaked around the resonance frequency (the bandwidth of the fundamental mode in the superconducting cavities in the TESLA damping ring is $\omega_{1/2} = \omega_\mathrm{r}/2Q_\mathrm{L} \approx 3\pi \times 10^3\,\mathrm{Hz}$; $\omega_0 \approx 2\pi \cdot 17.6 \times 10^3\,\mathrm{Hz}$).
For the 0-mode, principally the most unstable because all the bunches oscillate in phase [17], one obtains

$$\begin{aligned} \tau_0^{-1} &\approx \frac{N_\mathrm{b} N_\mathrm{e} e^2 \alpha_\mathrm{c}}{2T_0^2 E_\mathrm{b} \omega_\mathrm{s}} \big((h\omega_0 + \omega_\mathrm{s}) \mathfrak{Re} Z_\parallel(h\omega_0 + \omega_\mathrm{s}) + \\ &\qquad\qquad (-h\omega_0 + \omega_\mathrm{s}) \mathfrak{Re} Z_\parallel(-h\omega_0 + \omega_\mathrm{s}) \big) \\ &= \frac{N_\mathrm{b} N_\mathrm{e} e^2 \alpha_\mathrm{c}}{2T_0^2 E_\mathrm{b} \omega_\mathrm{s}} \big((h\omega_0 + \omega_\mathrm{s}) \mathfrak{Re} Z_\parallel(h\omega_0 + \omega_\mathrm{s}) - \\ &\qquad\qquad (h\omega_0 - \omega_\mathrm{s}) \mathfrak{Re} Z_\parallel(h\omega_0 - \omega_\mathrm{s}) \big) . \end{aligned} \tag{3.125}$$

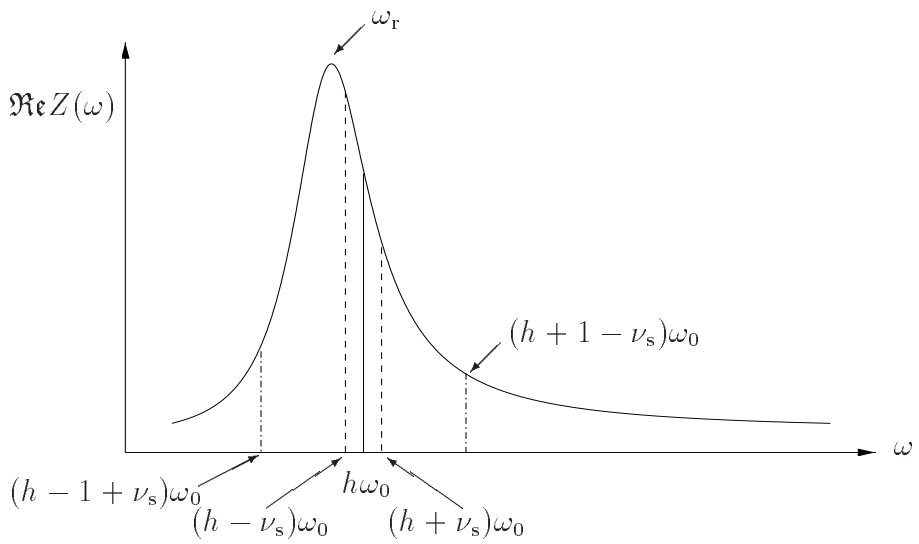

Figure 3.18: Illustration of the Robinson stability criterion and the effect on the nearby mode. The rf fundamental mode is detuned downwards so that ω_r is slightly below $h\omega_0$ to create Robinson damping. The shift leads, however, to unequal impedances of the upper and lower synchrotron sidebands of mode $N_b - 1$.

Beam stability (disregarding α_ε) requires $\tau_0^{-1} \leq 0$. The real part of the impedance must be lower at the frequency $h\omega_0 + \omega_s$ than at the frequency $h\omega_0 - \omega_s$. This implies that above transition the resonant frequency of the fundamental mode should be slightly detuned downwards from $h\omega_0$, and below transition slightly upwards (this condition is known as the *second Robinson stability criterion*). Then the 0-mode is damped, the effect is called "Robinson damping".

Nearby Mode

The necessity of detuning the resonant frequency of the fundamental mode below the rf frequency has a negative side effect. The shift leads to unequal impedances of the upper and lower synchrotron sidebands of the so-called nearby mode, the multibunch mode nearest in frequency to the accelerating mode. With Eq. (3.124), $\omega_r = \omega_{rf} + \Delta\omega$, and $\Re e Z_\parallel(\omega)$ as in Eq. (C.2) one obtains

$$\begin{aligned}\tau_{N_b-1}^{-1} &\approx \frac{\alpha_c I_b f_{rf}}{2(E_b/e)\nu_s}\left(\Re e Z_\parallel((h-1+\nu_s)\omega_0) - \Re e Z_\parallel((h+1-\nu_s)\omega_0)\right) \\ &\approx \frac{\alpha_c I_b f_{rf}}{2(E_b/e)\nu_s}\left(\frac{R_L}{1+4Q_L^2\left(\frac{(1-\nu_s)\omega_0+\Delta\omega}{\omega_{rf}}\right)^2} - \frac{R_L}{1+4Q_L^2\left(\frac{(1-\nu_s)\omega_0-\Delta\omega}{\omega_{rf}}\right)^2}\right). \qquad (3.126)\end{aligned}$$

The coupling factor β_{c0}, which minimizes the generator power (and by which the loaded impedance and quality factor are determined), and optimum cavity detuning (Eq. (3.90), page 38) deliver an instability growth rate of approximately 57 Hz for the TESLA damping ring. Increment of the coupling factor leads to larger instability growth rates.

3.4.2 Higher-Order Cavity Modes

The above analysis also applies to the higher-order modes (e.g. of a cavity). Whether a particular mode will cause for any mode μ a relatively large growth rate or not depends on its exact frequency and the impedance bandwidth. In the most pessimistic case, an upper limit for the growth rates due to a single HOM is given by

$$\tau_\mu^{-1} \leq \frac{\alpha_\mathrm{c} I_\mathrm{b} f_\mathrm{HOM}}{2(E_\mathrm{b}/e)\nu_\mathrm{s}} \mathfrak{Re}\, Z_\parallel(\omega_\mathrm{HOM}). \tag{3.127}$$

3.5 The Vlasov Equation

A different approach to describing the motion of a beam is mode representation, rather than a collection of individual particles (two and more particle models). This representation offers a formalism that can be used systematically to treat the instability problem and can be used to obtain analytic results for high mode numbers. The basic mathematical tool underlying this theory is the Vlasov equation.
The aim of this section is to give a short introduction to the Vlasov equation and to show how it may be applied to describe a phenomenon in which the longitudinal wake field distorts the potential well formed by the accelerating rf voltage. The longitudinal bunch distribution is thereby deformed (see also Section 3.6). Literature sources are [9, 17, 28].

Liouville's Theorem and the Vlasov Equation

For many physical systems, their evolution after a time t only depends on their state at that time. This is determined by the values of r coordinates q_i $(i = 1, \ldots, r)$ and their time derivatives $\dot{q}_i$, the integer r being the number of degrees of freedom. For a bunch of N particles, where, as studied here, the longitudinal motion along the beam axis is decoupled from the motion in the transverse plane, r is N.
Now, if the system is non-dissipative, the equations of motion can be written as a Hamiltonian system. Recall that such a system consists of $2n$ ordinary differential equations of the form

$$\dot{q}_i = \frac{\partial H(q,p,t)}{\partial p_i}, \qquad \dot{p}_i = -\frac{\partial H(q,p,t)}{\partial q_i}, \quad i = 1, \ldots, n, \tag{3.128}$$

where $H = H(q,p,t)$, called the Hamiltonian, is a smooth real-valued function defined for $(q,p,t) \in \mathcal{O}$, where $\mathcal{O}$ is some open set in $\mathbb{R}^n \times \mathbb{R}^n \times \mathbb{R}$. An example was encountered on page 23.
An ensemble of particles at a given moment t occupies a volume $V(t)$ in the (q,p) plane called phase space. At the time $t + \Delta t$, the particles occupy another volume $V(t + \Delta t)$ of exactly the same size; the preservation of the phase space volume (Liouville's theorem) is equivalent to the vanishing of the divergence of the velocity field $v = (\dot{q}, \dot{p})$.
Considering the immediate neighbourhood of a particle (q,p), this implies that the phase space density $\Psi(q,p,t)$ is constant, this being the Vlasov equation:

$$\frac{d\Psi(q,p,t)}{dt} = 0. \tag{3.129}$$

By the existence and uniqueness theorem, the particle trajectory in the extended phase space (q, p, t) is completely determined by the initial conditions (q_0, p_0) at time $t = t_0$. Consequently, trajectories either completely coincide or never intersect. Because of this, looking at a distribution of particles occupying an area in phase space, as the distribution evolves in time, no particle inside the distribution can leak out and no particle from the outside can penetrate into it. In both cases, the crossing of a trajectory of a boundary particle would be inevitable.

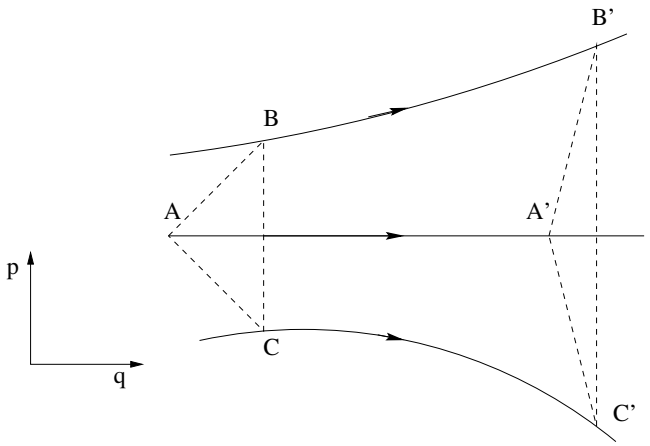

Figure 3.19: Phase space trajectories and Liouville's theorem. The phase space distribution of particles inside the triangle ABC at time t occupy the same phase space area at a time t' later. This area is symbolized by the triangle $A'B'C'$. The trajectories pertaining to the points on the border of the triangle ABC determine the border of the new triangle $A'B'C'$.

The absolute differentiation in Eq. (3.129) indicates that one follows the particle while measuring the density of its immediate neighbourhood, i.e. the local particle density does not change if the observer moves with the flow of particle. This may also be seen in the equivalent form

$$\frac{\partial \Psi(q,p)}{\partial t} + \frac{\partial \Psi(q,p)}{\partial q}\dot{q} + \frac{\partial \Psi(q,p)}{\partial p}\dot{p} = 0, \tag{3.130}$$

which expresses the development of the density as seen by a stationary observer.
One special case is when the phase space density has no explicit time dependence, i.e. a stationary distribution. For a system with one variable pair (p, q), the stationary distribution is a function of the Hamiltonian only,

$$\Psi(q,p) = \text{any function of } H(q,p). \tag{3.131}$$

The theorem of Liouville is visualized in Fig. 3.19 where the phase space trajectories of three particles are drawn. Their positions and the triangular surface element they determine are shown for two different times t. The form of the surface element changes, but its area stays constant.

For electron and positron beams, synchrotron radiation contributes to both damping and diffusion as discussed in Section 3.2, and one needs to modify the Vlasov equation accordingly (they are not incorporated in the Hamiltonian), hereby obtaining the Fokker-Planck equation. Nevertheless, when the instability occurs in a time shorter than the damping or diffusion times, the Vlasov treatment can also apply to electrons or positrons [17].

Potential-Well Distortion

The Vlasov technique may be applied in such a way so as to study how longitudinal wake fields affect the particle distribution within a bunch. Here the interest is primarily to explain the formalism of the Haissinski equation, by which the distorted distribution can be analytically or numerically calculated (see Section 3.6). The derivation follows that of [17].
First of all, the Vlasov equation needs to be constructed. The equations of motion for the canonically conjugate pair τ and ε are given by (3.29) and (3.30). Taking the derivative with respect to the distance s along the accelerator circumference (as in Section 3.4) instead of the time derivative delivers:

$$\tau' = \frac{\alpha_\mathrm{c}}{cE_\mathrm{b}}\varepsilon \tag{3.132}$$

$$\varepsilon' = \frac{eV_\mathrm{rf}\sin(\phi_\mathrm{s}+\omega_\mathrm{rf}\tau) - U_0}{C} = \frac{K(\tau)}{C}. \tag{3.133}$$

The Vlasov equation corresponding to Eq. (3.130) is thus

$$\frac{\partial\Psi}{\partial s} + \frac{\alpha_\mathrm{c}\varepsilon}{cE_\mathrm{b}}\frac{\partial\Psi}{\partial\tau} + \frac{K(\tau)}{C}\frac{\partial\Psi}{\partial\varepsilon} = 0. \tag{3.134}$$

The general stationary solution ($\partial\Psi/\partial s = 0$) can be written as

$$\begin{aligned} \Psi(\tau,\varepsilon) &= \text{any function of the Hamiltonian } H, \\ H &= \frac{1}{c}\left[\frac{\alpha_\mathrm{c}}{2E_\mathrm{b}}\varepsilon^2 - \frac{1}{T_0}\int_0^\tau K(t)dt\right] \end{aligned} \tag{3.135}$$

because the latter has no explicit time dependence.
As stated in Section 3.2, the energy distribution is Gaussian. This is met when taking the appropriate exponential function of the Hamiltonian,

$$\Psi(\tau,\varepsilon) \propto \exp\left(-\frac{cE_\mathrm{b}}{\alpha_\mathrm{c}\sigma_\varepsilon^2}H\right). \tag{3.136}$$

The value of σ_ε in the above equation is arbitrary, as long as the collective beam behaviour is governed by the Vlasov equation. However, if the beam behaviour is governed as for an electron or a positron beam by the Fokker-Planck equation, then Eq. (3.136) with a specific value for σ_ε will be the unique solution of the stationary beam distribution [17].
In Section 3.2, the distribution in τ was also said to be Gaussian in the absence of beam-induced fields. A further requirement is that the bunch length be much shorter than the rf wavelength ($\sigma_z \ll c/\omega_\mathrm{rf}$). Then, linearization of the rf voltage is valid. This yields a

parabolic potential well. However, as the bunch length increases, the bunch shape deviates from the Gaussian form; the potential well is distorted by the rf bucket.
Now the retarding voltage seen by a particle at longitudinal position τ, due to all the particles in front of it, is introduced (see Eq. (3.50); the wake is assumed to dissipate before the bunch completes one revolution). The corresponding Hamiltonian is

$$H = \frac{1}{c}\left[\frac{\alpha_\mathrm{c}}{2E_\mathrm{b}}\varepsilon^2 - \frac{1}{T_0}\int_0^\tau \left(K(t) + N_\mathrm{e}e^2\int_0^\infty \lambda(t-t')W_{\delta,\parallel}(t')dt'\right)dt\right]. \tag{3.137}$$

Substitution of Eq. (3.137) into Eq. (3.136) delivers the transcendental equation for the normalized line-charge density $\lambda(\tau)$

$$\lambda(\tau) = \lambda(0)\exp\left[\frac{E_\mathrm{b}}{\alpha_\mathrm{c}\sigma_\varepsilon^2 T_0}\int_0^\tau \left(K(t) + N_\mathrm{e}e^2\int_0^\infty \lambda(t-t')W_{\delta,\parallel}(t')dt'\right)dt\right].$$

For K as specified in Eq. (3.133) and using the Eqs. (3.14) and (3.25), the equation can be written as:

$$\lambda(\tau) = \lambda(0)\exp\left[\frac{-1}{\omega_\mathrm{rf}eV_\mathrm{rf}\cos\phi_\mathrm{s}\sigma_t^2}\int_0^\tau \Big(eV_\mathrm{rf}\sin(\phi_\mathrm{s}+\omega_\mathrm{rf}\tau) - U_0 + N_\mathrm{e}e^2\int_0^\infty \lambda(t-t')W_{\delta,\parallel}(t')dt'\Big)dt\right]. \tag{3.138}$$

This is the form of the Haissinski equation as it is presented in Section 3.6, Eq. (3.139), where the abbreviation $\dot{V}_\mathrm{RF} = \omega_\mathrm{rf}V_\mathrm{rf}\cos\phi_\mathrm{s}$ has been used.

Beyond some threshold current the energy spread begins to increase, and the Haissinski equation no longer holds. The regime, that is entered, is called the *turbulent regime*. The increase in energy spread is accompanied by an increase in the bunch length. Analytical approaches towards explaining this phenomenon, which is also referred to as *mode coupling* or *mode mixing*, begin with the Vlasov equation. The distribution $\Psi(q,p,s)$ is split into a stationary part $\Psi_0(H)$ and an oscillating perturbation $\Psi_1(q,p)$ which is assumed to be small

$$\Psi(q,p,s) = \Psi_0(H) + \Psi_1(q,p)e^{i\Omega s/c}.$$

Inserting the distribution Ψ into the Vlasov equation and linearizing it with respect to the perturbation Ψ_1, leads then to the *linearized Vlasov equation*, which forms the base of the further treatment. Examples of such procedures can be found in [17, 29].

3.6 The Haissinski Equation

The Haissinski equation [8] is a non-linear integral equation describing, in a suitable phase space, the evolution of the longitudinal particle density distribution of a bunch. The potential well formed by the accelerating rf voltage is distorted by the longitudinal wake field, and as a result the longitudinal beam distribution is deformed.

The equation was originally derived by Haissinski using the Fokker-Planck equation as a starting-point. Note that in the derivation in the previous section a number of assumptions were made.
The beam current distribution below the turbulent threshold, calculated with the Haissinski equation, is given by

$$\lambda(\tau) = K \exp\left(\frac{1}{\sigma_{t0}^2 e|\dot{V}_{\mathrm{RF}}|}\int_0^\tau \left[eV_{\mathrm{RF}}(t) - U_0 + eV_{\mathrm{ind}}(t)\right] dt\right), \tag{3.139}$$

where σ_{t0} and $\dot{V}_{\mathrm{RF}}$ are the natural bunch length and the slope of the rf voltage at the phase of the synchronous particle, positioned here at $t = 0$. Furthermore, V_{ind}, the transient induced voltage, is given by

$$V_{\mathrm{ind}}(t) = q_{\mathrm{b}} \int_0^\infty W_{\delta,\|}(t')\lambda(t - t')\, dt' \tag{3.140}$$

with $W_{\delta,\|}(t')$ a Green's function of the longitudinal wake field and q_{b} the bunch charge. The value of the normalization constant K in Eq. (3.139) is defined so that the integral of $\lambda(\tau)$ is equal to one.
Integral equation (3.139) can be converted into a differential one by taking the logarithm on both sides. Differentiation with respect to τ then yields

$$\frac{\lambda'}{\lambda} = -U_{\mathrm{P}}'(\tau) + \frac{V_{\mathrm{ind}}(\tau)}{|\dot{V}_{\mathrm{RF}}|\sigma_{t0}^2}, \tag{3.141}$$

where $U_{\mathrm{P}}(\tau) = -\int_0^\tau \left[V_{\mathrm{RF}}(t) - U_0/e\right]/(|\dot{V}_{\mathrm{RF}}|\sigma_{t0}^2)\, dt$ is the undisturbed potential.
Either Eq. (3.139) – or the alternative forms still to be shown – or (3.141) can be used to estimate the bunch distribution and length due to the distortion of the potential well by the wake fields.

When the rf voltage is linearized, Eq. (3.139) takes the form

$$\lambda(\tau) = K \exp\left(-\frac{\tau^2}{2\sigma_{t0}^2} + \frac{1}{|\dot{V}_{\mathrm{RF}}|\sigma_{t0}^2}\int_0^\tau V_{\mathrm{ind}}(t)\, dt\right) \tag{3.142}$$

and for the differential equation one obtains:

$$\frac{\lambda'}{\lambda} = -\frac{\tau}{\sigma_{t0}^2} + \frac{V_{\mathrm{ind}}(\tau)}{|\dot{V}_{\mathrm{RF}}|\sigma_{t0}^2}. \tag{3.143}$$

Example: inductive impedance

When the impedance of the ring is assumed to be purely inductive, i.e. when the induced voltage is given by

$$V_{\mathrm{ind}}(t) = -Lq_{\mathrm{b}}\frac{d\lambda}{dt} \tag{3.144}$$

with a constant inductance L, Eq. (3.143) can be written as

$$\frac{dy}{dx} = -\frac{xy}{1+y} \tag{3.145}$$

with the variables of $x = \tau/\sigma_{t0}$, $y = Lq_{\mathrm{b}}\lambda/(|\dot{V}_{\mathrm{RF}}|\sigma_{t0}^2)$ (see [11, 30] or also [31]). Here it is possible to define the normalized charge κ, the integral of y, as follows:

$$\kappa = \int_{-\infty}^{\infty} y\,dx = \frac{Lq_{\mathrm{b}}}{|\dot{V}_{\mathrm{RF}}|\sigma_{t0}^3}. \tag{3.146}$$

κ is, therefore, inversely proportional to $\alpha_{\mathrm{c}}^{3/2}$ (see Eqs. (3.14) and (3.25)).

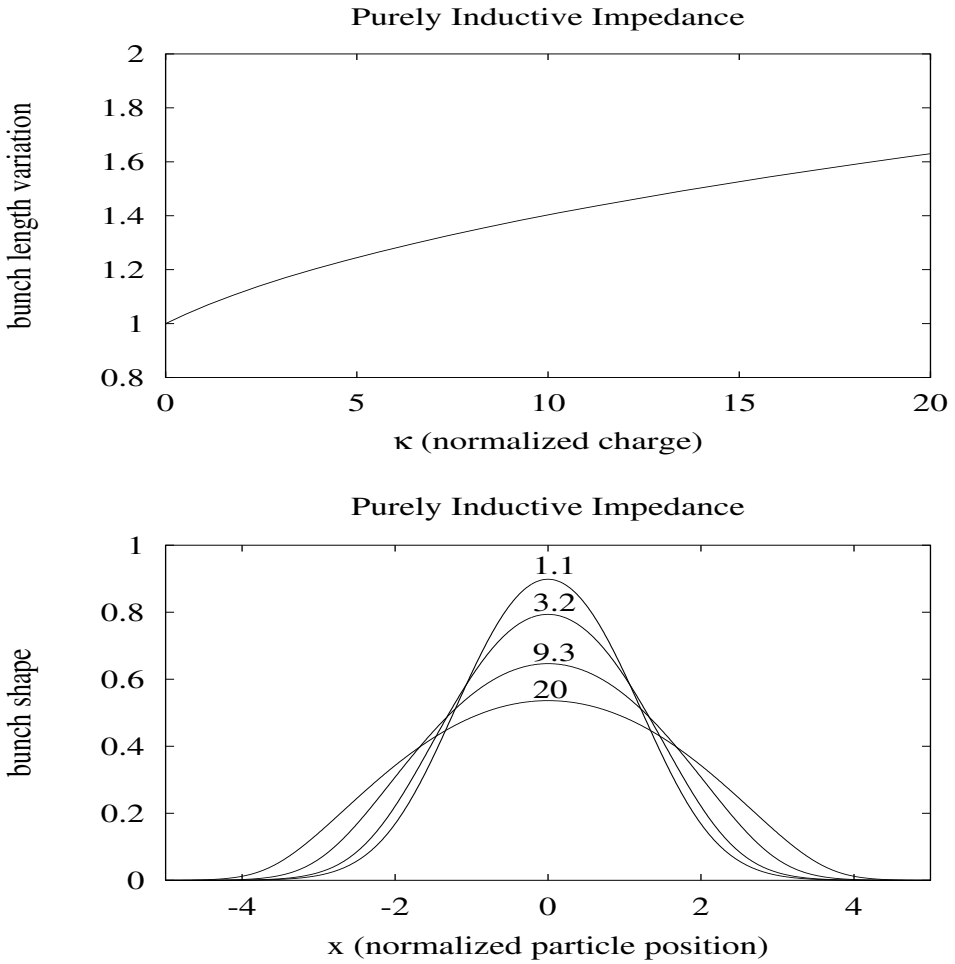

Figure 3.20: The bunch length variation as a function of the normalized bunch charge κ (top plot) and the bunch shape for several values of κ (bottom plot).

The numerical solution of Eq. (3.145) is shown in Figure 3.20 for several values of κ. The charge distribution for a perfect inductor is symmetric about $x = 0$, and it is almost

the same as the Gaussian distribution for low intensity regions. On the other hand, it is apparent that the solution of Eq. (3.145) is rather a parabolic than Gaussian distribution whenever $y(0) \gg 1$. The standard deviations σ_x for $\kappa \leq 20$ are shown in the top plot of Figure 3.20 by which one can see that σ_x varies linearly for small normalized charge regions.
The relative change in bunch length may be estimated for small κ as

$$\frac{\Delta\sigma_t}{\sigma_{t0}} \approx \frac{Lq_\mathrm{b}}{8\sqrt{\pi}|\dot{V}_\mathrm{RF}|\sigma_{t0}^3} = \frac{\kappa}{8\sqrt{\pi}}. \tag{3.147}$$

Eq. (3.147) is derived in the appendix. Solving Eq. (3.145) numerically, for example with the iterated trapezoidal rule, delivers, for small κ, practically identical values as can be seen in Table 3.1.

κ	Numerical Integration	Equation (3.147)
0.005016	0.00037	0.00035
0.529800	0.0352	0.0374

Table 3.1: Relative increase in bunch length for small normalized charges κ.

The approximation formula presented in [32] and cited in [33] and in the CDR [1] differs by a factor of $2\sqrt{2}$. This leads to a wrong estimation of the bunch lengthening effect. The authors in ref. [32] begin with the Haissinski equation (3.142) and insert the induced voltage according to Eq. (3.144). This leads to a term $\lambda(\tau)$ in the exponential function. It is then assumed that τ is small, and $\lambda(\tau)$ is expanded as a Gaussian function to the first order. This is the source of the mistake. Only at the end of the derivation do the authors consider small κ.

Example: resistive impedance

The Haissinski equation for a purely resistive impedance $Z_{\|}(\omega) = R$ can be solved analytically when the undisturbed potential-well term is approximated by $\tau^2/2\sigma_{t0}$. It is

$$\lambda(\tau) = \frac{\sqrt{2/\pi}\exp(-\tau^2/2\sigma_{t0}^2)}{\kappa\sigma_{t0}\left[\coth(\kappa/2) + \mathrm{erf}(\tau/\sqrt{2}\sigma_{t0})\right]}, \tag{3.148}$$

where the normalized charge κ is

$$\kappa = \frac{Rq_\mathrm{b}}{\sigma_{t0}^2|\dot{V}_\mathrm{RF}|}. \tag{3.149}$$

The solution, which was found by A. Ruggiero [34], is derived in the appendix (D.2).

The case of a purely capacitive impedance leads to an integro-differential equation. The numerical solution shows that the bunches remain essentially Gaussian, but with a reduced length [35].

Alternative form of the Haissinski equation

Shortly after the first publication of the Haissinski equation it was realized that the double integral

$$\int_0^\tau \int_0^\infty W_{\delta,\|}(t')\lambda(t-t')\,dt'\,dt \tag{3.150}$$

could be reduced to a single one by reversing the order of integration [36].
In the first step the integration variable of the second integral is changed, and due to causality, the upper integral limit can be extended to infinity to obtain:

$$\int_0^\tau \int_{-\infty}^t W_{\delta,\|}(t-t')\lambda(t')\,dt'\,dt = \int_0^\tau \int_{-\infty}^\infty W_{\delta,\|}(t-t')\lambda(t')\,dt'\,dt.$$

Reversing the order of integration leads to

$$\int_{-\infty}^\infty \lambda(t')\big(S(\tau-t')-S(-t')\big)\,dt' \tag{3.151}$$

where $S(t)$ is the *step function response* (wake function of a unit step):

$$S(t) = \int_0^t W_{\delta,\|}(t')\,dt'. \tag{3.152}$$

For example, a purely resistive impedance corresponds to a constant step function response ($S(t) = -R$, $t > 0$), because the delta wake function is the delta function times a factor $-R$.
Including the second part of the integral in Eq. (3.151), which is independent of τ, in the constant K, the Haissinski equation may be rewritten as

$$\lambda(\tau) = K \exp\left[-U_{\mathrm{P}}(\tau) + \frac{q_{\mathrm{b}}}{|\dot{V}_{\mathrm{RF}}|\sigma_{t0}^2}\int_{-\infty}^\tau S(\tau-t)\lambda(t)dt\right] \tag{3.153}$$

or alternatively

$$\lambda(\tau) = K \exp\left[-U_{\mathrm{P}}(\tau) + \frac{q_{\mathrm{b}}}{|\dot{V}_{\mathrm{RF}}|\sigma_{t0}^2}\int_0^\infty S(t)\lambda(\tau-t)dt\right]. \tag{3.154}$$

Eq. (3.154) is the form of the Haissinski equation which has been used to solve it numerically.

Numerical Integration

As will be elaborated in Section 4, quasi-Green's functions [37] are used instead of delta wake functions to estimate the self-induced voltage of a bunch. A quasi-Green's function is a wake potential generated by a Gaussian bunch with an rms bunch length smaller than that of the bunch under study. The Gaussian bunches are centred at zero and have a total bunch length of $10\sigma_t$.

The step function reflects this fact and is non-zero for negative t. To be precise, it is $S(t) \neq 0$ for $t > -5\sigma_{t,\mathrm{max}}^{\mathrm{QGF}}$, where $\sigma_{t,\mathrm{max}}^{\mathrm{QGF}}$ denotes the standard deviation of the largest Gaussian bunch being used to generate a quasi-Green's function (the wake in the TESLA damping ring consists of various components, for which quasi-Green's functions have been established; the corresponding Gaussian bunches differ in their rms values). The lower integral limit in Eq. (3.154) is set to $-5\sigma_{t,\mathrm{max}}^{\mathrm{QGF}}$.
The step function values $S_i = S(t_i)$ are established as

$$S_i = \Delta_t \sum_{j=\tilde{j}}^{i} W_{\mathrm{QGF},i}, \quad \text{with} \quad W_{\mathrm{QGF},i} = W_{\mathrm{QGF}}(t_i), \quad t_i = i\Delta_t$$

and where $\tilde{j}\Delta_t \approx -5\sigma_{t,\mathrm{max}}^{\mathrm{QGF}}$. The time step in the calculations Δ_t is $0.1\,\mathrm{mm}/c$ or slightly less.
The distribution estimates, λ_i, are obtained by an iteration process (the integral is normalized). The initial setting is that of a Gaussian distribution, evaluated between $-10\sigma_t$ and $10\sigma_t$. Each time, the estimation begins with the lowest indices, i.e. well ahead of the bunch centre where, in the limit, λ_i is zero. The integral in the exponent of Eq. (3.154) is calculated as

$$\int_{-5\sigma_{t,\mathrm{max}}^{\mathrm{QGF}}}^{\infty} S(t)\lambda(\tau - t)\,dt \approx \Delta_t \sum_{j=\tilde{j}} S_j \lambda_{i-j}.$$

As $\tilde{j}$ is negative, distribution values $\tilde{\lambda}_m$ from the previous iteration are needed to calculate λ_i for $i \leq m$. These are normalized, i.e. λ_m divided by $\sum_n \lambda_n$, so that $\Delta_t \sum_n \tilde{\lambda}_n = 1$.
Summarizing, the iteration process is

$$\lambda_i^k = K^k \exp\left[-U_{\mathrm{P}}(t_i) + \frac{q_{\mathrm{b}}}{|\dot{V}_{\mathrm{RF}}|\sigma_{t0}^2}\Delta_t \sum_{j=\tilde{j}} S_j \hat{\lambda}_{i-j}^k\right], \tag{3.155}$$

where

$$\hat{\lambda}_{i-j}^k = \begin{cases} i-j < i & : \quad \lambda_{i-j}^k \\ i-j \geq i & : \quad \tilde{\lambda}_{i-j}^{k-1} = \lambda_{i-j}^{k-1} / \sum_n \lambda_n^{k-1} \end{cases}$$

and

$$K^k = K^{k-1} / \sum_n \lambda_n^{k-1}; \quad K^0 = 1/\sqrt{2\pi\sigma_{t0}^2}.$$

The superscript pertains to the iteration number. The iteration process was stopped when the following conditions were fulfilled:

$$\begin{aligned} \Delta_t \Big| \sum_i \lambda_i^p - 1 \Big| &< \epsilon_1 \quad \text{for} \quad p = k-1, k, \\ \Delta_t \sum_i |\lambda_i^k - \tilde{\lambda}_i^{k-1}| &< \epsilon_2. \end{aligned}$$

ϵ_1 was chosen to be 1×10^{-4} and ϵ_2 as 5×10^{-5}.

Chapter 4

Simulation Technique

While the single and multibunch simulation techniques follow similar principles – both are based on the same equations of motion as described in Chapter 3 – the two cases differ substantially with respect to the calculation of the wake field effect. A résumé of the differences is shown in Table 4.1.

	Single bunch	Multibunch
Description	Macroparticles	One particle per bunch
Memory (turn-to-turn)	No	Yes
Bunch-to-bunch interaction	No	Yes
Wake field	Short-range	Long-range
Estimation of wake field effects with help of	Quasi-Green's functions	Higher-Order Modes, Beam loading (accelerating mode)

Table 4.1: Résumé of Simulation Technique Differences.

The multibunch simulation technique is closely related to the one-particle model with its rigidness and neglect of internal structure which is used in the derivation of the Robinson instability (Section 3.4).

4.1 Single Bunch Tracking

The simulation is based upon the usage of macroparticles and the incorporation of wake field effects into the equations of motion with the help of quasi-Green's functions (see [37]).

A bunch is represented by a variable number N_{par} of macroparticles (τ_k, ε_k) where

τ_k particle position in time, with origin at zero of the main rf,

ε_k particle energy deviation from nominal energy E_{b}.

The tracking equations in the program are such that it is possible to define different sections within the machine and track during one turn from one sector to another.

For simplicity, the equations of motion given here are for a full revolution where the phase space coordinates on turn $n+1$ are related to those on turn n by [37]

$$\tau_k^{n+1} = \tau_k^n + \frac{\alpha_c T_0}{E_b}\varepsilon_k^n - \frac{\alpha_c T_0 U_0}{2E_b} \tag{4.1}$$

$$\varepsilon_k^{n+1} = \varepsilon_k^n + e\sum_{i=1}^{m} V_{\mathrm{rf},i}\sin(\omega_{\mathrm{rf},i}\tau_k^{n+1} + \phi_i) - U_0 - \frac{2T_0}{T_\varepsilon}\varepsilon_k^n + 2\sqrt{\frac{T_0}{T_\varepsilon}}\sigma_{0\varepsilon}R_G + eW_k^{n+1} \tag{4.2}$$

with

$eV_{\mathrm{rf},i}$	peak energy gain from the rf i
$\omega_{\mathrm{rf},i}$	angular frequency of the rf i
ϕ_i	phase off-set from main rf (with index $i=1$, $\phi_1 = 0$)
$\sigma_{0\varepsilon}$	natural energy spread of the beam
R_G	Gaussian distributed random number with mean = 0 and rms = 1
W_k^n	longitudinal wake on the nth turn seen by the kth particle

Memory effects due to resonant modes in cavities are not included. The penultimate term on the right-hand side of the second equation describes the energy variation due to quantum excitation by photon emission. The third term on the right-hand side of the first equation reflects the continuous radiation loss, here between two successive turns. Due to this term, a synchronous particle has a non-zero amplitude. There is an option in the program to track without accounting for the continuous radiation loss, which is referred to as "switching off" the continuous synchrotron radiation loss term.
It is interesting to note that linearization of the rf voltage and neglect of the damping and quantum excitation terms lead to a symplectic mapping, in this special case via the leap-frog integration method.
When tracking with p identical sections, T_0 is replaced, for example, by $T_0^j = T_0/p$. Note that in the TESLA damping ring there is only one rf frequency, although the above equations show the possibility of having different frequencies.

Instead of using Green's functions (δ-wakes) to calculate the wake potentials, quasi-Green's functions are used: the wake potentials of Gaussian bunches with a smaller rms value than the bunch studied. The basic idea behind this technique is the following relationship between the wake potentials of two Gaussian bunches due to the one and same δ-wake.

$$W_{\sigma_{z,i}}(s) = \int_{-\infty}^{\infty} \lambda_{\sigma_{z,i}}(s-z)\, W_\delta(z)\, dz, \quad i = 1,2 \tag{4.3}$$

$$\Rightarrow W_{\sigma_{z,2}}(s) = \int_{-\infty}^{\infty} \lambda_{\sqrt{\sigma_{z,2}^2-\sigma_{z,1}^2}}(s-z)\, W_{\sigma_{z,1}}(z)\, dz. \tag{4.4}$$

Note

$$\sqrt{\sigma_{z,2}^2 - \sigma_{z,1}^2} = \sigma_{z,2}\sqrt{1-\left(\frac{\sigma_{z,1}}{\sigma_{z,2}}\right)^2} \approx \sigma_{z,2}, \quad \sigma_{z,1} \ll \sigma_{z,2},$$

so that

$$W_{\sigma_{z,2}}(s) \approx \int_{-\infty}^{\infty} \lambda_{\sigma_{z,2}}(s-z)\, W_{\sigma_{z,1}}(z)\, dz. \tag{4.5}$$

Figure 4.1: Macroparticle binning.

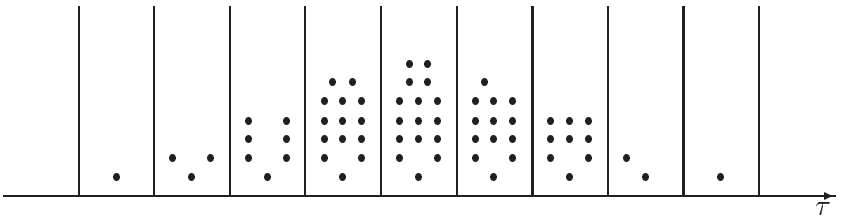

A trait of the numerical approximation is that $W_{\sigma_{z,1}}(z) \not\equiv 0$ for $z < 0$. In the following, the abbreviation QGF will stand for quasi-Green's function, and mean any wake potential which is being used instead of the Green's function, as in the above case $W_{\sigma_{z,1}}(z)$. The rms bunch length of the Gaussian bunch which generates the wake potential is sometimes abbreviated by σ_z^{QGF}.

To determine the wake potential seen by a macroparticle a binning technique is used. The bunch represented by the N_{par} macroparticles is divided into bins, each of the same pre-defined constant width. Then $\tau_{\mathrm{c}}(i)$, the centre of mass for every bin i, and $n_{\mathrm{b}}(i)$, the number of particles in bin i, are determined.

The wake field effect on each bin is calculated as:

$$W_{\mathrm{b}}(i) = \frac{q_{\mathrm{b}}}{N_{\mathrm{par}}} \sum_{j=1}^{N_{\mathrm{bin}}} n_{\mathrm{b}}(j) \cdot \mathrm{QGF}(\tau_{\mathrm{c}}(i) - \tau_{\mathrm{c}}(j)) \tag{4.6}$$

which corresponds to

$$q_{\mathrm{b}} W_{\lambda}(s) = q_{\mathrm{b}} \int_{-\infty}^{s} \lambda(z)\, W_{\delta}(s-z)\, dz$$

with λ a normalized line-charge density (i.e. $\int_{-\infty}^{\infty} \lambda(z) dz = 1$) and with the delta wake or Green's function $W_{\delta}(z)$.

The wake potential seen by a macroparticle (τ_k, ε_k) is then calculated by linear interpolation [38]

$$W(\tau_k) = W_{\mathrm{b}}(i) \cdot (1 - \Delta\tau) + W_{\mathrm{b}}(i+1) \cdot \Delta\tau, \tag{4.7}$$

where

$$\Delta\tau = \frac{\tau_k - \tau_{\mathrm{c}}(i)}{\tau_{\mathrm{c}}(i+1) - \tau_{\mathrm{c}}(i)} \quad \text{and} \quad \tau_{\mathrm{c}}(i) \le \tau_k < \tau_{\mathrm{c}}(i+1). \tag{4.8}$$

Therefore, there is no artificial jump of the wake potentials seen by the macroparticles due to the binning, i.e. the transition between two bins is continuous.

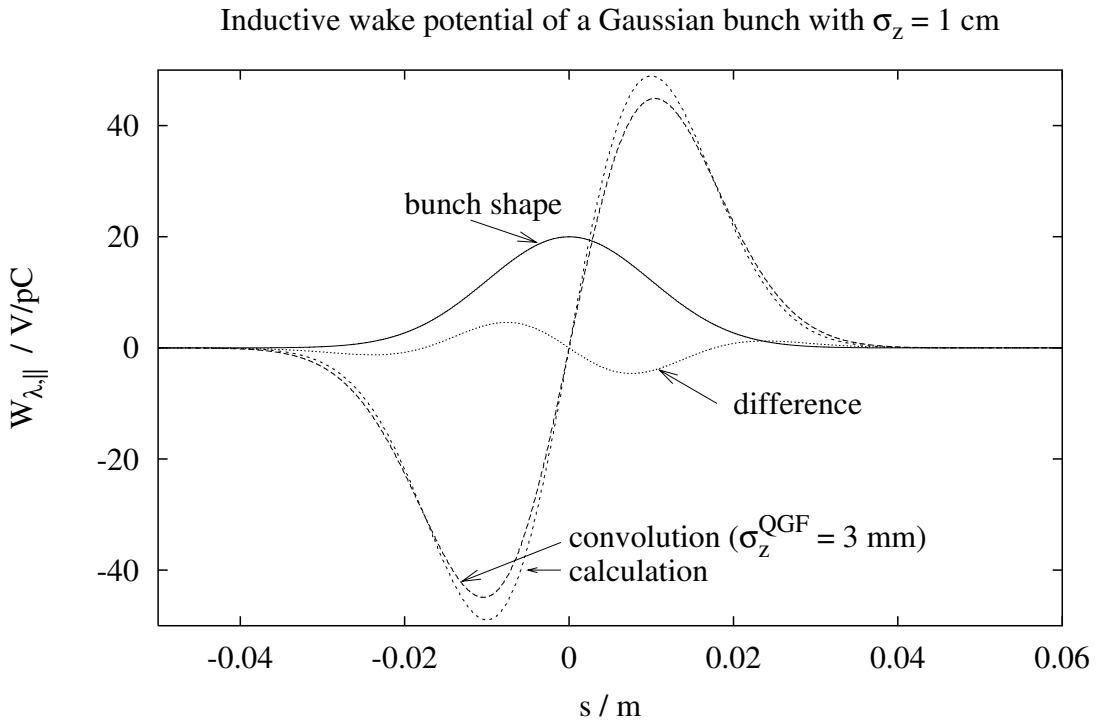

Figure 4.2: The assumed inductive wake potential of a Gaussian bunch with $\sigma_z = 1\,\mathrm{cm}$ in the damping ring ($L = 0.18\,\mu\mathrm{H}$). The term "calculation" refers here to the true inductive wake, and the term "convolution" to the wake obtained by using Eq. (4.9). "Difference" is the difference between the two wake potentials.

In a few cases, in order to test the influence of statistical fluctuations over the number of particles per bin, the wake calculation has been changed by doing the following: the number of particles per bin $n_\mathrm{b}(i)$ is replaced by the average over the bins $i-m$ to $i+m$, i.e. $\tilde{n}_\mathrm{b}(i) = (n_\mathrm{b}(i-m) + \cdots + n_\mathrm{b}(i) + \ldots n_\mathrm{b}(i+m))/(2m+1)$ and the centre of the mass is replaced by the middle of the bin. The above will be referred to as a "smoothed" calculation using $2m+1$ bins.
Figure 4.2 compares the inductive wake potential, $Z(w) = i\omega L$, of a Gaussian bunch with $\sigma_z = 1\,\mathrm{cm}$ in the dog-bone, with that obtainable by convolution using the wake of a Gaussian bunch with the rms bunch length 3 mm as a QGF. The convolution has been calculated by numerical approximation of

$$W_{\sigma_{z,2}}^{\sigma_{z,1}}(s) = \int_{-\infty}^{\infty} \lambda_{\sigma_{z,2}}(s-z)\, W_{\sigma_{z,1}}(z)\, dz \tag{4.9}$$

which corresponds to letting $N_\mathrm{bin} \to \infty$ and $N_\mathrm{par} \to \infty$ when using the binning technique. In the case of an inductive wake, $W_\delta(s) = -c^2 L \cdot \delta'(s)$, Eq. (4.9) can be solved analytically:

$$W_{\sigma_z}^{\sigma_z^\mathrm{QGF}}(s) = c^2 L \frac{s}{\sqrt{2\pi}} ((\sigma_z^\mathrm{QGF})^2 + \sigma_z^2)^{-3/2} \exp\left(-\frac{s^2}{2\sigma_z^2}\left(1 - \frac{1}{1+\varsigma^2}\right)\right) \tag{4.10}$$

with $\varsigma = \sigma_z / \sigma_z^\mathrm{QGF}$.

The relative error of the maximum absolute wake ($s = \pm\sigma_z$) is

$$e(\varsigma) = 1 - \varsigma^3(1+\varsigma^2)^{-3/2}\exp\left(\frac{1}{2(1+\varsigma^2)}\right). \tag{4.11}$$

A number of examples are given in Table 4.2.

ς	1	2	5/3	2.5	3.3	5	10
$e(\varsigma)$ / %	54.6	20.9	28.0	14.2	8.4	3.9	1.0

Table 4.2: The relative error of the maximum absolute wake for an inductive wake potential as a function of the relative width ς of the studied bunch and the QGF.

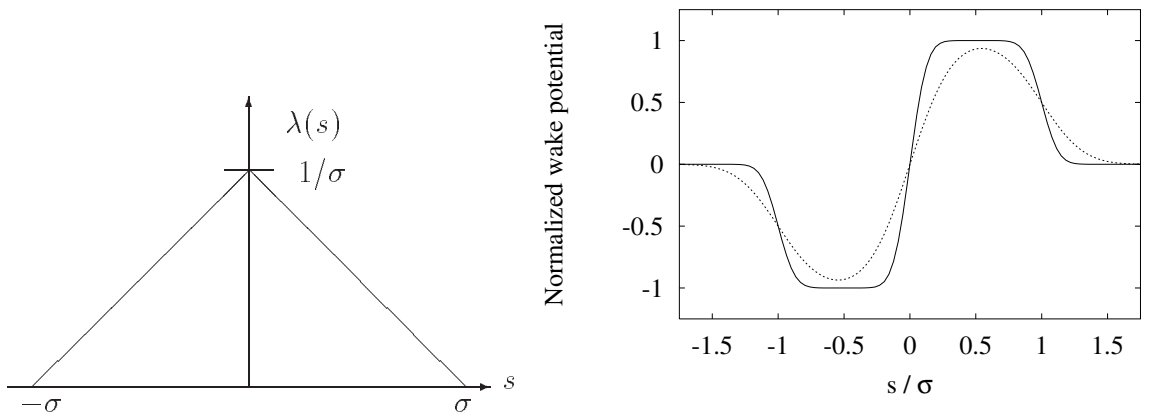

Figure 4.3: A bunch with the form of an isosceles triangle with the base 2σ, and its wake as calculated using a Gaussian QGF, $\varsigma = 10$ solid line, $\varsigma = 4$ dashed line ($\varsigma = \sigma/\sigma_z^{\mathrm{QGF}}$).

A further purely theoretical example is that of an inductive wake potential of a bunch with the form of an isosceles triangle with the base 2σ and

$$W_{\triangle,\sigma}(s) = -\,\mathrm{sign}(s)\frac{c^2 L}{\sigma^2}. \tag{4.12}$$

Equation (4.5) leads to

$$W_{\triangle,\sigma}^{\sigma_z^{\mathrm{QGF}}}(s) = \frac{c^2 L}{\sigma^2}\left(\mathrm{erf}\left(\frac{s}{\sqrt{2}\sigma_z^{\mathrm{QGF}}}\right) - \frac{1}{2}\,\mathrm{erf}\left(\frac{s-\sigma}{\sqrt{2}\sigma_z^{\mathrm{QGF}}}\right) - \frac{1}{2}\,\mathrm{erf}\left(\frac{s+\sigma}{\sqrt{2}\sigma_z^{\mathrm{QGF}}}\right)\right). \tag{4.13}$$

Due to the discontinuity of the step function, the particles in the middle of the bunch naturally see a relatively larger error, nevertheless the total error with respect to the whole bunch drops drastically with increasing ς (see Figure 4.3).

One advantage of the binning is that the evaluation of Eq. (4.6) is $\sim N_{\mathrm{bin}}^2$ operations, whereas the corresponding equation to Eq. (4.6) would otherwise lead to a term $\sim N_{\mathrm{par}}^2$ [37]. The filling of the bins (the particles are pre-sorted which is $\sim N_{\mathrm{par}} \log N_{\mathrm{par}}$ and the later interpolation (Eq. (4.7)) is $\sim N_{\mathrm{par}}$ but the total amounts to obviously fewer operations for larger particle numbers.

Elsewhere other binning techniques have been used in single bunch simulations. The following two have been applied in refs. [39, 40]:

- Variable bins arranged so that they all contain the same number of particles.
- A hybrid method where bins were used to describe the wake potential due to particles in earlier bins, but point charges were used for the wakes due to particles in the same bin.

An entirely different approach for calculating the wake field acting on the test particles is to treat them as randomly chosen samples of a charge distribution $\lambda(t)$, as was done in refs. [41, 42]. A sum of smooth functions is fitted to the density distribution in the bunch. Products of Gaussians and Hermite polynomials are a natural choice for this fit, because of the Gaussians present in the orthogonality relation for Hermite polynomials. The computer time is proportional to the product of the number of superparticles and the number of functions in the fit. The wake potential must be computed for all the functions. This line of approach to the wake field representation has also been carried out, for example, at CERN [43]. These methods require, however, two Fourier transformations – or approximations hereof – one being that of the used "quasi-" Green's function.
In [44] it is maintained that when the wake potential of the Gaussian distribution is obtained by numerical solution of Maxwell's equations, the use of numerical deviations to compute the wakes of higher-order Hermite polynomials leads to a rapid loss of accuracy. Better results could be obtained if the wake were computed analytically for a broad-band resonator model.
The simulation program TRISIM [44], which simulates the longitudinal-vertical motion of macroparticles, uses a method based on an expansion of the distribution of the charge density, and of its transverse moment, on a basis of linear interpolating functions.
Approaches to modelling the wake field effects that are similar to those in this thesis can be found, amongst others, in K. Bane's work, e.g. [45] (there the values of the Green's function belonging to the part in front of the bunch centre, $s < 0$, are "reflected", meaning added to the corresponding values for $s > 0$), and in [46], where the values of the Green's function for $s < 0$ were omitted.

4.2 Multibunch Simulation

In the multibunch simulation the wake fields which give rise to bunch-to-bunch interaction – the long-ranged wake fields – are accounted for; the short-ranged wake fields are neglected. The simulations must also take into account contributions from residual wake fields from previous revolutions, if they persist longer than the accelerator circumference. The calculation of the multiturn wake forces, therefore, involves double summations – one

over the macroparticles, the other over the previous revolutions – which would consume much computer time [17, p. 214]. For resonator impedances, however, this can be avoided by noting that the wake function can be written as a phasor [18]. This will be described in detail further below.

In the simulations, the higher-order modes have been distinguished from the fundamental cavity mode. When studying only HOMs it has been assumed that the compensation of the beam-loading effects due to the fundamental mode and the detuning is perfect, i.e. as if they were not present in the cavity. This is the first case studied.
Each bunch is represented by one macroparticle (τ_k, ε_k) which may be looked upon as the bunch centroid. The terminology in the equations below is exactly the same as on page 61, except that the index k represents the kth bunch rather than the kth particle within a bunch.

$$\tau_k^{n+1} = \tau_k^n + \frac{\alpha_\mathrm{c} T_0}{E_\mathrm{b}} \varepsilon_k^n - \frac{\alpha_\mathrm{c} T_0 U_0}{2 E_\mathrm{b}} \tag{4.14}$$

$$\varepsilon_k^{n+1} = \varepsilon_k^n + e F_\mathrm{b} \sum_{i=1}^{m} V_{\mathrm{rf},i} \sin(\omega_{\mathrm{rf},i} \tau_k^{n+1} + \phi_i) - U_0 - \frac{2 T_0}{T_\varepsilon} \varepsilon_k^n + e W_k^{n+1} \tag{4.15}$$

The only difference between (4.14) and (4.15) and the recurrence relations (4.1) and (4.2) is that the quantum excitation term is set to nil – as it reflects the average over the whole bunch and that the rf voltage is multiplied with the bunch form factor F_b (see Eq. (3.77), page 34). The effect of the wake fields is, as mentioned above, necessarily calculated in a different fashion from that of the short-range wake fields used for the single bunch tracking.

For the simulations, the simplified approximative wake of a cavity mode has been used. Eq. (3.71) reads

$$W_{\parallel,\delta}(t) = -2 k_{\delta,\parallel} \exp(-\Gamma t) \cos \omega_\mathrm{r} t \; \Theta(t)$$

with the cavity damping factor Γ and the resonance angular frequency ω_r. In order to take the bunch length into account, the loss factor must be corrected by the square of the bunch form factor (see page 34), hereby obtaining the effective wake as seen by a bunch. Assuming a Gaussian distribution it is

$$k_{\lambda,\parallel} = \exp\left[-(\omega_\mathrm{r} \sigma_t)^2\right] k_{\delta,\parallel} \tag{4.16}$$

where σ_t is the rms bunch duration.
The wake W_k^p due to this mode seen by the kth bunch on the pth revolution is then, summing over all the bunches and previous turns,

$$W_k^p = -k_{\lambda,\parallel} \left(q_k + 2\mathfrak{Re} \sum_{j=1}^{p-1} \sum_{\substack{j<p:m=1,\ldots,N_\mathrm{b} \\ j=p:m=1,\ldots,k-1}} q_m \exp\left[(t_k^p - t_m^j)(i\omega_\mathrm{r} - \Gamma)\right] \right) \tag{4.17}$$

with

$$t_k^p = (p-1)T_0 + (k-1)\Delta T_\mathrm{b} + \tau_k^p, \tag{4.18}$$

being the "arrival time" of the kth bunch on turn p. ΔT_b is the bunch spacing in the train. Letting $\underline{C}_k^p$ denote the double sum, the wake can be written as

$$W_k^p = -k_{\lambda,\|}(q_k + 2\mathfrak{Re}\underline{C}_k^p). \tag{4.19}$$

Note that $\underline{C}_1^1 = 0$. The double sums pertaining to two successive bunches are related to each other by

$$\underline{C}_k^p = \left(q_{k-1} + \underline{C}_{k-1}^p\right) \exp\left[(t_k^p - t_{k-1}^p)(i\omega_\mathrm{r} - \Gamma)\right], \tag{4.20}$$

where

$$\begin{aligned} q_0 &\equiv q_{N_\mathrm{b}}, \\ t_0^p &\equiv t_{N_\mathrm{b}}^{p-1}, \\ \underline{C}_0^p &\equiv \underline{C}_{N_\mathrm{b}}^{p-1}, \end{aligned}$$

yielding a simple recursion formula.
When dealing with cavities/higher-order modes with small quality factors, the exact wake function as given by Eq. (3.70) must be used.
An elegant way of establishing the induced wake voltage at a certain time is to describe the time development in matrix form with the help of the current in the inductance I_L [47]:

$$\begin{pmatrix} V(t_k^p) \\ I_L(t_k^p) \end{pmatrix} = e^{-\Gamma\Delta t} \begin{pmatrix} \cos\bar{\omega}_\mathrm{r}\Delta t - \frac{\Gamma}{\bar{\omega}_\mathrm{r}}\sin\bar{\omega}_\mathrm{r}\Delta t & -\frac{\omega_\mathrm{r}R}{\bar{\omega}_\mathrm{r}Q}\sin\bar{\omega}_\mathrm{r}\Delta t \\ \frac{\omega_\mathrm{r}Q}{\bar{\omega}_\mathrm{r}R}\sin\bar{\omega}_\mathrm{r}\Delta t & \cos\bar{\omega}_\mathrm{r}\Delta t + \frac{\Gamma}{\bar{\omega}_\mathrm{r}}\sin\bar{\omega}_\mathrm{r}\Delta t \end{pmatrix} \begin{pmatrix} V(t_{k-1}^p) \\ I_L(t_{k-1}^p) \end{pmatrix} \tag{4.21}$$

with $\Delta t = t_k^p - t_{k-1}^p$ and $\bar{\omega}_\mathrm{r} = \sqrt{\omega_\mathrm{r}^2 - \Gamma^2}$ the natural angular frequency. The above formula is derived in the appendix (Section C.2).
When bunch k crosses the cavity, it is sufficient to increase $V(t_k^p)$ by the kick $\Delta V = -2k_{\lambda,\|}q_k$, and continue the propagation.
The wake seen by bunch k on turn p in the rf cavity due to a certain mode m is (before having added the kick ΔV_m)

$$W_{k,m}^p = V_m(t_k^p) + \frac{1}{2}\Delta V_m = V_m(t_k^p) - \frac{1}{2}k_{\lambda,\|}^m q_k \tag{4.22}$$

where the index m has been added to the terms. The last term takes into account the fundamental theorem of beam loading: a bunch sees half of the wake voltage it induces during its passage.

The total wake seen by a single bunch at a cavity is the sum over all the modes

$$\sum_m W^p_{k,m}. \tag{4.23}$$

The second case to be studied is that which includes the beam loading in the fundamental cavity mode. Whereas Eq. (4.14) stays as it is, Eq. (4.15) needs to be modified and other aspects accounted for.
First, the coupling factor β_c is chosen relative to the optimal coupling factor $\beta_{\mathrm{c}0}$ as given by Eq. (3.92) (there is no differentiation between beams with and without gaps). Then the cavity resonance frequency and detuning are defined in accordance with the optimal tuning angle; in Eq. (3.90), the synchronous angle has been replaced by the nominal average bunch phase (in the standard tracking method: $\arcsin(U_0(1+U_0/E_\mathrm{b})/eF_\mathrm{b}V_\mathrm{rf})$). The cavity voltage $\underline{V}_\mathrm{c}$ is decomposed into a generator current and a beam component as in Section 3.3.5.

- The net beam loading voltage at the entry of the kth bunch on the pth revolution is given by $-2F_\mathrm{b}k_{\delta,\|}\underline{C}^p_{\mathrm{b},k}$. For beams without a gap, it converges towards $\underline{V}^\infty_\mathrm{b}$ (see Figure 3.13). The term $\underline{C}^p_{\mathrm{b},k}$ is calculated as its analogue for the higher-order mode wake fields $\underline{C}^p_k$ in Eq. (4.20).

- The component due to the generator current is denoted by $\underline{V}_\mathrm{g}$. The transient response of a resonant cavity to a step change in the driving current applied at $t=0$ is derived in Appendix C.3:

$$\underline{V}(t)e^{i\omega_\mathrm{rf}t} = \left[\underline{V}(0)e^{(-\Gamma+i\Delta\omega)t} + R_\mathrm{L}\underline{I}_\mathrm{g}\cos\psi\, e^{i\psi}(1-e^{(-\Gamma+i\Delta\omega)t})\right] e^{i\omega_\mathrm{rf}t}, \tag{4.24}$$

  where $\underline{V}(0)$ is the initial voltage in the cavity; in the algorithm the notation $\underline{V}_\mathrm{init}$ is used. The generator current can be switched on prior to the "arrival" of the first bunch at the cavities. The time, t_inj, is required to be an integer multiple of the rf oscillation period; the reference point being the zero phase of the rf oscillation the first bunch sees on its first turn. On future occasions, t_inj is referred to as the injection time.

Summarizing, the algorithm is:

$$\varepsilon^{n+1}_k = \varepsilon^n_k + eF_\mathrm{b}\mathfrak{Re}\underline{V}^{n+1}_{\mathrm{c},k} - U_0 - \frac{2T_0}{T_\varepsilon}\varepsilon^n_k + eW^{n+1}_k, \tag{4.25}$$

where

$$\underline{V}^p_{\mathrm{c},k} = \underline{V}^p_{\mathrm{g},k} - F_\mathrm{b}k_{\delta,\|}(q_k + 2\underline{C}^p_{\mathrm{b},k}) \tag{4.26}$$

with

$$\underline{C}^p_{\mathrm{b},k} = (\underline{C}^p_{\mathrm{b},k-1} + q_{k-1})e^{(-\Gamma+i\Delta\omega)(t^p_k - t^p_{k-1})}e^{i\omega_\mathrm{rf}(\tau^p_k-\tau^p_{k-1})} \tag{4.27}$$

$$\underline{V}^p_{\mathrm{g},k} = \left[\underline{V}_\mathrm{init}e^{(-\Gamma+i\Delta\omega)(t_\mathrm{inj}+t^p_k)} + \underline{I}_\mathrm{g}R_\mathrm{L}\cos\psi\, e^{i\psi}(1-e^{(-\Gamma+i\Delta\omega)(t_\mathrm{inj}+t^p_k)})\right] e^{i\omega_\mathrm{rf}\tau^p_k} \tag{4.28}$$

Note that $k_{\lambda,\|} = F_\mathrm{b}^2 k_{\delta,\|}$ and that in Eq. (4.27) the identity

$$e^{(-\Gamma+i\omega_\mathrm{r})(t_k^p - t_{k-1}^p)} = e^{(-\Gamma+i\Delta\omega)(t_k^p - t_{k-1}^p)} e^{i\omega_\mathrm{rf}(\tau_k^p - \tau_{k-1}^p)}$$

has been used.
The first choice of the generator current for a beam with $F_\mathrm{b} = 1$ and without a gap is clearly

$$\underline{I}_\mathrm{g} = \left[\frac{V_\mathrm{rf}}{R_\mathrm{L} \cos\psi e^{i\psi}} + 2I_\mathrm{b} e^{-i\hat{\phi}_\mathrm{s}} \right] e^{-i\pi/2}. \tag{4.29}$$

The first term is the constant current required without beam loading (delivers $V_\mathrm{rf} \cos\omega_\mathrm{rf}\tau$); the second term counterpoises the steady-state beam-loading voltage. The $e^{-i\pi/2}$ term has been added, because taking the real part of the cavity voltage $\underline{V}_\mathrm{c}$ corresponds to the cosine function, and $\cos(\phi - \pi/2) = \sin(\phi)$.
For the above generator current, $\mathfrak{Re}\underline{V}_\mathrm{g}$ converges upon

$$V_\mathrm{rf} \sin(\omega_\mathrm{rf}\tau) + 2I_\mathrm{b} R_\mathrm{L} \cos\psi \cos(\psi + \omega_\mathrm{rf}\tau - \phi_\mathrm{s}).$$

In the simulations, the bunch form factor $F_\mathrm{b} < 1$ and the nominal average bunch phase ϕ_nab takes the part of the synchronous phase; $\hat{\phi}_\mathrm{s}$ in Eq. (4.29) is substituted by $\hat{\phi}_\mathrm{nab} = \phi_\mathrm{nab} - \pi/2$.
The generator current has been calculated by the same method when studying the design beam in the dog-bone damping ring, since the above second term compensates approximately the average beam-loading voltage (see the analysis following Eq. (3.102), page 41).

Chapter 5

Impedance Model

In this chapter an impedance model for the dog-bone is presented. It distinguishes between single bunch and multibunch effects.
A preliminary impedance budget was established by V.D. Shiltsev in [33] by making comparisons to other machines and using analytical formulae. The data presented in Table 5.2 regarding single bunch effects has been revised and includes the rf cavity and fast kicker contributions as calculated with MAFIA.

5.1 Broad-band Impedance

With respect to single bunch dynamics, the wake potentials over the bunch length are of main interest. The actual impedance is often "replaced" by a *broad-band* impedance model, which is usually characterized by a small number of parameters, allowing analytical evaluation of stability limits or growth rates of single bunch instabilities. As many components of the dog-bone damping ring are not yet certain, a comparison to other machines is useful, primarily regarding inductive components.

5.1.1 A Broad-band Impedance Model

The following broad-band impedance model was proposed by S. Heifets, where the impedance is phenomenologically described by an expansion over $\sqrt{\omega}$ [48]:

$$Z_{\parallel}(\omega) = i\omega L + (1 + i\,\mathrm{sign}(\omega))R_{\mathrm{W}}\sqrt{|\omega|} + R_{\Omega} + (1 - i\,\mathrm{sign}(\omega))\frac{R_{\mathrm{c}}}{\sqrt{|\omega|}}. \qquad (5.1)$$

This model represents a further development of K. Bane's approach, applied in his analysis of the impedance of the SLC damping ring [49]. It has also been used to estimate the broad-band impedance for the SLAC B-factory [50] and for the DAΦNE main rings (Φ-factory) [51]. The model has the attractive feature that the different terms of the expansion have a physical interpretation, describing particular impedance-generating elements. However, the model diverges at low frequencies and needs to be supplemented by a cutoff.
The first term of the expansion represents a low frequency inductive impedance, which is typical for tapers (Glossary, page 173), shielded bellows, and small discontinuities such as

slots, shallow collimators, and so on. The second term reflects impedance due to resistive walls for a round pipe. The term resistive wall refers to the wake fields due to the finite conductivity of the chamber walls.
The third term in Eq. (5.1) describes some constant resistivity (in the dog-bone due to the fast kickers), and the last term has the same high frequency dependence as the impedance of a pillbox cavity with attached tubes [48]. It is referred to here as the diffraction-model impedance.
The corresponding wake potentials generated by Gaussian bunches are depicted in Figure 5.1. The diffraction-model wake potential is derived in Appendix C.4.

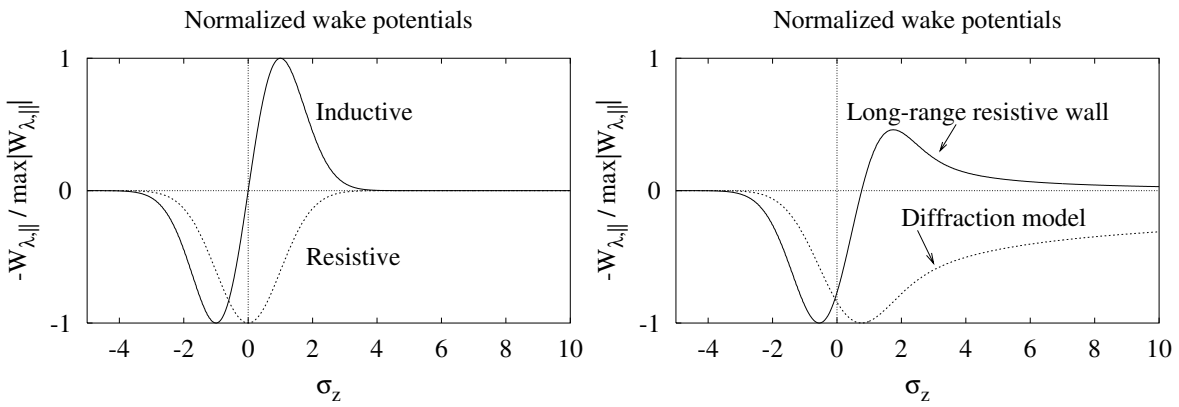

Figure 5.1: The left plot shows the corresponding normalized wake potentials generated by Gaussian bunches for an inductive (solid line) and a resistive (dots) impedance. To the right the corresponding long-range resistive wall (solid line) and diffraction-model (dots) wake potential are depicted.

The diffraction model [52] delivers an estimation of the high frequency impedance of a cavity by studying a single cavity in an infinitely long, perfectly conducting, cylindrical beam pipe. Since one is interested in the frequency dependence of the impedance, a sinusoidal beam current is considered. The associated electromagnetic field may be looked upon as being proportional to the instantaneous bunch current.
At high frequencies ($\omega \gg c/b$ with the pipe radius b), the electric (radial) and magnetic fields (azimuthal) at the wall look locally just like those in a free plane wave; and according to the diffraction model, the spreading of the electromagnetic fields in the cavity gap is the same as when a plane wave impinges on an obscuring screen.
The energy loss from the beam is given by the energy contained in the diffracted fields. Half of the loss comes from the energy diffracted into the geometric shadow of the screen (this corresponds to the energy deposited in the cavity). The second half is contained in the diffractive fields that propagate down the beam pipe.
Relating the power of the energy loss to the intensity of the beam current delivers the real part of the impedance (see [17, 52]).

In terms of the dog-bone damping ring, one has to consider the inductive impedance contributions, the resistive walls, and the wakes due to the rf cavities and fast kickers.

For the rf cavities and fast kickers, MAFIA calculations have been made.

5.1.2 Sources of Inductive Impedance

Elements in the ring like bellows, BPMs, tapers, etc. present discontinuities that usually have an impedance covering frequencies much higher than the frequencies within the bunch spectrum. Hence, the beam sees primarily the low frequency part of the object's impedance which is approximately purely imaginary and linear with a slope L; therefore, these elements give rise to a mostly inductive impedance (see [17, pp. 72–75], [30, 33]). The model is, as such, unphysical, as the beam loses no energy passing the object.
According to the above, whether an object is inductive or capacitive depends critically on the length of the driving charge. Vacuum chamber objects appear more inductive to longer bunches and more capacitive to shorter bunches [49]. K. Bane states, as a rule of thumb, that a Gaussian bunch will see a small obstruction in a tube of radius b as a good inductor if the bunch length obeys the relation $\sigma_z \gtrsim b/2$ [30].
The QD bellows of the SLC damping ring [30] which is displayed in Figure 5.2 has been used as an example (the SLC damping ring can be divided into various segments; a QD bellows belongs to a vacuum chamber segment centred on a defocusing quadrupole). It is modelled with MAFIA, once using the correct beam pipe radius, and once with the doubled value. The depth and length of the actual irises are left unchanged. The results for the rms bunch lengths $\sigma_z = 6\,\mathrm{mm}$ and $12\,\mathrm{mm}$ are shown in Figure 5.3. The wake potentials for the twofold beam pipe radius have been scaled by a factor two for comparison ($L \propto 1/b$, [30, 33]).

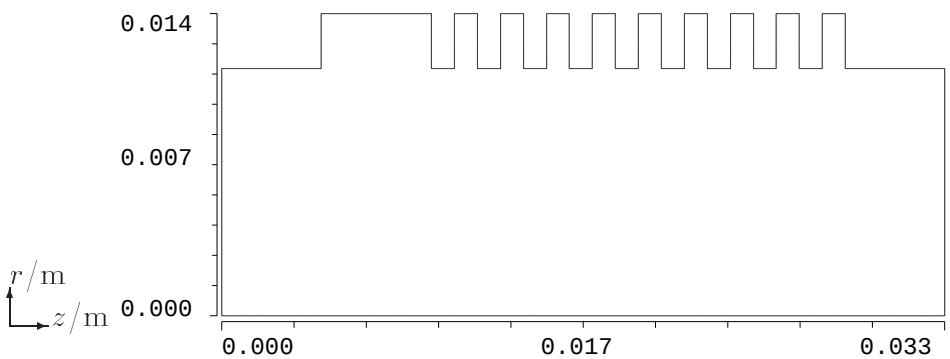

Figure 5.2: Schematic view of a QD bellows. The pipe radius is 11 mm.

The QD bellows is clearly a better inductor for the 12 mm bunch, but a distinct deterioration of the inductive character of the wakes for the larger radius in both cases is not noticeable. The inductance L is approximately 0.6 nH. If one increases the number of irises, for example to 100, one can see a deterioration of the inductive character of the wake potential produced by the Gaussian bunch with $\sigma_z = 12\,\mathrm{mm}$ when the pipe radius is doubled. The wake potentials generated by the bunch with $\sigma_z = 6\,\mathrm{mm}$ cannot be described as being inductive; they resemble the surface roughness wake potentials in ref. [53].

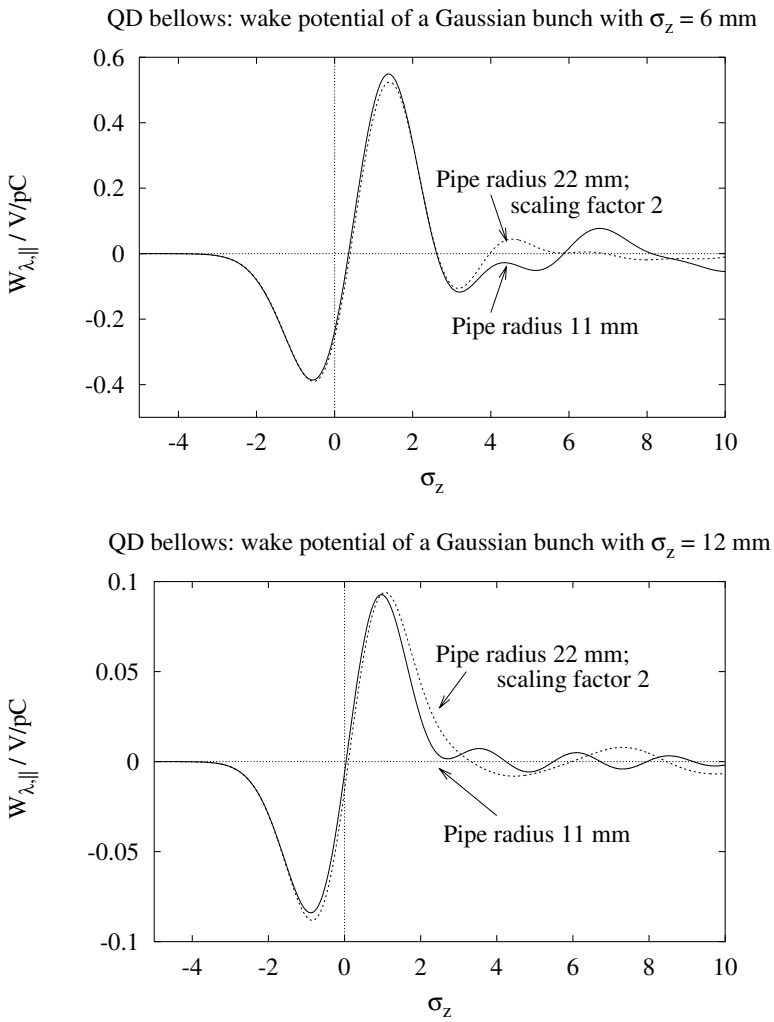

Figure 5.3: On the top, the wake potentials generated by a Gaussian bunch $\sigma_z = 6\,\mathrm{mm}$ in a QD bellows of the SLC damping ring (solid line) and in a bellows with the doubled pipe radius (dots). The bottom plot shows the corresponding wake potentials for a Gaussian bunch with an rms bunch length of 12 mm.

In the dog-bone damping ring, a major contribution of inductive impedance comes from the bellows. In the straight sections, the pump units are fitted with bellows. Adding one more per quadrupole leads to a total of approx. 1825. In the arcs there are bellows on both sides of the quadrupoles accumulating to 92. The same applies to the wiggler section, resulting in about 90 bellows.
The inductance of the shielded bellows at the PEP B-factory was used to estimate the inductive contribution of the bellows in the TESLA damping ring. The inductance of these shielded bellows is $5.6 \times 10^{-2}\,\mathrm{nH}$ (pipe radius $b = 3\,\mathrm{cm}$, see [50]). For the three sections in the damping ring, the above value is scaled to the appropriate radius ($L \propto 1/b$) and multiplied by the number of bellows. This leads to an inductance of $9.7 \times 10^{-8}\,\mathrm{H}$ corresponding to $Z_{||}/n$ of $10.75\,\mathrm{m}\Omega$.

As elaborated in the CDR [1], every quadrupole magnet will be equipped with a BPM. This means 304 in the straight sections, 92 in the arcs, and approx. 45 in the wiggler section. Assuming four-button BPMs with the button diameter $a = 1.5\,\mathrm{cm}$ and slot $w = 2\,\mathrm{mm}$ as installed in the PEP-II vacuum chamber leads to an inductance of $1.12 \times 10^{-7}\,\mathrm{H}$ and $Z_{\|}/n$ of $12.4\,\mathrm{m}\Omega$. The inductance of a BPM is estimated according to [32, 33]

$$L = \frac{1}{4\pi\epsilon_0}\frac{2wa^2}{\pi b^2} \tag{5.2}$$

with b the pipe radius.
For the simulation, advantage is taken of the fact that an inductive impedance $Z_{\|}(\omega) = i\omega L$ corresponds to a wake potential which is inversely proportional to the derivative of the charge distribution:

$$W_{\lambda,\|}(s) = -L \cdot c^2 \lambda'(s). \tag{5.3}$$

In the case of a Gaussian bunch (centred at zero) this leads to

$$W_{\lambda,\|}(s) = \frac{Lc^2 s}{\sqrt{2\pi}\sigma_z^3} \exp\left(-\frac{s^2}{2\sigma_z^2}\right), \tag{5.4}$$

which can be easily computed and used as a quasi-Green's function. The absolute maximum is reached at $s = \pm\sigma_z$ and is inversely proportional to σ_z^2.
In these simulation studies, the wake potentials generated by bunches with σ_z equal to 0.5 mm, 1 mm, and 2 mm were used.

5.1.3 Resistive Wall

The longitudinal monopole resistive wall impedance of a round pipe is well-known. For the bunch lengths studied, it is sufficient to use the long-range approximation; the corresponding formula for the wake potential of a Gaussian charge distribution has been used to calculate quasi-Green's functions.
An aluminium vacuum chamber with a conductivity $\sigma_0 = 3.5 \times 10^7\,\Omega^{-1}\mathrm{m}^{-1}$ is assumed (Section 2.3). In the straight sections the pipe will have a radius of $b = 5\,\mathrm{cm}$. The vacuum chamber in the wiggler section (approx. 400 m of the circumference) is elliptical, and the one in the arcs (approx. 800 m of the circumference) is rectangular.
The asymptotic forms of the longitudinal wake function for elliptic and rectangular pipes relate to the corresponding wake function for round pipes by a form factor, which is approximately one [55, 56]. The asymptotic forms are applicable for distances greater than approximately $10(b^2/(\mu_0 c\sigma_0))^{1/3} \approx 200\,\mu\mathrm{m}$ onwards (for aluminium and for the pipe radius or half the minor axis in the ellipse $b = 1\,\mathrm{cm}$; σ_0 is the conductivity); see [55, Figures 3 and 8].
Based on the above, one can assume round beam pipes for the wiggler and arc sections for the calculations. The pipe radius in the wigglers has been set to $b = 1\,\mathrm{cm}$ and in the arcs to $b = 1.5\,\mathrm{cm}$.

The longitudinal monopole resistive wall impedance per unit length of a round pipe in the long-range approximation reads for $\omega \geq 0$ [57]:

$$\bar{Z}_{\parallel}(\omega) = \frac{1}{2\pi b}\sqrt{\frac{Z_0\omega}{2\sigma_0 c}}(1+i), \tag{5.5}$$

for $\omega \leq 0$: $Z_{\parallel}(-\omega) = Z_{\parallel}^*(\omega)$ by the usual parity relation. The vacuum impedance $Z_0 = c\mu_0 \approx 377\,\Omega$.
The corresponding wake potential for a Gaussian charge distribution ($\tilde{\lambda}(\omega)$ denotes the Fourier transform) is

$$\begin{aligned} W_{\lambda,\parallel}(s) &= \frac{-1}{2\pi}\int_{-\infty}^{\infty} \bar{Z}_{\parallel}(\omega)\tilde{\lambda}(\omega)e^{i\omega s/c}d\omega \\ &= \frac{-1}{4\pi^2 b}\sqrt{\frac{Z_0}{2\sigma_0 c}}\int_{-\infty}^{\infty}(1+i\,\mathrm{sign}(\omega))\sqrt{|\omega|}e^{-\omega^2\sigma_z^2/2c^2}e^{i\omega s/c}d\omega \\ &= \frac{c}{4\pi b}\sqrt{\frac{Z_0}{\sigma_0}}\frac{1}{\sigma_z^{3/2}}\left|\frac{u}{2}\right|^{3/2}\{I_{1/4} - I_{-3/4} + \mathrm{sign}(u)(I_{-1/4} - I_{3/4})\}e^{-u^2/4} \end{aligned} \tag{5.6}$$

where u is a normalized distance between the bunch centre and the position of the test charge

$$u = \frac{s}{\sigma_z} \tag{5.7}$$

and the arguments of the Bessel functions I_ν are $u^2/4$. The amplitude of the wake potential relates to the radius b, the bunch length σ_z, and the conductivity σ_0 as

$$W_{\lambda,\parallel} \propto b^{-1}\sigma_0^{-1/2}\sigma_z^{-3/2}. \tag{5.8}$$

For long distances, Eq. (5.6) converges towards the wake of a point-like charge:

$$W_{\delta,\parallel}(s) = \frac{-c}{4\pi b}\sqrt{\frac{Z_0}{\pi\sigma_0}}s^{-3/2}. \tag{5.9}$$

Returning to the impedance, note that with $n = \omega/\omega_0$ Eq. (5.5) can be rewritten as

$$\left(\frac{\bar{Z}_{\parallel}}{n}\right) = \frac{\sqrt{Z_0}}{2b\sqrt{\pi n C\sigma_0}}(1+i). \tag{5.10}$$

At bunch frequencies $\omega\sigma_z/c \simeq 1$, i.e. $n_{\mathrm{eff}} \sim C/(2\pi\sigma_z)$, the effective broad-band contribution can hence be estimated to be [33]

$$\left(\frac{\bar{Z}_{\parallel}}{n}\right)_{\mathrm{eff}} = \frac{\sqrt{Z_0\sigma_z}}{\sqrt{2\sigma_0}bC}(1+i). \tag{5.11}$$

The broad-band impedance for the dog-bone damping ring is approximately $(Z_{\parallel}/n)^W_{\mathrm{eff}} \approx (1+i)\cdot 5.4\,\mathrm{m}\Omega$ ($\sigma_z = 9.5\,\mathrm{mm}$).
The loss factor is given by [57]

$$k_{\lambda,\parallel} = \frac{c}{4\pi^2 b\sigma_z^{3/2}}\sqrt{\frac{Z_0}{2\sigma_0}}\Gamma(3/4), \tag{5.12}$$

the total loss over the ring being $8.9\,\mathrm{V/pC}$.

5.1.4 Cavities

As stated in Section 2.4, eight 4-cell superconducting cavities, such as those installed at HERA but scaled in frequency from 500 MHz to 433 MHz, have been assumed for this study. The longitudinal wake potentials of Gaussian bunches with $\sigma_z \geq 1\,\mathrm{mm}$ have been calculated with the MAFIA T2 program (using the indirect integration method; therefore, the addition of the junction and the beam pipe on both ends of the 4-cell cavity; Figure 3.9, page 35). The wake potential of the Gaussian bunch with $\sigma_z = 1\,\mathrm{mm}$ has been smoothed due to a seemingly numerical inconsistency in the calculation (see Figure 5.4); for the calculation of the wake potential generated by a Gaussian bunch with $\sigma_z = 0.5\,\mathrm{mm}$ only one cell has been used. These two have been used as quasi-Green's functions.

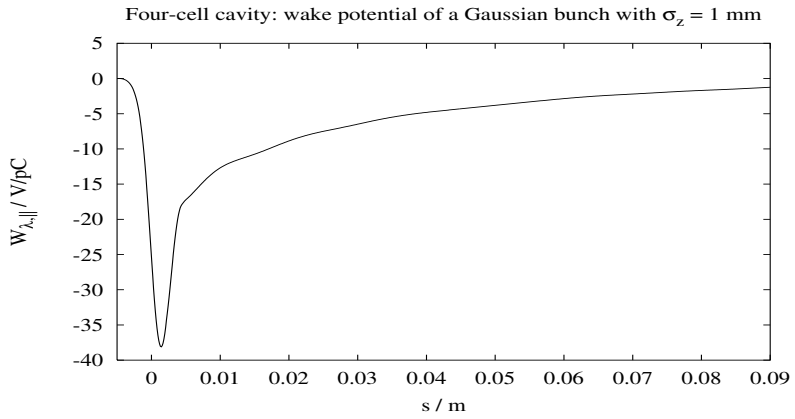

Figure 5.4: Wake potential generated by a Gaussian bunch with $\sigma_z = 1\,\mathrm{mm}$ in a four-cell cavity.

The impedance of the cavities at the bunch frequency $\omega_\mathrm{b} \approx 3 \times 10^{10}\,\mathrm{Hz}$ has been estimated by two methods. In the first, the "tail" of the wake potential calculated by MAFIA has been extended by an exponential decrease (see Figure 5.5), allowing one to perform a Fourier transformation at the bunch frequency. It is

$$\widetilde{W_{\lambda,||}}(\omega) = -Z_{||}(\omega)\tilde{\lambda}(\omega) \tag{5.13}$$

with $\widetilde{W_{\lambda,||}}(\omega)$ the Fourier transform of $W_{\lambda,||}(t)$ and $\tilde{\lambda}(\omega)$ that of $\lambda(t)$. This led to $Z_{||}(\omega_\mathrm{b}) = (68.1 - 66.4i)\,\Omega$. The second method was to fit a wake potential based on the diffraction model to the MAFIA calculation; the difference was weighted with the particle density. This yielded $R_\mathrm{c} \approx 1.1 \times 10^7\,\Omega\mathrm{s}^{-1/2}$ (the parameter pertaining to the diffraction model in Eq. (5.1)) and $Z_{||}(\omega_\mathrm{b}) = (1-i)\cdot 63.5\,\Omega$ (see Eq. (5.1)) in good agreement with the first result.
At the bunch frequency, one obtains, therefore, for the eight cavities:

$$\left(\frac{Z_{||}}{n}\right)_\mathrm{cav} \approx (1-i)\cdot 2\,\mathrm{m}\Omega. \tag{5.14}$$

Using the diffraction-model wake and the value obtained by the fit for R_c, and furthermore averaging over the bunch spectrum as in [33] leads to a value of about 20 % less.

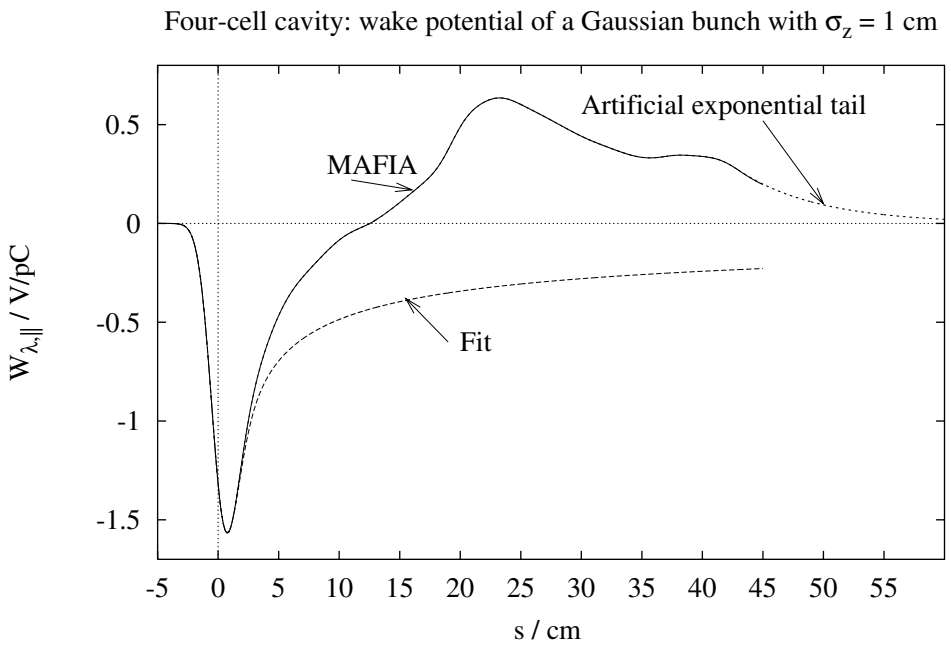

Figure 5.5: Wake potential generated by a Gaussian bunch with $\sigma_z = 1\,\mathrm{cm}$ in a four-cell cavity. An exponentially decreasing tail has been added for the Fourier transformation. Furthermore, a wake potential based on the diffraction model is fitted to the actual result.

5.1.5 Fast Kickers

For the impedance model, the installation of 40 very fast kickers has been assumed. A description of the very fast counter travelling wave kickers which are intended to be used for the extraction of the bunches can be found in [58]. The wake potentials generated by Gaussian bunches with $\sigma_z \geq 2\,\mathrm{mm}$ passing a fast kicker have been calculated using the MAFIA T3 module [59].

$\lvert W_{\max}\rvert$ / $10^{12}\mathrm{V/C}$	4.81	3.55	2.85	2.45	1.43
σ_z / mm	2	3	4	5	10

Table 5.1: Fast kicker: maximum absolute wake potential generated by various Gaussian bunches.

According to the data in Table 5.1, the maximum absolute wake created by a Gaussian bunch passing a fast kicker varies approximately as

$$|W_{\max}^{\mathrm{FK}}| \sim \frac{1}{\sigma_z^{3/4}}. \tag{5.15}$$

The contribution of the fast kickers to the impedance budget has been estimated in principally the same way as was done for the cavities. For the least-squares fit a purely resistive wake was used. The Fourier transformation method leads to the impedance

$Z_{\parallel}(\omega_{\mathrm{b}}) = (138 - 43i)\,\Omega$. The fit leads to $Z_{\parallel}(\omega_{\mathrm{b}}) = 114\,\Omega$. One has, therefore, a $Z_{\parallel}/n$ of approx. $17\,\mathrm{m}\Omega$ at the bunch frequency.

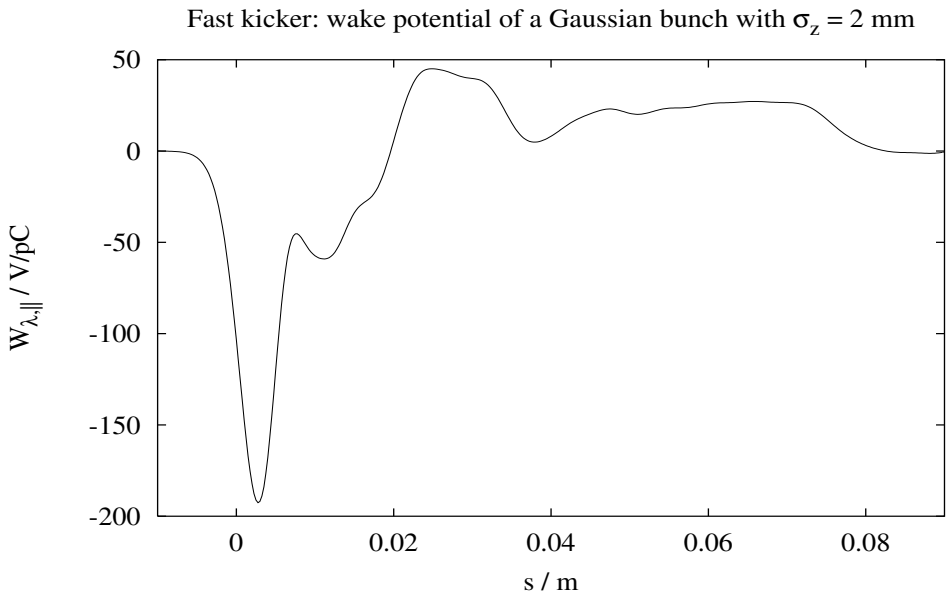

Figure 5.6: Wake potential generated by a Gaussian bunch with $\sigma_z = 2\,\mathrm{mm}$ in a fast kicker.

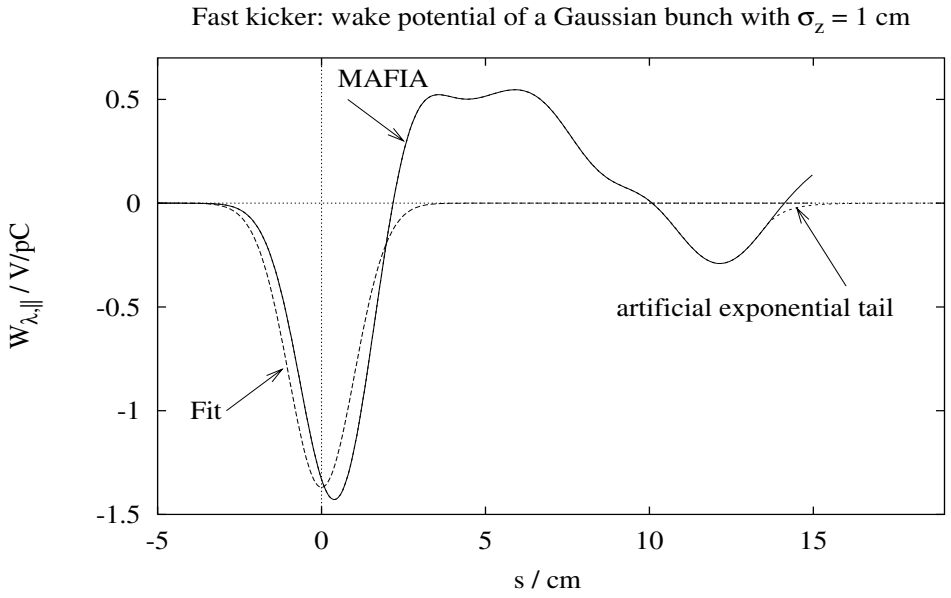

Figure 5.7: The wake potential generated by a Gaussian bunch with $\sigma_z = 1\,\mathrm{cm}$ in one fast kicker. An exponentially decreasing tail has been added at approximately $s = 13.5\,\mathrm{cm}$ for the Fourier transformation. Furthermore, a resistive wake is fitted to the fast kicker wake.

5.1.6 Summary of the contributions

Non-inductive components	$Z_{\parallel}/n$ / mΩ	$k_{\lambda,\parallel}$ / V/pC
Rf cavities	2.0	8.8
Resistive wall	5.4	8.9
Kickers	~ 17	38.9
Total	$\simeq 25$	56.6

Inductive components	$Z_{\parallel}/n$ / mΩ	$k_{\lambda,\parallel}$ / V/pC
Bellows	10.8	~ 3.4
BPMs	12.4	~ 1.7
Other components	~ 4	~ 2
Total	$\simeq 27$	$\simeq 7$

	$k_{\lambda,\parallel}$ / V/pC
All components	$\simeq 64$

Table 5.2: Estimation of the contributions to the non-inductive and purely inductive part of the longitudinal broad-band impedance.

5.2 Narrow-band Impedance

The multibunch effects are dominated by the *narrow-band* impedance (long-range wake functions) as was partly elaborated on page 30.

5.2.1 Cavities

The monopole modes of the a 4-cell 433 MHz cavity have been calculated using the MAFIA eigenvalue solver. The results are presented in Table 5.3. The fundamental mode, number four in the table, is pictured in Figure 3.9 on page 35. Figure 5.8 shows the strongest higher-order mode (number eight in Table 5.3), characterized by the largest loss factor.
Now, from the experience with the HERA-cavities including HOM-couplers, the strongest modes can be estimated to have an impedance of 60 kΩ (per 4-cell cavity) [1]. Hence, it is assumed that the strongest mode (number eight) should have a loaded quality factor of approximately 1100.
We now consider all the higher-order modes in the table. Their quality factors due to wall losses differ less than an order of magnitude.
If we assume that the wall currents in the beam pipe do not vary by more than an order of magnitude from the average value over the whole surface (which is mainly responsible for the total quality factor), then we can assume that the external quality factors due to

a coupler in the beam pipe will also not differ by more than an order of magnitude. This means that the achievable damping of the modes will be of the same order.
Since the loss factors in the table decrease rapidly, we feel it is justified to restrict our study to the higher-order modes with the numbers 7 and 8.

first pass-band		
	f / MHz	$k_{\delta,\parallel}$ / V/pC
1	425.857	6.67×10^{-6}
2	428.630	8.33×10^{-7}
3	431.434	3.29×10^{-5}
4	432.667	3.06×10^{-1}

higher-order modes		
	f / MHz	$k_{\delta,\parallel}$ / V/pC
5	764.397	5.04×10^{-3}
6	768.335	5.75×10^{-4}
7	775.391	6.19×10^{-2}
8	782.783	1.38×10^{-1}
9	897.499	3.81×10^{-4}
10	903.842	3.14×10^{-3}
11	913.670	1.91×10^{-4}
12	922.976	4.42×10^{-4}
13	1060.013	1.23×10^{-3}
14	1060.185	8.93×10^{-4}
15	1136.917	1.07×10^{-4}
16	1151.079	7.39×10^{-3}

Table 5.3: Monopole modes of the 433 MHz 4-cell cavities according to MAFIA calculations. The first four modes belong to the first pass-band. Number four is the π-mode.

According to Eq. (3.124) the instability growth rate of the main higher-order mode can be expected to be 24 Hz. This is approximately a factor two and a half smaller than the damping rate due to the synchrotron radiation.
The mode with the frequency $f = 775.391$ MHz, i.e. number 7, delivers a maximum growth rate of 11 Hz (for $\mu = 675$, $Q_{\mathrm{L}} = 1100$).

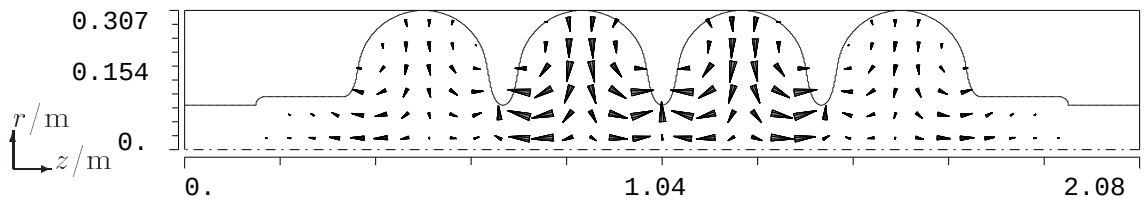

Figure 5.8: The major higher-order monopole mode of the 433 MHz four-cell cavity. The mode frequency f is approximately 782.78 MHz.

5.2.2 Resistive Wall and Beam Position Monitors

The longitudinal impedance due to resistive walls in the long-range approximation scales as $\sqrt{\omega}$ (see Eq. (5.5)). For the dog-bone ring parameters (see Section 5.1.3), one obtains $\mathfrak{Re}\, Z_{\|}(n) \approx 2.5\sqrt{|n|}\,\Omega$ with $n = \omega/\omega_0$.
We now use Eq. (3.124) on page 49 to estimate the instability growth rates of the multi-bunch modes.
The summation in Eq. (3.124),

$$\sum_{p=-\infty}^{\infty} (pN_{\mathrm{b}} + \mu + \nu_{\mathrm{s}})\sqrt{|pN_{\mathrm{b}} + \mu + \nu_{\mathrm{s}}|}, \tag{5.16}$$

has been performed numerically [33] and the maximum value estimated to be approximately $0.038 N_{\mathrm{b}}^{3/2}$; the maximum increment is approximately $\tau_{(\mu)}^{-1} = 4.4 \times 10^{-6}\,\mathrm{Hz}$. The instability is much weaker than the synchrotron radiation damping.

Additional sources of higher-order modes are beam position monitors. The resonant modes of PEP-II button-type beam position monitors have been analyzed in the past with MAFIA [60]. The resonance frequency was found to be $f = 6.8\,\mathrm{GHz}$, and the absolute impedance of one BPM at the resonance frequency was $|Z_{\|}| = 25\,\Omega$. Assuming 450 BPMs, as in Section 5.1.2, and simply multiplying the above numbers leads to a total impedance of approximately $11.25\,\mathrm{k}\Omega$. If we insert this impedance value and the resonance frequency into Eq. (3.127) (page 51), and multiply it by the bunch form factor to the square (recall Eq. (3.78), page 34), we obtain an upper limit of the instability growth rate of less than 1 Hz, which obviously gives no rise to concern.
We will, therefore, not consider resistive wall effects or the resonant frequencies of the beam position monitors in our simulation studies.

Chapter 6

Simulation Results

The ability to predict collective effects with the help of tracking simulations or estimate them by an analytical approach depends critically on the accuracy with which the impedance is known. As the details of the various equipment components are uncertain, the tracking simulations must be taken as what they are: results based on reasonable assumptions which indicate whether or not changes to the design or the installation of feedback systems are necessary.
In the first section, single bunch results are presented and in the second, multibunch tracking results.

6.1 Single Bunch Studies

In the previous section, reference is made only to the design rms bunch length of approx. 9.5 mm. In addition to applying the corresponding design momentum compaction factor $\alpha_c = 3.4 \times 10^{-4}$ in the tracking equations, $\alpha_c = 9.5 \times 10^{-5}$ is applied, which leads to an rms bunch length of approximately 5.0 mm. The synchrotron tune is 0.051.
Before turning to the actual tracking results, the convolution error due to the wake field simulation is discussed. The four wake components are studied individually.

6.1.1 Convolution Error

On the next page, Table 6.1 shows the maximum relative weighted error (relative to the maximum wake) when comparing the results of Eq. (4.9) for a number of QGFs using wake potentials of Gaussian bunches with the rms bunch lengths 5 mm and 1 cm as calculated with MAFIA or from known formulae.
In the case of the actual simulation, one must not forget that one has a limited number of particles and bins. The width of the bins is 2 mm or 3 mm. Using, for example, a random Gaussian distribution of 100 000 particles (a typical number), the results for the cavity and fast kicker are practically identical with those above when studying the bunch with $\sigma_z = 5$ mm.
In the case of the resistive wall and inductive wake, the results deteriorate noticeably. The convolution of the resistive wall quasi-Green's function with a Gaussian bunch with $\sigma_z = 5$ mm, where $\sigma_z^{\mathrm{QGF}} = 0.5$ mm, can lead to a maximum relative weighted error of

approximately 3 – 4 %. The convolution using an inductive quasi-Green's function with $\sigma_z^{\mathrm{QGF}} = 0.5\,\mathrm{mm}$ leads to an error of 9 – 15 %; with $\sigma_z^{\mathrm{QGF}} = 1\,\mathrm{mm}$, the error is 8 %. Note that the values of the resistive wall and the inductive wake potentials vary far more than those pertaining to the fast kickers and cavities.

studied bunch	quasi-Green's function, σ_z^{QGF} / mm									
	inductive			resistive wall			cavity		FK	$\sum$
	0.5	1	2	0.5	1	2	1	2	2	
$\sigma_z = 5\,\mathrm{mm}$	1.1			0.8			1.7		4.9	1.5
		4.2			3.0		1.7		4.9	3.4
			15.0			10.9		4.0	4.9	14.2
$\sigma_z = 1\,\mathrm{cm}$		1.1			0.8		0.8		1.3	1.1
			4.2			3.0		1.3	1.3	2.9

Table 6.1: Maximum relative weighted error in [%] (relative to the maximum wake potential) using the numerical calculation of Eq. (4.9) for the inductive, resistive wall, cavity, and fast kicker (FK) components, and the combined (total) wake potential ($\sum$).

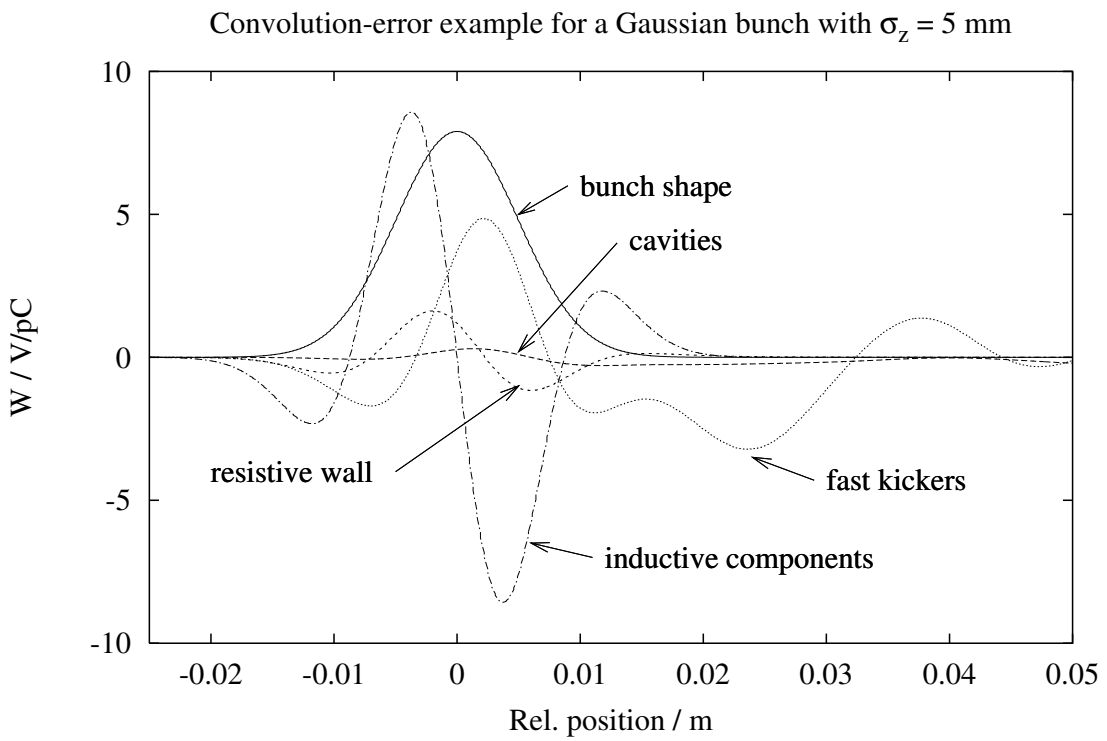

Figure 6.1: Convolution error when calculating the wake potential of a Gaussian bunch with $\sigma_z = 5\,\mathrm{mm}$ with the following quasi-Green functions: the wake potentials of Gaussian bunches with $\sigma_z = 1\,\mathrm{mm}$ pertaining to the cavity, resistive wall, and inductive components; the wake potential of a Gaussian bunch with the rms bunch length 2 mm is used for the fast kickers.

6.1.2 Tracking – General Remarks

For the simulation, different numbers of macroparticles, numbers of sections (1, 2, 4, and 8), and different quasi-Green's functions for the various wakes (the rms bunch lengths of the Gaussian bunches vary between $\sigma_z = 0.5\,\mathrm{mm}$, 1 mm, 2 mm, and 3 mm) are used.
Division of the dog-bone ring into sections is to be understood as follows. Using the case of two sections ($N_{\mathrm{sec}} = 2$) as an example, the ring is divided into practically identical parts with the difference being that the eight rf cavities are represented by just one cavity located in the first section which contains the total voltage. The synchrotron radiation loss is evenly divided amongst the sections.
The impact on the wake field calculation is explained in the appropriate places. There are a few exceptions at the beginning of the next subsection where the rf voltage is equally divided among the sections. These simulations are made for reasons of comparison; they are clearly marked.

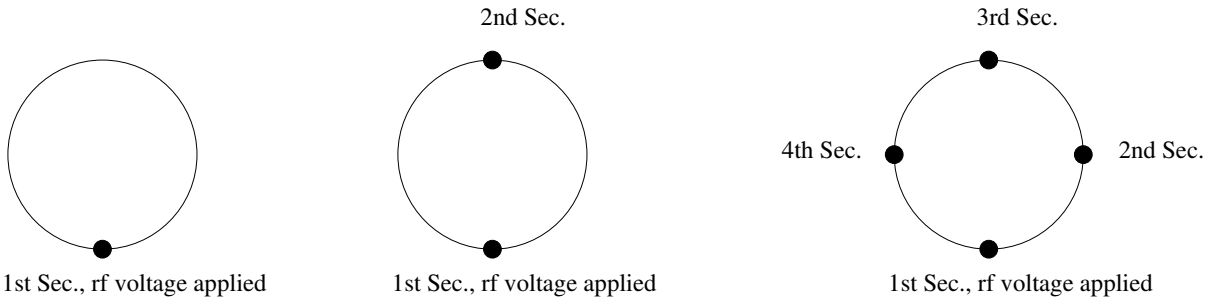

Figure 6.2: Model of the ring split into one (left), two (middle), and four (right) sections. The rf voltage is applied at the first "station".

The number of macroparticles used is primarily 100 000 or 200 000. The particles are tracked over either 3000 or 3500 turns, the latter being approximately equivalent to twelve damping times and the storage time.
The rms values for the bunch length and the energy spread, etc. per run are calculated as the average values over the final 500 turns. For example, when tracking over 3500 turns:

$$\sigma_z = \frac{c}{500} \sum_{n=3001}^{3500} \sqrt{\frac{1}{N_{\mathrm{par}}} \sum_{k=1}^{N_{\mathrm{par}}} (\tau_k^n - \bar{\tau}^n)^2} \tag{6.1}$$

where

$$\bar{\tau}^n = \frac{1}{N_{\mathrm{par}}} \sum_{k=1}^{N_{\mathrm{par}}} \tau_k^n . \tag{6.2}$$

Further commentary on this subject is presented in the next subsection, as the results depend on "where in the ring" the estimates are established. The bunch shapes are also obtained by averaging over the final 500 turns.

6.1.3 Tracking without Wake Fields

The formulae presented and partly derived in Section 3.2 are based upon the bunch particles seeing a continuous rf voltage and suffering a continuous synchrotron radiation loss.
The simulation comes closest to this situation by linearizing the rf-voltage term and distributing it and the synchrotron radiation loss evenly over a number of sections. Furthermore, the continuous radiation term is switched off, i.e. the third term on the right-hand side of Eq. (4.1). The tracking equations are then

$$\tau_k^{n+1} = \tau_k^n + \frac{\alpha_c T_0}{N_{\rm sec} E_{\rm b}} \varepsilon_k^n \qquad \text{and} \tag{6.3}$$

$$\varepsilon_k^{n+1} = \varepsilon_k^n + \frac{e\dot{V}_{\rm RF}}{N_{\rm sec}} (\tau_k^{n+1} - \tau_{\rm syn}) - \frac{2T_0}{N_{\rm sec} T_\varepsilon} \varepsilon_k^n + 2\sqrt{\frac{T_0}{N_{\rm sec} T_\varepsilon}} \sigma_{0\varepsilon} R_{\rm G}. \tag{6.4}$$

The superscript denotes the accomplished "number of sections" tracked; there are $N_{\rm sec}$ steps per turn.
The quantum excitation random term leads to a small increase of the rms energy spread. In the limit of large numbers it can be expressed as

$$\sigma_{\bar{\varepsilon}}^2 = \sigma_\varepsilon^2 + \sigma_a^2 \tag{6.5}$$

with $\sigma_a = 2\sqrt{T_0/(N_{\rm sec} T_\varepsilon)}\sigma_{0\varepsilon}$. It is

$$\sigma_{\bar{\varepsilon}}^2 \approx \sigma_{0\varepsilon}^2 \left(1 + \frac{4U_0}{N_{\rm sec} E_{\rm b}}\right). \tag{6.6}$$

For four sections, one can expect $\sigma_{\bar{\varepsilon}} \approx 3.205\,\text{MeV}$. The energy spread values presented in the Tables 6.2 and 6.3 are, however, calculated differently to minimize the increase. The quantum excitation terms in the last section did not enter the calculations, meaning that in the case of Eq. (6.4), $\varepsilon_k^{N_{\rm sec}}$ is replaced by

$$\varepsilon_k^{N_{\rm sec}-1} + \frac{e\dot{V}_{\rm RF}}{N_{\rm sec}} (\tau_k^{N_{\rm sec}} - \tau_{\rm syn}) - \frac{2T_0}{N_{\rm sec} T_\varepsilon} \varepsilon_k^{N_{\rm sec}-1}. \tag{6.7}$$

$N_{\rm par}$	σ_z / mm	σ_ε / MeV	$\bar{\phi}$ / deg	$\bar{\varepsilon}$ / MeV
1 000	9.37 ± 0.15	3.16 ± 0.05	154.66 ± 0.2	0 ± 0.14
10 000	9.51 ± 0.05	3.20 ± 0.02	154.66 ± 0.05	0 ± 0.03
25 000	9.55 ± 0.04	3.21 ± 0.02	154.66 ± 0.03	0 ± 0.02
50 000	9.52 ± 0.03	3.21 ± 0.01	154.66 ± 0.02	0 ± 0.01
100 000	9.52 ± 0.01	3.204 ± 0.005	154.66 ± 0.02	0 ± 0.01
200 000	9.52 ± 0.01	3.205 ± 0.004	154.66 ± 0.01	0 ± 0.007

Table 6.2: Zero-current tracking results. The *linearized* rf voltage $V_{\rm rf}$ and the synchrotron radiation loss U_0 are evenly distributed over four sections. The momentum compaction factor is $\alpha_c = 3.4 \times 10^{-4}$. The very last quantum excitation terms applied to the particles' energy do not enter the $\bar{\varepsilon}$ and σ_ε calculations.

The results for four sections – each representing one run lasting 3000 turns – are presented in Table 6.2. The four average values presented in the table, σ_z, σ_ε, $\bar{\phi}$, and $\bar{\varepsilon}$, are stated with the corresponding rms values (the numbers behind the $\pm$ sign). The values used per turn are those at the first station. Since all stations/sections are identical, the results are not affected by this choice.
We can see that the average values as a function of the number of macroparticles converge reasonably quickly. The average bunch phase (in degrees), as an example, is stated using two digits. This lies below today's accuracy of measurements. The numbers are, however, presented in this way to simply demonstrate the consistency of the numerical algorithm. The zero-current rms bunch length using Eq. (3.25) is 9.49 mm, the energy spread 3.2 MeV, and $\arcsin(U_0/eV_{\rm rf}) = 154.66°$.

Tracking: with continuous synchrotron radiation loss?	σ_z / mm	σ_ε / MeV	$\bar{\phi}$ / deg	$\bar{\varepsilon}$ / MeV
No	9.55 ± 0.01	3.211 ± 0.003	154.557 ± 0.008	0 ± 0.005
Yes	9.55 ± 0.01	3.211 ± 0.003	154.534 ± 0.008	1.337 ± 0.005

Table 6.3: Zero-current tracking results where the rf voltage $V_{\rm rf}$ and the synchrotron radiation loss U_0 are evenly distributed over four sections. The momentum compaction factor is $\alpha_{\rm c} = 3.4 \times 10^{-4}$.

In Table 6.3, the results of two simulations are shown in which the rf voltage is distributed over four sections but no longer linearized; hence the bunch centre does not reside at 154.66° – the Gaussian bunch form factor must be taken into account (Eq. (3.76) on page 34). For

$$\sigma_z = 5.0\,\text{mm}: \qquad F_{\rm b} = 0.9990, \qquad \arcsin(U_0/(eF_{\rm b}V_{\rm rf})) = 154.63°, \tag{6.8}$$

$$\sigma_z = 9.5\,\text{mm}: \qquad F_{\rm b} = 0.9963, \qquad \arcsin(U_0/(eF_{\rm b}V_{\rm rf})) = 154.56°. \tag{6.9}$$

The effect of the bunch form factor is also seen when solving the Haissinski equation (3.155).
The top line of Table 6.3 describes the results of tracking with the continuous radiation term switched off. The bottom line refers to the results where the continuous synchrotron radiation is accounted for (this is the case in the standard tracking method). The number of turns is 3000, while the number of macroparticles is 200 000. The effect of the continuous radiation term is seen in the non-zero average of ε; $U_0/(2N_{\rm sec}) = 1.3375$ MeV for $N_{\rm sec} = 4$. The average bunch phase is also affected. Note that the nominal average bunch phase is $\arcsin(U_0(1 + U_0/(N_{\rm sec}E_{\rm b}))/(eF_{\rm b}V_{\rm rf})) = 154.535°$, where $T_\varepsilon = T_0E_{\rm b}/U_0$ is used. The rms bunch length and energy spread are principally unaffected.
The simulation technique underlying the tracking results of Table 6.4 on page 87 is identical to the technique used where wake fields are applied. These are, therefore, the zero-charge results which are compared to the calculations with wake fields.
The bunches see the rf voltage in the first section, as explained earlier, whilst their loss of energy due to synchrotron radiation is distributed evenly among the various sections;

	$\alpha_c = 9.5 \times 10^{-5}$				$\alpha_c = 3.4 \times 10^{-4}$			
	σ_z / mm	σ_ε / MeV	$\bar{\phi}$ / deg	$\bar{\varepsilon}$ / MeV	σ_z / mm	σ_ε / MeV	$\bar{\phi}$ / deg	$\bar{\varepsilon}$ / MeV
Haissinski Eq.	5.02		154.63		9.52		154.56	
Tracking								
$N_{\mathrm{sec}} = 1$, (1)	5.09	3.25	154.54	5.35	10.00	3.36	154.46	5.35
$N_{\mathrm{sec}} = 2$, (1)	5.06	3.22	154.59	5.36	9.76	3.28	154.51	5.36
$N_{\mathrm{sec}} = 2$, (2)	4.99	3.22	154.94	−0.01	9.30	3.28	155.77	−0.01
$N_{\mathrm{sec}} = 4$, (1)	5.05	3.22	154.61	5.36	9.69	3.26	154.53	5.36
$N_{\mathrm{sec}} = 4$, (2)	5.00	3.22	154.87	2.67	9.35	3.26	155.48	2.67
$N_{\mathrm{sec}} = 4$, (3)	4.98	3.22	154.96	0.00	9.24	3.26	155.79	0.00
$N_{\mathrm{sec}} = 4$, (4)	5.00	3.22	154.87	−2.68	9.36	3.26	155.47	−2.67

Table 6.4: Zero-current rms bunch length, energy spread, average bunch phase, and energy for the two studied momentum compaction factors. The top line states the Haissinski equation values, the others those of various tracking calculations with 200 000 macroparticles using different numbers of sections. Only U_0 is evenly distributed. The particles see the rf voltage in the first section. The number in brackets behind N_{sec} denotes in which section the tracking results are established. For four sections, the rms of σ_z is 0.006 mm ($\alpha_c = 9.5 \times 10^{-5}$) and 0.009 mm ($\alpha_c = 3.4 \times 10^{-4}$), that of σ_ε 0.004 MeV and 0.003 MeV.

hence the tracking equations are not identical in every section and ($\bar{\phi}$, $\bar{\varepsilon}$) changes from section to section.
The bunch centre and average energy spread can be obtained by solving the steady-state equations

$$\bar{\tau}^n = \bar{\tau}^{n-1} + \frac{\alpha_c T_0}{N_{\mathrm{sec}} E_b} \left(\bar{\varepsilon}^{n-1} - \frac{U_0}{2 N_{\mathrm{sec}}} \right) \tag{6.10}$$

and

$$\bar{\varepsilon}^n = \left(1 - \frac{2T_0}{N_{\mathrm{sec}} T_\varepsilon} \right) \bar{\varepsilon}^{n-1} + \delta_{n,1} e F_b V_{\mathrm{rf}} \sin \omega_{\mathrm{rf}} \bar{\tau}^1 - \frac{U_0}{N_{\mathrm{sec}}}. \tag{6.11}$$

The upper label denotes the section number where $n = 0$ is to be looked upon as being $n = N_{\mathrm{sec}}$.
The average section energies relate to the energy in the first as

$$\bar{\varepsilon}^n = \varrho^{n-1} \bar{\varepsilon}^1 - \frac{U_0}{N_{\mathrm{sec}}} \frac{1 - \varrho^{n-1}}{1 - \varrho} \tag{6.12}$$

where

$$\varrho = 1 - \frac{2T_0}{N_{\mathrm{sec}} T_\varepsilon} = 1 - \frac{2U_0}{N_{\mathrm{sec}} E_b}. \tag{6.13}$$

The relationship between the position of the bunch centre for the first section and any other section is

$$\bar{\tau}^1 = \bar{\tau}^{N_{\rm sec}-k} + \frac{\alpha_{\rm c} T_0}{N_{\rm sec} E_{\rm b}} \sum_{j=0}^{k} \left(\bar{\varepsilon}^{N_{\rm sec}-j} - \frac{U_0}{2N_{\rm sec}} \right). \tag{6.14}$$

Inserting $k = N_{\rm sec} - 1$ one finds that

$$\sum_{j=1}^{N_{\rm sec}} \bar{\varepsilon}^j = \frac{U_0}{2}. \tag{6.15}$$

Solving this equation for $\bar{\varepsilon}^1$ gives

$$\bar{\varepsilon}^1 = \left(\frac{3-\varrho}{2(1-\varrho^{N_{\rm sec}})} - \frac{1}{N_{\rm sec}(1-\varrho)} \right) U_0, \tag{6.16}$$

which is $(\frac{1}{2} + O(1-\varrho))U_0$. The average section energies are approximately

$$\bar{\varepsilon}^n = \left(\frac{1}{2} - \frac{n-1}{N_{\rm sec}} \right) U_0, \tag{6.17}$$

which is apparent in Table 6.4.
The position of the bunch centre in the first section is obtained by setting $n = 1$ in Eq. (6.11) and substituting the left-hand side of Eq. (6.12) with $n = N_{\rm sec}$ for the term $\bar{\varepsilon}^0$:

$$eF_{\rm b} V_{\rm rf} \sin \omega_{\rm rf} \bar{\tau}^1 = \bar{\varepsilon}^1 (1 - \varrho^{N_{\rm sec}}) + \frac{U_0}{N_{\rm sec}} \frac{1-\varrho^{N_{\rm sec}-1}}{1-\varrho} \varrho + \frac{U_0}{N_{\rm sec}}. \tag{6.18}$$

The tracking calculations concur with the above result. The tracking also shows a change of the bunch length from section to section; furthermore the energy spread is larger than in the previous case where the rf voltage is distributed over four sections (Table 6.3). The increase is too large to be attributed only to the quantum excitation term as given by Eq. (6.6).
We show now in Figure 6.3 the various wake potential components pertaining to Gaussian bunches with the rms bunch lengths 5 mm and a 1 cm. The total wake potentials follow in Figure 6.4 on page 90.

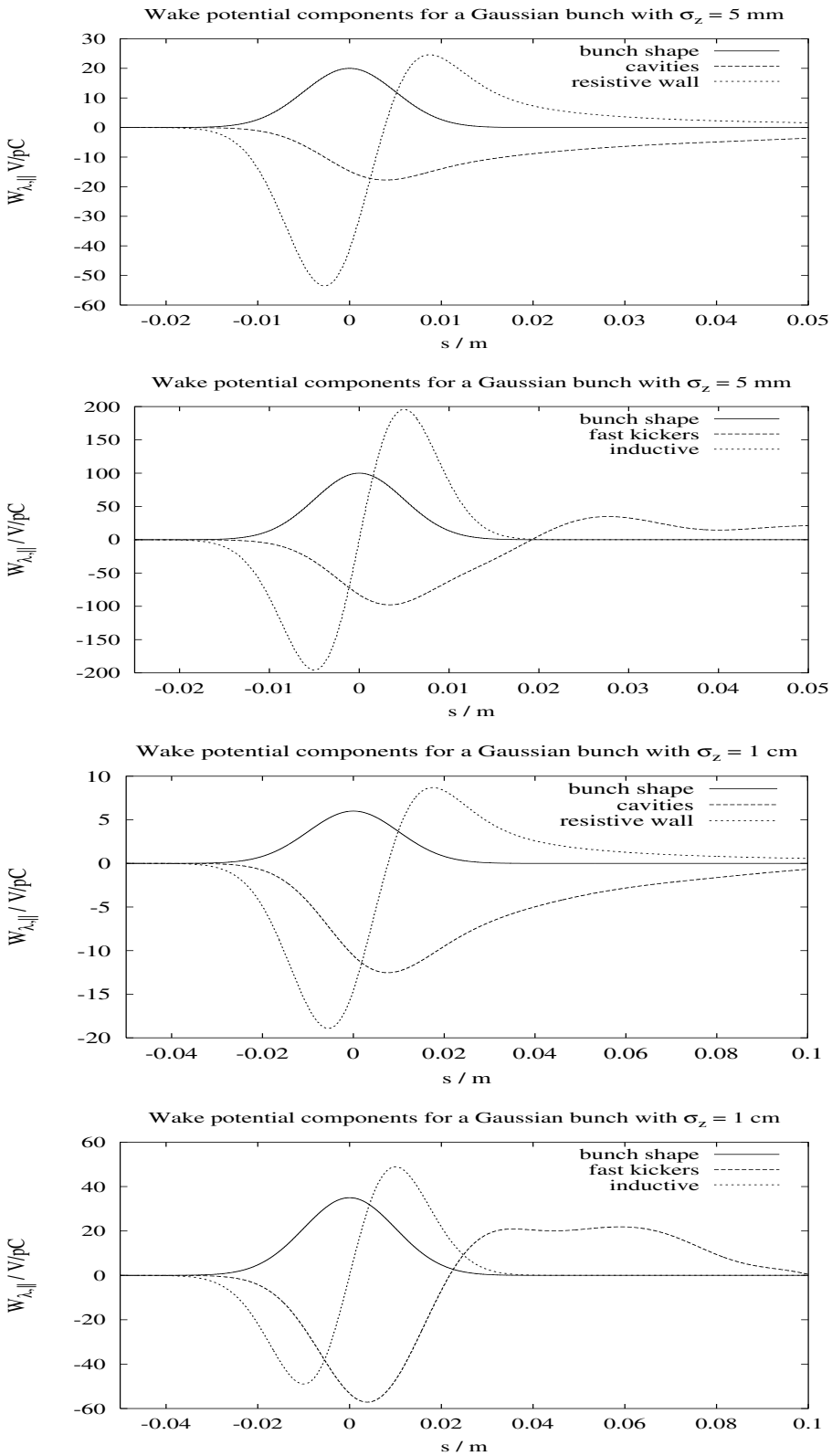

Figure 6.3: The wake potential components of a Gaussian bunch with the rms bunch length $\sigma_z = 5\,\mathrm{mm}$ (top two plots) and $\sigma_z = 1\,\mathrm{cm}$ (lower two plots).

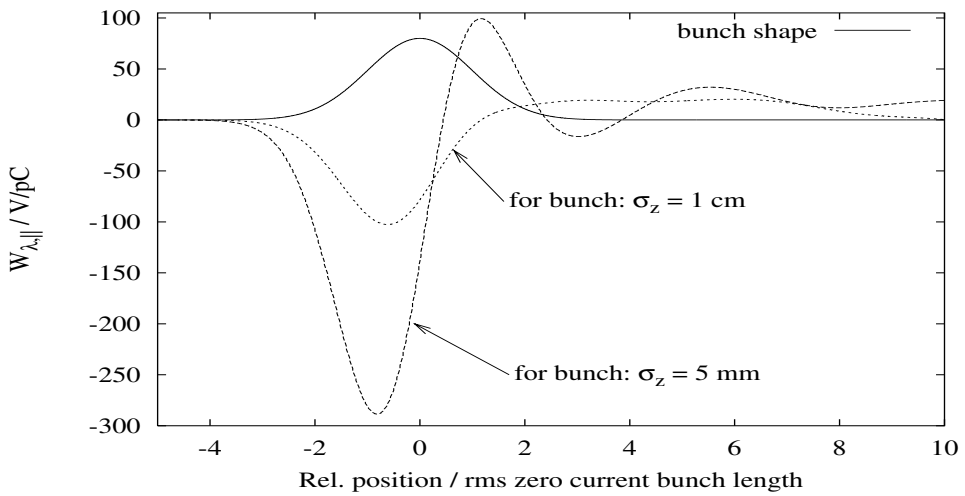

Figure 6.4: The wake potentials (all components) of Gaussian bunches with the rms bunch lengths 5 mm and a 1 cm.

6.1.4 Inductive Wake

The design momentum compaction factor $\alpha_c = 3.4 \times 10^{-4}$ leads to a bunch lengthening in the range of four percent at the design bunch population $N_e^{ref} = 3.63 \times 10^{10}$ ($L = 225\,\mathrm{nH}$). The normalized bunch charge κ (see Eq. (3.146)) is 0.67. Inserting κ into the first-order bunch lengthening estimate (3.147) gives 4.7 %.

Since the smaller of the two momentum compaction factors studied leads to a larger bunch lengthening and proves to be more interesting, it is the one which is discussed in more detail in this section.

$\alpha_c = 9.5 \times 10^{-5}$		N_e/N_e^{ref} 1	2	3	4
Haissinski Eq.	σ_z/σ_{z0}	1.23	1.38	1.49	1.59
$N_{sec} = 2$, $\sigma_z^{QGF} = 1\,\mathrm{mm}$	σ_z/σ_{z0}	1.22	1.37	1.49	1.59
$N_{sec} = 4$, $\sigma_z^{QGF} = 1\,\mathrm{mm}$	σ_z/σ_{z0}	1.23	1.37	1.49	1.59
$N_{sec} = 4$, $\sigma_z^{QGF} = 0.5\,\mathrm{mm}$	σ_z/σ_{z0}	1.23	1.38	1.50	1.60

Table 6.5: Relative bunch lengthening due to the purely inductive wake ($L = 225\,\mathrm{nH}$) for $\alpha_c = 9.5 \times 10^{-5}$. The Haissinski equation predictions are compared to the tracking results when using two sections and four sections. 100 000 macroparticles are used and the bin width is 0.3 mm. The values are calculated in all cases in the last section.

At the top of Table 6.5, the Haissinski equation predictions are presented which are derived by solving the differential equation (3.145) with the iterated trapezoid rule. Using the inductive wake potentials of Gaussian bunches with $\sigma_z = 0.5\,\mathrm{mm}$ and $\sigma_z = 1\,\mathrm{mm}$ as quasi-Green's functions and solving Eq. (3.154) (as explained on page 59) delivers

the same figures within the range of 1 %. The design bunch population ($\kappa = 4.58$ for $\alpha_c = 9.5 \times 10^{-5}$) gives rise to a bunch lengthening of approximately 23 %. Eq. (3.147) cannot be used for such large κ; it leads to an over-estimation (32 %).
We now turn to the tracking method. As the inductive impedance is spread more or less evenly over the ring, the macroparticles in each section see an equal proportion of the total inductance value. This is a more realistic approach than using one section and a lumped total inductance. The bunch-length tracking results of Table 6.5 are in accordance with the potential-well theory predictions. The values for the relative energy spread in the tracking calculations are also in accordance. They differ from the zero-current value by no more than 1 %.

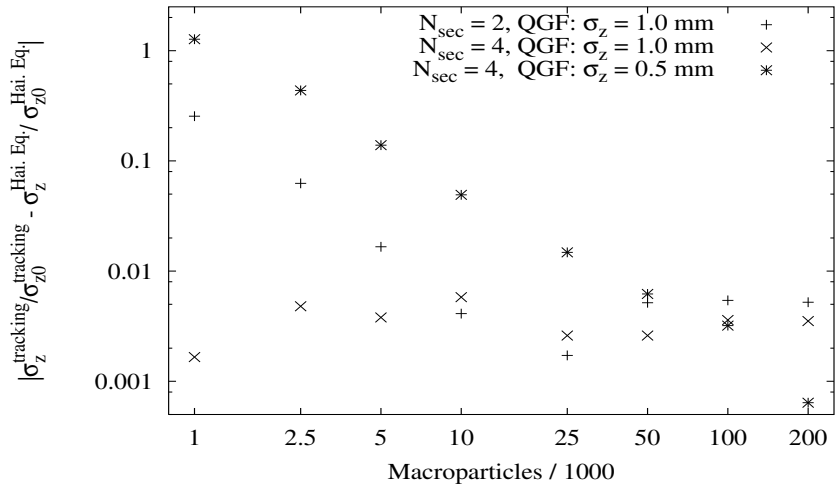

Figure 6.5: Deviation of the relative bunch length from the Haissinski equation prediction as a function of the number of macroparticles. The bunch population is $N_e = 4N_e^{ref}$. The width of the bins is 0.3 mm.

To check the influence of the number of macroparticles on the tracking results, we study the case $N_e = 4N_e^{ref}$, where the wake potential is the largest. With the help of Figure 6.5, we can see that already 25 000 macroparticles lead to satisfactory results. To be well on the safe side, 100 000 particles are used in the simulations for the above table. We must of course realize that all points in Figure 6.5 that lie below 0.01, the 1 % margin, must be viewed with caution. Our Haissinski equation solutions will include a small mistake and the tracking results (one simulation) are average values with an rms that is at best 0.1 %. This applies to all the following plots of this kind. We will look upon the "1 %" margin as what counts.
When, however, using two sections and the wake potential of a Gaussian bunch with an rms bunch length of 0.5 mm as a QGF, we find a discrepancy for the two larger bunch populations with respect to the bunch length and energy spread. This is shown in Figure 6.6 on the next page. This also happens when using only one section [61]. We can not tackle the problem by just using four sections and concentrating the inductance in two sections (this leads to the same bunch lengthening as for two sections); it must be

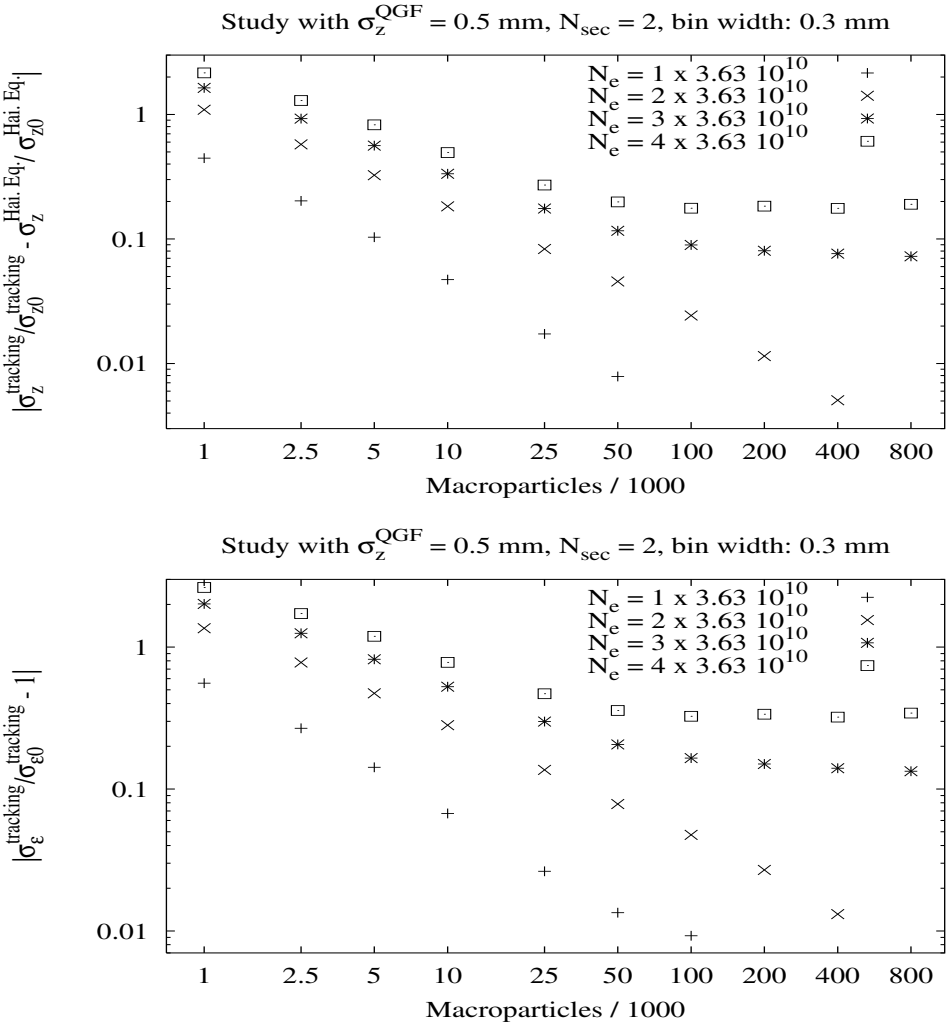

Figure 6.6: The deviation of the relative bunch length (top picture) and energy spread (bottom picture) as a function of the number of macroparticles when tracking with two sections and the inductive wake potential of a Gaussian bunch with $\sigma_z = 0.5\,\mathrm{mm}$ as a quasi-Green's function. The momentum compaction factor is set to $\alpha_c = 9.5 \times 10^{-5}$.

distributed.

In the following, the possibility of smoothing (see page 63) is investigated. Three cases are presented in Figure 6.7 on page 93, where the deviation of the relative bunch length from the Haissinski equation solution is shown as a function of the number of macroparticles. In two cases, the bin width of 0.3 mm is kept, as in the previous examples, and the smoothing factors 3 and 5 are applied. The third test uses a smaller bin width, 0.2 mm, and the smoothing factor 5.

The plots show that the discrepancy can be decreased by smoothing. We now look specifically at the two following combinations: bin width 0.3 mm/smoothing factor 3 and bin width 0.2 mm/smoothing factor 5. They indicate that smoothing over the same total width ($3 \times 0.3\,\mathrm{mm} = 0.9\,\mathrm{mm}$, $5 \times 0.2\,\mathrm{mm} = 1.0\,\mathrm{mm}$) leads to approximately the same

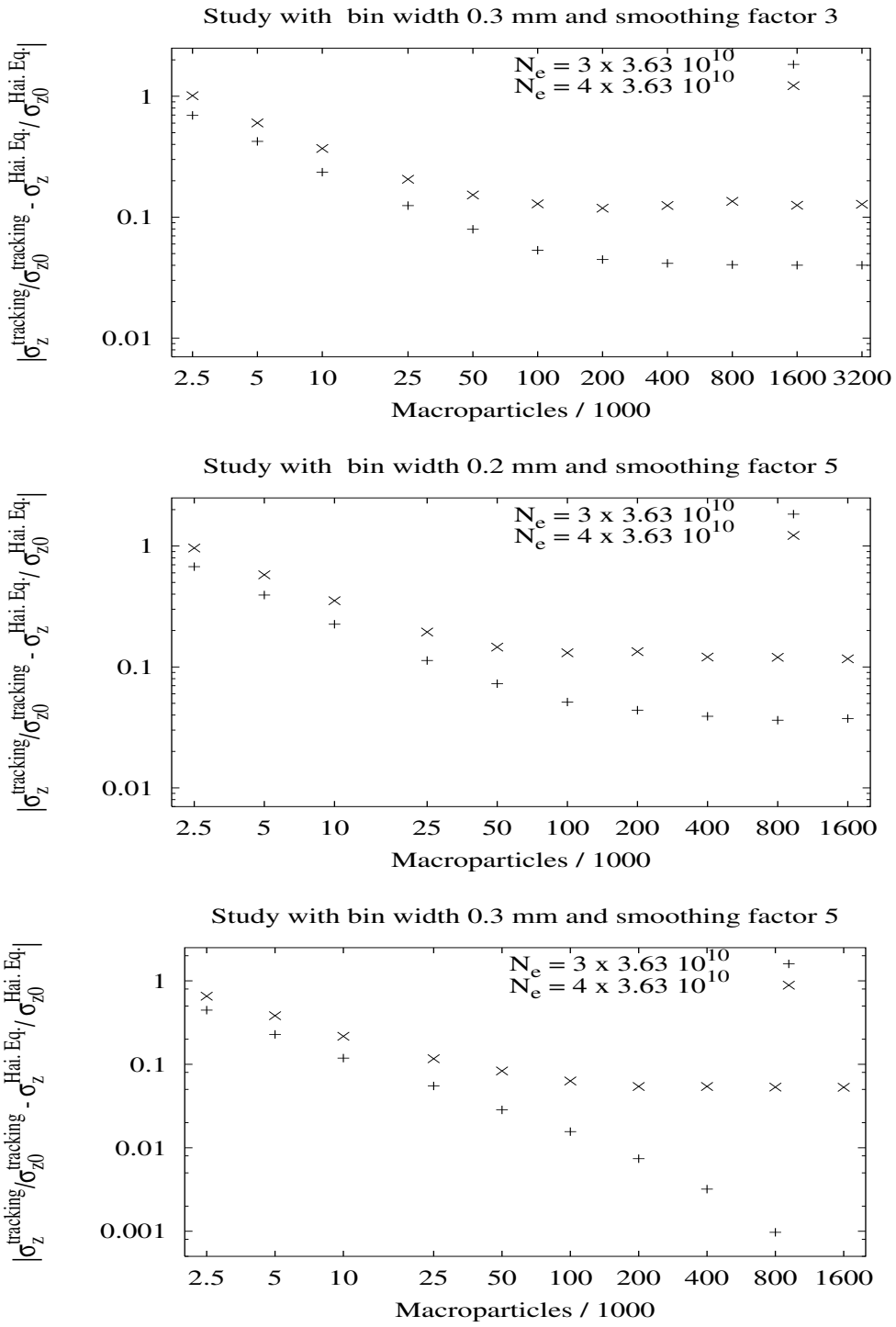

Figure 6.7: Three studies investigating the influence of smoothing (see page 63) on the relative bunch length, when tracking with two sections and the inductive quasi-Green's function, where $\sigma_z^{\mathrm{QGF}} = 0.5\,\mathrm{mm}$. The discrepancy between the tracking results and the Haissinski equation solutions are shown as a function of the number of macroparticles in the three plots.

results. The combination of the bin width 0.3 mm and the smoothing factor 5 leads to the solution of the Haissinski equation for the bunch population $N_\mathrm{e} = 3N_\mathrm{e}^\mathrm{ref}$, but fails when the bunch population is increased.
The bunch length deviations also correspond here to a rise in the energy spread. As an example, we find that for four times the reference bunch population, the relative energy spread rise converges as a function of the macroparticle number towards approximately 10 % for the case of smoothing factor 5 and bin width 0.3 mm and 25 % in the two other cases.

6.1.5 Resistive Wall

Since an extensive study of the effect of the resistive wall wake fields was done in [61], only a few examples are shown here. The simulation results concur extremely well with those obtained by the Haissinski equation as seen in Table 6.6.

$\alpha_\mathrm{c} = 9.5 \times 10^{-5}$		$N_\mathrm{e}/N_\mathrm{e}^\mathrm{ref}$ 1	2	3	4	10
Hai. Eq.:	σ_z/σ_{z0}	1.05	1.10	1.15	1.20	1.43
$N_\mathrm{sec} = 4$:	σ_z/σ_{z0}	1.05	1.10	1.15	1.20	1.43
Hai. Eq.:	$-\Delta\bar{\tau}/\sigma_{t0}$	0.13	0.23	0.33	0.41	0.79
$N_\mathrm{sec} = 4$:	$-\Delta\bar{\tau}/\sigma_{t0}$	0.13	0.23	0.33	0.41	0.78
$\alpha_\mathrm{c} = 3.4 \times 10^{-4}$		$N_\mathrm{e}/N_\mathrm{e}^\mathrm{ref}$ 1	2	3	4	10
Hai. Eq.:	σ_z/σ_{z0}	1.01	1.02	1.03	1.04	1.10
$N_\mathrm{sec} = 4$:	σ_z/σ_{z0}	1.01	1.02	1.03	1.04	1.10
Hai. Eq.:	$-\Delta\bar{\tau}/\sigma_{t0}$	0.03	0.05	0.08	0.11	0.24
$N_\mathrm{sec} = 4$:	$-\Delta\bar{\tau}/\sigma_{t0}$	0.03	0.05	0.08	0.10	0.23

Table 6.6: Relative (to the zero-current bunch length) bunch lengthening and change of the bunch centre ($\sigma_{t0} = \sigma_{z0}/c$) due to the resistive wall wake. On the top for $\alpha_\mathrm{c} = 9.5 \times 10^{-5}$ ($\sigma_z^\mathrm{QGF} = 0.5\,\mathrm{mm}$) and on the bottom for $\alpha_\mathrm{c} = 3.4 \times 10^{-4}$ ($\sigma_z^\mathrm{QGF} = 1.0\,\mathrm{mm}$). The Haissinski equation predictions and tracking results when using four sections (100 000 macroparticles, 0.2 mm bins, the relative bunch length and change of the bunch centre are evaluated in the third section) are shown.

Since the resistive wall wake field is spread throughout the entire chamber, it is split evenly among the tracking sections. At the design bunch population and for the momentum compaction factor, the resistive wall wake is practically insignificant due to the large vacuum chamber radius.
The same discrepancies as encountered for the two-section studies with the momentum compaction factor $\alpha_\mathrm{c} = 9.5 \times 10^{-5}$ and the inductive wake potential of a Gaussian bunch with $\sigma_z = 0.5\,\mathrm{mm}$ as a quasi-Green's function occur for the resistive wall wake when using only one section and bunch populations larger than approximately 15 times the design population. For two sections it already vanishes [61].
On the following page, Figures 6.8 and 6.9 show the deviations of the relative rms bunch length and energy spread as a function of the number of macroparticles. 25 000 macro-

particles lead to satisfactory results. To be on the safe side, the above table is established for 100 000 macroparticles.

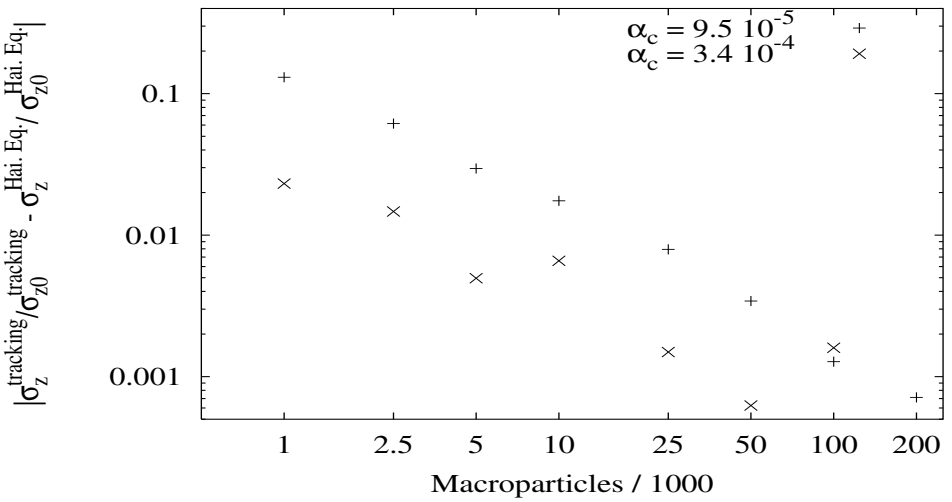

Figure 6.8: The deviation of the relative bunch length from the solution of the Haissinski equation as a function of the macroparticle number for the bunch population $N_e = 10N_e^{ref}$. For the study with the momentum compaction factor $\alpha_c = 9.5 \times 10^{-5}$, the quasi-Green's function is the wake potential of a Gaussian bunch with $\sigma_z = 0.5\,\mathrm{mm}$; for the study with $\alpha_c = 3.4 \times 10^{-4}$, it is the wake potential of a Gaussian bunch with $\sigma_z = 1.0\,\mathrm{mm}$. In both cases, the numbers are evaluated after the third of the four sections. The width of the bins is 0.2 mm; the number of turns tracked is 3500.

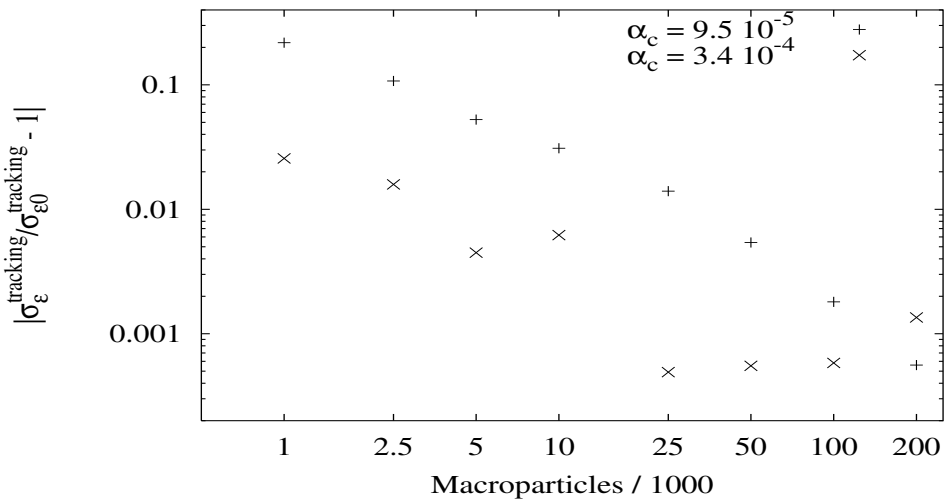

Figure 6.9: The deviation of the relative rms energy spread from unity as a function of the macroparticle number for the bunch population $N_e = 10N_e^{ref}$. The simulations are the same as in Figure 6.8.

Figure 6.10 shows the bunch shape and distorted potential well for the studied momentum compaction factors and for the bunch populations 3.63×10^{10} and 3.63×10^{11}.
The larger distortion of the bunch with the smaller compaction factor value at a comparatively lower beam intensity can easily be seen. A common feature is that the distributions "lean forward" so that the parasitic energy loss, a consequence of the real (resistive) part of the impedance, is compensated by the rf voltage.

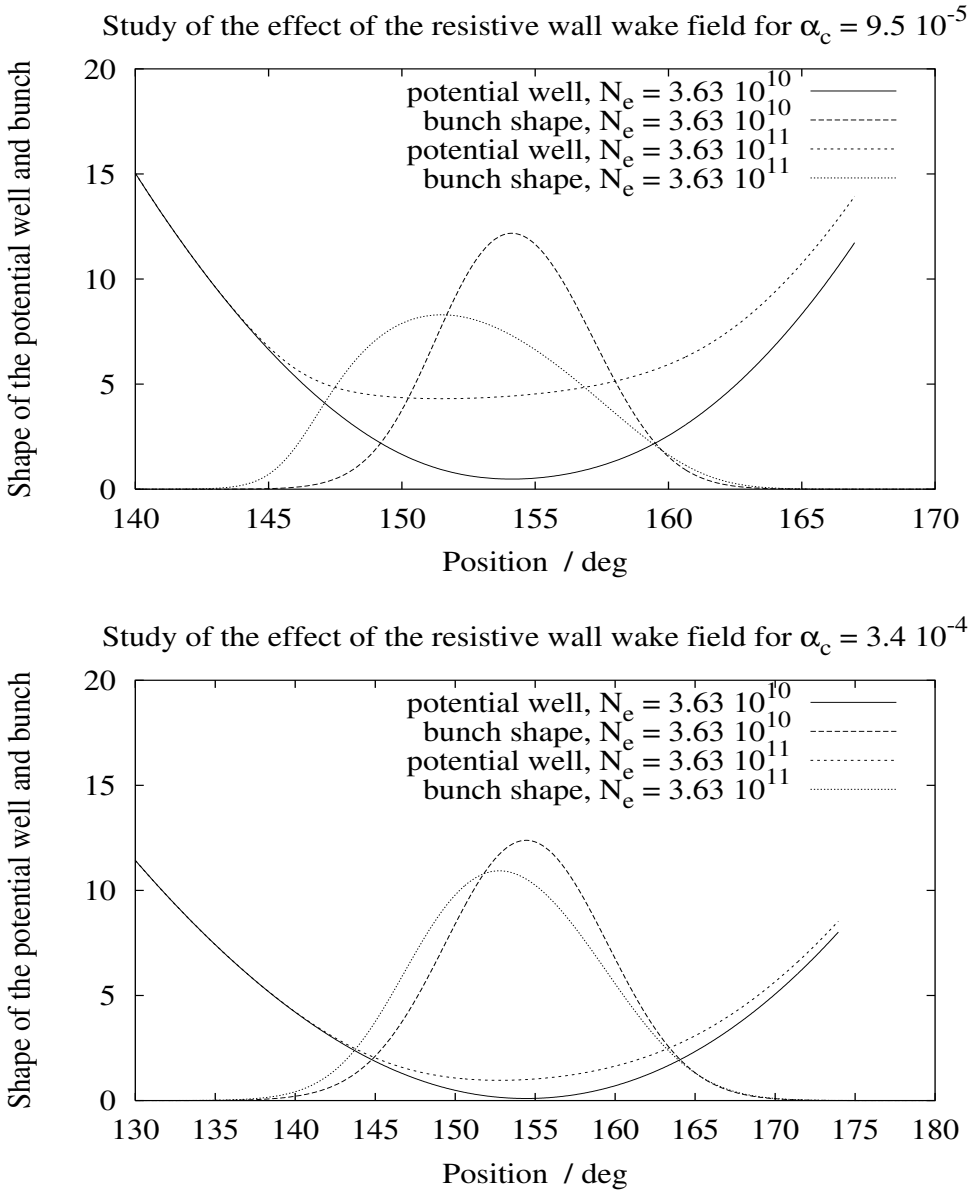

Figure 6.10: Resistive wall wake. Shape of the potential well and the bunch according to the solution of the Haissinski equation. On the top for the momentum compaction factor $\alpha_c = 9.5 \times 10^{-5}$ and for the design and tenfold charge, on the bottom the same for $\alpha_c = 3.4 \times 10^{-4}$.

6.1.6 Cavities

The wake potential due to the cavities is the smallest for all the studied cases (see for example Figure 6.3). Being capacitive in nature, the wake can be expected to lead to a bunch shortening which is evident from Table 6.7. The tracking results for one and two sections are compared there to the solutions of the Haissinski equation for the momentum compaction factors $\alpha_c = 9.5 \times 10^{-5}$ and $\alpha_c = 3.4 \times 10^{-4}$. They concur well. 200 000 macroparticles are used in the tracking calculations; the bin width is 0.2 mm. The QGF is the wake potential of a Gaussian bunch with rms bunch length 0.5 mm in the case of the smaller of the two momentum compaction factors and the wake potential of a Gaussian bunch with $\sigma_z = 1$ mm in the larger case.

$\alpha_c = 9.5 \times 10^{-5}$		N_e/N_e^{ref}					
		1	3	5	7	9	11
Hai. Eq.:	σ_z/σ_{z0}	0.99	0.97	0.95	0.93	0.92	0.90
$N_{sec} = 1$:	σ_z/σ_{z0}	0.99	0.97	0.95	0.94	0.92	0.91
$N_{sec} = 2$:	σ_z/σ_{z0}	0.99	0.97	0.95	0.93	0.92	0.90
Hai. Eq.:	$-\Delta\bar{\tau}/\sigma_{t0}$	0.07	0.22	0.37	0.52	0.68	0.85
$N_{sec} = 2$:	$-\Delta\bar{\tau}/\sigma_{t0}$	0.07	0.22	0.37	0.52	0.68	0.84
$\alpha_c = 3.4 \times 10^{-4}$		N_e/N_e^{ref}					
		1	3	5	7	9	11
Hai. Eq.:	σ_z/σ_{z0}	1.00	0.99	0.98	0.97	0.97	0.96
$N_{sec} = 1$:	σ_z/σ_{z0}	1.00	0.99	0.98	0.98	0.97	0.96
$N_{sec} = 2$:	σ_z/σ_{z0}	1.00	0.99	0.98	0.97	0.96	0.95
Hai. Eq.:	$-\Delta\bar{\tau}/\sigma_{t0}$	0.03	0.08	0.14	0.19	0.25	0.31
$N_{sec} = 2$:	$-\Delta\bar{\tau}/\sigma_{t0}$	0.03	0.08	0.14	0.19	0.26	0.30

Table 6.7: Relative (to the zero-current bunch length) bunch shortening and change of the bunch centre in units of the rms bunch length due to the wake in the cavities. On the top for $\alpha_c = 9.5 \times 10^{-4}$ and on the bottom for $\alpha_c = 3.4 \times 10^{-4}$. The first and fourth row show the Haissinski equation predictions, the others show the tracking results when using one section or two sections (data from the 2nd section).

6.1.7 Fast Kicker

The fast kicker wake leads to a bunch shortening for $\alpha_c = 9.5 \times 10^{-5}$ and charges up to seven times the design bunch population. A minimum bunch length is obtained in the range of five times the design bunch population (for the solution of the Haissinski equation as well as for the simulation), as seen in Table 6.8.
An extreme rise in bunch length can be seen at approx. the eightfold of the design bunch charge. This concurs with the predicted solution of the Haissinski equation. The bunch lengthening can be explained by the appearance of a second potential-well minimum, as is clearly visible in Figures 6.11 (page 98) and 6.12 (page 99). The decrease in stability of the bunch centre is disproportionately large for larger charges.

$\alpha_c = 9.5 \times 10^{-5}$		N_e/N_e^{ref}					
		1	3	5	7	8	8.5
Hai. Eq.:	σ_z/σ_{z0}	0.95	0.86	0.82	0.94	1.19	1.38
$N_{sec} = 2$:	σ_z/σ_{z0}	0.95	0.86	0.81	0.92	1.16	1.34
	rms $\bar{\phi}$ / deg	0.004	0.006	0.011	0.07	0.18	0.42
$\alpha_c = 3.4 \times 10^{-4}$		N_e/N_e^{ref}					
		1	3	5	7	7.5	8
Hai. Eq.:	σ_z/σ_{z0}	0.99	0.98	0.98	1.00	1.01	1.01
$N_{sec} = 2$:	σ_z/σ_{z0}	0.99	0.98	0.98	1.00	1.02	1.15
	rms $\bar{\phi}$ / deg	0.008	0.009	0.033	0.27	3.2	12.2

Table 6.8: Relative (to the zero-current bunch length) bunch shortening/lengthening due to the wake in the fast kickers for $\alpha_c = 9.5 \times 10^{-5}$ and $\alpha_c = 3.4 \times 10^{-4}$. The top row shows the expected relative bunch length values from the Haissinski equation, the second the tracking results when using two sections (data from the 2nd section). The position of the bunch centre becomes steadily unstable with increasing bunch charge (bottom line). The wake potential of a Gaussian bunch with $\sigma_z = 2\,\mathrm{mm}$ is used as a quasi-Green's function.

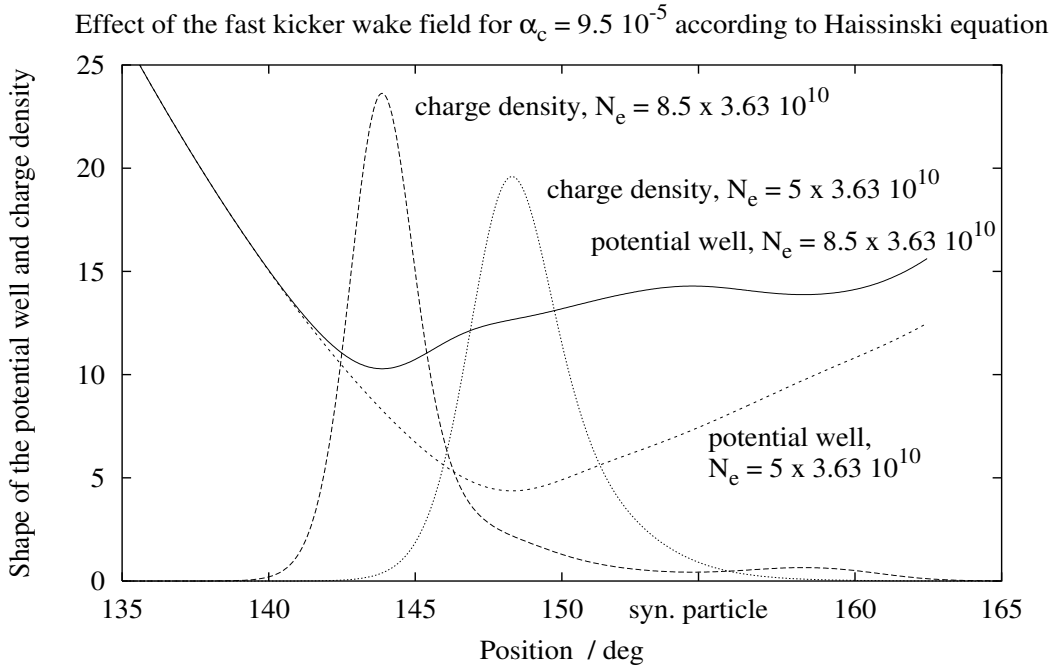

Figure 6.11: Two solutions of the Haissinski equation using the wake potential (fast kickers) of a Gaussian bunch with $\sigma_z = 2\,\mathrm{mm}$ as a quasi-Green's function for the case $\alpha_c = 9.5 \times 10^{-5}$.

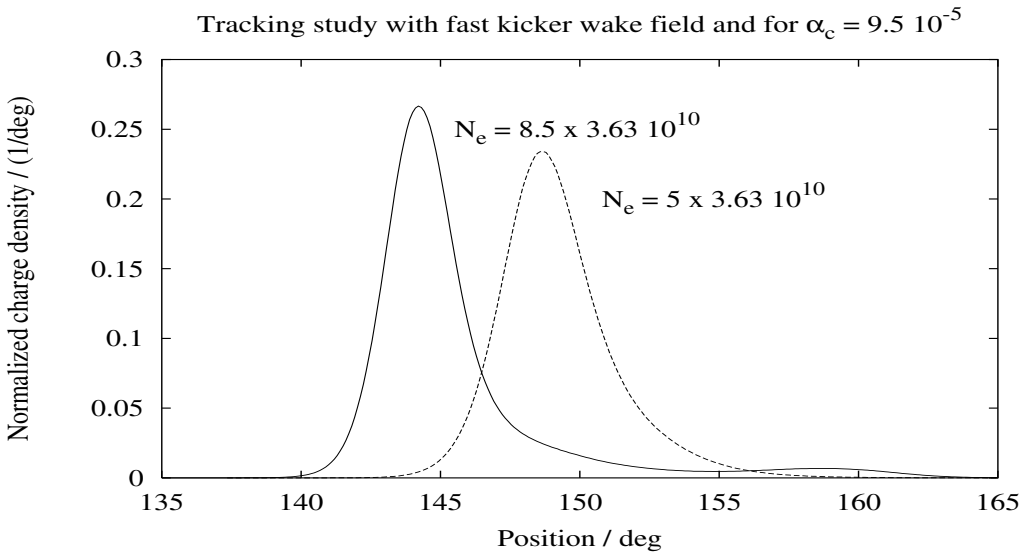

Figure 6.12: Two tracking results for $\alpha_c = 9.5 \times 10^{-5}$ when using the wake potential in the fast kickers ($\sigma_z^{\mathrm{QGF}} = 2\,\mathrm{mm}$) as a QGF. The number of macroparticles is $N_{\mathrm{par}} = 200\,000$, N_{sec} is 2; the width of the bins is 0.2 mm.

The design momentum compaction factor is characterized by a negligible bunch shortening for bunch populations up to 1.7×10^{11} particles. The rms value of the average bunch position increases drastically for populations above $7N_e^{\mathrm{ref}}$. For the factor 7.5 it is already 3.2°, indicating that the bunch is undergoing a larger fluctuation in relation to its position. There is a corresponding rise in the energy spread. The results are less dramatic, but show the same signs as when using the wake potential of a Gaussian bunch with an rms bunch length of 3 mm as a quasi-Green's function.
Figure 6.13 (page 100) shows the bunch shape for the fivefold and sevenfold design bunch charge. They are compared to the shape of a bunch (having the same zero-current bunch length) that sees the effect of a resistive wake potential and where the normalized bunch charge $\kappa = 2.14$ (see Eq. (3.149)). κ corresponds to the fivefold design bunch population and $R = 40 \times 114\,\Omega$, the resistivity of the wake potential of a Gaussian bunch with $\sigma_z = 1\,\mathrm{cm}$ passing a fast kicker, as was estimated in Section 5.1.5.
To compensate for the energy loss due to the wake, the bunch moves forward so that it sees, on the average, a larger effective rf voltage (see Table 6.9). The effect is greater than that of the combined resistive wall and cavity wakes.

	N_e/N_e^{ref}			
	1	2	3	4
$\alpha_c = 9.5 \times 10^{-5}$, $-\Delta\bar{\tau}/\sigma_{t0}$	0.39	0.80	1.25	1.72
$\alpha_c = 3.4 \times 10^{-4}$, $-\Delta\bar{\tau}/\sigma_{t0}$	0.12	0.25	0.38	0.51

Table 6.9: Change of the bunch centre in rms bunch length units due to the fast kicker wake field, according to the solution of the Haissinski equation.

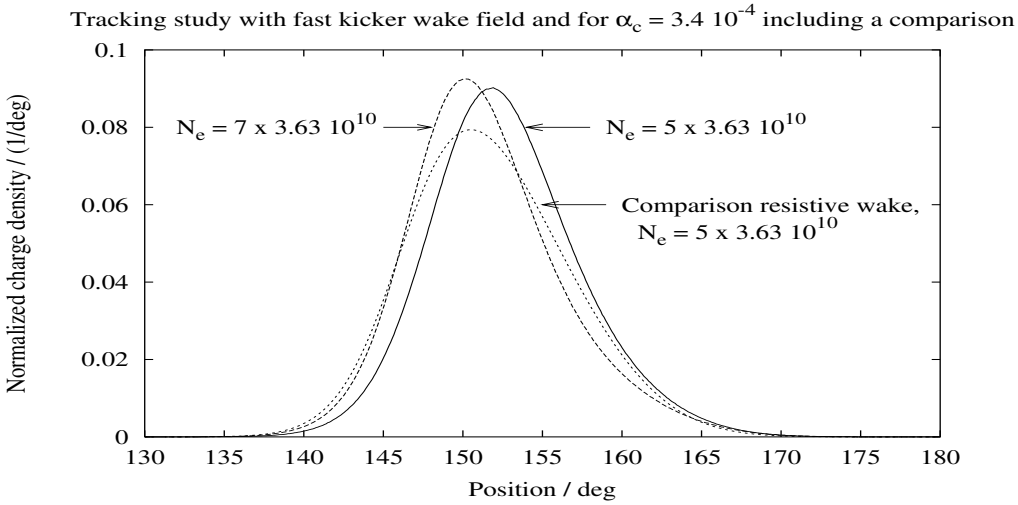

Figure 6.13: Two tracking results for the case $\alpha_c = 3.4 \times 10^{-4}$. The tracking parameters are as follows: $N_{par} = 200\,000$, $N_{sec} = 2$; the width of the bins is 0.2 mm, and the wake potential pertaining to the fast kicker and $\sigma_z^{QGF} = 2\,mm$ is used as a QGF. The results are compared to a purely resistive wake potential, pertaining to a bunch with the same nominal rms bunch length and with the fivefold design bunch charge seeing a resistivity of $4560\,\Omega = 40 \times 114\,\Omega$.

6.1.8 Total Wake

The case of the design momentum compaction factor is studied first. The components of the quasi-Green's function are the wake potentials with $\sigma_z^{QGF} = 1\,mm$ for the inductive, the resistive wall, and the cavity components, and $\sigma_z^{QGF} = 2\,mm$ for the fast kickers.

$\alpha_c = 3.4 \times 10^{-4}$		N_e/N_e^{ref} 1	2	3	4
Hai. Eq.:	σ_z/σ_{z0}	1.05	1.09	1.13	1.17
$N_{sec} = 4$:	σ_z/σ_{z0}	1.04	1.09	1.13	1.17
Hai. Eq.:	$-\Delta\bar{\tau}/\sigma_{t0}$	0.17	0.33	0.47	0.61
$N_{sec} = 4$:	$-\Delta\bar{\tau}/\sigma_{t0}$	0.17	0.32	0.46	0.60

Table 6.10: Relative bunch lengthening (top) and change of the bunch centre (bottom) due to the total wake for $\alpha_c = 3.4 \times 10^{-4}$. The first row shows the Haissinski equation predictions, the second the average tracking results when using four sections.

The numbers in Table 6.10 represent the average of four simulations where there are slight variations in the number of particles, the width of the bins, the number of turns, and the section where the values are established:

- $N_{par} = 100\,000$, bin-width: 0.3 mm, 3000 turns, 4th-section values
- $N_{par} = 200\,000$, bin-width: 0.2 mm, 3500 turns, 4th-section values

- $N_{\mathrm{par}} = 200\,000$, bin-width: 0.2 mm, 3500 turns, 3rd-section values
- $N_{\mathrm{par}} = 200\,000$, bin-width: 0.3 mm, 3500 turns, 3rd-section values

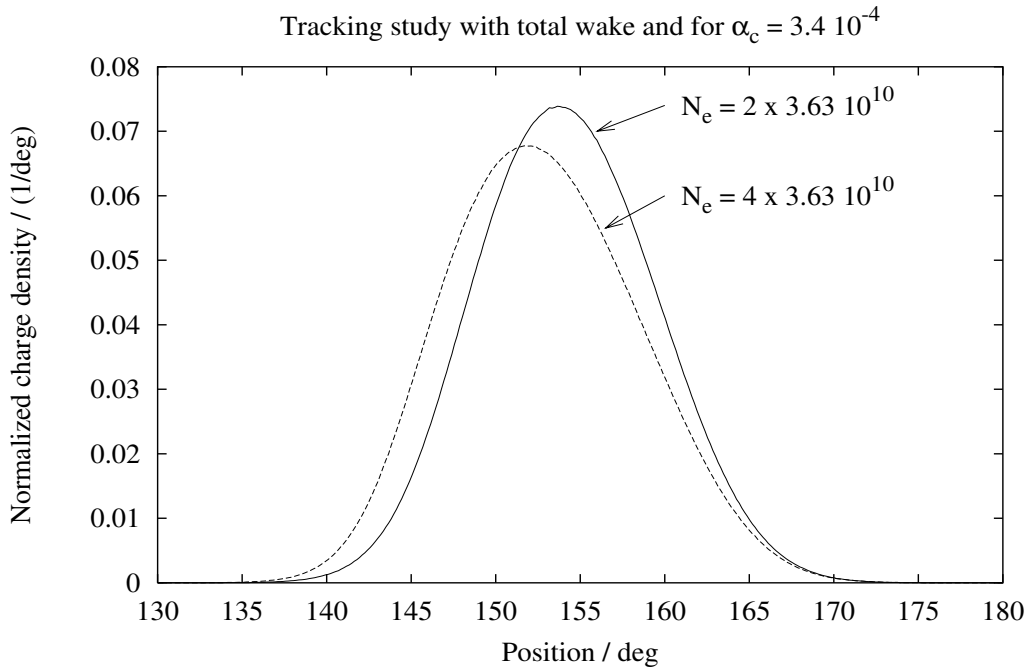

Figure 6.14: Two tracking results for the total wake and $\alpha_{\mathrm{c}} = 3.4 \times 10^{-4}$. The number of macroparticles in the simulation is 200 000, four sections are used (the density is evaluated in the third section), and the bin width is 0.3 mm.

The individual results differ less than 1 % from the average result, which is in full agreement with the predictions calculated with the Haissinski equation. Nine iterations are needed to solve the equation for the design bunch population, 22 for the fourfold population.
The relative bunch lengthening is consistent with what would be expected due to the inductive component. The individual relative energy spreads varied by less than 1 %. The absolute rms values for the bunch length and energy spread are, for example, for the fourth simulation, in all cases not larger than 0.02 cm and 0.005 MeV.
With respect to the position of the bunch centre, the differences are minimal. The individual tracking results differ only in the third decimal in the total range of 0.001 (in rms zero-current bunch length units). The main contributor to the change of the average bunch position is the wake potential in the fast kickers. For the design bunch charge, the appropriate values in the Tables 6.6, 6.7, and 6.9 add up to that of Table 6.10.

Two, four, and eight sections are used for the tracking calculations with the momentum compaction factor $\alpha_{\mathrm{c}} = 9.5 \times 10^{-5}$. The results correspond to those of the inductive wake, underlining its influence as the largest component and its negative influence in the two-section calculations. The relative bunch lengthening is seen to match that of the inductive wake.

We begin our study by looking at the following case: As quasi-Green's functions we choose $\sigma_z^{\mathrm{QGF}} = 2\,\mathrm{mm}$ for the fast kickers and $\sigma_z^{\mathrm{QGF}} = 0.5\,\mathrm{mm}$ for the cavity, resistive wall, and inductive components. The tracking uses bins with the width 0.2 mm, involves four sections, and lasts 3000 turns. In Figure 6.15, we compare the deviation of the relative bunch lengthening from the solution of the Haissinski equation as a function of the number of macroparticles. We find an agreement between the tracking results and the Haissinski solution for the studied bunch populations. Again, we must remember that the "1 % margin" is what counts, and not make ourselves believe that the accuracy is perhaps 0.1 % or less. Each point in the figure represents only one simulation; our Haissinski solution contains an error and the zero-current tracking rms bunch length can vary to a certain limit. We should expect that the employment of 100 000 macroparticles in our further studies will lead to "correct" results.

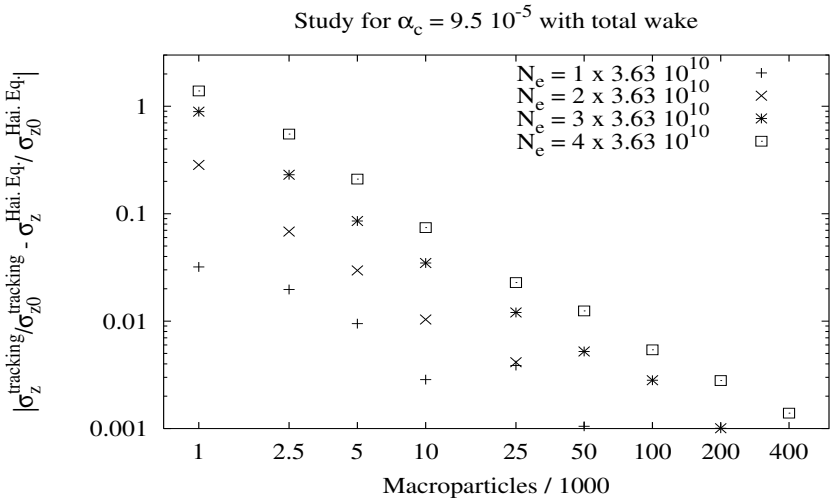

Figure 6.15: Deviation of the relative bunch length from the Haissinski equation prediction as a function of the number of macroparticles. The number of sections is $N_{\mathrm{sec}} = 4$. The width of the bins is 2 mm.

Our next studies use these 100 000 macroparticles and last 3000 turns. In all cases, the fast kicker component of the quasi-Green's function is generated by a Gaussian bunch with $\sigma_z = 2\,\mathrm{mm}$. The further details are:

- $N_{\mathrm{sec}} = 2$ (evaluations in 2nd section), bin-width: 0.2 mm, inductive, cavity, and resistive wall components: $\sigma_z^{\mathrm{QGF}} = 1\,\mathrm{mm}$
- $N_{\mathrm{sec}} = 2$ (evaluations in 2nd section), bin-width: 0.2 mm, cavity and resistive wall QGF components: $\sigma_z^{\mathrm{QGF}} = 0.5\,\mathrm{mm}$, inductive QGF: $\sigma_z^{\mathrm{QGF}} = 1\,\mathrm{mm}$
- $N_{\mathrm{sec}} = 4$ (evaluations in 4th section), bin-width: 0.3 mm, cavity and resistive wall QGF components: $\sigma_z^{\mathrm{QGF}} = 0.5\,\mathrm{mm}$, inductive QGF: $\sigma_z^{\mathrm{QGF}} = 1\,\mathrm{mm}$
- $N_{\mathrm{sec}} = 8$ (evaluations in 5th section), bin-width: 0.2 mm, inductive, cavity, and resistive wall QGF components: $\sigma_z^{\mathrm{QGF}} = 0.5\,\mathrm{mm}$

We find in all four cases that the relative bunch lengthening results do not differ from those using the Haissinski equation by more than 1 %. The results of the Haissinski solution are presented in Table 6.11.

$\alpha_c = 9.5 \times 10^{-5}$		N_e/N_e^{ref} 1	2	3	4
Haissinski Eq.:	σ_z/σ_{z0}	1.22	1.37	1.50	1.62
Haissinski Eq.:	$-\Delta\bar{\tau}/\sigma_{t0}$	0.49	0.89	1.24	1.55

Table 6.11: Relative bunch lengthening (top) and change of the bunch centre (bottom) due to the total wake for $\alpha_c = 9.5 \times 10^{-5}$ according to the Haissinski equation predictions. It takes 76 iterations to solve the Haissinski equation with the requested margins for the fourfold bunch population.

Our last studies consider the case that the inductive component of the quasi-Green's function is generated by a Gaussian bunch with $\sigma_z = 0.5\,\mathrm{mm}$ and that the tracking is based on using two sections. The σ_z^{QGF} of the cavity and resistive wall QGF components are also 0.5 mm.
The results resemble those in Section 6.1.4 when tracking with two sections and using the inductive wake potential generated by a Gaussian bunch with an rms bunch length of 0.5 mm as a quasi-Green's function. The rms bunch lengths do not converge towards the solutions of the Haissinski equation for the two bunch populations $3 \times N_e^{ref}$ and $4 \times N_e^{ref}$; see Figure 6.16. There is also a corresponding rise in the relative energy spread, which is not shown here.
We may conclude, however, that no instability has been detected due to our tracking results with four sections.

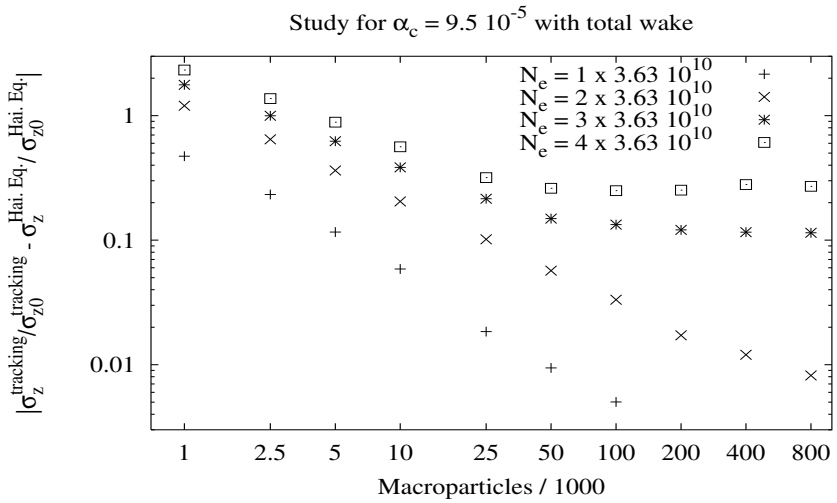

Figure 6.16: Deviation of the relative bunch length from the Haissinski equation prediction as a function of the number of macroparticles. The number of sections is $N_{sec} = 2$. The inductive component of the QGF is generated by a Gaussian bunch with $\sigma_z = 0.5\,\mathrm{mm}$. The width of the bins is 3 mm.

6.2 Multibunch Tracking

The bunch train in the dog-bone damping ring consists of 1130 bunches, corresponding to the harmonic number 24 570 with every 21st bucket filled, except in the approx. 3.5 % gap at the end of the train for ion-clearing (Glossary, page 171).
To begin with, simulations are presented which study higher-order mode effects in the absence of beam loading. Thereafter, simulations are presented which take into account the beam loading in the fundamental mode.
In all the presented simulations the design momentum compaction is, unless otherwise stated, $\alpha_c = 3.4 \times 10^{-4}$, corresponding to an rms bunch length of 9.5 mm. At the end of the two subsections there are short discussions regarding studies with $\alpha_c = 9.5 \times 10^{-5}$.

6.2.1 Simulations with Higher-Order Modes

In the following examples studying the higher-order modes, it is assumed that the compensation of beam-loading effects in the fundamental mode is perfect. We study here the worst case, where the modes are identical in all the eight cavities. Assuming a Gaussian bunch with the design bunch length $\sigma_z = 9.5\,\mathrm{mm}$, the loss factors of the two strongest higher-order modes $k_{\lambda,\parallel}$ are approximately $0.976\,k_{\delta,\parallel}$ (see Eq. (3.78), page 34 and Table 5.3, page 80). The bunch form factor with respect to the fundamental mode is approximately 0.996.
A summary of the various initial settings for the bunch phases and energy deviations used in the simulations is presented in Table 6.12. The tracking calculations begin as if all the bunches would enter the damping ring on the first turn.

		initial bunch phase		initial energy deviation
		in general	exemptions	
case	A	$\phi_i = 154.56°$	$\phi_{20} = 148°$	$\varepsilon_i = 0$
	B	$\phi_i = 154.56°$	$\phi_i = 148°, \quad i \in \{30n \mid n \in \mathbb{N} \wedge 30n \leq N_\mathrm{b}\}$	$\varepsilon_i = 0$
	C	$\phi_i = 154.56°$	$\phi_i = 148°, \quad i \in \{31n \mid n \in \mathbb{N} \wedge 31n \leq N_\mathrm{b}\}$	$\varepsilon_i = 0$
	D	$\phi_i = 154.47°$	$\phi_i = 148°, \quad i \in \{30n \mid n \in \mathbb{N} \wedge 30n \leq N_\mathrm{b}\}$	$\varepsilon_i = U_0/2$
		initial bunch phase		initial energy deviation
	E	$\langle\phi_i\rangle = 154.47°$, $\langle\phi_i\rangle_\mathrm{rms} = 1°$		$\langle\varepsilon_i\rangle = U_0/2$, $\langle\varepsilon_i\rangle_\mathrm{rms} = 1\,\mathrm{MeV}$
	F	$\langle\phi_i\rangle = 154.47°$, $\langle\phi_i\rangle_\mathrm{rms} = 3°$		$\langle\varepsilon_i\rangle = U_0/2$, $\langle\varepsilon_i\rangle_\mathrm{rms} = 2\,\mathrm{MeV}$

Table 6.12: Starting conditions. In case A, the bunch with the number 20 is positioned at 148°, while all the other bunches are set at $\phi_i = 154.56°$. The initial energy deviation is zero. In case B, ε_i is again zero, but every 30th bunch starts at 148°; the remaining bunches begin at 154.56°. In cases E and F, the initial bunch phases and energy deviations are Gaussian distributions. The nominal average bunch phase is $154.56° = \arcsin(U_0/eF_\mathrm{b}V_\mathrm{rf})$ when the continuous radiation term is switched off. The nominal average bunch phase is otherwise $\arcsin(U_0(1 + U_0/E_\mathrm{b})/eF_\mathrm{b}V_\mathrm{rf}) = 154.47°$; furthermore the energy deviation of the synchronous particle is $U_0/2$ and not 0.

Instability Growth Rate and Mode Number

The instability growth rate prediction for the major HOM as given by Eq. (3.124) is compared with tracking results. The synchrotron tune is modified to account for the bunch form factor correction of the rf voltage and to compensate for the average beam-loading loss; nevertheless it should be stated that the effect is marginal. Since equidistant bunches are assumed in the derivation of Eq. (3.124), the number of bunches is raised to 1170 for the first three test runs (i.e. there is no gap) for the purpose of comparison.
In the first example, the beam current is set to $I_\mathrm{b} = 0.696\,\mathrm{A}$, six times the design current, and the continuous radiation term is turned off. The initial condition is as follows: one bunch (number 20) has a relatively large offset from the nominal average bunch phase (it is positioned at 148.0°), while the remaining bunches are set at the nominal average bunch angle $\phi_\mathrm{nab} = 154.56°$ (starting conditions A). None of the bunches has an energy deviation. The bunch with the offset is chosen to be number 20, allowing us to easily differentiate stability effects before and after the gap when tracking with 1130 bunches.
We determine in a first step the maximum deviations (positive and negative studied separately), measured in degrees, from a reference angle ϕ_ref over all bunches per turn:

$$\max_{\substack{k=1,\ldots,1170\\ \phi_k^n > \phi_\mathrm{ref}}} (\phi_k^n - \phi_\mathrm{ref}) \quad \text{and} \quad \max_{\substack{k=1,\ldots,1170\\ \phi_k^n < \phi_\mathrm{ref}}} |\phi_k^n - \phi_\mathrm{ref}|. \tag{6.19}$$

Then, in a second step, we divide the results by degrees and take the natural logarithm hereof (ϕ_k^n, k bunch, n turn). The reference angle is chosen to be the new average bunch angle, 154.44°, which includes the average steady-state beam loading due to the higher-order mode (the average beam loading is in principle nothing else than the zeroth-order term in Eq. (3.112), which does not effect the dynamics and does not enter into the derivation of the multibunch instability growth rate).
Figure 6.17 shows for the first 400 turns only the curve resulting from the negative deviation; the curve resulting from the positive deviation is included for the later turns. In accordance to Section 3.4, an "instability" should make itself apparent as

$$\max_k(\Delta\phi_k^n) = \max_k|\phi_k^n - \phi_\mathrm{ref}| \propto \exp\left((\tau_\mu^{-1} - \alpha_\varepsilon) n T_0\right); \tag{6.20}$$

hence the gradient of the two curves in Figure 6.17 should be approximately $\tau_\mu^{-1} - \alpha_\varepsilon$. The result of a least-squares fit between turns 600 and 1000 is 75.4 Hz for the positive deviation and 76.8 Hz for the negative deviation, giving an average of 76 Hz. According to Eq. (3.124), the strongest mode is the one with number 1094. It is $(37{\cdot}1170{+}1094{+}\nu_\mathrm{s})f_0 = 782.782\,\mathrm{MHz}$. The corresponding instability rate is approx. 144 Hz; deducting the damping rate (59 Hz) leaves 85 Hz. Figure 6.18 shows that the instability is due to a variety of modes centred around the strongest one, so that the over-all growth rate is in reasonable agreement with the tracking result.
In Figure 6.19 on page 107, the analytical instability rates for the strongest modes are compared to the results obtained by studying the Fourier transform amplitudes on different turns, i.e. by calculating

$$\frac{1}{T_0} \ln A_\mu^{n_i}, \quad i = 1, \ldots, 21,$$

beam parameters	
N_b	1170
I_b	0.696 A
σ_{q_b}	0
HOM parameters	
f_hom	782.78 MHz,
	$Q_\mathrm{L} = 1100$
starting conditions	
case	A
tracking parameters	
damping	yes
cont. synchrotron radiation	no

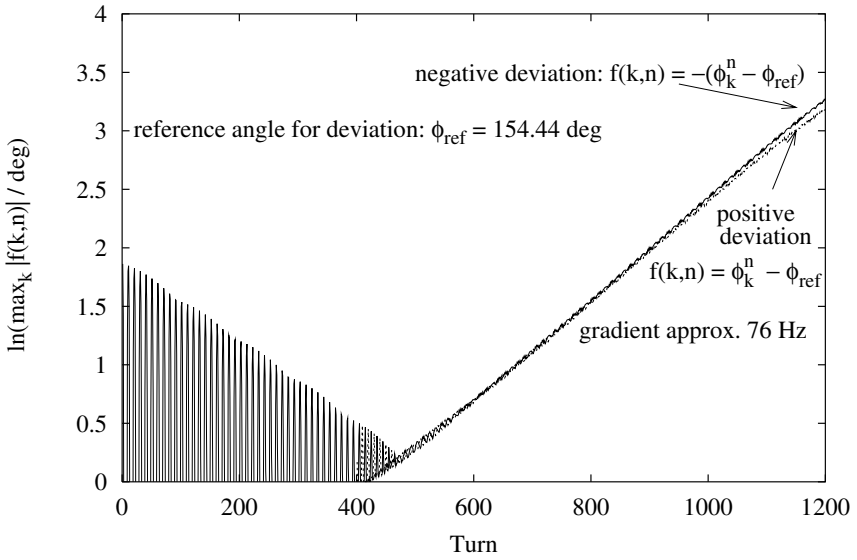

Figure 6.17: Tracking simulation for 1170 bunches at the beam current $I_\mathrm{b} = 0.696\,\mathrm{A}$. The initial condition is such that one bunch has a large offset. The logarithm of the maximum deviation in both directions from the reference angle over all bunches per turn is shown.

beam parameters	
N_b	1170
I_b	0.696 A
σ_{q_b}	0
HOM parameters	
f_hom	782.78 MHz,
	$Q_\mathrm{L} = 1100$
starting conditions	
case	A
tracking parameters	
damping	yes
cont. synchrotron radiation	no

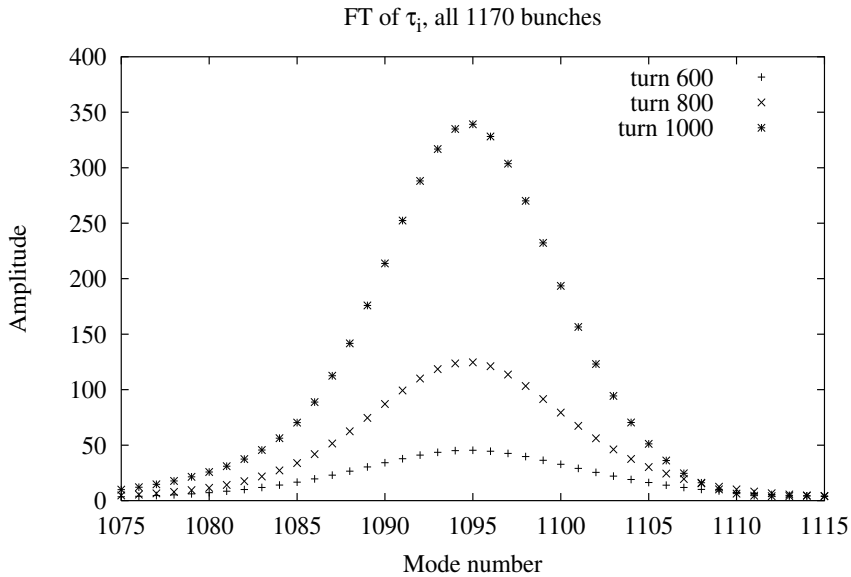

Figure 6.18: Fourier transform of the bunch positions τ_i, $i = 1, \ldots, N_\mathrm{b}$ on three turns for a tracking simulation with the starting conditions A.

where A_μ^n is the amplitude pertaining to the μth mode on the nth revolution and by applying a least-squares fit to obtain the gradient. The discrepancy between the results is certainly noticeable but not too large. The method must, however, be applied with care when looking at weaker modes.

beam parameters	
N_b	1170
I_b	0.696 A
σ_{q_b}	0
HOM parameters	
f_hom	782.78 MHz,
	$Q_\mathrm{L} = 1100$
starting conditions	
case	A
tracking parameters	
damping	yes
cont. synchrotron radiation	no

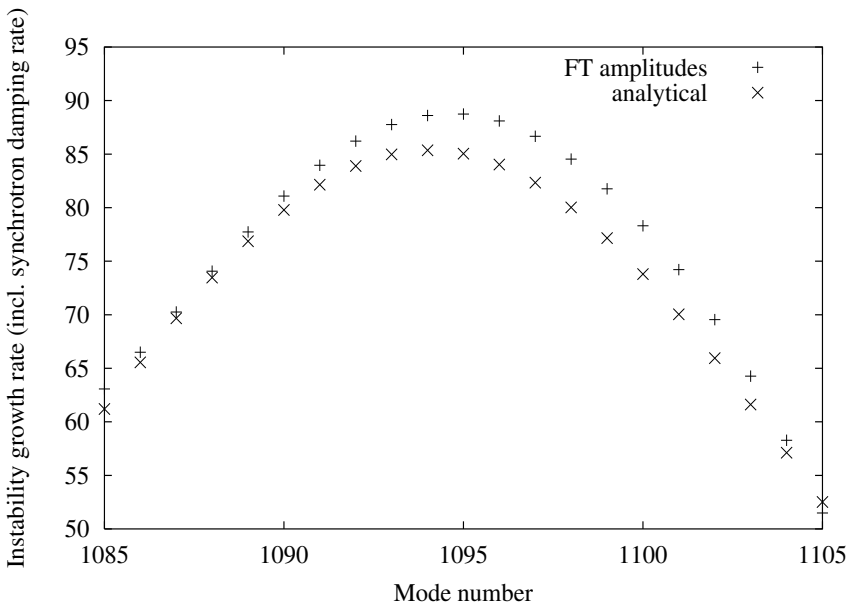

Figure 6.19: Comparison of the instability growth rate as estimated by the Fourier transform of the bunch positions τ_i, $i = 1, \ldots, N_\mathrm{b}$ on turns 600, 620, ... , 980, and 1000 with the analytical result of Eq. (3.124).

The oscillation over the first approximately 400 turns results from the damped synchrotron oscillation of the offset bunch 20 (proof of which is seen in Figure 6.20). When studying individual bunches, the approximate invariant amplitude of motion is used ([47, 62]; see Appendix F):

$$\frac{180^\circ}{\pi}\sqrt{(\phi_k^n - \phi_\mathrm{ref})^2 + \frac{2\pi h \alpha_\mathrm{c}}{E_\mathrm{b}}(\phi_k^n - \phi_\mathrm{ref})(\varepsilon_k^n - \varepsilon_\mathrm{ref}) + \frac{\alpha_\mathrm{c}^2 h^2}{\nu_\mathrm{s}^2 E_\mathrm{b}^2}(\varepsilon_k^n - \varepsilon_\mathrm{ref})^2}. \tag{6.21}$$

The term under the square root is in radians to the square. The numbers in Figure 6.20 denote the bunch number. As a reference curve, the maximum value of the positive and negative deviation, as calculated in Eq. (6.19), is added:

$$\max_k |\phi_k^n - \phi_\mathrm{ref}|.$$

The damped synchrotron oscillation of the offset bunch 20 is clearly visible. Furthermore, one can see how the "instability" propagates down the bunch train ("delayed" deviation). The instability growth rates of the individual bunches with respect to certain time periods can be larger than that given by Eq. (3.124) which presents the "steady-state". When approaching the maximum bunch deviation at that time, the individual instability rate converges towards that of the train. Distinct kinks are not to be seen.

beam parameters	
N_b	1170
I_b	0.696 A
σ_{q_b}	0
HOM parameters	
f_hom	782.78 MHz,
	$Q_\mathrm{L} = 1100$
starting conditions	
case	A
tracking parameters	
damping	yes
cont. synchrotron radiation	no

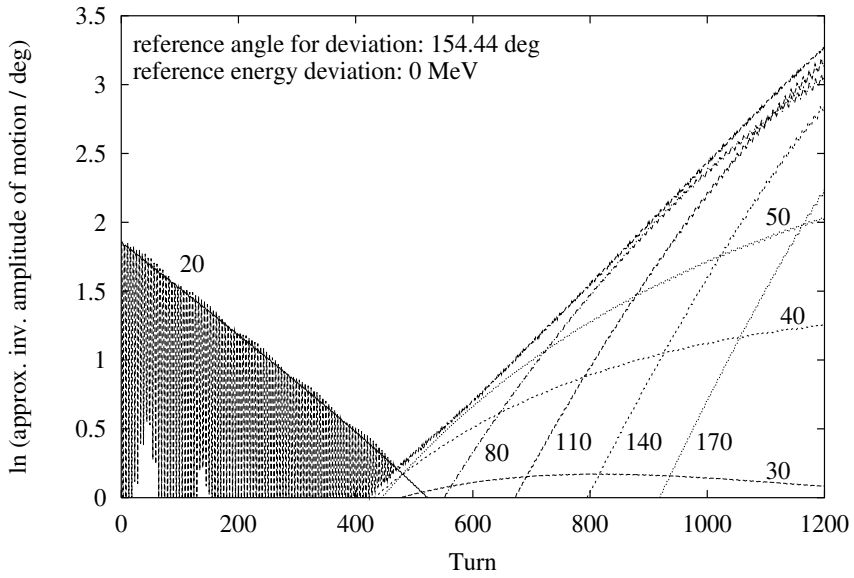

Figure 6.20: Tracking simulation for 1170 bunches at the beam current $I_\mathrm{b} = 0.696\,\mathrm{A}$ with the higher-order mode $f_\mathrm{hom} = 782.78\,\mathrm{MHz}$ and quality factor 1100 (same example as that of Figure 6.17). The logarithm of the approximate invariant amplitude for eight chosen bunches vs turn number is displayed.

beam parameters	
N_b	1170
I_b	0.464 A
σ_{q_b}	0
HOM parameters	
f_hom	782.78 MHz,
	$Q_\mathrm{L} = 1100$
starting conditions	
case	B
tracking parameters	
damping	yes
cont. synchrotron radiation	no

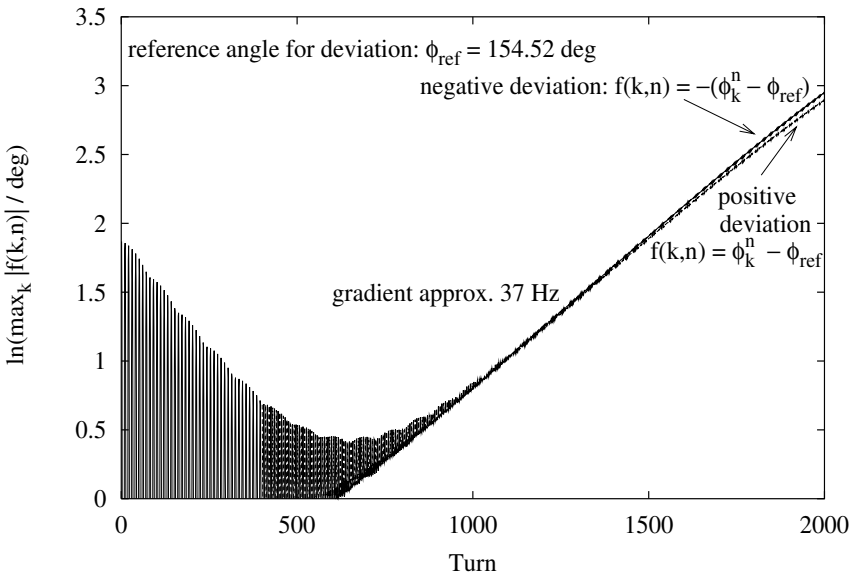

Figure 6.21: Tracking simulation for 1170 bunches at the beam current $I_\mathrm{b} = 0.464\,\mathrm{A}$. Every 30th bunch is initially offset. The logarithm of the maximum deviation in both directions from the reference angle over all bunches per turn is shown.

In a second example, the beam current is reduced to $I_\mathrm{b} = 0.464\,\mathrm{A}$ (four times the design beam current). The starting position of the bunch train is changed so that every 30th bunch is offset at 148° (starting conditions B). The slope of the maximum positive and negative deviations over all bunches, depicted in Figure 6.21, are 37 Hz and 38 Hz, respectively (evaluated for turns 1200 to 2000). The reference angle is, in accordance with the first example, the angle required at the cavities to compensate for the synchrotron radiation loss and the steady-state HOM beam-loading effect.

beam parameters	
N_b	1170
I_b	0.464 A
σ_{q_b}	0
HOM parameters	
f_hom	782.78 MHz,
	$Q_\mathrm{L} = 1100$
starting conditions	
case	B
tracking parameters	
damping	yes
cont. synchrotron radiation	no

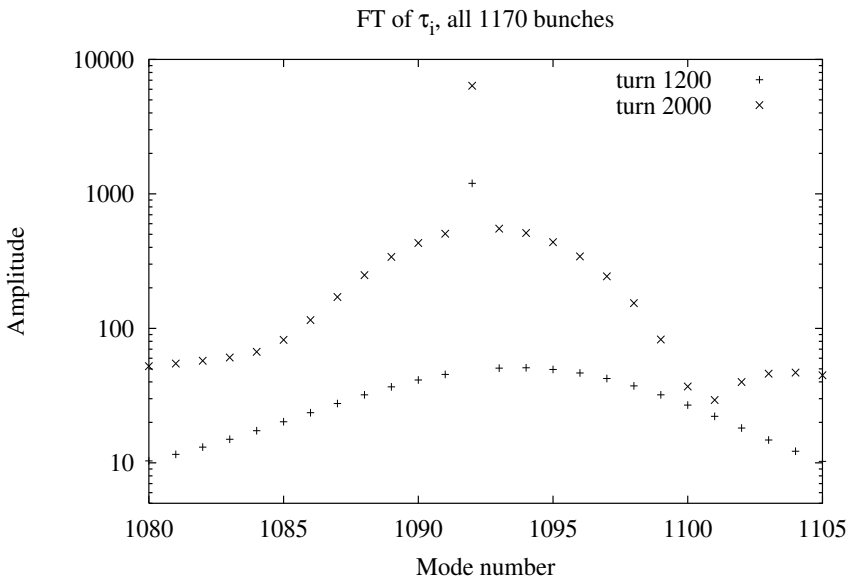

beam parameters	
N_b	1170
I_b	0.464 A
σ_{q_b}	0
HOM parameters	
f_hom	782.78 MHz,
	$Q_\mathrm{L} = 1100$
starting conditions	
case	C
tracking parameters	
damping	yes
cont. synchrotron radiation	no

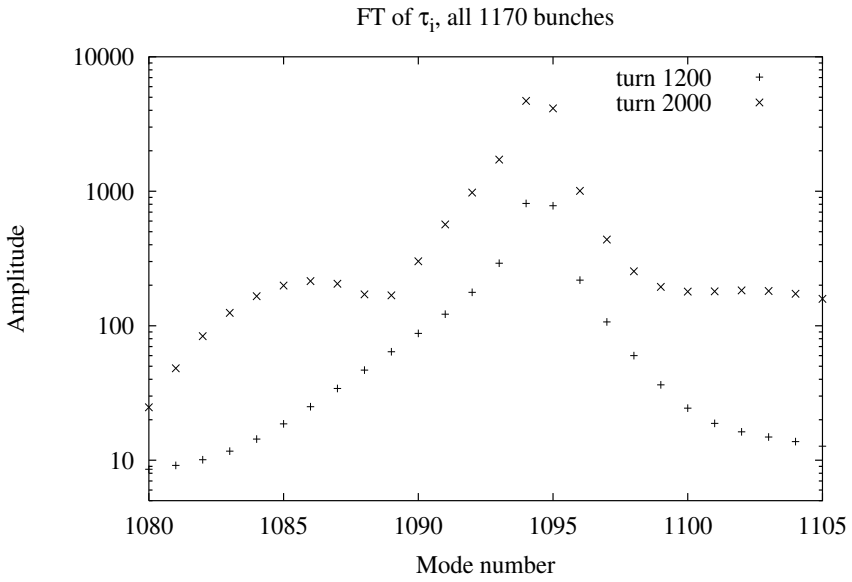

Figure 6.22: The Fourier transforms of the bunch positions τ_i, $i = 1, \ldots, N_\mathrm{b}$ on the 1200th and 2000th revolution. In the top plot, the simulation conditions are the same as in Figure 6.21.

Referring to Eq. (3.124), our analytical formula, we find that the growth rates of the strongest modes 1092 to 1096 lie between 36 Hz and 37 Hz.
The Fourier transform of the bunch positions on two turns, depicted in Figure 6.22, shows that the main mode underlying the instability is $\mu = 1092$. Comparison of the Fourier transform amplitudes leads to an instability growth rate of approximately 37 Hz. The values of the neighbouring modes are approximately 51 Hz.

If we change the starting conditions so that every 31st bunch is offset at 148°, we find that the modes $\mu = 1094$ and $\mu = 1095$ are the dominant ones (see lower plot in Figure 6.22). Studying the amplitudes of the Fourier transforms during turns 1200 to 2000, we obtain an instability growth rate of 39 Hz for $\mu = 1094$ and the rate 37 Hz for the mode $\mu = 1095$. Recalling Eq. (3.120)

$$\underline{\tau}_n \propto e^{i2\pi\mu n/N_\mathrm{b}},$$

we note that $31 \cdot (1 - 1094/1170) \approx 2.01$ and $31 \cdot (1 - 1095/1170) \approx 1.99$, and also that $30 \cdot (1 - 1092/1170) = 2$. We excite specifically a mode μ, if the spacing of the offset bunches Δn multiplied by μ and divided by the number of possible modes (maximum number of possible bunches N_b) is approximately an integer.

beam parameters	
N_b	1130
I_b	0.464 A
σ_{q_b}	0
HOM parameters	
f_hom	782.78 MHz,
	$Q_\mathrm{L} = 1100$
starting conditions	
case	D
tracking parameters	
damping	yes
cont. synchrotron radiation	yes

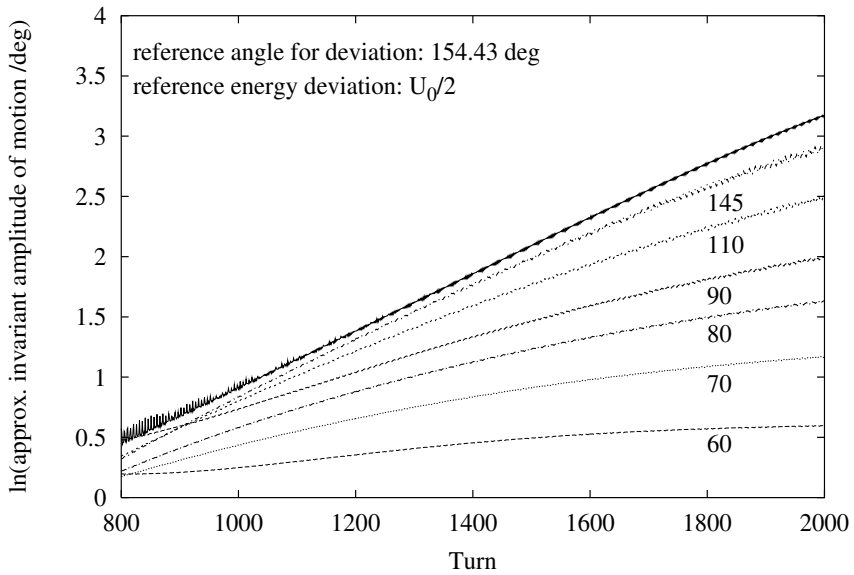

Figure 6.23: Tracking simulation for 1130 bunches at the beam current $I_\mathrm{b} = 0.464$ A with the higher-order mode $f_\mathrm{hom} = 782.78$ MHz and quality factor 1100. The logarithm of the approximate invariant amplitude for six chosen bunches vs turn number is displayed. The maximum value of the positive and negative deviation as calculated in Eq. (6.19) has been added (top curve).

The fourth example resembles the actual situation in the dog-bone ring with 1130 bunches. Furthermore, in this study, as in all of the following, the continuous synchrotron radiation term is switched on. The initial conditions are, in principle, the same as in the second

example but modified to account for the continuous radiation term (starting conditions D). For example, the energy deviation of the bunches is set to $U_0/2$, the energy deviation of the synchronous particle (see Eq. (6.15)). $U_0/2$ is at the same time the reference energy deviation when calculating the approximate invariant amplitude of motion. Examples are depicted in Figure 6.23. The reference angle is characterized by

$$\sin\phi_{\mathrm{ref}} = \left(U_0 + U_0^2/E_{\mathrm{b}} + U_{\text{HOM beam loading}}\right)/eF_{\mathrm{b}}V_{\mathrm{rf}}. \tag{6.22}$$

The second term on the right-hand side of the equation accounts for the energy deviation of the synchronous particle not being zero but $U_0/2$ (it is $(2T_0/T_\varepsilon)U_0/2 = U_0^2/E_{\mathrm{b}}$ with $T_\varepsilon = T_0E_{\mathrm{b}}/U_0$).

beam parameters	
N_{b}	1130
I_{b}	0.464 A
$\sigma_{q_{\mathrm{b}}}$	0
HOM parameters	
f_{hom}	782.78 MHz,
	$Q_{\mathrm{L}} = 1100$
starting conditions	
case	D
tracking parameters	
damping	yes
cont. synchrotron radiation	yes

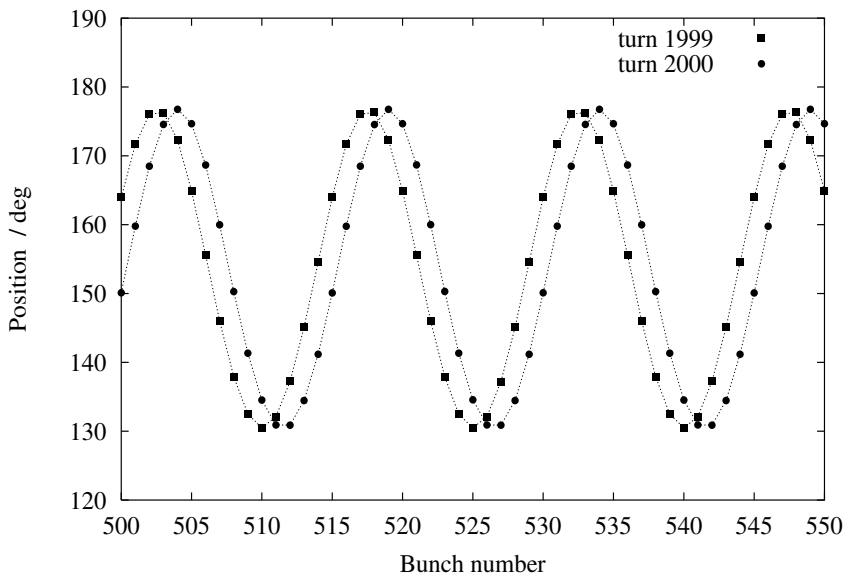

Figure 6.24: Bunch positions 500 to 550 on turns 1999 and 2000 for a tracking simulation with 1130 bunches at the beam current $I_{\mathrm{b}} = 0.464\,\mathrm{A}$.

The gradients of the maximum deviation in the positive and negative directions are 39 Hz and 40 Hz, respectively (evaluated for turns 1200 to 2000). We compare these results with the instability rate prediction of Eq. (3.124), which applies to the case when there is no gap (1170 bunches): 37 Hz (the damping rate has been deducted). We find that they agree.

The longitudinal positions of 51 bunches in the middle of the train are displayed in Figure 6.24 for two consecutive turns. The relative positions are visible as well as the change of position due to the synchrotron oscillation.

Two heuristic approaches to studying the mode numbers are depicted in Figure 6.25 and explained in the corresponding caption. The growth rate of the amplitude of the Fourier transform pertaining to strongest mode is 38 Hz in the first case (top picture) and 39 Hz in the second case (bottom plot).

beam parameters	
N_b	1130
I_b	0.464 A
σ_{q_b}	0
HOM parameters	
f_hom	782.78 MHz,
	$Q_\mathrm{L} = 1100$
starting conditions	
case	D
tracking parameters	
damping	yes
cont. synchrotron	
radiation	yes

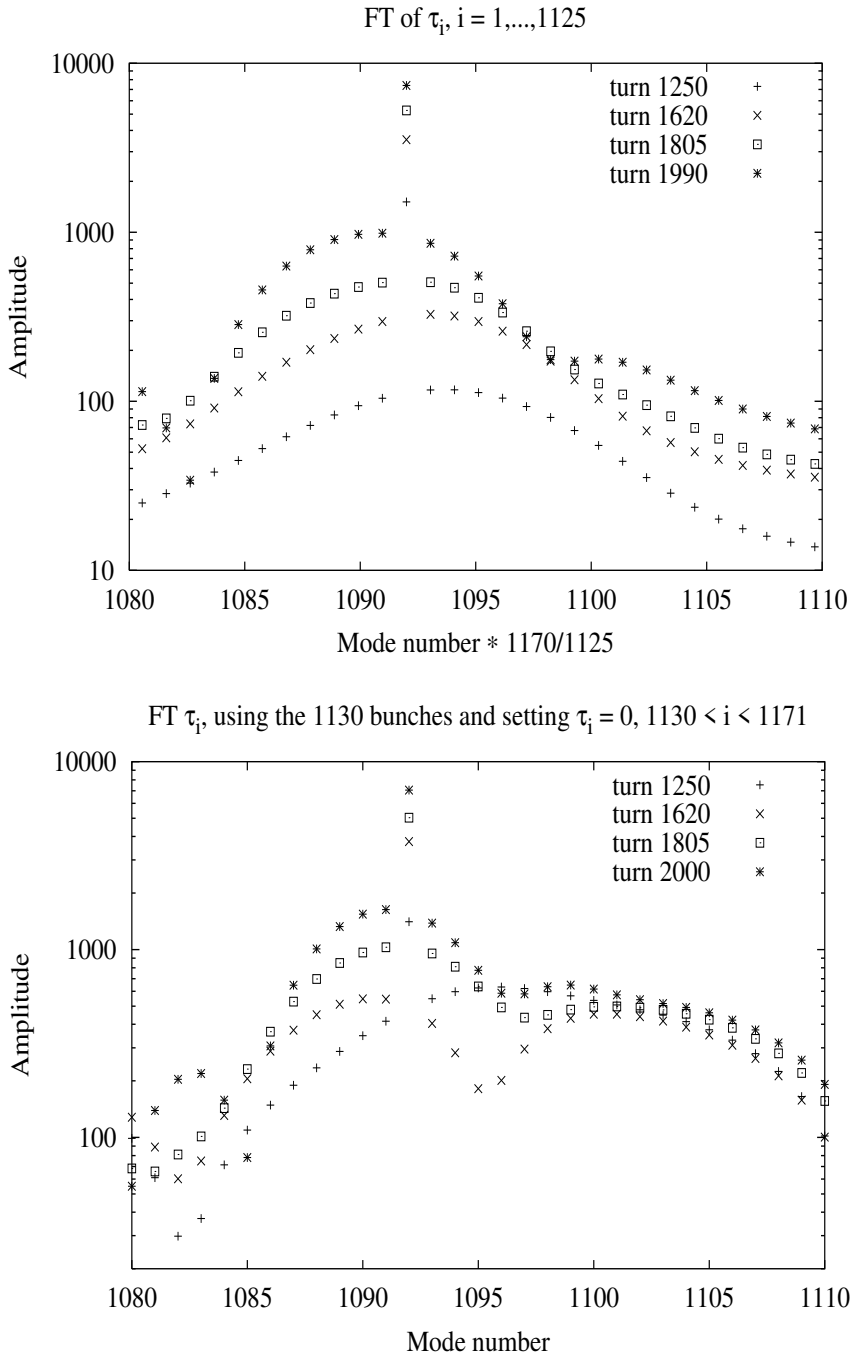

Figure 6.25: Two heuristic approaches to studying the relative positions of the bunches for a tracking simulation with 1130 bunches at the beam current $I_\mathrm{b} = 0.464\,\mathrm{A}$. For the top picture, Fourier transformations have been performed for the bunch positions τ_i, $i = 1, \ldots, 1125$ on four different turns and the mode numbers have been multiplied by 1170/1125. The bottom picture is obtained by applying a Fourier transformation to 1170 samples where the "missing" data of the non-existent bunches due to the gap are simply set to zero.

Design Beam Current, Various Loaded Quality Factors

The aim of the following simulations at the design beam current is to establish an upper limit for the quality factor of the major higher-order mode at which a feedback system would still be unnecessary. We also study fluctuations in the distribution of the bunch charges. A summary of the loaded quality factor settings used in the following simulations is presented in Table 6.13.

		$f_{\mathrm{hom}} = 782.783\,\mathrm{MHz}$:	$f_{\mathrm{hom}} = 775.391\,\mathrm{MHz}$:
case	Q1s	$Q_{\mathrm{L}} = 2200$	–
	Q2s	$Q_{\mathrm{L}} = 2500$	–
	Q3s	$Q_{\mathrm{L}} = 2750$	–
	Q4s	$Q_{\mathrm{L}} = 3000$	–
	Q1t	$Q_{\mathrm{L}} = 2200$	$Q_{\mathrm{L}} = 5000$
	Q2t	$Q_{\mathrm{L}} = 2500$	$Q_{\mathrm{L}} = 5500$
	Q3t	$Q_{\mathrm{L}} = 2750$	$Q_{\mathrm{L}} = 6000$
	Q4t	$Q_{\mathrm{L}} = 3000$	$Q_{\mathrm{L}} = 6000$

Table 6.13: Studied modes and loaded quality factors. "s" is an abbreviation that only a single (the strongest) higher-order mode is studied, "t" is an abbreviation for two modes.

Before we begin with our simulations, we insert the higher-order mode frequencies, loaded quality factors, and loss factors (Table 5.3, page 80) into Eq. (3.124) and subtract the synchrotron radiation damping rate. We realize that Eq. (3.124) applies to a bunch train without a gap, but we would like to get an estimation; in our previous simulation, the instability growth rate prediction proved to be accurate. For the cases Q1s to Q4s and mode number $\mu = 1094$, we obtain the following values: $-11\,\mathrm{Hz}$, $-4\,\mathrm{Hz}$, $1\,\mathrm{Hz}$, and $7\,\mathrm{Hz}$. For the second frequency, the largest growth rates (mode number $\mu = 675$) are $-10\,\mathrm{Hz}$, $-5\,\mathrm{Hz}$, and $0\,\mathrm{Hz}$.

We begin our studies with an initial bunch positioning identical to the previous fourth example (starting conditions D). We start with the quality factor setting Q1s, and then look at the other cases.

In our first study with setting Q1s, the bunch charges fluctuate. We assume a Gaussian distribution with a $\sigma_{q_{\mathrm{b}}}$ of 5 % centred about the nominal value. We perform, in total, 50 simulations, using a random generator each time to obtain the charge distribution, and we compare the average oscillation amplitude (difference between the largest and smallest bunch phase per turn) for turns 2401 to 2500 and during the last 100 turns. We find in the former case, on average, an amplitude of 0.07° and in the latter case, on average, an amplitude of 0.06° (the rms is smaller than 0.01°). Figures 6.26 and 6.27 (same simulation) show typical situations. The former shows a situation near the tail of the bunch after 3500 turns, where there is a small oscillation. The situation is similar to that in Figure 6.24. A comparison of the situation at the beginning and the end of the train is displayed in Figure 6.27. The impact of the gap is evident. The average damping rate between turns 2000 and 2500 is approximately 7 Hz. This value is established by studying the maximum deviations in the positive and negative directions from the reference angle 154.46°; this is

the angle required to compensate for the synchrotron radiation loss and the static HOM beam-loading effects. For the simulation where all the bunch charges are equal, we obtain the same results.

beam parameters	
N_b	1130
I_b	0.116 A
σ_{q_b}	5 %
HOM parameters	
f_hom	782.78 MHz,
	$Q_\mathrm{L} = 2200$
starting conditions	
case	D
tracking parameters	
damping	yes
cont. synchrotron radiation	yes

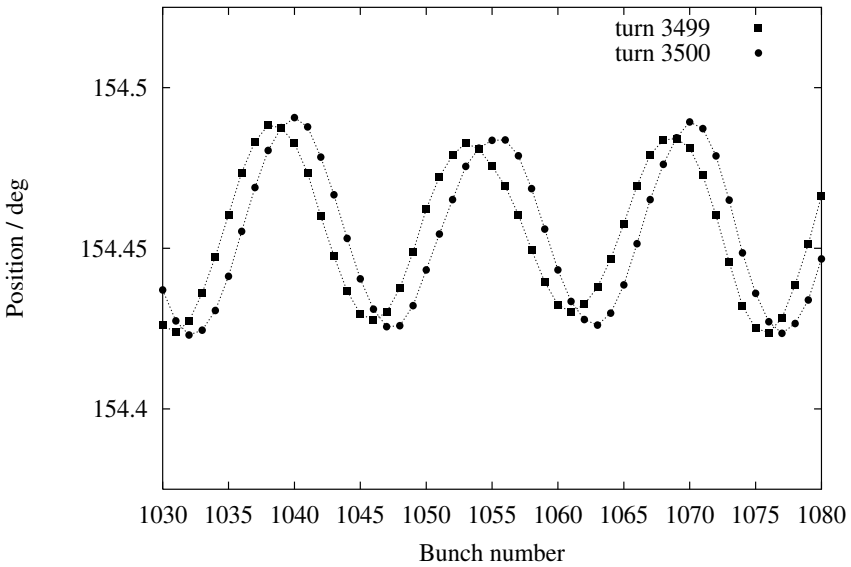

Figure 6.26: The longitudinal positions of 51 bunches near the end of the train are shown on two consecutive turns for a simulation with Q1s and starting conditions D. The bunches have a Gaussian charge distribution of $\sigma_{q_\mathrm{b}} = 5\,\%$ around the nominal bunch population.

beam parameters	
N_b	1130
I_b	0.116 A
σ_{q_b}	5 %
HOM parameters	
f_hom	782.78 MHz,
	$Q_\mathrm{L} = 2200$
starting conditions	
case	D
tracking parameters	
damping	yes
cont. synchrotron radiation	yes

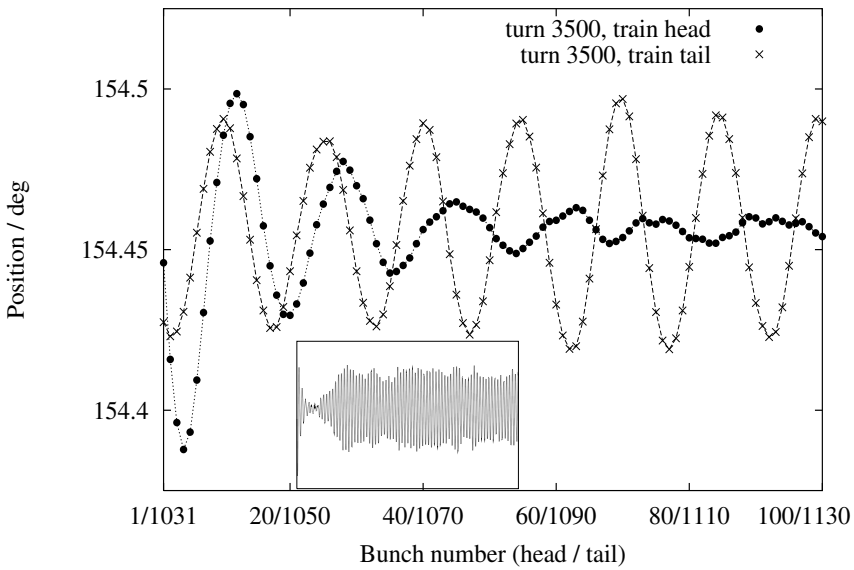

Figure 6.27: The longitudinal positions of the first and last 100 bunches are shown for turn 3500 using the same tracking simulation as in Figure 6.26. The inset depicts the oscillation amplitude over the whole bunch train.

beam parameters	
N_b	1130
I_b	0.116 A
σ_{q_b}	0 %
HOM parameters	
f_hom	782.78 MHz, $Q_\mathrm{L} = 2500$
f_hom	775.39 MHz, $Q_\mathrm{L} = 5500$
starting conditions	
case	D
tracking parameters	
damping	yes
cont. synchrotron radiation	yes

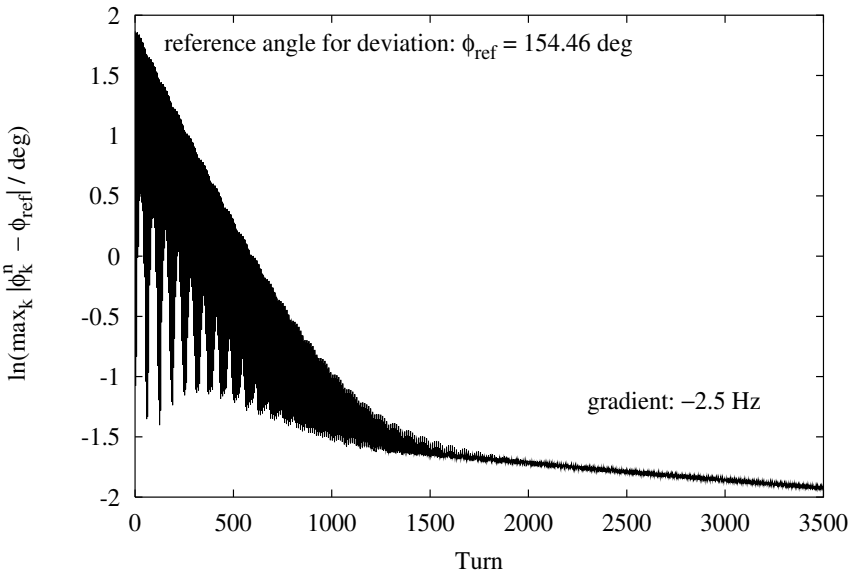

Figure 6.28: Results of a tracking simulation for the combination Q2t and D. The logarithm of the maximum deviation in both directions from the reference angle over all bunches per turn is shown. It is subject to a damping rate of approximately 2.5 Hz (turns 2500 – 3500).

beam parameters	
N_b	1130
I_b	0.116 A
σ_{q_b}	0 %
HOM parameters	
f_hom	782.78 MHz, $Q_\mathrm{L} = 2500$
f_hom	775.39 MHz, $Q_\mathrm{L} = 5500$
starting conditions	
case	D
tracking parameters	
damping	yes
cont. synchrotron radiation	yes

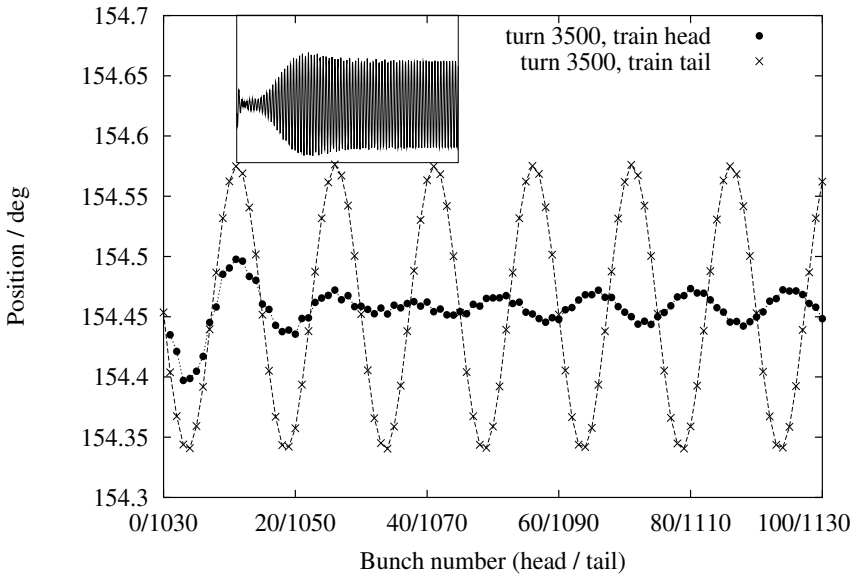

Figure 6.29: The longitudinal bunch positions at the beginning and end of the bunch train after 3500 revolutions are depicted for the same simulation as in Figure 6.28. A comparison with Figure 6.27 reveals a clearly visible – even if still small – increase of the oscillation amplitude at the tail. The average oscillation amplitude during the last 100 turns is approximately 0.14°.

beam parameters	
N_b	1130
I_b	0.116 A
σ_{q_b}	5 %
HOM parameters	
f_hom	782.78 MHz, $Q_\mathrm{L} = 3000$
f_hom	775.39 MHz, $Q_\mathrm{L} = 6000$
starting conditions	
case	D
tracking parameters	
damping	yes
cont. synchrotron radiation	yes

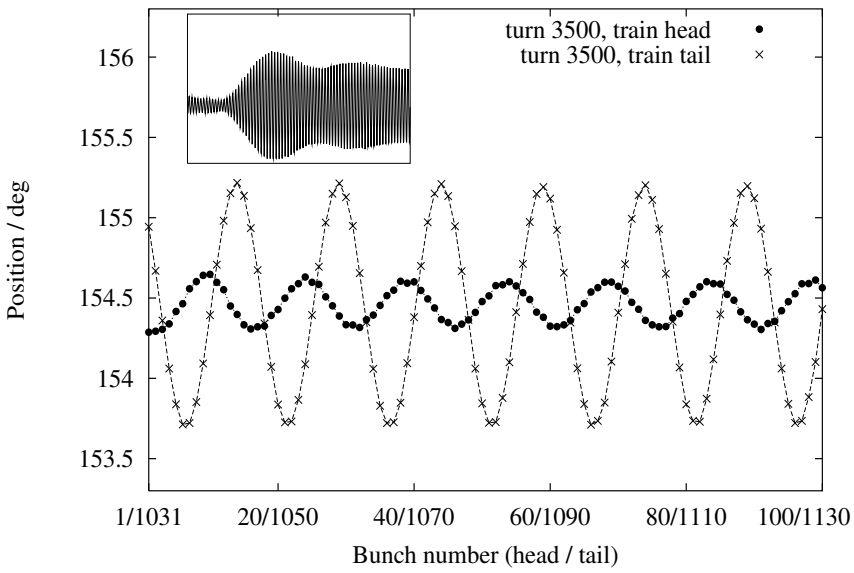

Figure 6.30: Result of a tracking simulation where every 30th bunch is originally offset by approx. 5.5°. The first and last 100 bunches are shown for turn 3500. The inset depicts the oscillation amplitude over the whole bunch train.

We also perform for each of the other loaded quality factor settings, 50 simulations with a Gaussian distribution of the bunch-charge values and one simulation where the bunch charges are all equal. We focus our studies again on the oscillation amplitudes during turns 2401 – 2500 and 3401 – 3500 and the maximum deviation of the bunches per turn from the reference angle $\phi_\mathrm{ref} = 154.46°$ during the last 1000 turns (2501 – 3500).
The results of the simulations without charge fluctuation are the same as the average results of the simulations with charge fluctuation. The relative rms-values are not larger than 5 %. The differences between the simulations with two higher-order modes and the corresponding ones with only $f_\mathrm{hom} = 782.783\,\mathrm{MHz}$ are negligible. For the simulations with the settings Q2s/Q2t, comparison of the maximum deviation over all bunches in both directions from the reference angle leads to a damping rate of approximately 2 Hz (an example is depicted in Figure 6.28). For the simulations with Q3s/Q3t and Q4s/Q4t, we find growth rates: approximately 2 Hz and 8 Hz, respectively. Consequently, the oscillation amplitudes grow; for example, the average oscillation amplitude grows by 0.4° during the last 1000 turns for the cases Q4s/Q4t. The longitudinal bunch positions at the beginning and end of the train on turn 3500, as well as the oscillation amplitude throughout the train are depicted for a typical simulation with charge fluctuation and settings Q4t in Figure 6.30. The oscillation at the head of the bunch train (after the gap) is relatively small, then grows and reaches a steady-state value after approximately a third of the train.
A summary of our results with respect to the average oscillation amplitude during turns 3401 to 3500 for the simulations without charge fluctuation are presented in Figures 6.31 and 6.32. There, we see quite clearly, that the oscillation amplitudes increase when using larger quality factors.

beam parameters	
N_b	1130
I_b	0.116 A
σ_{q_b}	0 %
tracking parameters	
damping	yes
cont. synchrotron radiation	yes

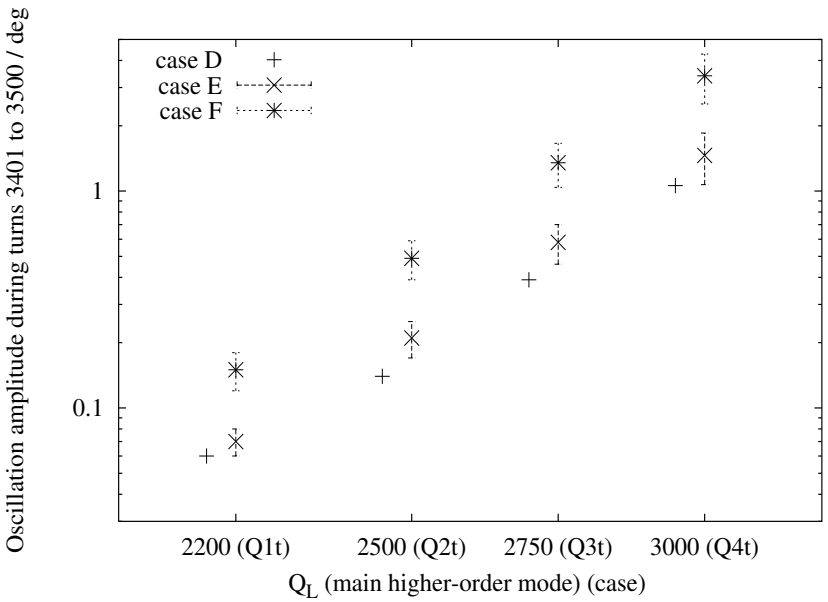

Figure 6.31: The average oscillation amplitude during turns 3401 to 3500 for simulations with the main higher-order mode using different loaded quality factors (Q1t, Q2t, Q3t, and Q4t). The crosses denoting the values for case D have been depicted with a slight offset in the horizontal direction to avoid possible overlap with the "x"s/error bars pertaining to case E.

beam parameters	
N_b	1130
I_b	0.116 A
σ_{q_b}	0 %
tracking parameters	
damping	yes
cont. synchrotron radiation	yes

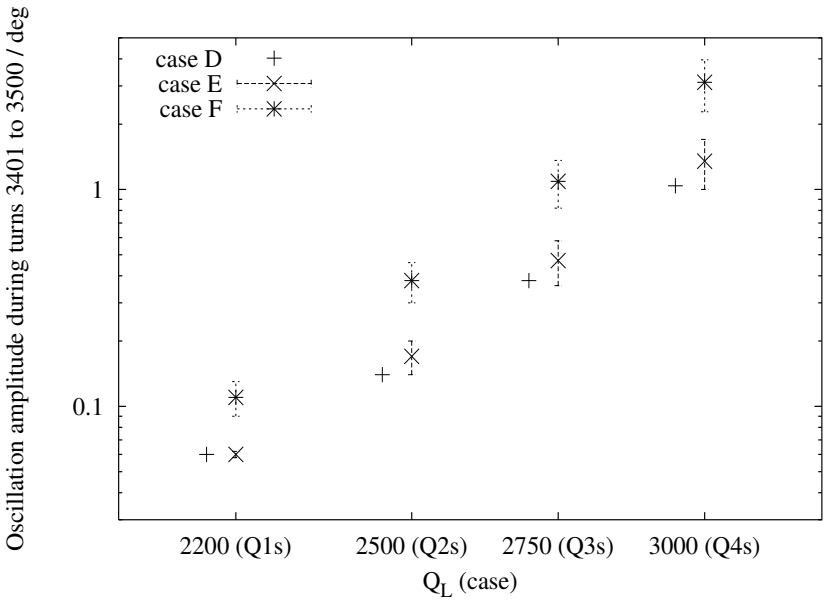

Figure 6.32: The average oscillation amplitude during turns 3401 to 3500 for simulations with the main higher-order mode using different loaded quality factors (Q1s, Q2s, Q3s, and Q4s).

In the preceding simulations, we could expect the major higher-order mode to be excited by our starting conditions D. Now, we would like to test different initial conditions.
We choose the starting-condition cases E and F, where the initial bunch positions and energy deviations are Gaussian distributions (Table 6.12, page 104). We study all the loaded quality factor settings listed in Table 6.13.
For every setting, we perform four sets of 50 simulations: two sets for each of the two starting conditions. The first set is with charge fluctuation, the second without. In the first set we use a different charge distribution in every simulation, as well.
Our first result is that the differences between the results with and without charge fluctuation with respect to the average oscillation amplitude are small (relative to the amplitude). This is depicted in Figure 6.33 for the starting conditions F. The size of the error bars reflects the standard deviations. At the same time, we see that the average results of the simulations using both modes (Q1t – Q4t) are slightly larger than the corresponding simulations using only the main higher-order mode (Q1s – Q4s). This, nevertheless, confirms that the oscillation amplitudes (and growth rates) depend, on average, primarily on the loaded quality factor of the major higher-order mode.

beam parameters	
N_b	1130
I_b	0.116 A
σ_{q_b}	0 %, 5 %
starting conditions	
case	F
tracking parameters	
damping	yes
cont. synchrotron radiation	yes

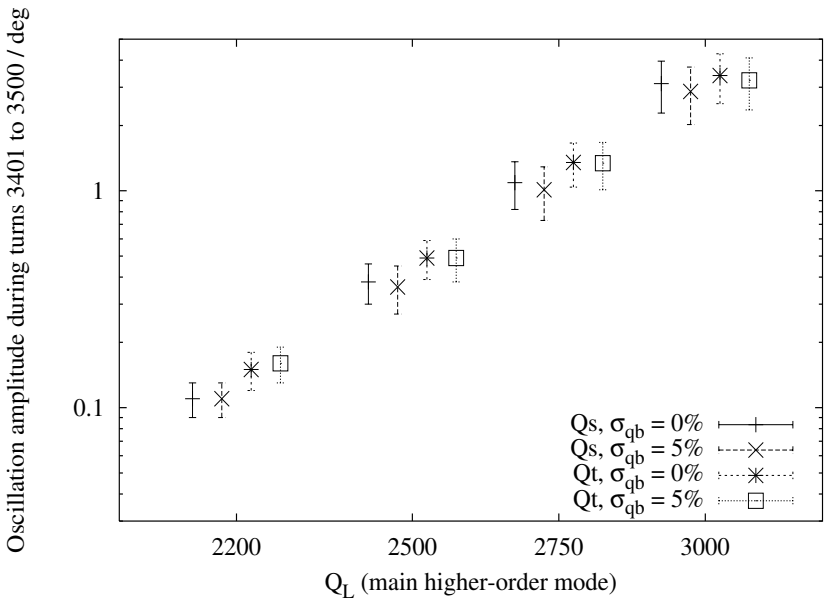

Figure 6.33: The average oscillation amplitude during turns 3401 to 3500 for simulations with the starting conditions F. Qs refers to the loaded quality factor settings Q1s, Q2s, Q3s, and Q4t, and Qt refers to the loaded quality factor settings with both modes. The results have been depicted with offsets in the horizontal direction to avoid overlapping.

A summary of the average oscillation amplitude during turns 3401 to 3500 when using equal bunch charges and the starting conditions E and F is presented in Figures 6.31 and 6.32. The initial condition F delivers, on average, larger oscillation amplitudes than those with the initial condition E, which are again larger than those with condition D. As seen by the error bars, which reflect the standard deviations, there is a noticeable variation between the individual simulations. For example, for the combination Q3t

beam parameters	
N_b	1130
I_b	0.116 A
σ_{q_b}	0 %
HOM parameters	
f_hom	782.78 MHz, $Q_\mathrm{L} = 2750$
f_hom	775.39 MHz, $Q_\mathrm{L} = 6000$
starting conditions	
case	F
tracking parameters	
damping	yes
cont. synchrotron radiation	yes

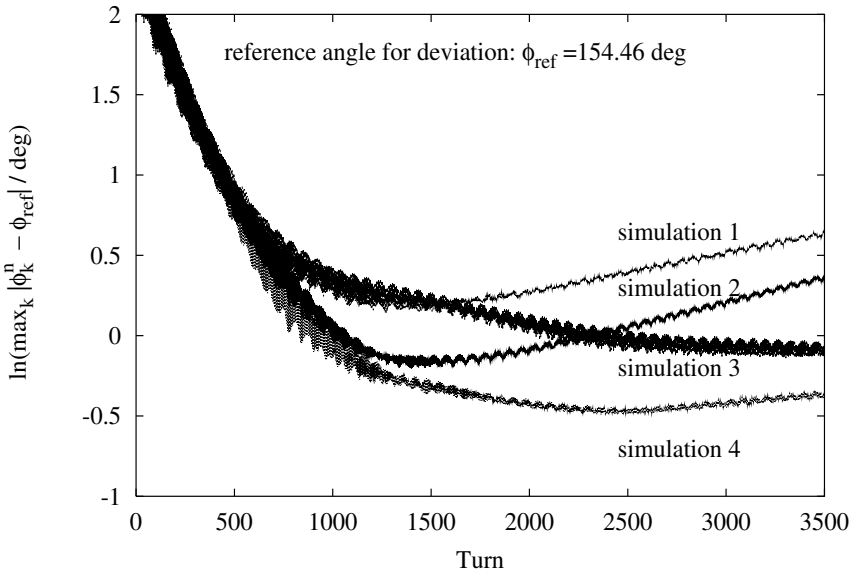

Figure 6.34: The logarithm of the maximum deviation in both directions from the reference angle over all bunches per turn is shown for four simulations. The average oscillation amplitude of simulation number 1 during the last 100 turns is 1.85°, that of simulation number four 0.68°. The growth rate (turns 2500 – 3500) of the second simulation is 5.5 Hz.

beam parameters	
N_b	1130
I_b	0.116 A
σ_{q_b}	0 %
HOM parameters	
f_hom	782.78 MHz, $Q_\mathrm{L} = 2750$
f_hom	775.39 MHz, $Q_\mathrm{L} = 6000$
starting conditions	
case	F
tracking parameters	
damping	yes
cont. synchrotron radiation	yes

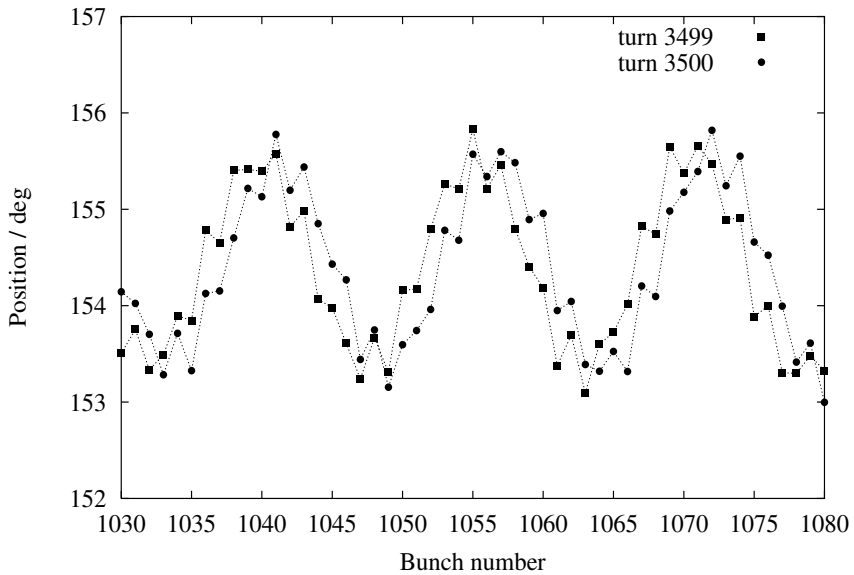

Figure 6.35: The longitudinal positions of 51 bunches near the end of the train are shown on two consecutive turns for a simulation with quality factor settings Q3t and starting conditions F.

and F without charge fluctuation, we obtain, on average, an amplitude of 1.34° with the rms 0.33° during turns 3401 – 3500. The average growth rate during the last 1000 turns varies between −1.5 Hz and 5.5 Hz. We show four examples in Figure 6.34. In total, three of the 50 simulations are characterized by negative growth rates; if, however, we track 5000 turns, we see that all three growth rates become positive after approximately 4500 turns. The longitudinal positions of some bunches near the train tail are depicted for a further example in Figure 6.35. In Figure 6.36, we show for settings Q4t (without charge fluctuation) three simulations based on different starting-condition cases.

beam parameters	
N_b	1130
I_b	0.116 A
σ_{q_b}	0 %
HOM parameters	
f_hom	782.78 MHz, $Q_\mathrm{L} = 3000$
f_hom	775.39 MHz, $Q_\mathrm{L} = 6000$
starting conditions	
case	D, E, F
tracking parameters	
damping	yes
cont. synchrotron radiation	yes

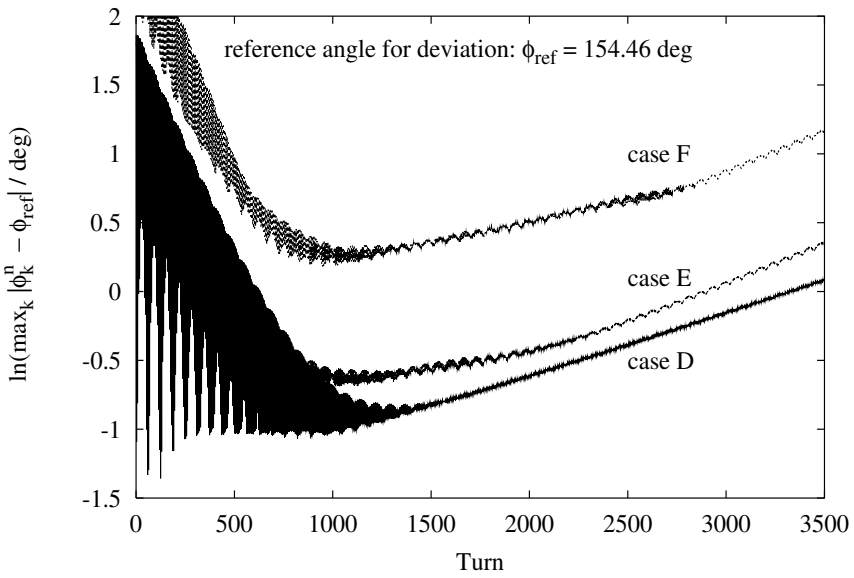

Figure 6.36: The logarithm of the maximum deviation in both directions from the reference angle over all bunches per turn is shown for the initial condition D, as well as an example for the conditions E and F. The average oscillation amplitudes of turns 3401 to 3500 are 1.1° (case D), 1.4° (case E), and 3.1° (case F).

Instead of studying the oscillation amplitude with respect to the longitudinal position, we can study the oscillation amplitude of the energy deviation. Figure 6.37 poses, for example, an alternative to Figure 6.31. If we multiply the energy-deviation amplitudes by

$$\frac{180^\circ}{\pi} \cdot \frac{2\pi h \alpha_\mathrm{c}}{E_\mathrm{b}}, \tag{6.23}$$

we obtain the corresponding "longitudinal-position" amplitudes in degrees, so that in fact, it is sufficient to study one of the oscillation amplitudes. We encountered the above factor in Eq. (6.21) (page 107) when studying the approximate invariant amplitude of motion. The factor is approximately 1.5 for the dog-bone damping ring parameters.

Before coming to a conclusion, we would like to check the extent to which our results depend on the explicit HOM frequencies. We use a random generator to calculate a Gaussian

beam parameters	
N_b	1130
I_b	0.116 A
σ_{q_b}	0 %
tracking parameters	
damping	yes
cont. synchrotron radiation	yes

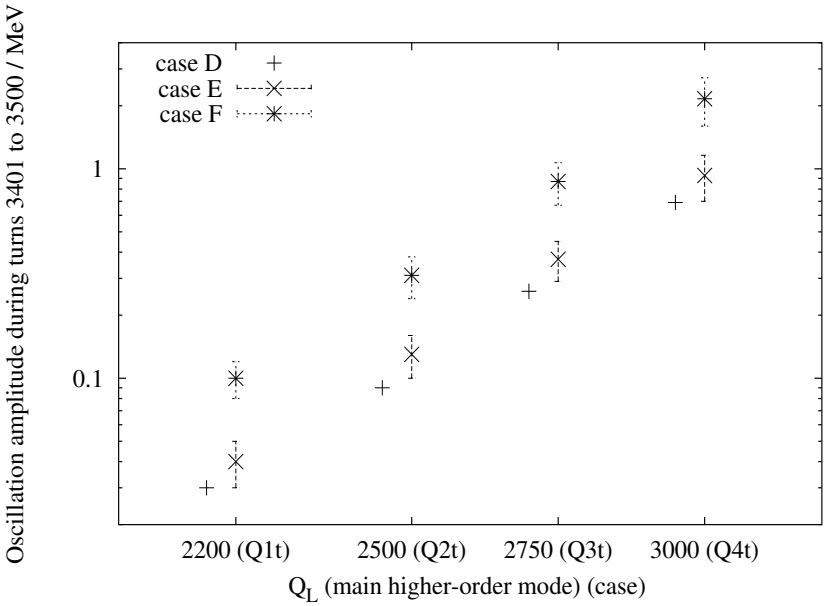

Figure 6.37: The average oscillation amplitude with respect to the energy deviation during turns 3401 to 3500 for simulations with the main higher-order mode using different loaded quality factors (Q1t, Q2t, Q3t, and Q4t). The crosses denoting the values for case D have been depicted with a slight offset in the horizontal direction to avoid possible overlap with the "x"s/error bars pertaining to case E.

distribution of 50 frequencies centred around 782.0 MHz with an rms of 0.5 MHz (the maximum range allowed is ± 1.5 MHz) and another 50 frequencies centred around 775.0 MHz, also with an rms of 0.5 MHz. Then we repeat a certain test with these frequencies (the starting conditions are identical in the 50 simulations).
We begin with the loaded quality factors as in case Q1t, and we choose the starting condition E without charge fluctuation, then F. Our results match those obtained when using the "correct" frequencies 782.78 MHz and 775.39 MHz within the limits of 0.01°; no signs of a growing amplitude are detected anywhere.
In a third and fourth test, we choose the loaded quality factors of case Q4t, and the starting conditions E and F. In case E, we find an average growth rate of 8.6 Hz (rms: 1.5 Hz) for turns 2500 to 3500 and an average oscillation amplitude of 1.5° (rms: 0.4°), which fits in well with our results above. In case F, we find approximately the same average growth rate; the average oscillation amplitude is 3.5° (rms 0.9°). We conclude that the explicit frequencies within the allowed range are not so important. The oscillation modes lie approximately 17 kHz apart and the frequency bandwidth of the two higher-order modes are larger than 60 kHz in the tests, so that we always manage to "excite" some oscillation mode.

We have studied on the preceding pages the worst case, which is that the higher-order mode frequencies in all eight cavities are identical. Summarizing, one can conclude that a loaded quality factor of the main higher-order mode not larger than $Q_\mathrm{L} = 2200$ is

desirable. We found in our studies for this case that the typical damping rate is on the order of 8 Hz. For our various starting conditions, the maximum amplitudes after the storage time in the damping ring did not exceed 0.2° or 0.2 MeV. These values are much smaller than the rms-values of the bunch length in phase, approximately 5° or the energy spread within a bunch 3 MeV. For loaded quality factors of the main higher-order mode of $Q_{\mathrm{L}} = 2750$ or more, we found positive growth rates and saw how the oscillation amplitudes could grow beyond 2 MeV or 2°.

We take a short look now at the possibility of variable frequencies in the cavities. With the help of a random generator, we calculate for each simulation sixteen frequencies, eight distributed around 782.78 MHz and eight around 775.39 MHz. Our random generator settings are a Gaussian distribution with a standard deviation of 100 kHz. The loaded quality factor settings which we study are those of Q4t; the bandwidth of the main higher-order mode is approximately 130 kHz.
We perform 200 simulations with the starting conditions F (no charge fluctuation); in every simulation, a different initial distribution of the bunches is used. The vast majority of the simulations show no signs of an instability. Those that do (positive growth rate during the last 1000 turns), we investigate in more detail. We find that the distributions of the "main higher-order mode" frequencies have, taken by themselves, a standard deviation of approximately 55 kHz or less. We have eleven simulations where the standard deviations lie between 40 kHz and 50 kHz. The oscillation amplitudes during the last 100 turns lie between 0.4° and 1.5°, and the growth rates lie between 0.4 Hz and 3 Hz. In our simulations, we also have one where the standard deviation of the "main higher-order mode" frequencies is 30 kHz. In this particular case, the instability growth rate is 6 Hz and the oscillation amplitude is 2°.

Simulations with $\alpha_{\mathrm{c}} = 9.5 \times 10^{-5}$

The instability growth rates are smaller for the same loaded quality factor settings when the momentum compaction factor is reduced. The change of the synchrotron tune has only a marginal impact on the impedance values (for the plausible quality factors and studied frequency range – the frequency bandwidth varied between 7 and $20\,f_0$ for the main higher-order mode) but the multiplier in Eq. (3.124) scales as $\sqrt{\alpha_{\mathrm{c}}}$; hence, the analytical instability growth rates for $\alpha_{\mathrm{c}} = 3.4 \times 10^{-4}$ are about 1.9 times larger than those for $\alpha_{\mathrm{c}} = 9.5 \times 10^{-5}$ (which corresponds to an rms bunch length of 5 mm).
For example, Eq. (3.124) predicts an instability growth rate of approx. 51 Hz ($\mu = 1094$) for the strongest higher-order mode with a quality factor $Q_{\mathrm{L}} = 4400$. This means that the strongest modes should see an effective damping rate in the range of 7 Hz. A simulation with 1130 bunches, the starting conditions D, and no charge fluctuation confirms this effect. The gradient of the maximum deviation of the bunches from the appropriate reference angle is −9 Hz (established by a least-squares fit for turns 1000 to 2000). Furthermore, a comparison of the Fourier transform amplitudes (using 1125 bunches) between revolutions 1000 and 2000 shows that the decline of the largest amplitude on turn 2000 corresponds to an effective damping rate of 14 Hz.

6.2.2 Simulations including the Fundamental Mode

The aim of the following studies is to investigate the effects of the beam loading in the accelerating mode and the consequent detuning. Characteristic of the presented simulations is that they all use the standard algorithm (the continuous synchrotron radiation term is switched on) and that the bunch-length correction factors are applied as indicated in Section 4.2. The beam current is set to the design current $I_\mathrm{b} = 0.116\,\mathrm{A}$. Only in our last simulations with $\alpha_\mathrm{c} = 3.4 \times 10^{-4}$ do we include the two higher-order modes studied in the previous section.

Nearby-Mode Studies

The main point of interest of the first two simulations is to check the instability growth rate prediction due to the effect of the unequal impedances of the upper and lower synchrotron sidebands of the nearby mode.
Keeping matters simple, it is assumed that analogously to the HOM studies the bunches enter the ring with ΔT_b, i.e. the ring is filled within the first turn, and that the transient beam-loading effects could be held to a minimum. This is done by choosing the initial cavity voltage $\underline{V}_\mathrm{init}$ to be $V_\mathrm{rf} e^{-i\pi/2}$ and setting the injection time t_inj to nil. The precise starting conditions for the bunches are an energy deviation $\varepsilon_i = U_0/2$ (the steady-state energy deviation) and a phase $\phi_i = \arcsin(U_0/(eV_\mathrm{rf})) = 154.66°$. The coupling parameter is set to $\beta_\mathrm{c} = 1.1\beta_{\mathrm{c}0}$ (see Eq. (3.90), page 38).

beam parameters	
N_b	1170
I_b	0.116 A
σ_{q_b}	0
starting conditions	
ϕ_i	154.66°
ε_i	$U_0/2$
tracking parameters	
$\beta_\mathrm{c}/\beta_{\mathrm{c}0}$	1.1
filling	1st turn
t_inj	0
$\underline{V}_\mathrm{init}$	$V_\mathrm{rf} e^{-i\pi/2}$
damping	yes
cont. synchrotron radiation	yes

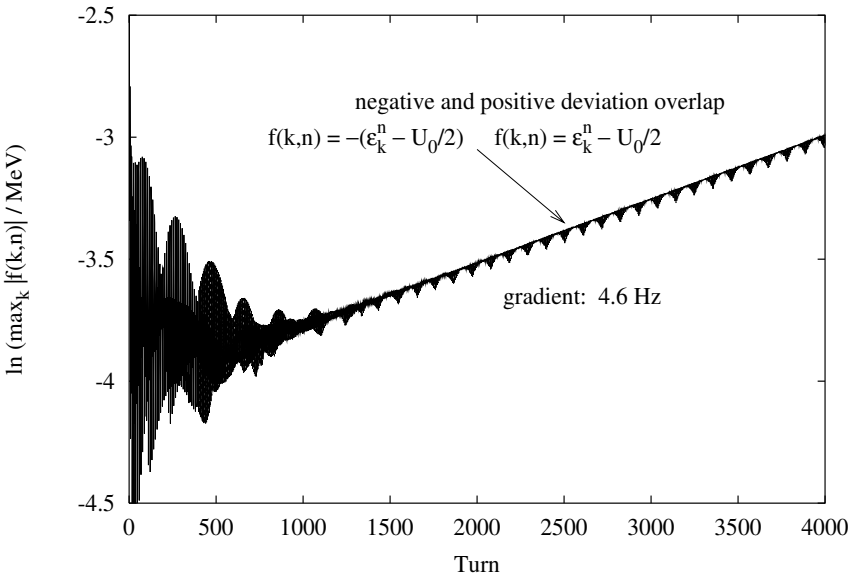

Figure 6.38: Tracking simulation for 1170 bunches at the design beam current with the coupling factor $\beta_\mathrm{c} = 1.1\beta_{\mathrm{c}0}$. The logarithm of the maximum absolute relative energy deviations in both directions over all bunches per turn is shown. The transient beam-loading effects are minimized in the simulation.

1170 bunches are used in the first study, corresponding to a beam without a gap, which is the assumption in the derivation of Eq. (3.124), the instability growth rate formula.

As an alternative to studying the deviations of the bunch positions from a reference angle, we choose to study the relative energy deviations $\varepsilon_k^n - U_0/2$ (see Figure 6.38). $U_0/2$ is the steady-state energy deviation (the energy deviation of the synchronous particle). The gradient (4.6 Hz) is in agreement with the value obtained by Eq. (3.124) after deducting the damping rate (3.6 Hz). The corresponding oscillation of the bunch positions and mode numbers can be seen in Figure 6.39. A comparison of the Fourier transform amplitudes pertaining to the nearby mode between turns 2000 and 4000 delivers a growth rate of 4.7 Hz.

beam parameters	
N_b	1170
I_b	0.116 A
σ_{q_b}	0
starting conditions	
ϕ_i	154.66°
ε_i	$U_0/2$
tracking parameters	
$\beta_\mathrm{c}/\beta_\mathrm{c0}$	1.1
filling	1st turn
t_inj	0
$\underline{V}_\mathrm{init}$	$V_\mathrm{rf}e^{-i\pi/2}$
damping	yes
cont. synchrotron radiation	yes

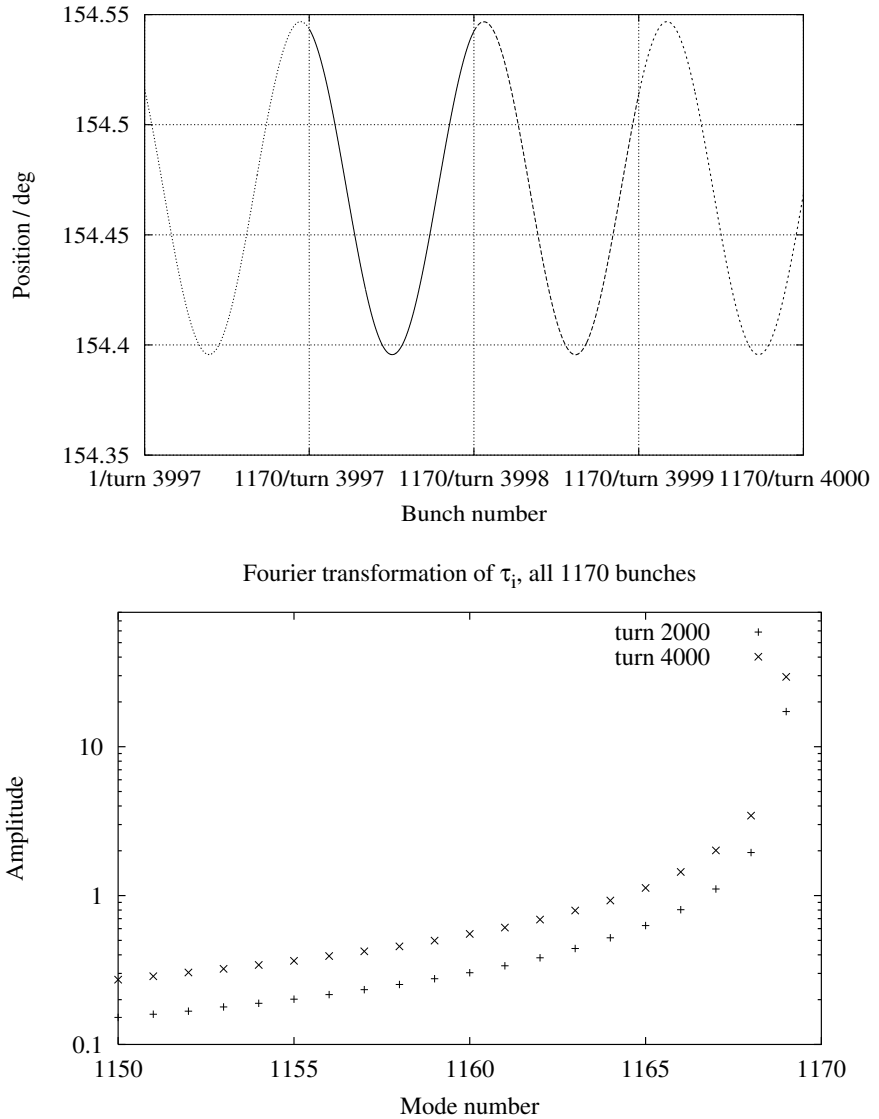

Figure 6.39: Tracking simulation for 1170 bunches with the coupling factor $\beta_\mathrm{c} = 1.1\beta_\mathrm{c0}$ where the initial beam-loading effects are minimized. After 4000 turns the oscillation amplitude is smaller than 0.1° (top plot). The bottom picture shows the Fourier transform of the bunch positions on turns 2000 and 4000. The strongest mode is $\mu = 1169$, the nearby mode. The instability seen in Figure 6.38 results from this mode.

beam parameters	
N_b	1130
I_b	0.116 A
σ_{q_b}	0
starting conditions	
ϕ_i	154.66°
ε_i	$U_0/2$
tracking parameters	
$\beta_\mathrm{c}/\beta_{\mathrm{c}0}$	1.1 & 1.2
filling	1st turn
t_inj	0
$\underline{V}_\mathrm{init}$	$V_\mathrm{rf}e^{-i\pi/2}$
damping	yes
cont. synchrotron radiation	yes

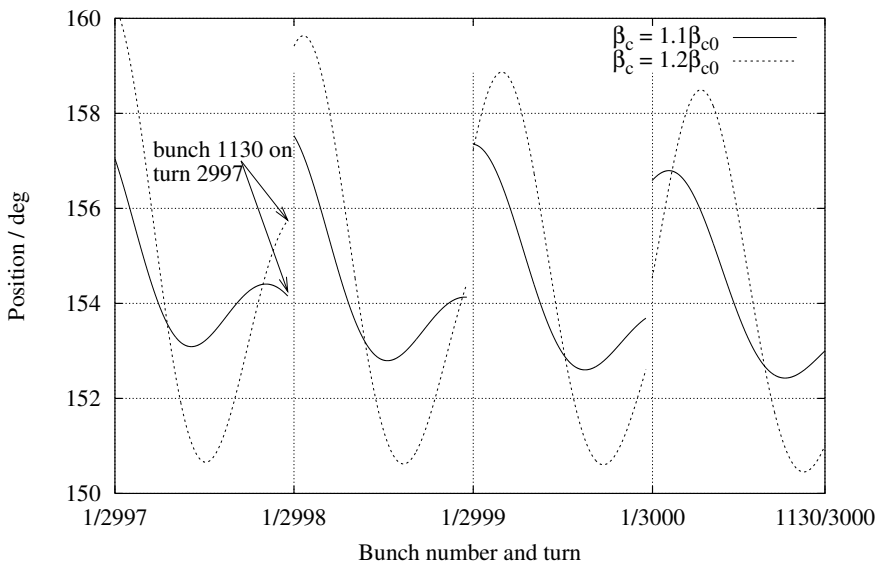

Figure 6.40: Comparison of the effect of the coupling factors $\beta_\mathrm{c} = 1.1\beta_{\mathrm{c}0}$ and $\beta_\mathrm{c} = 1.2\beta_{\mathrm{c}0}$ with respect to the nearby mode. The oscillation amplitude of the latter is distinctly larger. Due to the beam gap (simulations with 1130 bunches) there is a phase shift between the bunch tail and head.

beam parameters	
N_b	1130
I_b	0.116 A
σ_{q_b}	0
starting conditions	
ϕ_i	154.66°
ε_i	$U_0/2$
tracking parameters	
$\beta_\mathrm{c}/\beta_{\mathrm{c}0}$	1.1
filling	1st turn
t_inj	0
$\underline{V}_\mathrm{init}$	$V_\mathrm{rf}e^{-i\pi/2}$
damping	yes
cont. synchrotron radiation	yes

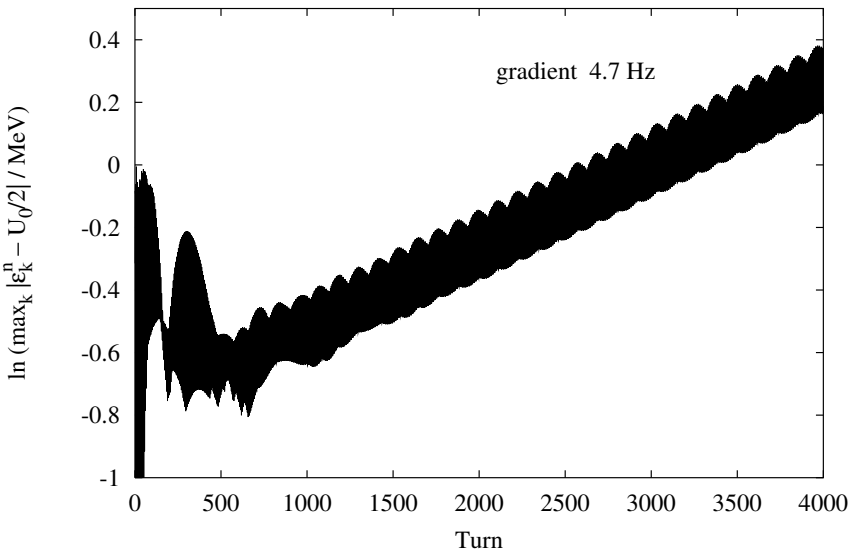

Figure 6.41: Tracking simulation for 1130 bunches at the design beam current and with the coupling factor $\beta_\mathrm{c} = 1.1\beta_{\mathrm{c}0}$ where the initial beam-loading effects are held to a minimum. The logarithm of the maximum absolute relative energy deviation over all bunches per turn is shown: $\ln(\max_k|\varepsilon_k^n - U_0/2|/\mathrm{MeV})$.

In the second simulation, the number of bunches is reduced to 1130 as proposed in the CDR [1]. The steady-state beam-loading voltages before and after the gap differ; hence the bunches adjust themselves to pick up a constant accelerating voltage. The phase shift between the train tail and head is clearly visible in Figure 6.40. The instability growth rate is established by studying the relative energy deviations of the bunches (Figure 6.41). The gradients of the least-squares fit for the positive and negative deviations are 4.7 Hz (turns 2000 to 4000). Increasing the coupling factor to $1.2\beta_{c0}$ leads to the gradients 10.2 Hz (Eq. (3.124) delivers 9.0 Hz). A plot showing the Fourier transform of the longitudinal positions of the first 1024 bunches in the train on turns 2000 and 4000 is presented in Figure 6.42.

beam parameters	
N_b	1130
I_b	0.116 A
σ_{q_b}	0
starting conditions	
ϕ_i	154.66°
ε_i	$U_0/2$
tracking parameters	
β_c/β_{c0}	1.1
filling	1st turn
t_{inj}	0
$\underline{V}_{init}$	$V_{rf}e^{-i\pi/2}$
damping	yes
cont. synchrotron radiation	yes

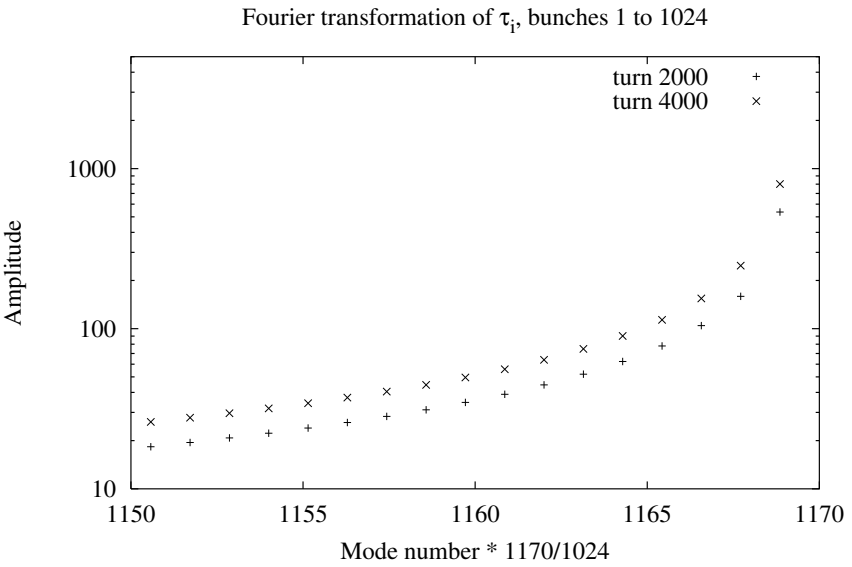

Figure 6.42: Tracking simulation for 1130 bunches at the design beam current with the coupling factor $\beta_c = 1.1\beta_{c0}$. Fourier transformations have been performed for the bunch positions τ_i, $i = 1, \ldots, 1024$ on turns 2000 and 4000; the mode numbers have been multiplied by 1170/1024.

Studies with "large" transient beam-loading effects; filling of the ring in one turn

For the sake of comparison, the case is studied where the damping ring is filled within one turn and transient beam-loading effects play a considerable rôle. The initial cavity voltage $\underline{V}_{init}$ is set to nil and the injection time t_{inj} is chosen to be $21\,020/f_{rf} \approx 1001\Delta T_b$ (for $\beta_c = 1.4\beta_{c0}$). This time was calculated to minimize the average absolute difference between the voltage seen by bunches positioned at τ_{nab} on their first turn and the synchrotron

radiation loss, i.e.

$$\sum_{k=1}^{N_\mathrm{b}} |eF_\mathrm{b}\mathfrak{Re}\underline{V}^1_{\mathrm{c},k} - U_0|,$$

with $t^1_k = (k-1)\Delta T_\mathrm{b} + \tau_\mathrm{nab}$ (t_inj is increased in steps of $20/f_\mathrm{rf}$; $\underline{V}^1_{\mathrm{c},k}$ is introduced on page 68). The energy deviation of the bunches after the first turn is depicted in Figure 6.43: the train head sees a surplus of energy and the train tail too little. The starting positions of the bunches are identical to those of the nearby-mode studies.

beam parameters	
N_b	1130
I_b	0.116 A
σ_{q_b}	0
starting conditions	
ϕ_i	154.66°
ε_i	$U_0/2$
tracking parameters	
$\beta_\mathrm{c}/\beta_{\mathrm{c}0}$	1.4
filling	1st turn
t_inj	$1001\Delta T_\mathrm{b}$
$\underline{V}_\mathrm{init}$	0
damping	yes
cont. synchrotron radiation	yes

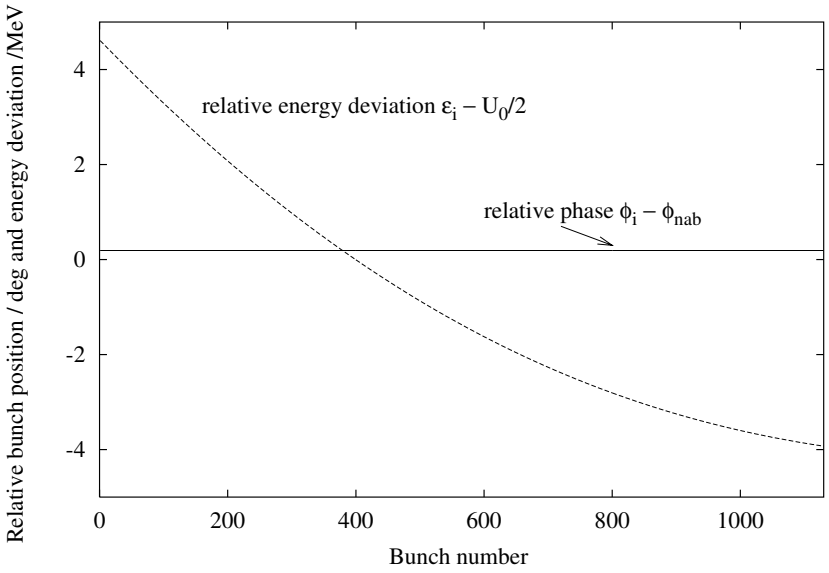

Figure 6.43: The relative bunch phases $\phi_i - \phi_\mathrm{nab}$ and relative energy deviations $\varepsilon_i - U_0/2$ after the first turn for a tracking simulation with the injection time $t_\mathrm{inj} = 1001\Delta T_\mathrm{b}$ and $\underline{V}_\mathrm{init} = 0\,\mathrm{MeV}$. The initial phases, in this simulation identical to those after turn 1, are $\phi_i = \arcsin(U_0/(eV_\mathrm{rf})) = 154.66°$ and not $\phi_\mathrm{nab} = 154.47°$.

The initial transient effects can be clearly seen by studying the average bunch positions and energy deviations depicted in Figure 6.44. It takes about ten revolutions before the train effectively begins to recover. With time, the average values then gradually oscillate with larger and larger amplitudes.
The initial beam-loading effects are, in effect, so large that the coupling factor is raised to $\beta_\mathrm{c} = 1.4\beta_{\mathrm{c}0}$. The coupling factors $\beta_\mathrm{c} = 1.2\beta_{\mathrm{c}0}$ and $\beta_\mathrm{c} = 1.3\beta_{\mathrm{c}0}$ result in a loss of the beam after only 20 and 35 revolutions, respectively (see Figure 6.45, page 129). The coupling factor $\beta_\mathrm{c} = 1.35\beta_{\mathrm{c}0}$ leads to a situation similar to that described here for $\beta_\mathrm{c} = 1.4\beta_{\mathrm{c}0}$.

beam parameters	
N_b	1130
I_b	0.116 A
σ_{q_b}	0
starting conditions	
ϕ_i	154.66°
ε_i	$U_0/2$
tracking parameters	
$\beta_\mathrm{c}/\beta_{\mathrm{c}0}$	1.4
filling	1st turn
t_inj	$1001\Delta T_\mathrm{b}$
$\underline{V}_\mathrm{init}$	0
damping	yes
cont. synchrotron radiation	yes

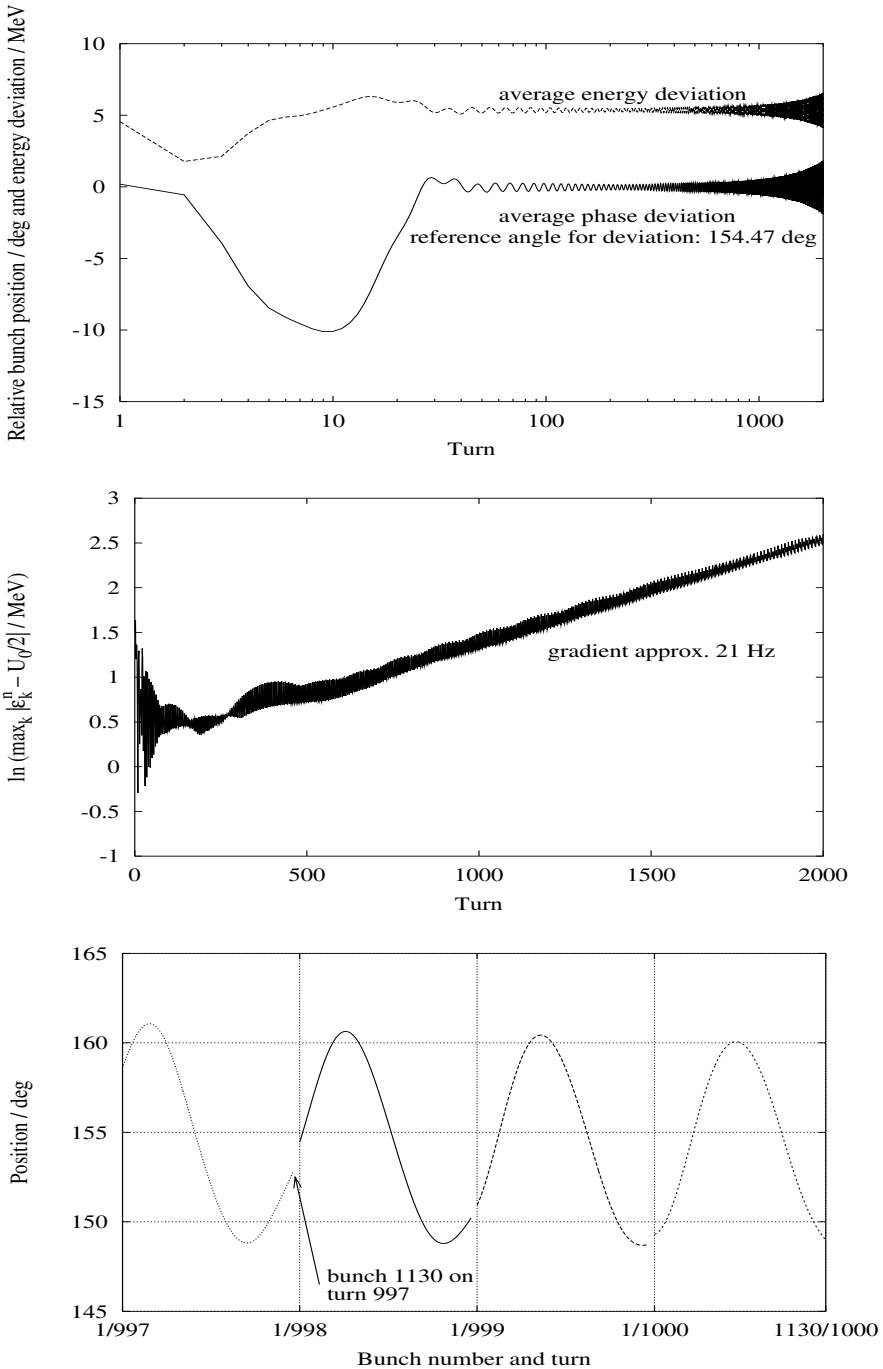

Figure 6.44: Tracking simulation for 1130 bunches at the design beam current with the coupling factor $\beta_\mathrm{c} = 1.4\beta_{\mathrm{c}0}$ and where the initial beam-loading effects are not held to a minimum (filling period: one turn). The average energy deviation and bunch phase relative to the angle $\phi_\mathrm{nab} = 154.47°$ are depicted for the first 2000 turns in the top plot. The logarithm of the maximum relative energy deviation over all bunches per turn is shown in the middle plot. The instability is seen in the amplitude of the beam oscillation, which is larger than five degrees after only 1000 revolutions.

beam parameters	
N_b	1130
I_b	0.116 A
σ_{q_b}	0
starting conditions	
ϕ_i	154.66°
ε_i	$U_0/2$
tracking parameters	
$\beta_\mathrm{c}/\beta_{\mathrm{c}0}$	1.3
filling	1st turn
t_inj	$1030\Delta T_\mathrm{b}$
$\underline{V}_\mathrm{init}$	0
damping	yes
cont. synchrotron radiation	yes

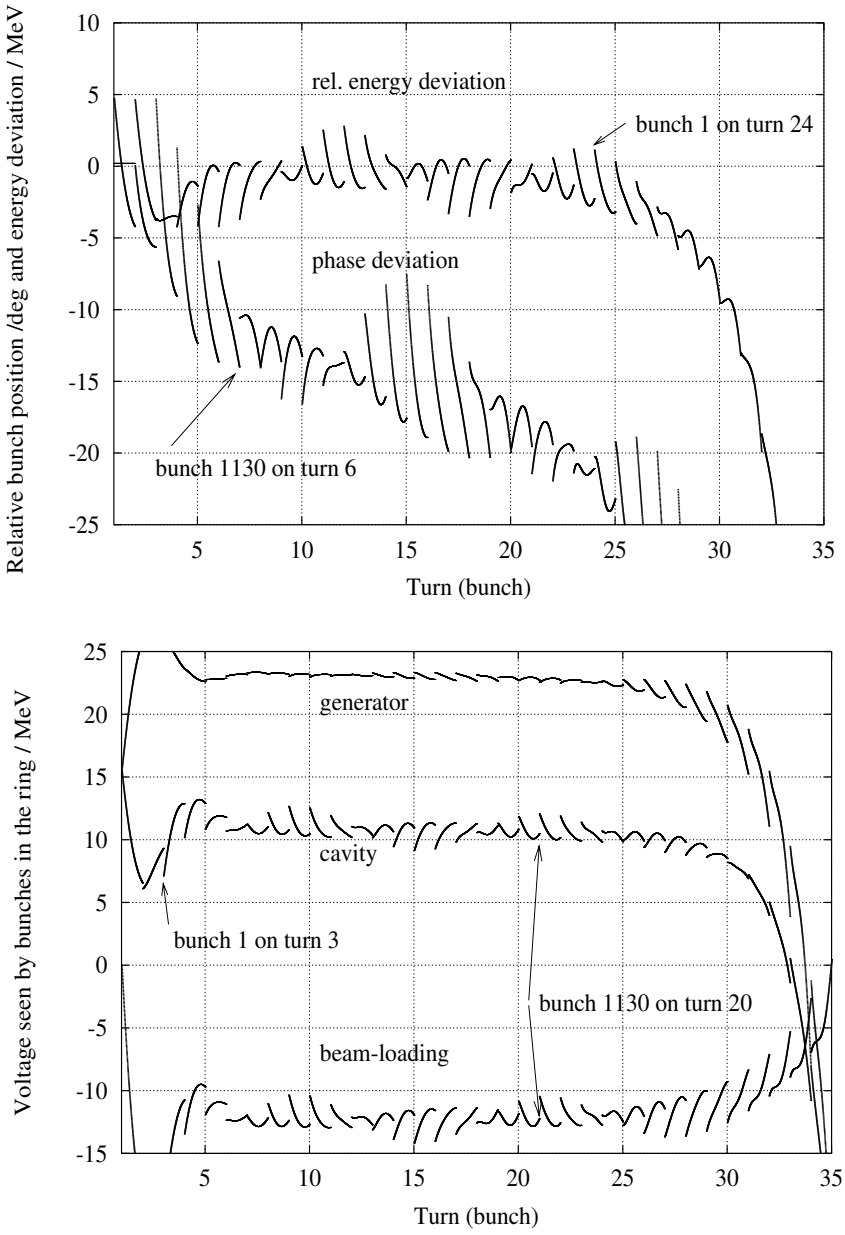

Figure 6.45: Tracking simulation for 1130 bunches at the design beam current with the coupling factor $\beta_\mathrm{c} = 1.3\beta_{\mathrm{c}0}$. The dog-bone ring is filled within one revolution and the initial beam-loading effects are not held to a minimum – as can be seen in both plots. The top shows the relative position $\phi_i - \phi_\mathrm{nab}$ and the relative energy deviation $\varepsilon_i - U_0/2$ of the bunches. The synchrotron oscillation of the bunches located at the head of the train can be seen very clearly between turns 15 and 25. The various voltage components seen by the bunches are depicted in the bottom picture. Since the focusing of the beam is not strong enough, the phase offset of the bunch train gradually gets larger and eventually the beam is lost.

Transient beam loading – filling of the dog-bone over 14 revolutions

As in the analysis in Section 3.3.5, it is assumed here that the bunches enter the ring as 1, 15, 29, ... , 1121, 2, 16, 30, ... , 1122, 3, 17, and so forth. The number 1 pertains, as always, to the bunch train head when the dog-bone damping ring has been filled and 1130 marks the train tail. The coupling factor is $\beta_c = 1.1\beta_{c0}$. There is, however, no significant change with respect to the results when it is increased to $1.2\beta_{c0}$.

beam parameters	
N_b	1130
I_b	0.116 A
σ_{q_b}	0
starting conditions	
ϕ_i	154.47°
ε_i	$U_0/2$
tracking parameters	
β_c/β_{c0}	1.1
filling	14 turns
t_{inj}	$1985\Delta T_b$
$\underline{V}_{init}$	0
damping	yes
cont. synchrotron radiation	yes

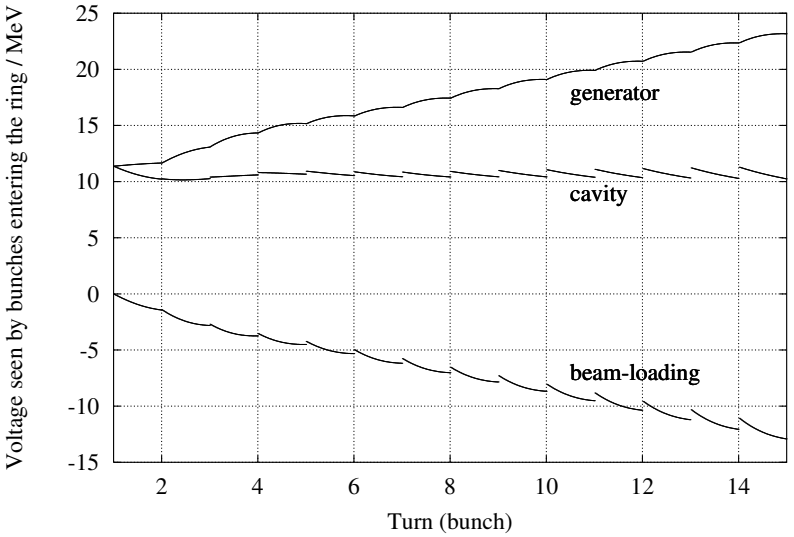

Figure 6.46: The various voltage components seen by the bunches when they enter the damping ring.

Analogously to the previous study, the initial cavity voltage $\underline{V}_{init}$ is set to nil and the injection time $t_{inj} = 41\,680/f_{rf} \approx 1985\Delta T_b$ is chosen to minimize the average absolute difference between the voltage seen by bunches positioned at τ_{nab} on turn one and the synchrotron radiation loss, i.e.

$$\sum_{k=1}^{N_b} \delta_{1,k \bmod 14} \left| eF_b \mathfrak{Re} \underline{V}^1_{c,k} - U_0 \right|,$$

with $t^1_k = (k-1)\Delta T_b + \tau_{nab}$ and $\delta_{1,k \bmod 14} = 1$ for $k = 1, 15, 29, \ldots$ and 0 for all other values of k. The initial generator current is set to

$$\underline{I}_g = \left[\frac{V_{rf}}{R_L \cos\psi e^{i\psi}} + 2\frac{I_b}{14} e^{-i\hat{\phi}_{nab}} \right] e^{-i\pi/2}$$

with $\hat{\phi}_{nab} = \phi_{nab} - \pi/2$ and then raised in steps of

$$2\frac{I_b}{14} e^{-i\hat{\phi}_{nab}} e^{-i\pi/2}$$

in the following 13 revolutions, always at the zero phase of the first bucket. The initial transient beam-loading effects are not entirely cancelled this way but they are much

beam parameters	
N_b	1130
I_b	0.116 A
σ_{q_b}	0
starting conditions	
ϕ_i	154.47°
ε_i	$U_0/2$
tracking parameters	
$\beta_\mathrm{c}/\beta_{\mathrm{c}0}$	1.1
filling	14 turns
t_inj	$1985\Delta T_\mathrm{b}$
$\underline{V}_\mathrm{init}$	0
damping	yes
cont. synchrotron radiation	yes

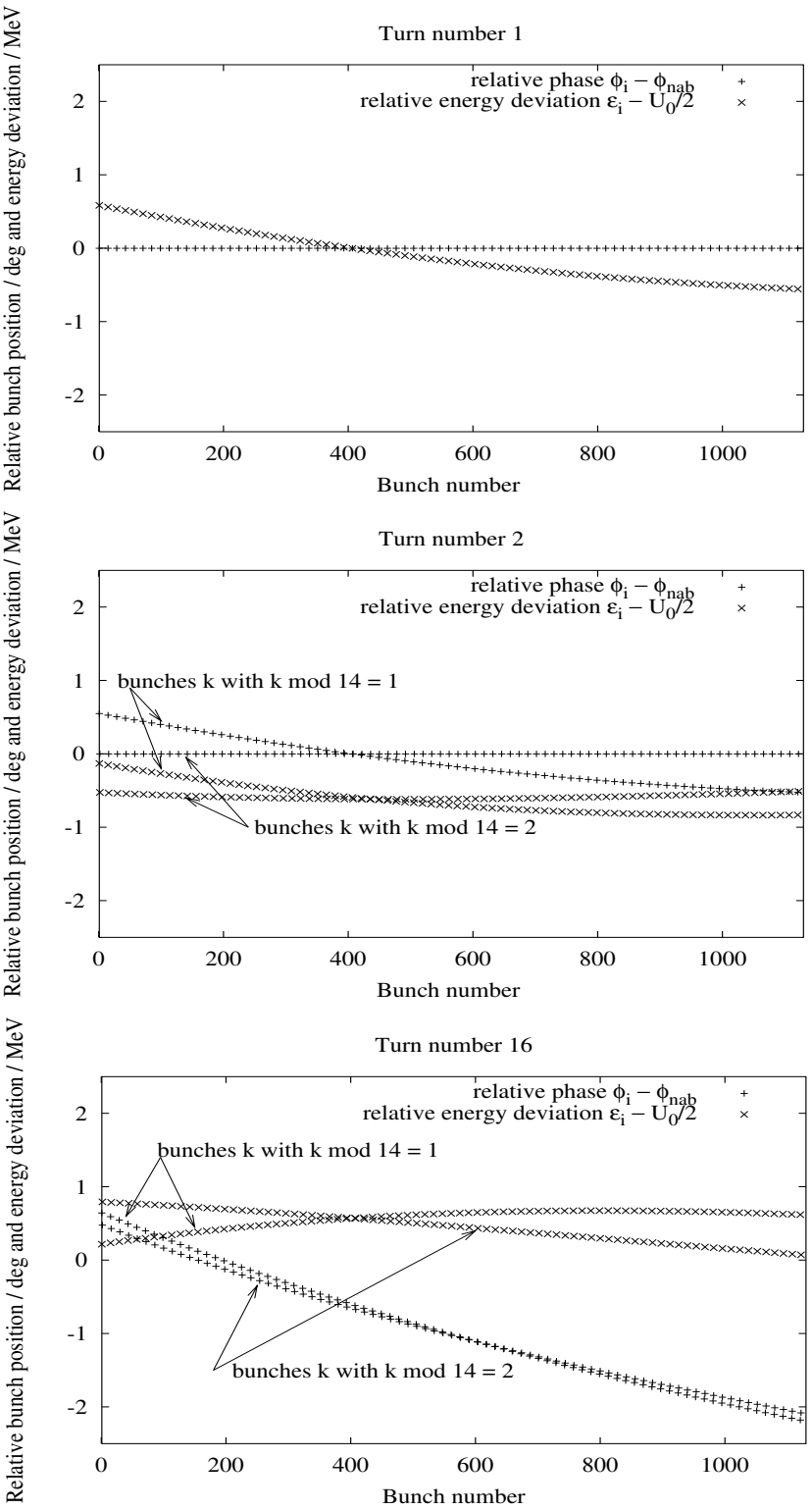

Figure 6.47: The relative bunch phases $\phi_i - \phi_\mathrm{nab}$ and relative energy deviations $\varepsilon_i - U_0/2$ on the first, second, and 16th turn. Tracking simulation for 1130 bunches at the design beam current with the coupling factor $\beta_\mathrm{c} = 1.1\beta_{\mathrm{c}0}$.

smaller than in the last study where the ring was filled within the first revolution. The situation comes closer to that of the nearby-mode study with 1130 bunches.
Initially, there are stronger transient beam-loading effects: as in the previous example the first bunches on the first turn pick up too much energy while the later bunches and those arriving on the second turn see too little (see Figure 6.47); hence, unlike the nearby-mode studies or the previous study, there are neighbouring bunches in the train at the beginning with quite different phases and energy deviations. The bunches arriving after the fourth turn see, according to their position in the train, approximately the same cavity voltage on their first turn (see Figure 6.46). However, even then the phases of the bunches differ slightly due to the synchrotron oscillation. This is depicted in Figure 6.48. The distinction between the bunches which enter the damping ring on the first three turns and those afterwards is quite clear. The starting conditions of the bunches are $\varepsilon_i = U_0/2$ and $\phi_i = \phi_{\mathrm{nab}} = 154.47°$.

beam parameters	
N_b	1130
I_b	0.116 A
σ_{q_b}	0
starting conditions	
ϕ_i	154.47°
ε_i	$U_0/2$
tracking parameters	
$\beta_\mathrm{c}/\beta_{\mathrm{c}0}$	1.1
filling	14 turns
t_inj	$1985\Delta T_\mathrm{b}$
$\underline{V}_\mathrm{init}$	0
damping	yes
cont. synchrotron radiation	yes

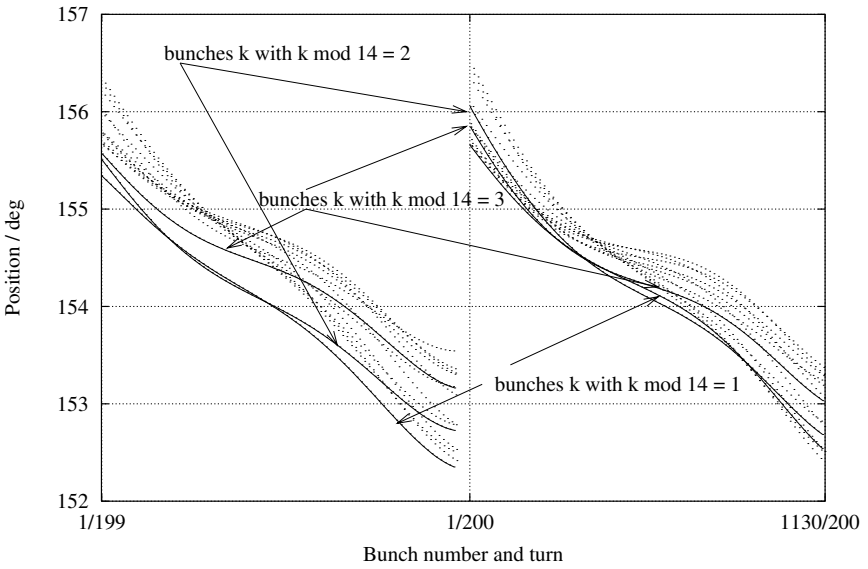

Figure 6.48: The phase positions of the bunches on turns 199 and 200. The bunches which arrive within the first three revolutions are plotted as lines, one per turn.

We now make further studies lasting 1000 turns where the distribution of the bunch charges, the longitudinal starting positions, and the energy deviations are Gaussian distributions. The distribution of the bunch charges has a standard deviation of 5 % centred around the nominal charge value. The starting positions vary as follows:

- $\langle\phi_i\rangle = \arcsin(U_0/eV_\mathrm{rf})$, $\langle\phi_i\rangle_\mathrm{rms} = 2°$, $\langle\varepsilon_i\rangle = U_0/2$, $\langle\varepsilon_i\rangle_\mathrm{rms} = 1\,\mathrm{MeV}$,
- $\langle\phi_i\rangle = \arcsin(U_0/eV_\mathrm{rf})$, $\langle\phi_i\rangle_\mathrm{rms} = 3°$, $\langle\varepsilon_i\rangle = U_0/2$, $\langle\varepsilon_i\rangle_\mathrm{rms} = 1\,\mathrm{MeV}$,
- $\langle\phi_i\rangle = \arcsin(U_0/eV_\mathrm{rf})$, $\langle\phi_i\rangle_\mathrm{rms} = 3°$, $\langle\varepsilon_i\rangle = U_0/2$, $\langle\varepsilon_i\rangle_\mathrm{rms} = 1.5\,\mathrm{MeV}$,
- $\langle\phi_i\rangle = 158°$, $\langle\phi_i\rangle_\mathrm{rms} = 3°$, $\langle\varepsilon_i\rangle = U_0/2$, $\langle\varepsilon_i\rangle_\mathrm{rms} = 1.5\,\mathrm{MeV}$,

- $\langle \phi_i \rangle = 150°$, $\langle \phi_i \rangle_{\mathrm{rms}} = 3°$, $\langle \varepsilon_i \rangle = U_0/2$, $\langle \varepsilon_i \rangle_{\mathrm{rms}} = 1.5\,\mathrm{MeV}$,
- $\langle \phi_i \rangle = 145°$, $\langle \phi_i \rangle_{\mathrm{rms}} = 3°$, $\langle \varepsilon_i \rangle = U_0/2$, $\langle \varepsilon_i \rangle_{\mathrm{rms}} = 2.0\,\mathrm{MeV}$,
- $\langle \phi_i \rangle = 145°$, $\langle \phi_i \rangle_{\mathrm{rms}} = 0°$, $\langle \varepsilon_i \rangle = U_0/2$, $\langle \varepsilon_i \rangle_{\mathrm{rms}} = 0\,\mathrm{MeV}$.

The beam proves to be stable in all of the cases.

Phase shift between the bunch train tail and head in the absence of the nearby-mode instability

The aim of this study is to establish the bunch phases in the absence of the nearby-mode instability. The instability is caused by the unequal impedances of the upper and lower synchrotron side bands; the impedance at $(h-1+\nu_\mathrm{s})\omega_0$ is larger than at $(h+1-\nu_\mathrm{s})\omega_0$. By assuming that there is an additional idling cavity with the resonance frequency

$$\omega_\mathrm{r} = 2\pi \cdot 433.346\,\mathrm{MHz} \approx (h+1-\nu_\mathrm{s})\omega_0,$$

we are able to enlarge the total impedance at the upper side band. A very small bandwidth is needed, since the impedance of the idling cavity should not influence other modes. The bandwidth is chosen to be approximately $0.0015\,\omega_0$ by assuming the quality factor to be 8×10^6. The loss factor is $k_{\delta,\parallel} = 0.009\,\mathrm{V/pC}$, which corresponds to the growth rate $\tau_{1169}^{-1} \approx -73\,\mathrm{Hz}$, so that the overall growth rate, including the rf cavities (without synchrotron radiation damping), at $\beta_\mathrm{c} = 1.1\beta_{\mathrm{c}0}$ is negative.

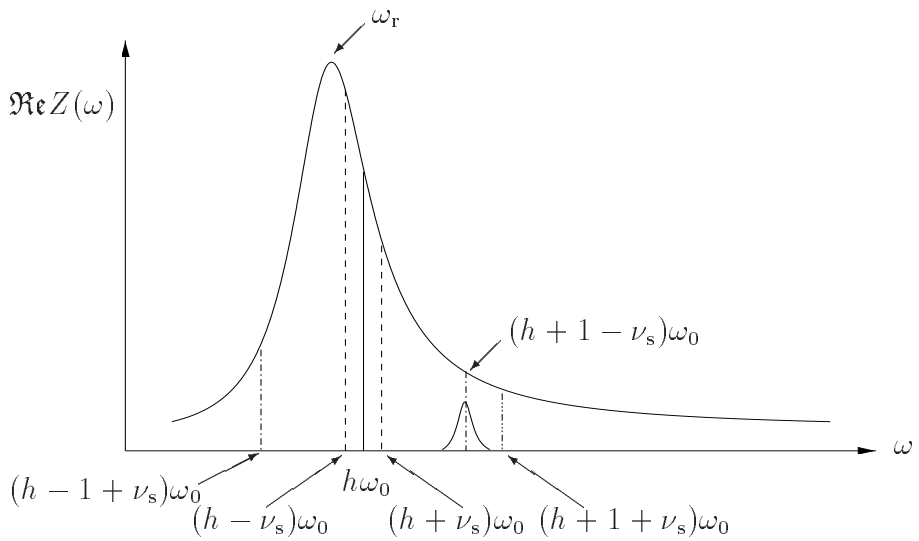

Figure 6.49: Illustration of the impedance budget after adding an idling cavity with the resonance frequency $\omega_\mathrm{r} \approx (h+1-\nu_\mathrm{s})\omega_0$. The total impedance at $(h+1-\nu_\mathrm{s})\omega_0$ is a little bit larger than at the frequency $(h-1+\nu_\mathrm{s})\omega_0$ so that the nearby mode is damped. The bandwidth of the idling cavity impedance is small enough not to influence the $+1$ mode at $(h+1+\nu_\mathrm{s})\omega_0$.

In the study, the initial data settings are chosen to be $\varepsilon_i = U_0/2$ and $\phi_i = 154.66°$. The phase distribution of the bunches is shown in Figure 6.50 for turns 1997 to 2000; the phase shift is approximately 3°.
Note that the choice of larger loss factors (an order of magnitude larger) for the idling cavity leads to a modulation of the distribution of the bunch phases due to the induced steady-state voltage in the idling cavity.

beam parameters	
N_b	1130
I_b	0.116 A
σ_{q_b}	0
starting conditions	
ϕ_i	154.66°
ε_i	$U_0/2$
tracking parameters	
$\beta_\mathrm{c}/\beta_{\mathrm{c}0}$	1.1
filling	14 turns
t_inj	0
$\underline{V}_\mathrm{init}$	$V_\mathrm{rf}e^{-i\pi/2}$
damping	yes
cont. synchrotron radiation	yes

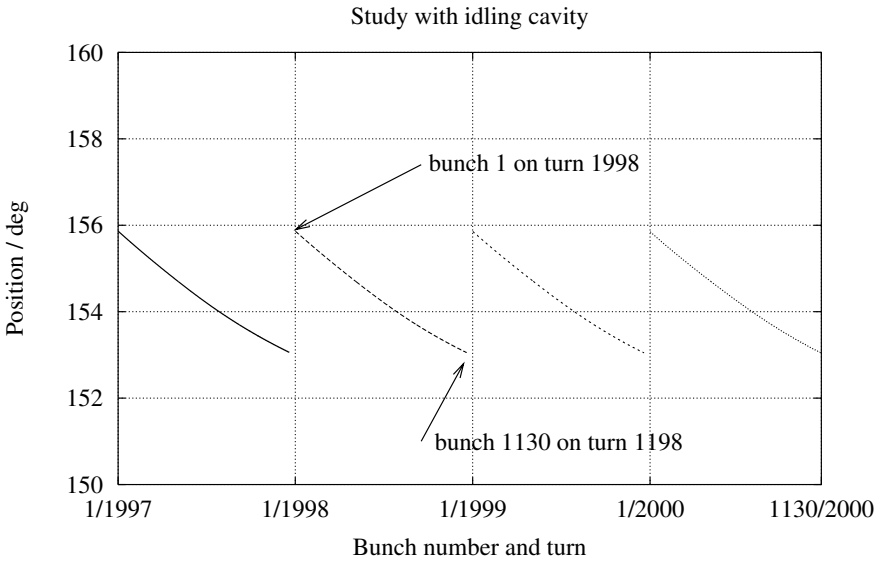

Figure 6.50: Tracking simulation for 1130 bunches at the design beam current with the coupling factor $\beta_\mathrm{c} = 1.1\beta_{\mathrm{c}0}$. An additional idling cavity with the resonance frequency $\omega_\mathrm{r} \approx (h + 1 - \nu_\mathrm{s})\omega_0$ is assumed in order that there be no nearby-mode instability.

Higher-Order Modes and Beam Loading

We now investigate the effects of the two higher-order modes studied in Section 6.2.1 when there are beam-loading effects due to the accelerating mode. In our simulations, we add a mode of an idling cavity to damp the nearby-mode instability. We study, as previously, the starting conditions D, E, and F. These are the injection errors with which we fill the ring over 14 turns. In the light of our results in Section 6.2.1, we feel that it is sufficient to study the case where all bunch charges are equal and where both higher-order modes are accounted for. The loaded quality factor settings are Q1t to Q4t (Table 6.13, page 113).
Our results with respect to the average oscillation amplitude of the energy deviation during turns 3401 – 3500 are summarized in Figure 6.52 on page 136. A comparison with Figure 6.37 on page 121 shows that the overall picture is the same, but that the corresponding values are smaller. The average damping rate for the case with the loaded quality factor of the main higher-order mode set to $Q_\mathrm{L} = 2200$ (case Q1t) is approximately 12 Hz. Our conclusion in the previous section that this loaded quality factor is acceptable still holds.

beam parameters	
N_b	1130
I_b	0.116 A
σ_{q_b}	0
HOM parameters	
f_hom	782.78 MHz, $Q_\mathrm{L} = 3000$
f_hom	775.39 MHz, $Q_\mathrm{L} = 6000$
starting conditions	
case	E, see Table 6.12, page 104
tracking parameters	
$\beta_\mathrm{c}/\beta_\mathrm{c0}$	1.1
filling	14 turns
t_inj	0
$\underline{V}_\mathrm{init}$	$V_\mathrm{rf} e^{-i\pi/2}$
damping	yes
cont. synchrotron radiation	yes

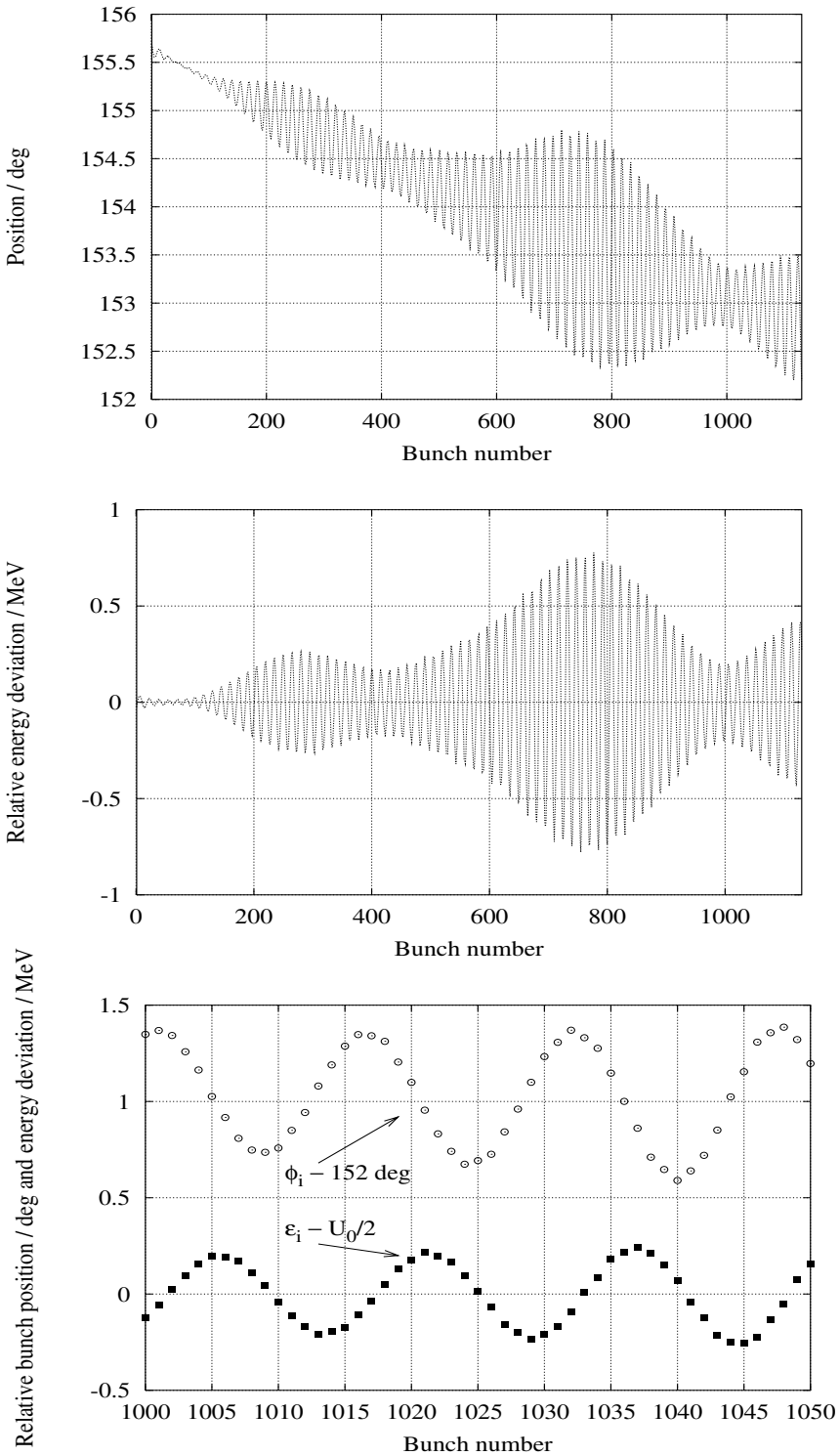

Figure 6.51: Results for turn 3500 of a simulation with the effects of beam loading in the accelerating mode, the effects pertaining to the two strongest higher-order modes for the case Q4t, as well as a mode of an idling cavity to damp the nearby-mode instability (as described on page 133).

beam parameters	
N_b	1130
I_b	0.116 A
σ_{q_b}	0
starting conditions	
case	D, E, F, see Table 6.12, page 104
tracking parameters	
$\beta_\mathrm{c}/\beta_{\mathrm{c}0}$	1.1
filling	14 turns
t_inj	0
$\underline{V}_\mathrm{init}$	$V_\mathrm{rf} e^{-i\pi/2}$
damping	yes
cont. synchrotron radiation	yes

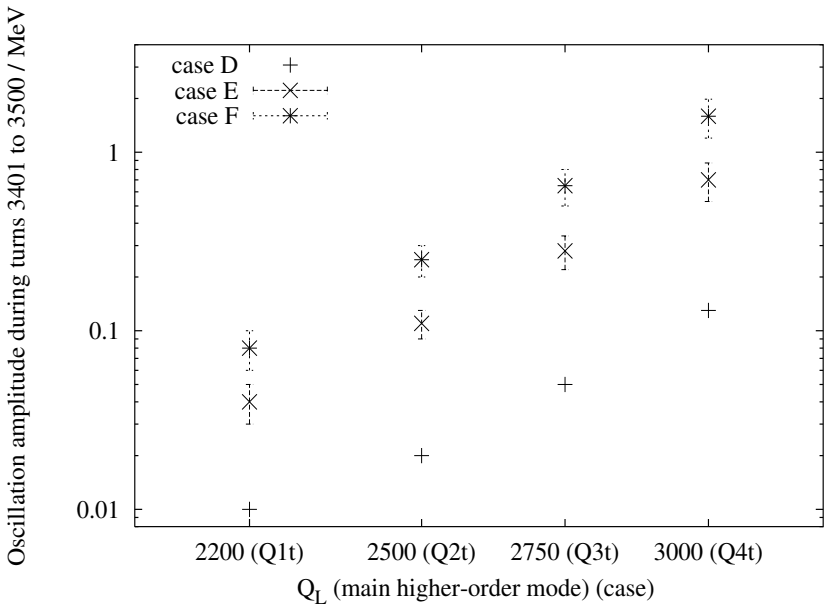

Figure 6.52: The average oscillation amplitude during turns 3401 to 3500 for simulations for the two strongest higher-order modes using different loaded quality factors (Q1t, Q2t, Q3t, and Q4t) and with the mode of an idling cavity which damps the nearby-mode instability. The size of the error bars reflects the standard deviations. 50 simulations are performed each time for the cases E and F.

Simulations with $\alpha_\mathrm{c} = 9.5 \times 10^{-5}$

The analytical treatise in Section 3.4 predicts, analogously to the higher-order modes, a smaller instability growth rate of the nearby mode for the same loaded quality factor. To begin with, the multiplier in Eq. (3.126) scales as the square root of the momentum compaction factor. In addition, the impedance term in brackets decreases with smaller synchrotron tunes. This is easily seen by studying the terms $(1-\nu_\mathrm{s})f_0 \pm \Delta f$ and contemplating that $f_0 \approx 17 \times 10^3\,\mathrm{Hz}$ and $\Delta f \approx -3200\,\mathrm{Hz}$. The analytical growth rates for five coupling factors are listed in Table 6.14 (Eq. (3.124) is used): they are much smaller than the synchrotron damping rate and, therefore, give no reason for concern.

	$\beta_\mathrm{c}/\beta_{\mathrm{c}0}$ 1.0	1.1	1.2	1.3	1.4
Analytical (1170 bunches): $\tau^{-1}_{(1169)}$ / Hz	26.1	28.6	31.1	33.5	35.9
Tracking w. 1170 bunches, gradient of max. pos./neg. relative energy deviation / Hz		28.5	30.9	33.0	35.7
Tracking w. 1130 bunches, gradient of max. pos./neg. relative energy deviation / Hz		27.1	29.5	31.9	34.2

Table 6.14: Instability growth rates at design beam current and for the momentum compaction factor $\alpha_\mathrm{c} = 9.5 \times 10^{-5}$.

To check these results, the damping term is switched off in the tracking simulations. This means that the nominal average bunch phase ϕ_{nab} is $\arcsin(U_0/(eF_{\mathrm{b}}V_{\mathrm{rf}}))$, which is otherwise not the case when applying the standard algorithm. The disadvantage of having no damping term is, of course, that "unwanted" effects are not damped; hence the starting conditions are chosen to be the same for all the bunches and that of the synchronous particle: $\varepsilon_i = U_0/2$ and $\phi_i = \arcsin(U_0/eV_{\mathrm{rf}})$ (there is also no charge fluctuation). The ring is filled within the first turn; furthermore, the transient beam-loading effects are minimized by setting $t_{\mathrm{inj}} = 0$ and $\underline{V}_{\mathrm{init}} = V_{\mathrm{rf}}e^{-i\pi/2}$.

beam parameters	
N_{b}	1130
I_{b}	0.116 A
$\sigma_{q_{\mathrm{b}}}$	0
starting conditions	
case	D, see Table 6.12, page 104
tracking parameters	
$\beta_{\mathrm{c}}/\beta_{\mathrm{c0}}$	1.1
filling	1st turn
t_{inj}	0
$\underline{V}_{\mathrm{init}}$	$V_{\mathrm{rf}}e^{-i\pi/2}$
damping	yes
cont. synchrotron radiation	yes

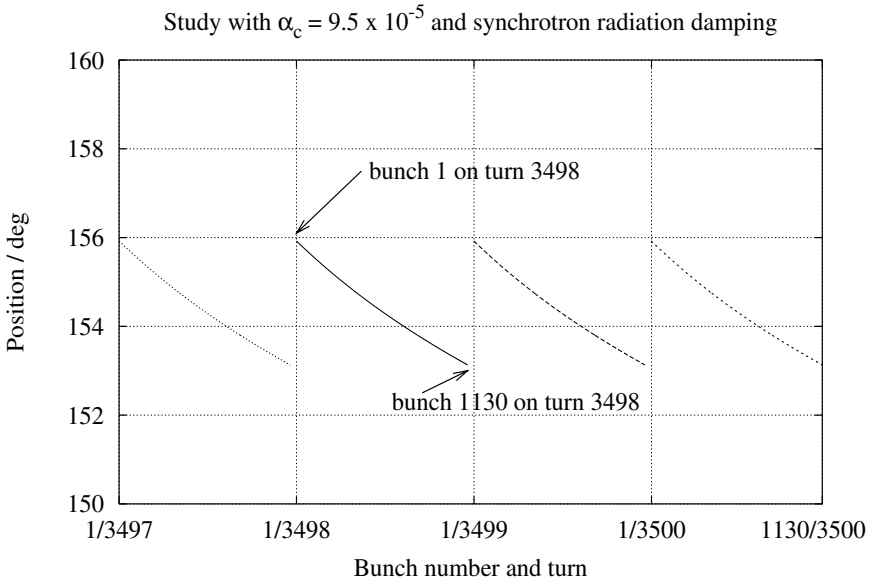

Figure 6.53: Tracking simulation (with synchrotron radiation damping) for 1130 bunches at the design beam current with the coupling factor $\beta_{\mathrm{c}} = 1.1\beta_{\mathrm{c0}}$. The momentum compaction factor is 9.5×10^{-5}.

Two tests are run per coupling factor, one with 1170 bunches (no gap in the beam) and one with 1130. In both cases, the phase focusing of the generator voltage/detuning proves to be insufficient for the coupling factor β_{c0}. The beam is lost between revolutions 100 and 150 for 1130 bunches and 400 and 500 for 1170 bunches due to beam-loading effects. Apart from this result, the predicted growth rates are confirmed by the simulations. The method applied to calculate the growth rates is studying the gradient of the maximum positive/negative relative energy deviation. For the simulations with 1170 bunches, the gradient is calculated by a least-squares fit for turns 3000 to 4000. For the simulations with 1130 bunches, the least-squares fit is for turns 1000 to 2000. The numbers in Table 6.14 represent the average values obtained for the positive and negative deviations. The values pertaining to the positive and negative deviations differ for the simulations with 1170 bunches by less than 0.1 Hz and differ for the simulations with 1130 bunches by no more than 1 Hz. In all four simulations with 1130 bunches, the instability becomes so large that the beam is lost between turns 2250 and 2450.

Chapter 7

Comparison with other programs

The results of the single bunch tracking program are compared in the first section of this chapter to those of a program which solves the Vlasov equation based on a series expansion of the disturbance Ψ_1 (applied to the dog-bone damping ring). The second section looks at an application of the tracking code to the SLAC damping ring, where instabilities were observed and where other tracking results are available. In the third section, the results of the multibunch tracking program are compared to those of another code for the B-factory.

7.1 K. Oide and K. Yokoya's Code

Single bunch dynamics in the TESLA damping ring have also been investigated with a program written by K. Oide and K. Yokoya [63].
Their method begins by solving the Haissinski equation (including the wake potential), thereby obtaining the static solution $\Psi_0(p,q)$. The general distribution $\Psi(p,q)$ is then expanded to first order, leading to the linearized Vlasov equation. In order to study the stability of this equation as exactly as possible, the single-particle action-angle variables (J,ϕ) are introduced. In this way, the potential-well distortion is fully included in the solution of the equation (the zeroth-order potential-well distortion term due to the wake of Ψ_0 is not neglected). In the next step, the distribution $\Psi_1(J,\phi,\theta)$ is expanded into a Fourier series $\sum_m e^{i(m\phi-\Omega\theta)}\psi_m(J)$, with $\theta=\omega_{s0}t$ the phase of the synchrotron motion. This leads, after a few more steps, to a finite matrix eigenvalue problem, which the code solves. A positive imaginary part of an eigenvalue Ω indicates an instability (growth of the energy spread).

	case		
	A	B	C
Momentum compaction factor α_c	27×10^{-5}	7×10^{-5}	5×10^{-5}
Synchrotron frequency f_s / kHz	1.304	0.675	0.571
Natural bunch length σ_{z0} / mm	10.1	5.2	4.4

Table 7.1: The three cases studied by K. Yokoya.

The program was applied by Kaoru Yokoya to the dog-bone damping ring [4], using the same parameters as in the tracking calculations presented in [61] and [64]. These differ slightly from the CDR-parameters [1]. The circumference is 20 km, the energy of the beam 3.3 GeV, the synchrotron radiation loss per turn U_0 is 12 MeV, and the peak rf voltage $V_{\rm rf}$ is 24 MV. The design bunch current is 0.09 mA, which corresponds to a bunch population of $N_{\rm e} = 3.75 \times 10^{10}$. The natural energy spread $\sigma_{\varepsilon 0}$ is 3.44 MeV. Three cases with different momentum compaction factors were studied; they are listed in Table 7.1. The quasi-Green's function is depicted in Figure 7.1.

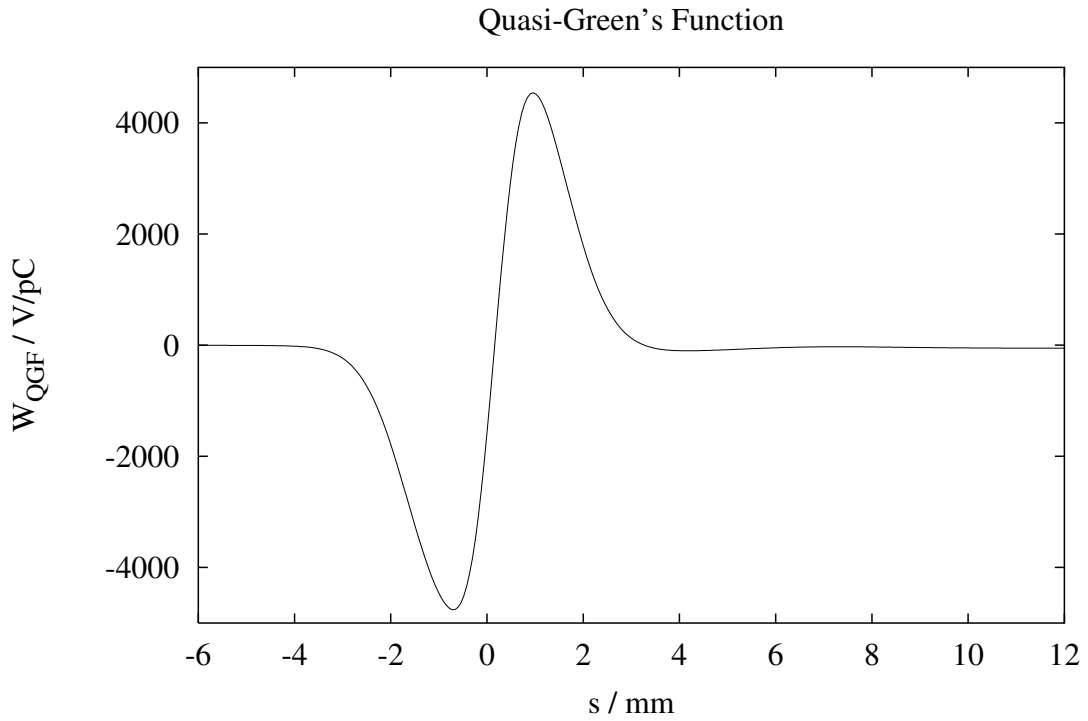

Figure 7.1: The quasi-Green's function used in the calculations by Kaoru Yokoya. The components are as follows: an inductive wake potential with $\sigma_z^{\rm QGF} = 1$ mm, the wake potentials of a Gaussian bunch with $\sigma_z = 0.5$ mm for the cavities and the resistive walls, and a wake potential for the fast kickers generated by a Gaussian bunch with $\sigma_z = 2$ mm. The weighting of the individual wakes is very similar to that in Section 6.1 and is described in [61].

Figure 7.2 shows the normalized rms bunch length according to the Haissinski solution as a function of the bunch population. The asterisks on the curves represent the point at which the system becomes unstable as obtained by K. Yokoya. In all three cases, the threshold currents are larger than the design current by a factor of at least five.
The diamonds in the figure represent the bunch populations at which the tracking results indicate an instability. To check the consistency of the thresholds, various combinations of the number of sections, width of the bins, and number of macroparticles were used. The ring was divided into either four or eight sections (only eight sections for the case $\alpha_{\rm c} = 27 \times 10^{-5}$), the width of the bins was either 0.2 mm or 0.3 mm, and the number of

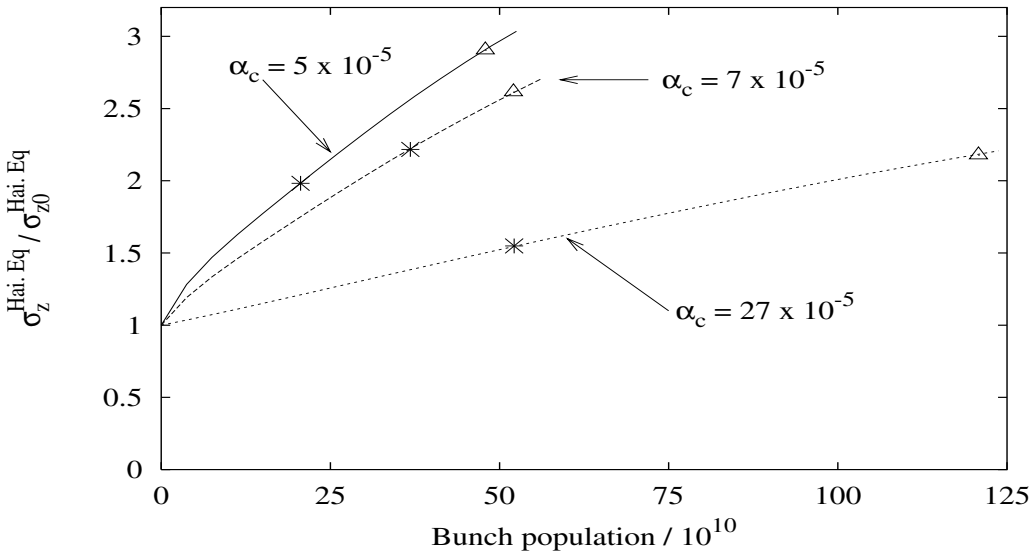

Figure 7.2: The normalized rms bunch length from the Haissinski equation. The asterisks indicate the energy-spread increase threshold as found by K. Yokoya [4]. The diamonds indicate the thresholds obtained by tracking.

macroparticles varied between 25 000 and 200 000. The rise of the energy spread proved to be independent of these variables.
As can be easily seen in Figure 7.2, the tracking thresholds are higher than those calculated by K. Yokoya. The ratios in the three cases vary between approximately 1.3 and 2.5.
With respect to the bunch lengthening and the change of bunch centre-of-mass positions, the tracking results agreed with the those of Yokoya.

7.2 SLC Damping Ring

Tracking simulations have been applied to the SLC damping rings (the old chamber but with bellow sleeves) and compared to the results in [45].
In 1992, a longitudinal single bunch instability was observed in the SLC damping rings. Beyond a threshold current corresponding to a bunch population of 3×10^{10} a "saw-tooth" variation in bunch length and energy spread was observed, a phenomenon that made it practically impossible to operate the SLC collider above the threshold.
As in the tracking studies in [45], the revolution time T_0 was taken to be 118 ns and the rf frequency f_{rf} to be 714 MHz. The beam energy E_{b} was 1.15 GeV, the peak rf voltage 0.8 MV, and the synchrotron radiation loss per turn 0.076 MeV. The momentum compaction factor α_{c} was set to 0.015. The relative energy spread σ_{E0} was 0.07 %. This led to a nominal rms bunch length σ_{z0} of 4.9 mm and the synchrotron frequency 100 kHz, which corresponds to 85 turns per synchrotron period.
The real damping time was used in the simulations (this was also always the case for the dog-bone damping ring studies). Hence, there are 15 142 turns per damping time. The number of macroparticles N_{par} was 100 000.

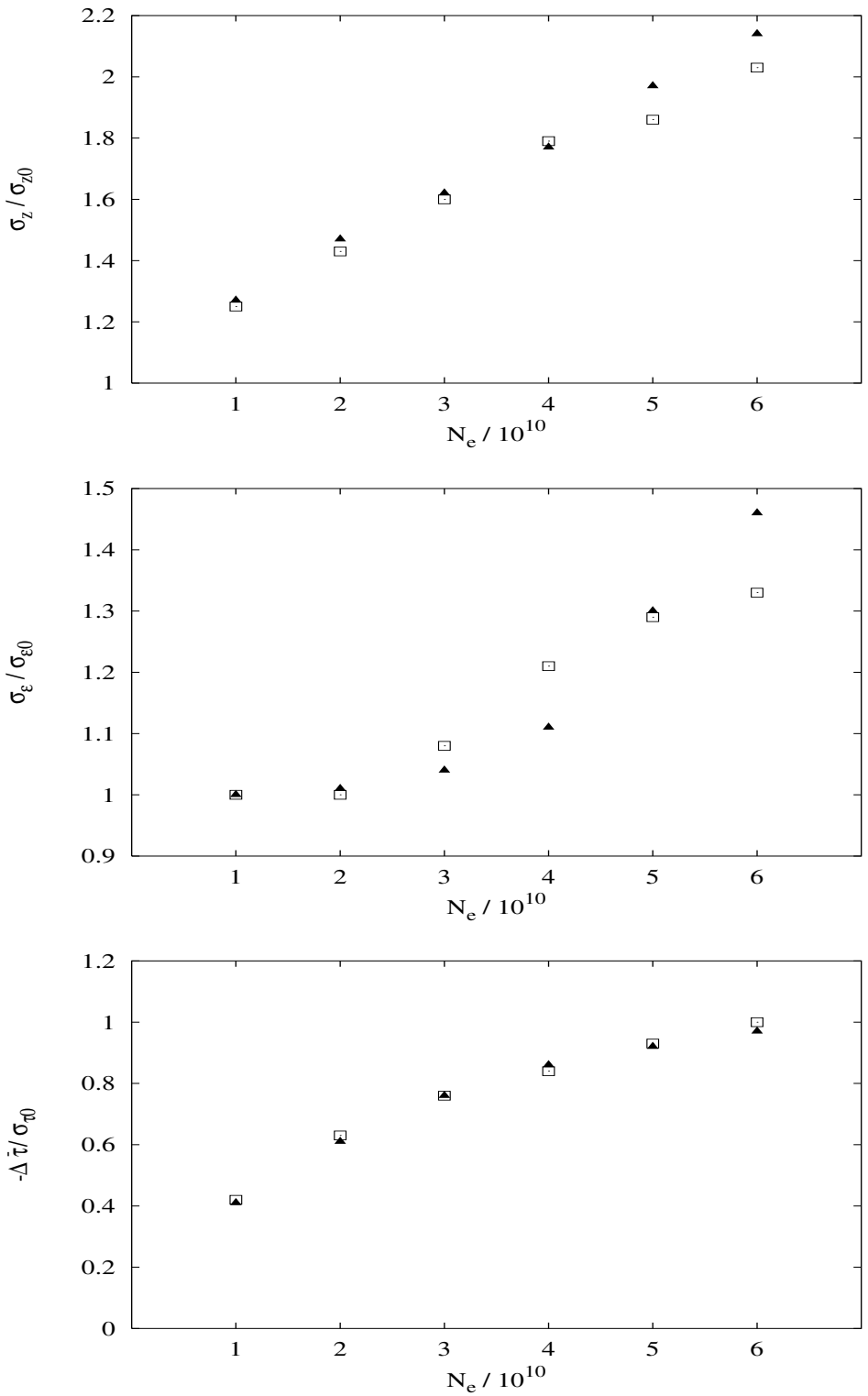

Figure 7.3: SLC damping ring tracking results. The average bunch properties as a function of the bunch population N_e. The boxes are Karl Bane's results (the values are estimates derived from the measurements of a figure in ref. [45]). The black triangles pertain to the tracking program used in this thesis.

Karl Bane used 300 000 macroparticles but reduced the damping time by a factor of approximately 10 to $T_\varepsilon = 0.17\,\mathrm{ms}$. This leads to only 1445 turns per damping time [45]. The program was started with the zero-current distribution for $N_\mathrm{e} = 1$, 2, and 3×10^{10} and ran for 45 000 turns (approx. three damping times). For the populations 4×10^{10} – 6×10^{10}, the starting position of each was the same as the ending position of the run immediately preceding it.

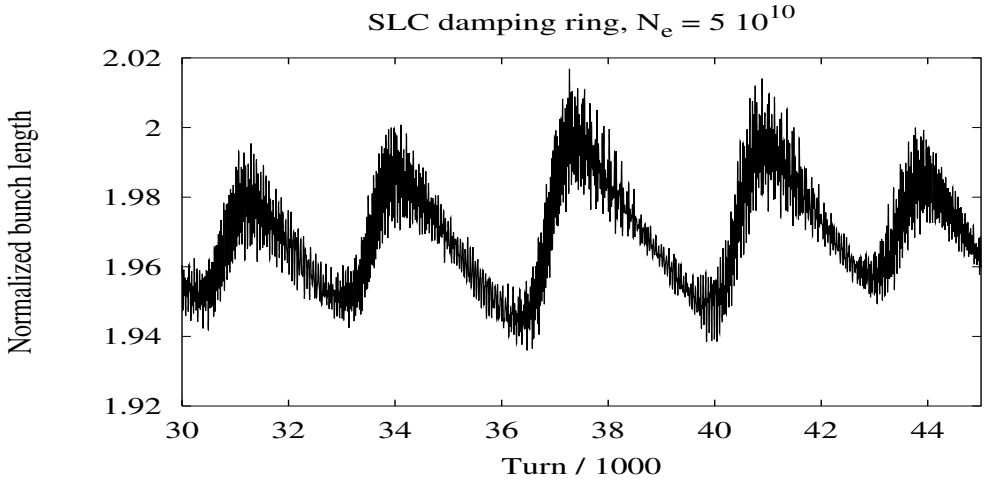

Figure 7.4: Turn-by-turn normalized rms bunch length σ_z/σ_{z0} for the SLC damping ring with $N_\mathrm{e} = 5 \times 10^{10}$.

Beyond a threshold of $N_\mathrm{e} = 3 \times 10^{10}$, the energy spread of the beam in the old SLC damping ring increased and a "saw-tooth instability" appeared. The possibility of such an instability occurring was shown by T. Weiland in his tracking studies in 1981 [37].
The results for the rms bunch length and the shift of the bunch centre concur extremely well with those of Karl Bane (see Figure 7.3). At the bunch population 5×10^{10}, a reasonably regular overshoot pattern in the moments as a function of time could be seen, too (see Figure 7.4). Here, the bunch length varied about 4 % over a cycle. The lengthening time was about $11/f_{\mathrm{s}0}$ and the shortening time was slightly more than twice as long. K. Bane obtained his tracking results (the boxes in Figure 7.3) by the following method: the properties of the distributions were averaged over the final of three damping times (the program was started with the potential-well bunch distribution).

7.3 Multibunch Tracking

Simulation of longitudinal coupled bunch instabilities at the B-factory due to higher-order modes is the subject of reference [62] by Kathleen Thompson. The general behaviour of the bunch train without bunch-by-bunch feedback is exemplified by the maximum bunch excursion of the individual bunches. The "identical" results were obtained with the presented multibunch tracking code. An example is shown in Figure 7.5.
The input data are as follows: the beam energy is 9 GeV, the nominal energy spread is 6.1×10^{-4}, the synchrotron loss per turn is 3.52 MeV, V_rf is 18.5 MeV, the momentum

compaction factor is 2.41×10^{-3}, the circumference is 2199.32 m, the harmonic number is 3492, the resonance frequency of the cavities is 787.272 MHz, the quality factor is 70, and the loss factor per cavity is 0.1014 V/pC; in total there are 20 cavities. The voltage and wake function were not multiplied by a bunch form factor.

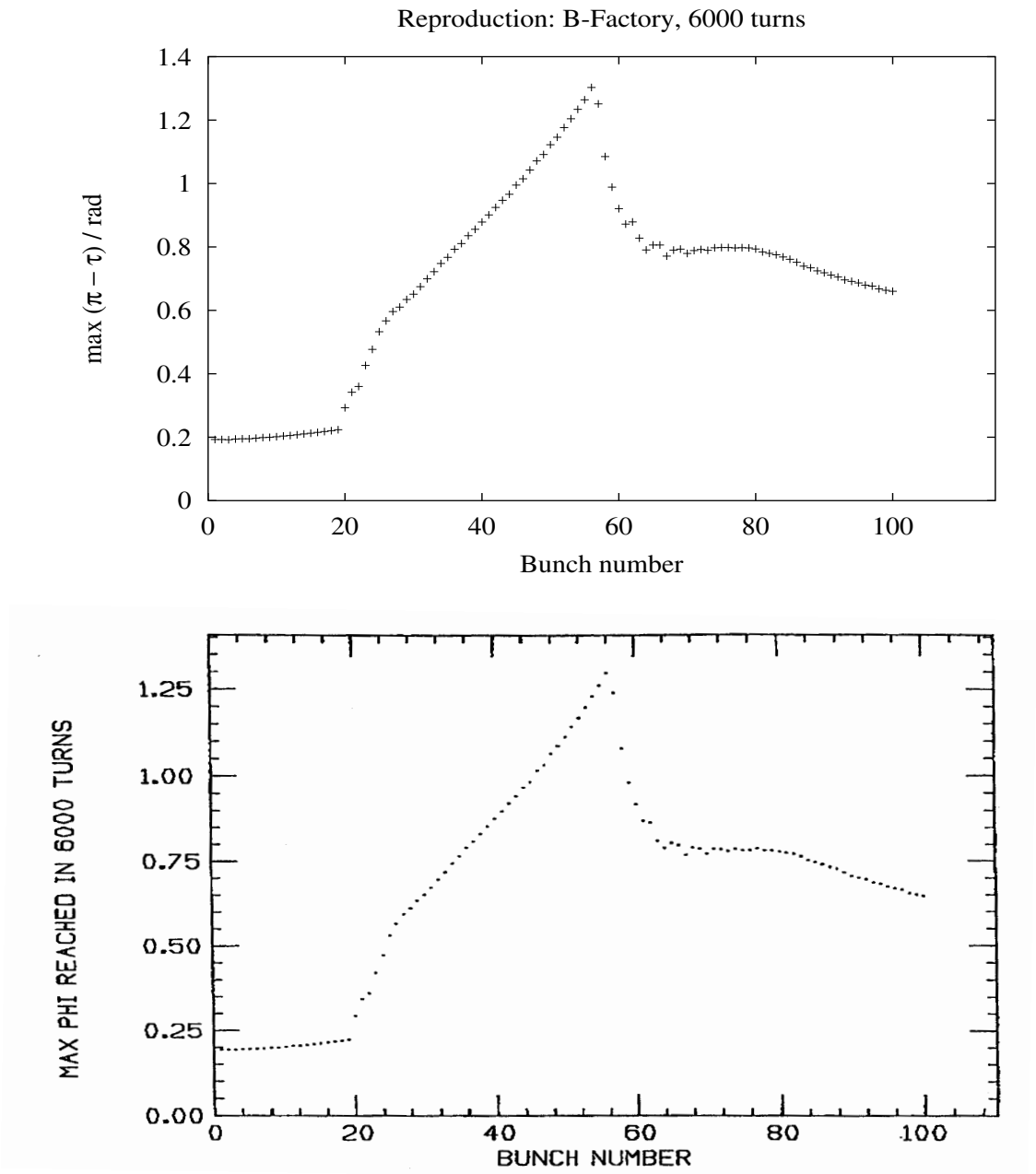

Figure 7.5: Reproduction of the simulation results in [62] for the B-factory (top plot) and original (bottom plot). The initial conditions are as follows: with the exception of number 20 at $\phi = 163.30°$, the bunches are positioned at the synchronous phase ($\phi_s = 169.03°$); the energy deviation of all the bunches is zero. The beam current is $I_b = 1.48$ mA ($N_e = 4 \times 10^{10}$). There is no damping in the simulation, and the continuous synchrotron radiation term is switched off.

Chapter 8

Summary and Conclusion

In this thesis, longitudinal dynamics in a storage ring in general have been studied, with an emphasis on the TESLA damping ring, as specified by the Conceptual Design Report [1] (Chapters 2 and 3). Single and coupled bunch effects have been looked into separately, once by analytical methods and once with the help of tracking codes. The former are described in detail in Chapter 3, the latter in Chapter 4.

Single Bunch Effects

The single bunch tracking program is based upon using macroparticles and incorporating wake field effects into the equations of motion with the help of so-called quasi-Green's functions: the wake potentials generated by Gaussian bunches with a smaller rms value than the bunch tracked. Furthermore, a binning technique was applied in the calculation of the wake potential. The program has been applied to the SLC damping ring, where a saw-tooth instability occurred (Chapter 7). The extremely close correspondence between the tracking results, those of K. Bane, and the measurements point toward the trustworthiness of the code. Furthermore, a comparison with K. Yokoya's and K. Oide's code regarding the dog-bone damping ring showed partly a good agreement.
The impedance model for the TESLA damping ring to study single bunch dynamics accounts for the resistive wall effect due to the aluminium vacuum chamber, the fast kickers, and the rf cavities. The wake potentials of the fast kickers and rf cavities were calculated with MAFIA. The BPMs and the bellows have been assumed to give rise to an inductive impedance. The BPM contribution may be overestimated, as comparisons with MAFIA calculations show a discrepancy of the maximum wake amplitude of up to a factor of two.
A summary of the estimates of the different contributions to the broad-band impedance is given in Table 5.2. The contributions amount to approx. 25 mΩ.
The purely inductive part of the impedance $Z_{\parallel}^{\mathrm{ind}}(\omega) = i\omega L$ gives rise to bunch lengthening. A first-order estimate of the bunch lengthening based upon the Haissinski equation, has been derived and is given by Eq. (3.147). This predicts a bunch lengthening of about 3 % which has been confirmed by the tracking results, as well as a calculation with the Haissinski equation; in both situations, all the wake field components have been included. The numerical solution of the Haissinski equation is described in Section 3.6.

Besides the total wake, the individual components have also been studied at multiples of the design bunch charge (see Section 6.1). The inductive wake component is the dominating term. The results concur with those of the Haissinski equation. Simulations up to four times the nominal bunch charge were also made with the momentum compaction factor $\alpha_c = 9.5 \times 10^{-5}$, corresponding to a nominal bunch length of 5 mm. Here, too, the results in the light of bunch lengthening are dominated by the inductive component. Instabilities did not occur.
A relatively new research area is surface roughness. The main concern is that these wakes could play a crucial rôle in linear colliders and free electron lasers, where ultrashort bunches are used. However, the model used to describe the surface roughness wake field effect [53] has yet to be verified by measurements. With respect to long bunches in synchrotrons or damping rings, the roughness wake fields might influence the beam dynamics as well. Above a threshold current, the wake potentials are suspected to cause saw-tooth instabilities.
For the dog-bone damping ring and the design bunch length and current, surface roughness should only lead to an inductive wake contribution [54]. If one assumes a surface roughness of 400 nm, and uses the formulae in ref. [53] with the relative permittivity $\epsilon = 2$, one obtains for a Gaussian bunch with an rms of 1 cm an inductance L of approx. 5×10^{-8} H, which corresponds to $Z_{||}/n = 5.5\,\mathrm{m}\Omega$. The wake potential generated by a Gaussian bunch with $\sigma_z = 1$ mm, which could be used as a quasi-Green's function, would also be inductive. An inductive wake leads only to bunch lengthening.

The *transverse* broad-band impedance has been estimated in ref. [33], showing that the mode-coupling instability is not a concern for the damping ring.

Multibunch Effects

Long-range wake fields in a storage ring cause different bunches to interact.
The possible effects of the rf cavities are, for example:

- longitudinal and transverse coupled bunch instabilities due to the higher-order modes,
- longitudinal coupled bunch instabilities caused by the accelerating mode,
- and a shift of the longitudinal bunch position due to beam loading.

In Section 3.4, analytical formulae have been derived for the case of N_b equally spaced and populated bunches. The analysis shows that the multibunch motion can be described by a total of N_b modes, each corresponding to a characteristic relative phase shift of the bunches. The growth rate of the corresponding amplitudes is given by Eq. (3.124). The simulation results in Section 6.2 showed that Eq. (3.124) could still be applied to the dog-bone damping ring even though the bunch train has a gap. It was also applicable when the bunch populations varied by a Gaussian distribution of 5 % around the nominal bunch population N_e^{ref}.

A comparison of the analytical growth rate predictions with the damping rate results in the following limit to ensure no coupled bunch instabilities develop.

$$\sum_{p=-\infty}^{+\infty} f_{pk} \cdot Z_{\parallel}(\omega_{pk}) e^{-(\omega_{pk}\sigma_z/c)^2} < \alpha_\varepsilon \frac{2(E_\mathrm{b}/e)\nu_\mathrm{s}}{\alpha_\mathrm{c} I_\mathrm{b}}, \tag{8.1}$$

where $\omega_{pk} = \omega_0(pN_\mathrm{b} + k + \nu_\mathrm{s})$ and $f_{pk} = \omega_{pk}/2\pi$. The damping rate in the TESLA damping ring is $\alpha_\varepsilon = U_0/(T_0 E_\mathrm{b})$, so that the above inequation can be rewritten as:

$$\sum_{p=-\infty}^{+\infty} f_{pk} \cdot Z_{\parallel}\big(\omega_{pk}\big) e^{-(\omega_{pk}\sigma_z/c)^2} < \frac{2\nu_\mathrm{s} U_0/e}{\alpha_\mathrm{c} T_0 I_\mathrm{b}} = \frac{\sqrt{2h} U_0 \sqrt{V_\mathrm{rf}} \sqrt[4]{1-1/q^2}}{N_\mathrm{b} N_\mathrm{e} e^2 \sqrt{\pi \alpha_\mathrm{c} E_\mathrm{b}/e}}. \tag{8.2}$$

Inserting the design values for the dog-bone damping ring leads to

$$\sum_{p=-\infty}^{+\infty} \frac{f_{pk}}{\mathrm{GHz}} \frac{\mathfrak{Re} Z_{\parallel}(\omega_{pk})}{\mathrm{k}\Omega} e^{-(\omega_{pk}\sigma_z/c)^2} < 930. \tag{8.3}$$

First, the higher-order modes are considered. In the TESLA damping ring, they arise mainly from the rf cavities. The frequencies and corresponding loss factors were obtained by applying the MAFIA eigenvalue solver to a 4-cell 433 MHz cavity (see Section 5.2). The impedance of the strongest mode was (based on the experience with the HERA-cavities including HOM-couplers) estimated to be 60 kΩ per 4-cell cavity. This corresponds to a quality factor of approximately 1100. A conservative limit of the contribution of the strongest mode in inequality (8.3) is 380, a factor of 2.4 smaller than the stability limit. This is in the worst case, that the higher-order mode frequencies are identical in all eight cavities. The results of our simulations, which were were carried out for various starting conditions (injection errors) showed that a loaded quality factor of $Q_\mathrm{L} = 2200$ is still fully acceptable. The damping rate is approximately −10 Hz. The oscillation amplitudes of the bunch energies at the end of the storage time were smaller than 5 % of the rms energy spread within a bunch. This corresponds to an oscillation amplitude of the longitudinal phase of approximately 0.2°. We also know that within the range of ±1.5 MHz (this is the range we tested) our results are, with respect to the instability growth rates, independent of the explicit higher-order mode frequency. For the quality factors $Q_\mathrm{L} = 2750$ and $Q_\mathrm{L} = 3000$, we found that the instability growth rates were larger than the synchrotron damping rate. We also performed simulations where the higher-order mode frequencies in the eight cavities varied. If the frequencies have a standard deviation of 100 kHz, the instability growth rates are smaller than the synchrotron damping rate.

Additional sources of higher-order modes are beam position monitors. Our estimations are based on a study of the resonant modes of PEP-II button-type beam position monitors [60]. If we insert the resonance frequency and impedance values as stated on page 81, the left-hand side of the Eq. (8.3) amounts to approximately 10 for the BPMs. Furthermore, the long-range wake fields due to the resistive walls were found also to be negligible due to the large pipe diameter in the straight sections (see also page 81).

The second point of interest with respect to inequation (8.3) is the so-called nearby mode. The rf cavities are detuned to compensate for the reactive part of the beam loading and to minimize the required rf power. At the same time, this helps to avoid the Robinson instability. The detuning leads, however, to unequal impedances of the upper and lower synchrotron sidebands, which leads to an instability of the multibunch mode nearest in frequency. In the simulations incorporating the beam-loading effect in the accelerating mode, the coupling factor β_c was set to be 1.1 times the optimum coupling factor β_{c0} (see Eq. (3.92)) to ensure phase stability. The beam loading was accounted for by decomposing the cavity voltage into a generator current and a beam current component. The cavity tuning was set to be optimal (i.e. Eq. (3.90) is fulfilled).
The simulations have shown that, in agreement with the analytical results, the growth rate of the nearby mode is slightly larger than that of the damping rate. The growth rate for $\beta_c = 1.1\beta_{c0}$ is approximately 3.5 Hz larger than the damping rate; the corresponding value in Eq. (8.3) is 987.
The instability of the nearby mode could be addressed with a simple feedback loop (like the "nearby-mode" feedback in HERA).
A further aspect of the accelerating mode is the initial transient beam loading. This has been studied in Section 3.3.5 as well as in the simulations. Due to the fact that the bunch train is stored in a compressed mode, the damping ring requires 14 revolutions to be filled. As a consequence, the transient beam loading appears to be a less severe problem than if the ring were filled within one turn. If the generator current is increased linearly, for example in 14 steps, the transient effects can be minimized. To be precise, one begins with the generator current that would be required without any beam loading and ends with the current that the rf system requires where the effects of the steady-state beam loading are included. The current used in the simulations is the beam current as seen over the whole ring, and not the current within the bunch train, which is slightly larger. The bunches are not distributed uniformly over the ring, due to the gap for ion-clearing. As a consequence, each bunch sees a different wake field (beam loading) induced by the preceding bunches. In order to pick up the same energy at the cavities, so as to keep the revolution frequency unchanged, the tail bunches advance from the nominal position and the head bunches arrive delayed. The simulations show a phase shift of approximately 3°. With respect to the average phase, this means a maximum shift of ±1.5°. This value is approximately a third of the rms bunch length evaluated in degrees (1 cm ≡ 5°) and will not cause a problem. We note that the bunch compressor performs a longitudinal phase space rotation so that extracted phase errors from the damping ring do not translate into linac phase errors. Energy errors, however, translate into linac phase errors. As we discussed on the previous page, the energy error due to the higher-order modes is less than 5 % of the uncorrelated energy spread and, therefore, causes no problems.

The impact of a smaller momentum compaction factor (assumed to be independent of all other nominal damping ring values) has been shown in the simulations and is apparent from Eq. (8.2). The growth rates of the higher-order multibunch modes scale as approx. $\sqrt{\alpha_c}$ and are, therefore, decreased. The same applies, in principle, also to the nearby mode, although here the two impedances of the synchrotron sidebands are more strongly influenced by the momentum compaction factor via the synchrotron tune than the higher-order mode impedances.

Note that the left-hand side of expression (8.2) with respect to the nearby mode is approximately

$$\sum_{p=-\infty}^{+\infty} f_{pk} \cdot Z_{\parallel}(\omega_{pk})\, e^{-(\omega_{pk}\sigma_z/c)^2} \approx \frac{(N_{\mathrm{cav}} k_{\delta,\parallel})\beta_{\mathrm{c}} f_{\mathrm{rf}}^3 e^{-(\omega_{\mathrm{rf}}\sigma_z/c)^2}}{\pi Q_0} \frac{-(1-\nu_{\mathrm{s}}) f_0 \Delta f}{\left[(1-\nu_{\mathrm{s}})^2 f_0^2 - (\Delta f)^2\right]^2} \qquad (8.4)$$

An increase in the current, which is the case in the new set of TESLA parameters (Table 1; $N_{\mathrm{b}} \times N_{\mathrm{e}}$ is factor 1.38 larger), can be seen to have a large impact with respect to the nearby mode. Assuming the rf cavities to have the same power limit as stated in Section 2.4 would mean increasing the number of cavities. Furthermore, the optimum coupling factor is proportional to the current and the number of cavities. This again influences the detuning frequency Δf which is proportional to β_{c0}.

Feedback systems will be required to counteract multibunch instabilities occurring in the *transverse plane* [1]. One source is the transverse higher-order modes of the rf cavities. Based on the experience with the multibunch feedback systems in PETRA [65] and HERA, which are capable of providing a damping rate of several kHz, one can assume that a similar system for the damping ring will be able to guarantee suppression of HOM-driven transverse instabilities.
Another source giving rise to an instability is the transverse resistive wall effect of the vacuum chamber. This instability, however, is much easier to damp than the one driven by the cavity-HOMs, because it requires only a rather low-bandwidth feedback. It is conceivable, though, that a broad-band feedback can be made strong enough to damp the instability driven by the resistive wall effect as well, so that an additional system may not be necessary [1].

Appendix A

Formula Symbols

Table A.1: Most commonly used symbols.

c	velocity of light
C	circumference, capacity
e	elementary electric charge
E_b	nominal beam energy
f_0	revolution frequency
f_rf	rf frequency
F_b	bunch form factor
G	curvature function
h	longitudinal harmonic number $= \omega_\mathrm{rf}/\omega_0$
I	current
I_b	beam current
I_g	generator current
J_ε	damping partition number
$k_{\delta,\parallel}$	longitudinal loss factor of a point charge
$k_{\lambda,\parallel}$	longitudinal loss factor of a charge distribution
L	inductance
N_b	number of bunches in a bunch train
N_e	bunch population
$N_\mathrm{e}^\mathrm{ref}$	reference bunch population: 3.63×10^{10}
N_par	number of macroparticles (simulation)
P_b	power transferred to the beam (acc. mode)
P_c	power dissipated in the cavity (acc. mode)
P_r	reflected power (acc. mode)
P_γ	rate of loss of energy by radiation
q	overvoltage factor
q_b	bunch charge
Q	quality factor of a cavity mode
Q_L	loaded quality factor of a cavity mode
r_0	classical electron radius ($e^2/4\pi\epsilon_0 mc^2$), m rest mass of an electron
R	shunt impedance (resistance)

cont. on the next page

Most commonly used symbols – cont.

R_{L}	loaded shunt impedance
T_0	revolution time
T_ε	(synchrotron radiation) damping time
U_0	average synchrotron radiation loss per turn
V	voltage
V_{b}	beam-loading voltage
V_{g}	generator-induced voltage
V_{c}	total cavity voltage
V_{rf}	peak rf voltage
$\dot{V}_{\mathrm{RF}}$	slope of the rf voltage at the synchronous phase
W_k^n	wake on the nth turn seen by the kth particle (bunch)
$W_{\delta,\parallel}$	longitudinal delta wake function
$W_{\lambda,\parallel}$	longitudinal wake function of a charge distribution
$Z_\parallel$	longitudinal impedance
α_{c}	momentum compaction factor
α_ε	(synchrotron radiation) damping rate
β	velocity factor $= v/c$
β_{c}	coupling factor
β_{c0}	optimum coupling factor
γ	energy factor $= E/mc^2$
Γ	attenuation coefficient $= \omega_{\mathrm{r}}/2Q$
ΔT_{b}	bunch spacing (in time)
ε	energy deviation
κ	normalized bunch charge
λ	normalized longitudinal charge density
ν_{s}	synchrotron tune $= \omega_{\mathrm{s}}/\omega_0$
ν_{s0}	nominal synchrotron tune
$\sigma_{\varepsilon 0}$	natural energy spread of the beam
σ_{E0}	relative natural energy spread of the beam
σ_t	rms bunch length (in time) $= \sigma_z/c$
σ_z	rms bunch length (in distance)
τ	time displacement, longitudinal position
ϕ	phase angle
ϕ_{s}	synchronous phase (for $\sin\omega_{\mathrm{rf}}\tau$)
$\hat{\phi}_{\mathrm{s}}$	$\pi - \phi_{\mathrm{s}}$
ϕ_{nab}	nominal average bunch phase
ψ	detuning angle
ω_{r}	resonance frequency
$\bar{\omega}_{\mathrm{r}}$	natural angular frequency, $\sqrt{\omega_{\mathrm{r}}^2 - \Gamma^2}$
ω_{rf}	angular rf frequency
ω_{s}	synchrotron frequency
ω_{s0}	nominal synchrotron frequency

Appendix B

Fourier Transformation Relationships

The conventions used for the Fourier transformations in this work are based upon:

$$f(t) = \int_{-\infty}^{\infty} F(\omega) e^{i\omega t} \frac{d\omega}{2\pi} \quad \text{and} \tag{B.1}$$

$$F(\omega) = \int_{-\infty}^{\infty} f(t) e^{-i\omega t} dt. \tag{B.2}$$

For a Gaussian line-charge density, the formulae yield:

$$\lambda(s) = \frac{1}{\sqrt{2\pi}\sigma_z} \exp\left(-(s/\sigma_z)^2/2\right), \tag{B.3}$$

$$\tilde{\lambda}(\omega) = \exp\left(-(\sigma_z \omega/c)^2/2\right). \tag{B.4}$$

The longitudinal impedance is defined as the negative of the Fourier transform of the longitudinal wake function. The transformations read in the time and space domain:

$$Z_{\|}(\omega) = -\int_{-\infty}^{\infty} W_{\delta,\|}(t) e^{-i\omega t} dt \qquad \text{and} \quad Z_{\|}(\omega) = \frac{-1}{c} \int_{-\infty}^{\infty} W_{\delta,\|}(s) e^{-i\omega s/c} ds, \tag{B.5}$$

$$W_{\delta,\|}(t) = \frac{-1}{2\pi} \int_{-\infty}^{\infty} Z_{\|}(\omega) e^{i\omega t} d\omega \qquad \text{and} \quad W_{\delta,\|}(s) = \frac{-1}{2\pi} \int_{-\infty}^{\infty} Z_{\|}(\omega) e^{i\omega s/c} d\omega. \tag{B.6}$$

A number of Fourier transform pairs are listed in Table B.1. Another pair is given by the *Convolution Theorem*. The convolution of two functions $g(t)$ and $h(t)$, denoted by $g \star h$, is defined by

$$g \star h \equiv \int_{-\infty}^{\infty} g(\tau) h(t-\tau)\, d\tau. \tag{B.7}$$

Its transform pair is $G(\omega)H(\omega)$. In other words, the Fourier transform of the convolution is just the product of the individual Fourier transforms. Note that the wake potential of a bunch is obtained by the convolution of the charge distribution with the wake function of a point charge.
The following identity (the Poisson sum formula) is also used:

$$\sum_{k=-\infty}^{\infty} f(k\mathcal{L}) = \frac{1}{\mathcal{L}} \sum_{p=-\infty}^{\infty} F\left(\frac{2\pi p}{\mathcal{L}}\right), \tag{B.8}$$

	Time domain $f(t)$	Frequency domain $F(\omega)$
Differentiation w.r.t. t	$f'(t)$	$i\omega F(\omega)$
Frequency shifting	$e^{i\hat{\omega}t}f(t)$	$F(\omega - \hat{\omega})$
Time shifting	$f(t+a)$	$e^{i\omega a}F(\omega)$
	$e^{-i(t+a)\hat{\omega}}f'(t+a)$	$i(\omega+\hat{\omega})e^{i\omega a}F(\omega+\hat{\omega})$
Time scaling	$f(at)$	$\frac{1}{\|a\|}F(\omega/a)$
Frequency scaling	$\frac{1}{\|a\|}f(t/a)$	$F(a\omega)$
	1	$2\pi\delta(\omega)$
	$\delta(t)$	1

Table B.1: Fourier transform pairs.

where $f(t)$ and $F(\omega)$ are arbitrary Fourier transform pairs. In other words, summing a function at a regular interval $\mathcal{L}$ is equal to summing over its Fourier transform at the regular intervals $2\pi/\mathcal{L}$. One special case of Eq. (B.8) is

$$2\pi \sum_{k=-\infty}^{\infty} \delta(y - 2\pi k) = \sum_{p=-\infty}^{\infty} e^{ipy}. \tag{B.9}$$

Appendix C

Cavities

C.1 The Impedance of a Single Cavity Mode

The impedance of the equivalent circuit model for a cavity mode, Figure 3.7 on page 32, is

$$Z_{\parallel}(\omega) = \frac{1}{\frac{1}{R} + \frac{1}{i\omega L} + i\omega C} = \frac{R}{1 + iQ\left(\frac{\omega}{\omega_{\mathrm{r}}} - \frac{\omega_{\mathrm{r}}}{\omega}\right)}, \tag{C.1}$$

where the quality factor Q (see Eq. (3.62)) has been used. The real and imaginary impedance components are depicted in Figure C.1. Two equivalent expressions for them are (with Γ from Eq. (3.68)):

$$\mathfrak{Re}\, Z_{\parallel}(\omega) = 2k_{\parallel}\frac{2\Gamma\omega^2}{(\omega^2 - \omega_{\mathrm{r}}^2)^2 + (2\Gamma\omega)^2} = R\frac{1}{1 + Q^2(\omega/\omega_{\mathrm{r}} - \omega_{\mathrm{r}}/\omega)^2}, \tag{C.2}$$

$$\mathfrak{Im}\, Z_{\parallel}(\omega) = 2k_{\parallel}\frac{-(\omega^2 - \omega_{\mathrm{r}}^2)\omega}{(\omega^2 - \omega_{\mathrm{r}}^2)^2 + (2\Gamma\omega)^2} = R\frac{-Q(\omega/\omega_{\mathrm{r}} - \omega_{\mathrm{r}}/\omega)}{1 + Q^2(\omega/\omega_{\mathrm{r}} - \omega_{\mathrm{r}}/\omega)^2}. \tag{C.3}$$

The complex impedance may also be written in the form $Z_{\parallel}(\omega) = |Z_{\parallel}(\omega)|e^{i\psi}$ where the absolute value is

$$|Z_{\parallel}(\omega)| = \frac{R}{\sqrt{1 + Q^2\left(\frac{\omega_{\mathrm{r}}}{\omega} - \frac{\omega}{\omega_{\mathrm{r}}}\right)^2}} \tag{C.4}$$

and the phase ψ is given by

$$\tan\psi = Q\left(\frac{\omega_{\mathrm{r}}}{\omega} - \frac{\omega}{\omega_{\mathrm{r}}}\right). \tag{C.5}$$

For large quality factors, the absolute impedance drops at the frequencies $\omega_{\mathrm{r}} \pm \Gamma$ to $1/\sqrt{2}$ of its maximum value and the real part of the impedance to half its maximum value. The frequency dependence of the amplitude is known as the Lorentz curve; for large quality factors, Γ matches the definition of the bandwidth (see also below).

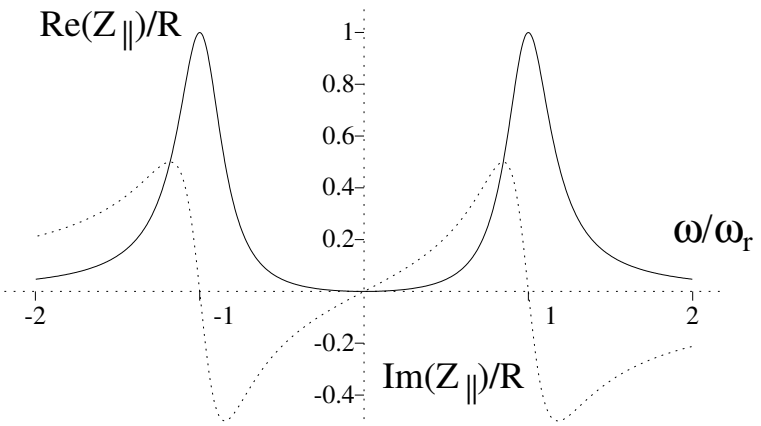

Figure C.1: Real (solid line) and imaginary (dashed line) parts of the impedance of an LRC circuit ($Q = 3$) which acts as a model for the impedance of a single cavity mode.

Another possibility for describing the impedance is

$$Z_{\parallel}(\omega) = \frac{R}{1 - i \tan\psi}. \tag{C.6}$$

The case of an rf-driven cavity is noteworthy, which is encountered in Section 3.3.5. A sinusoidal driving current $I(t)$ results in a voltage $V(t)$ according to

$$V(t) = Z_{\parallel} \cdot I(t). \tag{C.7}$$

Since this is a multiplication in the complex plane, one gets the same time dependence for $V(t)$ but with the phase shift ψ, which is called the *tuning angle*:

$$V(t) = \widehat{V} \sin(\omega t + \psi). \tag{C.8}$$

The peak voltage is $\widehat{V} = |Z_{\parallel}| \cdot \hat{I}$.
Now, if the generator frequency ω is very close to the fundamental cavity resonance ω_{r} it is possible to use the following approximations

$$\tan\psi \approx 2Q_{\mathrm{L}} \frac{\Delta\omega}{\omega} \tag{C.9}$$

and

$$\widehat{V}(\Delta\omega) \approx \frac{R\hat{I}}{\sqrt{1 + \left(2Q_{\mathrm{L}} \frac{\Delta\omega}{\omega}\right)^2}}, \tag{C.10}$$

where $\Delta\omega = \omega_{\mathrm{r}} - \omega$. The frequency dependence of the peak voltage is the same as that of the absolute impedance. The bandwidth $\omega_{1/2}$ of a loaded cavity is defined as the frequency bandwidth where the voltage drops to $1/\sqrt{2}$ of its maximum $\widehat{V}$:

$$\omega_{1/2} = \frac{\omega}{2Q_{\mathrm{L}}}. \tag{C.11}$$

As mentioned in Section 3.3.3, the wake function can be obtained by calculating it as the Fourier transform of the circuit impedance. Rewriting the impedance starting with Eq. (C.1) as

$$Z_{\parallel}(\omega) = \frac{R\omega\omega_{\mathrm{r}}}{iQ[\omega^2 - \omega_{\mathrm{r}}^2 - i\omega\omega_{\mathrm{r}}/Q]} = \frac{R\omega\omega_{\mathrm{r}}}{iQ[\omega - (\bar{\omega}_{\mathrm{r}} + i\Gamma)][\omega - (-\bar{\omega}_{\mathrm{r}} + i\Gamma)]} \tag{C.12}$$

shows that it is a rational function, the degree of the denominator being larger than the numerator, with two poles in the upper complex plane. $\bar{\omega}_{\mathrm{r}}$ is defined in Eq. (3.69).
For $t > 0$, one has:

$$\begin{aligned} W_{\delta,\parallel}(t) &= \frac{-1}{2\pi} \int_{-\infty}^{\infty} Z_{\parallel}(\omega) \exp(i\omega t)\, d\omega \\ &= \frac{-1}{2\pi} \cdot 2\pi i \sum_{\mathfrak{Im}\ \omega>0} \mathrm{Res}_{\omega}\, Z_{\parallel}(\tilde{\omega}) \exp(i\tilde{\omega}t) \\ &= \frac{-R\omega_{\mathrm{r}}}{Q} \left(\frac{i\Gamma + \bar{\omega}_{\mathrm{r}}}{2\bar{\omega}_{\mathrm{r}}} \exp((-\Gamma + i\bar{\omega}_{\mathrm{r}})t) + \frac{i\Gamma - \bar{\omega}_{\mathrm{r}}}{-2\bar{\omega}_{\mathrm{r}}} \exp((-\Gamma - i\bar{\omega}_{\mathrm{r}})t) \right) \\ &= \frac{-1}{C} \exp(-\Gamma t) \left(\cos\bar{\omega}_{\mathrm{r}}t - \frac{\Gamma}{\bar{\omega}_{\mathrm{r}}} \sin\bar{\omega}_{\mathrm{r}}t \right). \end{aligned} \tag{C.13}$$

Two factors have been used here: the residue theorem and the vanishing of the integration of $Z_{\parallel}(\omega)\exp(i\omega t)$ over the path $\gamma_1+\gamma_2+\gamma_3$ in the upper complex plane, as shown in Figure C.2, in the limit $r_1, r_2, s \to \infty$ (see [66, Theorem 6.2]).

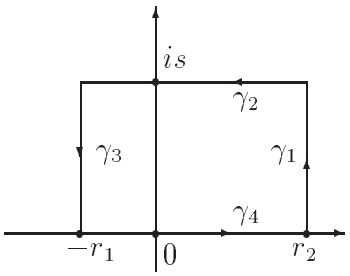

Figure C.2: Integration path of the Fourier transformation to obtain the wake function.

C.2 Time Development of the Wake Function of a Cavity Mode with Repetitive Beam Loading

As in Eq. (4.21), during the following derivation the index m for the different modes has been omitted.
The wake function at a time t after a delta-impulse is given by Eq. (3.70):

$$V(t) = 2k_{\delta,\parallel} \exp(-\Gamma t) \left(\cos\bar{\omega}_{\mathrm{r}}t - \frac{\Gamma}{\bar{\omega}_{\mathrm{r}}} \sin\bar{\omega}_{\mathrm{r}}t \right) V(0),$$

where $\omega_\mathrm{r} = 1/\sqrt{LC}$ is the resonant angular frequency, $\Gamma = \omega_\mathrm{r}/2Q$ is the cavity damping factor, and $\bar{\omega}_\mathrm{r} = \sqrt{\omega_\mathrm{r}^2 - \Gamma^2}$ is the natural angular frequency.
The wake function can be written as $V(t) = V_r(t) - (\Gamma/\bar{\omega}_\mathrm{r})V_i(t)$ if $V_r(t)$ and $V_i(t)$ denote the real and imaginary components of $2k_{\delta,\parallel}\exp[(-\Gamma + i\bar{\omega}_\mathrm{r})t]$.
Using the cosine and sine addition theorems

$$\begin{aligned} \cos\bar{\omega}_\mathrm{r}t_2 &= \cos\bar{\omega}_\mathrm{r}\Delta t\cos\bar{\omega}_\mathrm{r}t_1 - \sin\bar{\omega}_\mathrm{r}\Delta t\sin\bar{\omega}_\mathrm{r}t_1 \\ \text{and} \quad \sin\bar{\omega}_\mathrm{r}t_2 &= \sin\bar{\omega}_\mathrm{r}\Delta t\cos\bar{\omega}_\mathrm{r}t_1 + \cos\bar{\omega}_\mathrm{r}\Delta t\sin\bar{\omega}_\mathrm{r}t_1, \end{aligned}$$

where $\Delta t = t_2 - t_1$, it is possible to relate the terms V_r and V_i of any two times t_1 and t_2:

$$\begin{pmatrix} V_r(t_2) \\ V_i(t_2) \end{pmatrix} = e^{-\Gamma\Delta t}\begin{pmatrix} \cos\bar{\omega}_\mathrm{r}\Delta t & -\sin\bar{\omega}_\mathrm{r}\Delta t \\ \sin\bar{\omega}_\mathrm{r}\Delta t & \cos\bar{\omega}_\mathrm{r}\Delta t \end{pmatrix}\begin{pmatrix} V_r(t_1) \\ V_i(t_1) \end{pmatrix}.$$

By exchanging the wake voltages and inductance currents for V_r and V_i the desired equation is obtained in three steps.
Using the abbreviations $S = \sin\bar{\omega}_\mathrm{r}\Delta t$ and $C = \cos\bar{\omega}_\mathrm{r}\Delta t$ and replacing $V_r(t_2)$ with the wake voltage at the time t_2 one obtains

$$\begin{pmatrix} V(t_2) \\ V_i(t_2) \end{pmatrix} = e^{-\Gamma\Delta t}\begin{pmatrix} C - \frac{\Gamma}{\bar{\omega}_\mathrm{r}}S & -S - \frac{\Gamma}{\bar{\omega}_\mathrm{r}}C \\ S & C \end{pmatrix}\begin{pmatrix} V_r(t_1) \\ V_i(t_1) \end{pmatrix}.$$

In a second step, the wake voltage at the time t_1 is introduced on the right-hand side of the equation, yielding

$$\begin{pmatrix} V(t_2) \\ V_i(t_2) \end{pmatrix} = e^{-\Gamma\Delta t}\begin{pmatrix} C - \frac{\Gamma}{\bar{\omega}_\mathrm{r}}S & -(1 + (\frac{\Gamma}{\bar{\omega}_\mathrm{r}})^2)S \\ S & C + \frac{\Gamma}{\bar{\omega}_\mathrm{r}}S \end{pmatrix}\begin{pmatrix} V(t_1) \\ V_i(t_1) \end{pmatrix}.$$

The current in the inductance $\dot{I}_L(t) = V(t)/L$ so that $I_L(t) = V_i(t)/(L\bar{\omega}_\mathrm{r})$.
Utilizing the relationship $L = R/(\omega_\mathrm{r}Q)$ one arrives at the desired form

$$\begin{pmatrix} V(t_2) \\ I_L(t_2) \end{pmatrix} = e^{-\Gamma\Delta t}\begin{pmatrix} C - \frac{\Gamma}{\bar{\omega}_\mathrm{r}}S & -\frac{\omega_\mathrm{r}R}{\bar{\omega}_\mathrm{r}Q}S \\ \frac{\omega_\mathrm{r}Q}{\bar{\omega}_\mathrm{r}R}S & C + \frac{\Gamma}{\bar{\omega}_\mathrm{r}}S \end{pmatrix}\begin{pmatrix} V(t_1) \\ I_L(t_1) \end{pmatrix}.$$

C.3 Transient Behaviour of a Cavity driven by a Harmonic Current

The differential equation for a driven LCR circuit as expressed in Eq. (3.67) is taken as the starting-point:

$$\ddot{V}(t) + 2\Gamma\dot{V}(t) + \omega_\mathrm{r}^2 V(t) = 2\Gamma R_\mathrm{L}\dot{I}(t), \tag{C.14}$$

where the loaded cavity impedance, R_L, and $\Gamma = \omega_\mathrm{r}/(2Q_\mathrm{L})$ have been used.
The current is assumed to be harmonic with a frequency ω close to the resonance frequency ω_r so that the approximation

$$\omega_\mathrm{r}^2 - \omega^2 \approx 2\omega\Delta\omega \tag{C.15}$$

with $\Delta\omega = \omega_\mathrm{r} - \omega$ is valid. A further assumption in the derivation of the transient behaviour of the cavity is that the loaded quality factor is sufficiently large so that $\Gamma/\omega_\mathrm{r} \ll 1$ holds.
For the current and voltage an ansatz is chosen where the fast rf oscillation is separated from the slowly changing amplitudes and phases:

$$V(t) = \mathfrak{Re}\,\underline{V}(t)e^{i\omega t},$$
$$I(t) = \mathfrak{Re}\,\underline{I}(t)e^{i\omega t}.$$

Substitution of these expressions for the current and voltage in Eq. (C.14) delivers

$$\ddot{\underline{V}} + (2i\omega + \Gamma)\dot{\underline{V}} + (\omega_\mathrm{r}^2 - \omega^2 + 2i\omega\Gamma)\underline{V} = 2R_\mathrm{L}\Gamma(\dot{\underline{I}} + i\omega\underline{I}).$$

Application of the approximation (C.15) and division by 2ω leads then to

$$\frac{1}{2\omega}\ddot{\underline{V}} + \left(\frac{\Gamma}{\omega} + i\right)\dot{\underline{V}} + (\Delta\omega + i\Gamma)\underline{V} = R_\mathrm{L}\frac{\Gamma}{\omega}(\dot{\underline{I}} + i\omega\underline{I}).$$

The small second-order term of the voltage can be neglected. Substituting the resonance frequency for the rf frequency and solving for the first-order term gives:

$$\begin{aligned}\dot{\underline{V}} &= \frac{1}{\Gamma/\omega_\mathrm{r} + i}\left[(-\Delta\omega - i\Gamma)\underline{V} + R_\mathrm{L}\frac{\Gamma}{\omega_\mathrm{r}}(\dot{\underline{I}} + i\omega_\mathrm{r}\underline{I})\right] \\ &= \frac{1}{1 + (\Gamma/\omega_\mathrm{r})^2}\left[\left(-\Gamma - \Delta\omega\frac{\Gamma}{\omega_\mathrm{r}} + i\left(\Delta\omega - \Gamma\frac{\Gamma}{\omega_\mathrm{r}}\right)\right)\underline{V}\right. \\ &\qquad \left. + R_\mathrm{L}\frac{\Gamma}{\omega_\mathrm{r}}\left(\frac{\Gamma}{\omega_\mathrm{r}} - i\right)\dot{\underline{I}} + R_\mathrm{L}\Gamma\left(1 + i\frac{\Gamma}{\omega_\mathrm{r}}\right)\underline{I}\right]. \end{aligned} \tag{C.16}$$

Neglecting all the terms with Γ/ω_r, which was assumed to be much smaller than one, the differential equation can be reduced to

$$\dot{\underline{V}} = (-\Gamma + i\Delta\omega)\underline{V} + R_\mathrm{L}\Gamma\underline{I}. \tag{C.17}$$

This differential equation is of the form

$$\dot{x}(t) = Ax(t) + Bu(t)$$

whose solution is simply

$$x(t) = e^{At}x(0) + B\int_0^t e^{A(t-t')}u(t')dt';$$

hence

$$\underline{V}(t) = \underline{V}(0)e^{(-\Gamma + i\Delta\omega)t} + R_\mathrm{L}\Gamma\int_0^t e^{(-\Gamma + i\Delta\omega)(t-t')}\underline{I}(t')dt'. \tag{C.18}$$

For a constant current $\underline{I}$, one obtains

$$\begin{aligned}\underline{V}(t) &= \underline{V}(0)e^{(-\Gamma+i\Delta\omega)t} + R_{\mathrm{L}}\Gamma\underline{I}\int_0^t e^{(-\Gamma+i\Delta\omega)(t-t')}dt' \\ &= \underline{V}(0)e^{(-\Gamma+i\Delta\omega)t} + \frac{R_{\mathrm{L}}\Gamma\underline{I}}{(\Gamma-i\Delta\omega)}(1-e^{(-\Gamma+i\Delta\omega)t}).\end{aligned}$$

Defining, as elsewhere, $\tan\psi = \Delta\omega/\Gamma$, the above equation can be rewritten as

$$\underline{V}(t) = \underline{V}(0)e^{(-\Gamma+i\Delta\omega)t} + R_{\mathrm{L}}\underline{I}\cos\psi e^{i\psi}(1-e^{(-\Gamma+i\Delta\omega)t}). \tag{C.19}$$

The inverse of Γ is called the cavity filling time.

C.4 The Diffraction-Model Wake Potential of a Gaussian bunch

The diffraction-model impedance has the same high frequency dependence as the impedance of a pillbox with attached tubes [48].
According to the convolution theorem, the longitudinal wake potential of a normalized charge density can be expressed by the impedance of a point charge and the Fourier transform of the distribution:

$$W_{\lambda,\parallel}(t) = \frac{-1}{2\pi}\int_{-\infty}^{\infty} Z_{\parallel}(\omega)\tilde{\lambda}(\omega)e^{i\omega t}d\omega. \tag{C.20}$$

For a Gaussian bunch and the impedance

$$Z_{\parallel}(\omega) = \frac{1-i\,\mathrm{sign}(\omega)}{\sqrt{|\omega|}}R_{\mathrm{c}}, \tag{C.21}$$

one obtains

$$\begin{aligned}W_{\lambda,\parallel}(t) &= \frac{-1}{2\pi}\int_{-\infty}^{\infty}\frac{1-i\,\mathrm{sign}(\omega)}{\sqrt{|\omega|}}R_{\mathrm{c}}\,e^{-(\omega\sigma_t)^2/2}e^{i\omega t}d\omega \\ &= \frac{-R_{\mathrm{c}}}{2\pi}\int_0^{\infty}\left((1-i)\frac{1}{\sqrt{\omega}}e^{-(\omega\sigma_t)^2/2}e^{i\omega t} + (1+i)\frac{1}{\sqrt{\omega}}e^{-(\omega\sigma_t)^2/2}e^{-i\omega t}\right)d\omega.\end{aligned} \tag{C.22}$$

According to ref. [67], the following equality holds:

$$\int_0^{\infty}\frac{1}{\sqrt{\omega}}e^{-a\omega^2-i\omega t}d\omega = \frac{\pi\sqrt{|t|}}{\sqrt{8a}}\left(I_{-1/4}(b) - i\,\mathrm{sign}(t)I_{1/4}(b)\right)e^{-b}, \tag{C.23}$$

where $b = t^2/8a$; therefore, with $a = \sigma_t^2/2$ the wake potential of a Gaussian distribution is

$$\begin{aligned}W_{\lambda,\parallel}(t) &= \frac{-R_{\mathrm{c}}}{2\pi}\frac{\pi\sqrt{|t|}}{\sqrt{8a}}\left((1-i)\left[I_{-1/4}(b) - i\,\mathrm{sign}(-t)I_{1/4}(b)\right]\right. \\ &\qquad \left. + (1+i)\left[I_{-1/4}(b) - i\,\mathrm{sign}(t)I_{1/4}(b)\right]\right)e^{-b} \\ &= \frac{-R_{\mathrm{c}}\sqrt{|t|}}{2\sigma_t}\left(I_{-1/4}(t^2/4\sigma_t^2) + \mathrm{sign}(t)I_{1/4}(t^2/4\sigma_t^2)\right)e^{-t^2/4\sigma_t^2}.\end{aligned} \tag{C.24}$$

The loss factor can be evaluated as

$$\begin{aligned} k_{\lambda,\|} &= -\int_{-\infty}^{\infty} W_{\lambda,\|}(t)\lambda(t)dt \\ &= \frac{R_\mathrm{c}}{2\sigma_t}\int_{-\infty}^{\infty} \sqrt{|t|} I_{-1/4}(t^2/4\sigma_t^2) e^{-t^2/4\sigma_t^2} \frac{1}{\sqrt{2\pi}\sigma_t} e^{-t^2/2\sigma_t^2} dt \\ &= \frac{R_\mathrm{c}}{\sqrt{2\pi}\sigma_t^2}\int_0^{\infty} \sqrt{t} I_{-1/4}(t^2/4\sigma_t^2) e^{-3t^2/4\sigma_t^2} dt. \end{aligned}$$

Now let $x = t^2/4\sigma_t^2$; a change of variable leads to

$$k_{\lambda,\|} = \frac{R_\mathrm{c}}{\sqrt{2\pi}\sigma_t^2}\sqrt{2}\sigma_t^{3/2}\int_0^{\infty} x^{-1/4} I_{-1/4}(x) e^{-3x} dx. \tag{C.25}$$

The integral can be found in [68, p. 712] which says that

$$\int_0^{\infty} x^\nu I_\nu(bx) e^{-ax} dx = \frac{(2b)^\nu \Gamma(\nu + 1/2)}{\sqrt{\pi}(a^2 - b^2)^{\nu+1/2}}\,. \tag{C.26}$$

With $\nu = -1/4$, $a = 3$, and $b = 1$ the loss factor can be determined as

$$k_{\lambda,\|} = \frac{\Gamma(1/4)}{2\pi\sqrt{\sigma_t}} R_\mathrm{c}\,. \tag{C.27}$$

Appendix D

Potential-Well Distortion

D.1 A Bunch Lengthening Estimate for a Potential Well Distorted by an Inductive Impedance.

The starting-point is the Haissinski equation.
The induced voltage

$$V_{\rm ind}(t) = -Lq_{\rm b}\,\frac{d\lambda}{dt} \tag{D.1}$$

is inserted into Eq. (3.142)

$$\lambda(\tau) = \lambda(0)\exp\left(-\frac{\tau^2}{2\sigma_{t0}^2} + \frac{1}{|\dot{V}_{\rm RF}|\sigma_{t0}^2}\int_0^\tau V_{\rm ind}(t)dt\right),$$

where the rf voltage has been linearized, hereby giving

$$\lambda(\tau) = \lambda(0)\exp\left(-\frac{\tau^2}{2\sigma_{t0}^2} - \kappa\sigma_{t0}\left[\lambda(\tau) - \lambda(0)\right]\right). \tag{D.2}$$

The normalized charge κ is defined by Eq. (3.146). The goal is to find an approximate expression for the bunch shape and the bunch length for small distortions, i.e. for small κ. In the following, all equations are expanded to first order in κ; hence, when the bunch distribution at the synchronous phase $\lambda(0)$ is multiplied with κ, it is replaced by its zeroth-order term pertaining to a Gaussian distribution: $1/\sqrt{2\pi\sigma_{t0}^2} = \lambda^G(0)$.
Beginning with Eq. (D.2), one has

$$\lambda(\tau) \approx \lambda(0)\exp\left(-\frac{\tau^2}{2\sigma_{t0}^2}\right)\left(1 - \kappa\sigma_{t0}\left[\lambda(\tau) - \lambda^G(0)\right]\right), \tag{D.3}$$

where the exponential function has been expanded to first order in κ.
Gathering the terms with $\lambda(\tau)$, it follows that

$$\lambda(\tau)\left[1 + \frac{\kappa}{\sqrt{2\pi}}\exp\left(-\frac{\tau^2}{2\sigma_{t0}^2}\right)\right] \approx \lambda(0)\exp\left(-\frac{\tau^2}{2\sigma_{t0}^2}\right)\left[1 + \frac{\kappa}{\sqrt{2\pi}}\right].$$

Therefore,

$$\begin{aligned}\lambda(\tau) &\approx \lambda(0)\exp\left(-\frac{\tau^2}{2\sigma_{t0}^2}\right)\left[1+\frac{\kappa}{\sqrt{2\pi}}\right]\left[1-\frac{\kappa}{\sqrt{2\pi}}\exp\left(-\frac{\tau^2}{2\sigma_{t0}^2}\right)\right]\\ &\approx \lambda(0)\exp\left(-\frac{\tau^2}{2\sigma_{t0}^2}\right)\left(1+\frac{\kappa}{\sqrt{2\pi}}\left[1-\exp\left(-\frac{\tau^2}{2\sigma_{t0}^2}\right)\right]\right). \qquad \text{(D.4)}\end{aligned}$$

Substituting Eq. (D.4) into the normalization condition, $1 = \int_{-\infty}^{\infty}\lambda(\tau)d\tau$, delivers $\lambda(0)$ to first order in κ, and consequently $\lambda(\tau)$. It is

$$\begin{aligned}1 &\approx \lambda(0)\int_{-\infty}^{\infty}\left[1+\frac{\kappa}{\sqrt{2\pi}}\right]\exp\left(-\frac{\tau^2}{2\sigma_{t0}^2}\right)-\frac{\kappa}{\sqrt{2\pi}}\exp\left(-\frac{\tau^2}{\sigma_{t0}^2}\right)d\tau\\ &= \lambda(0)\left(\left[1+\frac{\kappa}{\sqrt{2\pi}}\right]\sqrt{2\pi}\sigma_{t0}-\frac{\kappa}{\sqrt{2\pi}}\sqrt{\pi}\sigma_{t0}\right)\\ &= \lambda(0)\sqrt{2\pi}\sigma_{t0}\left(1+\frac{\kappa}{\sqrt{2\pi}}(1-1/\sqrt{2})\right)\end{aligned}$$

so that

$$\lambda(0) \approx \frac{1}{\sqrt{2\pi}\sigma_{t0}}\left[1-\frac{\kappa}{\sqrt{\pi}}\frac{\sqrt{2}-1}{2}\right]. \qquad \text{(D.5)}$$

To evaluate the change in bunch length, the rms to the square is calculated to first order in κ using Eqs. (D.4) and (D.5). Applying the former equation gives

$$\begin{aligned}\int_{-\infty}^{\infty}\lambda(\tau)\tau^2 d\tau \approx \lambda(0)\int_{-\infty}^{\infty}&\left[1+\frac{\kappa}{\sqrt{2\pi}}\right]\tau^2\exp\left(-\frac{\tau^2}{2\sigma_{t0}^2}\right)\\ &-\frac{\kappa}{\sqrt{2\pi}}\tau^2\exp\left(-\frac{\tau^2}{\sigma_{t0}^2}\right)d\tau.\end{aligned}$$

Since $\int_{-\infty}^{\infty}\tau^2\exp(-\tau^2/(2b^2))d\tau = \sqrt{2\pi}b^3$, one obtains

$$\begin{aligned}\int_{-\infty}^{\infty}\lambda(\tau)\tau^2 d\tau &\approx \lambda(0)\left(\left[1+\frac{\kappa}{\sqrt{2\pi}}\right]\sqrt{2\pi}\sigma_{t0}^3-\frac{\kappa}{\sqrt{2\pi}}\sqrt{\pi}\sigma_{t0}^3/2\right)\\ &= \lambda(0)\sigma_{t0}^3\sqrt{2\pi}\left[1+\frac{\kappa}{\sqrt{2\pi}}(1-2^{-3/2})\right].\end{aligned}$$

Inserting Eq. (D.5) for $\lambda(0)$ leads to

$$\begin{aligned}\int_{-\infty}^{\infty}\lambda(\tau)\tau^2 d\tau &\approx \sigma_{t0}^2\left[1-\frac{\kappa}{\sqrt{\pi}}\frac{\sqrt{2}-1}{2}\right]\left[1+\frac{\kappa}{\sqrt{\pi}}\frac{2\sqrt{2}-1}{4}\right]\\ &\approx \sigma_{t0}^2\left(1+\frac{\kappa}{4\sqrt{\pi}}\right). \qquad \text{(D.6)}\end{aligned}$$

The relative change in bunch length relates to small κ according to Eq. (D.6) as

$$\frac{\Delta\sigma_t}{\sigma_{t0}} \approx \frac{\kappa}{8\sqrt{\pi}} = \frac{Lq_{\mathrm{b}}}{8\sqrt{\pi}|\dot{V}_{\mathrm{RF}}|\sigma_{t0}^3}. \qquad \text{(D.7)}$$

D.2 Derivation of the Resistive Impedance Potential-Well Solution

Eq. (3.148) is derived by using the differential equation option [70].
Eq. (3.141) reads in this case (the delta wake function is the delta function times a factor $-R$)

$$\frac{\lambda'}{\lambda} = -U_{\mathrm{P}}'(\tau) - \kappa\lambda, \tag{D.8}$$

where the normalized charge κ is defined by Eq. (3.149).
The above differential equation is of the Bernoulli type. It is converted to a linear equation by the substitution $\lambda = 1/y$:

$$y' = U_{\mathrm{P}}'(\tau)y + \kappa. \tag{D.9}$$

The solution of homogeneous differential equation is a constant times the exponent of $U_{\mathrm{P}}(\tau)$. A particular solution of the inhomogeneous equation is found by variation of the constant. Consequently, the complete solution is

$$\lambda(\tau) = \frac{\exp[-U_{\mathrm{P}}(\tau)]}{C + \kappa\int_0^\tau \exp[-U_{\mathrm{P}}(t)]dt}. \tag{D.10}$$

The constant C is determined through the normalization condition,

$$\int_{-\infty}^{\infty} \frac{\exp[-U_{\mathrm{P}}(\tau)]}{C + \kappa\int_0^\tau \exp[-U_{\mathrm{P}}(t)]dt} d\tau = 1. \tag{D.11}$$

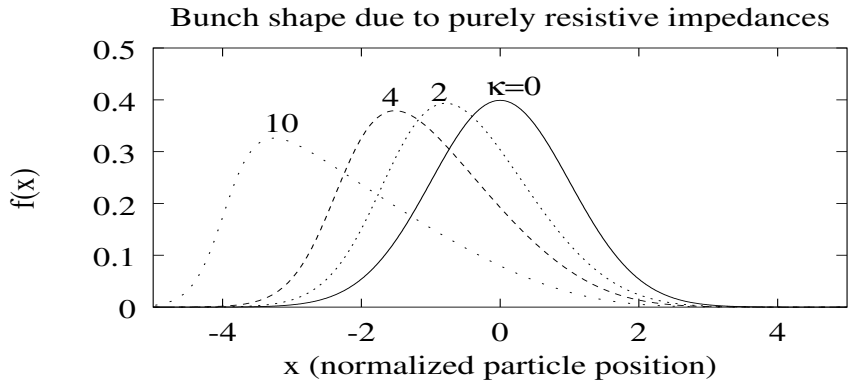

Figure D.1: Bunch shape for different beam intensities according to Eq. (D.15), where $\lambda(x) = f(x)/\sigma_{t0}$ and $x = \tau/\sigma_{t0}$.

Using the fact that the numerator is proportional to the derivative of the denominator, we can evaluate the integral to get

$$\ln\left(\frac{C + \kappa\int_0^{\infty} \exp[-U_{\mathrm{P}}(t)]dt}{C + \kappa\int_0^{-\infty} \exp[-U_{\mathrm{P}}(t)]dt}\right) = \kappa. \tag{D.12}$$

For a symmetric potential $U_{\mathrm{P}}(t)$, one can continue the analytical derivation using the relationship

$$\operatorname{arctanh} x = \frac{1}{2} \ln \frac{1+x}{1-x}, \tag{D.13}$$

and hence obtain

$$C = \frac{\kappa \int_0^\infty \exp[-U_{\mathrm{P}}(t)]dt}{\tanh(\kappa/2)}. \tag{D.14}$$

For a parabolic potential well, $U_{\mathrm{P}}(\tau) = \tau^2/2\sigma_{t0}^2$, the integral in the denominator of (D.14) becomes simply $\sigma_{t0}\sqrt{\pi/2}$, and the full solution can be written as

$$\lambda(\tau) = \frac{\sqrt{2/\pi}\exp(-\tau^2/2\sigma_{t0}^2)}{\kappa\sigma_{t0}\left[\coth(\kappa/2) + \operatorname{erf}(\tau/\sqrt{2}\sigma_{t0})\right]}. \tag{D.15}$$

The resistivity of the 40 fast kickers (approx. $40 \times 114\,\Omega$) seen by the 9.5 mm bunch corresponds to a κ-value of approximately two.

Appendix E

Multibunch Beam Signal

Particles in a storage ring oscillate in the longitudinal and transverse dimensions; therefore, it is natural to use the frequency domain for analyzing many beam generated signals. As will be seen, the synchrotron oscillation introduces a frequency modulation which corresponds to the frequencies appearing in the formulae of multibunch instabilities.
Observed at a fixed location where the source of the impedance is located, the beam signal of N_b circulating point bunches of equal charge in N_b equidistant buckets executing the μth multibunch mode Ω_μ and including synchrotron oscillation is

$$S(t) \propto \sum_{k=-\infty}^{\infty} \sum_{m=0}^{N_\mathrm{b}-1} \delta\left(t - \left\{kT_0 + \frac{m}{N_\mathrm{b}}T_0 + \hat{\tau}\cos(\Omega_\mu t + \Phi_m^\mu)\right\}\right) \tag{E.1}$$

with

$$\Phi_m^\mu = \frac{2\pi\mu m}{N_\mathrm{b}}, \quad \mu = 0, 1, \ldots, N_\mathrm{b} - 1. \tag{E.2}$$

The δ-function in Eq. (E.1) can be replaced by using the identity

$$\sum_{p=-\infty}^{\infty} \exp(ip\omega_0 y) = T_0 \sum_{k=-\infty}^{\infty} \delta(y - kT_0), \tag{E.3}$$

which follows from (B.9) and $|a|\delta(ax) = \delta(x)$.
This leads to

$$S(t) \propto \sum_{p=-\infty}^{\infty} \sum_{m=0}^{N_\mathrm{b}-1} \exp ip\omega_0 \left(t - \left\{\frac{m}{N_\mathrm{b}}T_0 + \hat{\tau}\cos(\Omega_\mu t + \Phi_m^\mu)\right\}\right). \tag{E.4}$$

This can be rewritten using Bessel functions,

$$\exp(-ix\cos\Phi) = \sum_{l=-\infty}^{\infty} i^{-l} J_l(x) e^{il\Phi}, \tag{E.5}$$

and thus the beam signal may be expressed as

$$S(t) \propto \sum_{p=-\infty}^{\infty} \sum_{l=-\infty}^{\infty} \sum_{m=0}^{N_\mathrm{b}-1} i^{-l} J_l(p\omega_0\hat{\tau}) \exp\left(ip\omega_0\Big(t - \frac{m}{N_\mathrm{b}}T_0\Big) + il(\Omega_\mu t + \Phi_m^\mu)\right).$$

The sum over the factors determined by the bunch number (label "m") reduces to one term:

$$\begin{aligned} S(t) &\propto \sum_{p=-\infty}^{\infty} \sum_{l=-\infty}^{\infty} i^{-l} J_l(p\omega_0\hat{\tau}) \exp(i(p\omega_0 + l\Omega_\mu)t) \sum_{m=0}^{N_\mathrm{b}-1} \exp\left(2\pi i(-p+l\mu)\frac{m}{N_\mathrm{b}}t\right) \\ &\propto \sum_{p=-\infty}^{\infty} \sum_{l=-\infty}^{\infty} i^{-l} J_l(p\omega_0\hat{\tau}) \exp(i(p\omega_0 + l\Omega_\mu)t) N_\mathrm{b}\delta_{(-p+l\mu),nN_\mathrm{b}} \\ &\propto \sum_{p=-\infty}^{\infty} \sum_{l=-\infty}^{\infty} i^{-l} J_l((pN_\mathrm{b} + l\mu)\omega_0\hat{\tau}) \exp\left(i(pN_\mathrm{b}\omega_0 + l\mu\omega_0 + l\Omega_\mu)t\right). \end{aligned}$$

The Fourier transform of the signal is given by

$$S(\omega) = \int_{-\infty}^{\infty} e^{-i\omega t} S(t) dt.$$

Application of the identity $\int e^{-i\omega t} dt = 2\pi\delta(\omega)$ delivers the beam spectrum in the form

$$S(\omega) \propto \sum_{p=-\infty}^{\infty} \sum_{l=-\infty}^{\infty} i^{-l} J_l((pN_\mathrm{b} + l\mu)\omega_0\hat{\tau}) \delta\left(\omega - (pN_\mathrm{b}\omega_0 + l\mu\omega_0 + l\Omega_\mu)\right). \tag{E.6}$$

The spectrum is a line spectrum. Firstly, there is a set of δ-functions which correspond to the static potential-well effect. They are located at $\omega = pN_\mathrm{b}\omega_0$ and their amplitudes are proportional to $J_0(\omega\hat{\tau})$. Secondly, for every rotation harmonic which is an integer multiple of N_b, i.e. for each p, there is a set of sidebands around $pN_\mathrm{b}\omega_0$. The lth sideband ($l = \pm$ integers) occurs at $pN_\mathrm{b}\omega_0 + l\mu\omega_0 + l\Omega_\mu$; therefore, it is mode-dependent. Their spectral strengths are proportional to $J_l(\omega\hat{\tau})$ as well. As the argument of the Bessel functions is proportional to the oscillation amplitude $\hat{\tau}$, the width of the spectrum behaves like $\hat{\tau}^{-1}$. Consequently, when considering small synchrotron oscillation amplitudes, one may neglect all terms with $|l| > 1$. This can also be seen when the cosine term in the exponential function in Eq. (E.4) is approximated by the first-order Taylor expansion instead of by using Bessel functions,

$$\begin{aligned} \exp\left(-ip\omega_0\hat{\tau}\cos(\Omega_\mu t + \Phi_m^\mu)\right) &\approx 1 - ip\omega_0\hat{\tau}\cos(\Omega_\mu t + \Phi_m^\mu) \\ &= 1 - \frac{ip\omega_0\hat{\tau}}{2}\left(\exp\left(i(\Omega_\mu t + \Phi_m^\mu)\right) + \exp\left(-i(\Omega_\mu t + \Phi_m^\mu)\right)\right). \end{aligned}$$

The first term relates to the rotation harmonics which are integer multiples of the number of bunches, while the exponential terms relate to the side bands.

When accounting for finite bunch lengths, further form factors are introduced. They are not to be confused with the Bessel form factors which arise from the beam executing synchrotron oscillations.
Further information on this subject can be obtained from [17, 69].

Appendix F

Approximate Invariant Amplitude of Motion

The approximate invariant of motion is frequently used to evaluate the instability rate in multibunch dynamics.
Disregarding wake fields, the tracking equations (4.14) and (4.15) can be written in the following matrix form:

$$\begin{pmatrix} \tau^{n+1} \\ \varepsilon^{n+1} \end{pmatrix} = \begin{pmatrix} 1 & \alpha_c T_0/E_b & \alpha_c T_0/E_b \\ \dot{V}^*_{RF} & 1+\alpha_c \dot{V}^*_{RF} T_0/E_b - 2T_0/T_\varepsilon & \alpha_c \dot{V}^*_{RF} T_0/E_b \end{pmatrix} \begin{pmatrix} \tau^n \\ \varepsilon^n \\ -U_0/2 \end{pmatrix}, \quad \text{(F.1)}$$

where $\dot{V}^*_{RF} = eF_b\dot{V}_{RF}$, if the rf voltage is linearized and under the assumption that there is only one rf frequency and no phase offset.
If the damping term is neglected, one can define the relative coordinates $\hat{\tau}^n = \tau^n/T_0$ and $\hat{\varepsilon}^n = (\varepsilon^n - U_0/2)/E_b$ and rewrite the matrix as

$$\begin{pmatrix} \hat{\tau}^{n+1} \\ \hat{\varepsilon}^{n+1} \end{pmatrix} = \begin{pmatrix} 1 & \alpha_c \\ e\dot{V}^*_{RF} T_0/E_b & 1+\alpha_c \dot{V}^*_{RF} T_0/E_b \end{pmatrix} \begin{pmatrix} \hat{\tau}^n \\ \hat{\varepsilon}^n \end{pmatrix}. \quad \text{(F.2)}$$

In case the continuous synchrotron radiation term is switched off, $\hat{\varepsilon}$ is simply ε/E_b. The determinant of the above matrix is due to neglecting the damping term equal to one. Remembering basic accelerator optics, one has an equivalent of the Courant-Snyder Invariant:

$$-c(\hat{\tau}^n)^2 + (a-d)\hat{\tau}^n\hat{\varepsilon}^n + b(\hat{\varepsilon}^n)^2 = \text{const}, \quad \text{(F.3)}$$

where the matrix has been abbreviated in the form $\begin{pmatrix} a & b \\ c & d \end{pmatrix}$. Expression (F.3) is equivalent to

$$(\hat{\tau}^n)^2 + \alpha_c\hat{\tau}^n\hat{\varepsilon}^n - \alpha_c \frac{E_b/e}{T_0 F_b \dot{V}_{RF}}(\hat{\varepsilon}^n)^2 = \text{const}. \quad \text{(F.4)}$$

Substituting the synchrotron tune into the above relationship leads to (use $\nu_{\mathrm{s}}^2 = \omega_{\mathrm{s}}^2/\omega_0^2$ and Eq. (3.14))

$$(\hat{\tau}^n)^2 + \alpha_{\mathrm{c}}\hat{\tau}^n\hat{\varepsilon}^n + \frac{\alpha_{\mathrm{c}}^2}{(2\pi\nu_{\mathrm{s}})^2}(\hat{\varepsilon}^n)^2 = \text{const.} \tag{F.5}$$

In Section 6.2.1, the approximate invariant amplitude of motion is studied in the form

$$2\pi h\sqrt{(\hat{\tau}^n)^2 + \alpha_{\mathrm{c}}\hat{\tau}^n\hat{\varepsilon}^n + \frac{\alpha_{\mathrm{c}}^2}{(2\pi\nu_{\mathrm{s}})^2}(\hat{\varepsilon}^n)^2} \tag{F.6}$$

after it has been transformed from radians to degrees.

Appendix G

Glossary

This is a glossary of accelerator physics related terms that are used in this thesis but that are not explained at the moment of introduction (but only later) or not at all. The references [17, 71, 72, 73, 74, 75, 76] have served to set up this glossary.

1. Accelerator coordinates

   The coordinates and momenta of a particle are usually expressed in terms of a path called the equilibrium, ideal, or closed orbit. This is the path that an ideal particle would follow. They are separated into the horizontal x and vertical y (the transverse planes) and the longitudinal planes z, see Figure G.1.

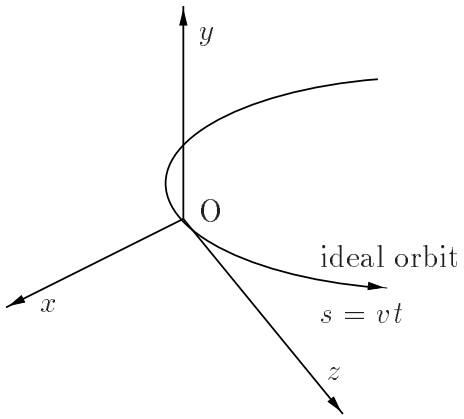

Figure G.1: Accelerator coordinates. The quantities x, y, and z are the horizontal, vertical, and longitudinal coordinates of a particle relative to a reference particle O, which travels along the circumference with $s = vt$.

2. Accelerator lattice

   The geometric arrangement of magnets in a linac or storage ring.

3. Acceptance

   The maximum emittance at which a particle trajectory can be transported in a beam line or stored in a ring. The acceptance limit can be defined either by the

vacuum system aperture ("geometric acceptance") or non-linearities of the magnet lattice ("dynamic acceptance"). Similarly, in the longitudinal plane "acceptance" denotes energy deviation.

4. Aperture
   In optics, the effective diameter of a lens or mirror. In accelerator terminology, a measure of the transport line's effective opening.

5. Beam Position Monitors (BPMs)
   Beam position monitors are employed in accelerators to measure the position of the beam centroid with respect to the vacuum chamber walls. Button BPMs consist of several (usually four) button pickup electrodes.

6. Beamstrahlung
   The synchrotron radiation emitted by each bunch of particles as it passes through the electromagnetic field of the opposing bunch.

7. Bellows
   Bellows are sections of corrugated vacuum chamber which are installed mainly to permit longitudinal displacement of the rigid chambers due to temperature variations, in particular if the chambers have to be heated to high temperatures to obtain a better vacuum.

8. Betatron function and oscillation

   Betatron oscillation is the transverse oscillation of particles about the equilibrium orbit. The restoring force for the betatron oscillations is provided by the quadrupole magnets which focus separately in the vertical and horizontal planes; therefore, there are both horizontal and vertical betatron oscillations.

   In a storage ring, betatron oscillations are described by Hill's equation

$$\frac{d^2x}{ds^2} + k(s)x = 0,$$

   where $k(s)$ is a periodic function: $k(s+L) = k(s)$ and x is a transverse coordinate. L is the circumference of the equilibrium orbit. The general solution of the above equation is

$$x = \sqrt{a\beta(s)}\cos(\Psi(s) + \alpha) \tag{G.1}$$

$$\Psi(s_1 \to s_2) = \int_{s_1}^{s_2} \frac{ds}{\beta(s)}\,. \tag{G.2}$$

   The constant a is called the particle (or trajectory) emittance. It sets an overall scale factor for the magnitude of x, whereas the beta or amplitude function $\beta(s)$ gives the position dependence of the amplitude of x. $\beta(s)$ has the same periodicity as $k(s)$ and its value is determined by the design of the accelerator lattice, whereas the value of a is determined by other factors. The function $\Psi(s_1 \to s_2)$ is the *phase*

advance from s_1 to s_2. The phase advance over one revolution is called the betatron tune

$$Q = \frac{1}{2\pi}\Psi(s \to s + L).$$

With the help of the beta function, one can show that for a given $\beta(s)$ and a, all solutions lie on an ellipse in the (x, x') phase space (horizontal or vertical). The area of this phase ellipse divided by π is the constant a.

The emittance ϵ of a beam is defined by one-half of the ensemble average of the single particle emittances,

$$\epsilon = \frac{1}{2}\langle a \rangle.$$

9. Bunch compressor

   In the bunch compressor, the particles travel on curved trajectories that have different path lengths for particles of different energy. As a result, a reduction of the bunch length is possible if the bunch has an appropriate longitudinal energy profile.

10. Chromaticity

    The ratio of the betatron tune spread to the relative momentum spread of the beam.

$$\xi = \frac{\Delta Q}{\Delta p/p_0}.$$

    The focusing and bending properties of the magnets are sensitive to particle momentum. This results in a focusing and bending dispersion of the beam in a manner analogous to an optical system. Particles of different momentum have a different betatron oscillation frequency, and, consequently, different tunes.

11. Coherent/incoherent tune
    Incoherent tune pertains to the tune of a single particle, whereas the coherent tune refers to the collective motion of the entire beam.

12. Collimator
    A collimator is a restriction of the vacuum chamber which serves the purpose of removing beam particles with excessively large transverse oscillation amplitudes.

13. Defocusing/focusing quadrupole magnet
    A quadrupole magnet focuses the beam in one plane and defocuses in the other. It is common use for "focusing" to denote a quadrupole which focuses in the horizontal plane.

14. Dispersion
    Quality of a beam transport system at a given point that defines the variation of the transverse position of the beam with variations in beam momentum.

Let D be the dispersion. Then a particle with a momentum offset $\Delta p/p_0$ follows a closed orbit which is given by $D\Delta p/p_0$ relative to the closed orbit of an ideal particle, and it executes betatron oscillations around this closed orbit. Neglecting the betatron oscillations, we see that the momentum offset changes the path length or circumference of the closed orbit. The relative path increment is called the *momentum compaction factor.*

15. Drift space

    A drift space is a space between magnets, which is free of magnetic fields.

16. Emittance (normalized transverse)

    The definition of beam emittance in a storage ring has been given above (see 8). In context with linear accelerators, a related quantity, the normalized emittance ϵ_{N} is also often used:

$$\epsilon_{\mathrm{N}} = \frac{p_0}{m_0 c}\epsilon = \beta\gamma\epsilon;$$

    β and γ are the usual relativistic factors.

    In an accelerating structure, the longitudinal momentum p_0 increases, whereas the transverse momentum p_x remains unchanged. The trajectory slope $x' = p_x/p_0$ shrinks and the transverse emittance ϵ is reduced; an effect which is called *adiabatic damping.* By multiplying ϵ with p_0, the adiabatic damping is removed, and the invariant quantity ϵ_{N} is obtained.

17. FODO cell

    The term "FODO" cell describes a sequence of focusing and defocusing quadrupole magnets with dipole magnets or drift spaces – denoted by "O" – between them.

18. Harmonic number

    The ratio of the rf frequency to the revolution frequency.

19. Ion clearing

    The circulating particles in a stored beam collide with residual gas molecules producing positive ions and electrons. An electron beam captures the ions and repels the electrons towards the vacuum chamber walls. If there are no natural or artificial clearing mechanisms, the neutralising ions accumulate up to the point where the remaining trapping potential is effectively zero (meaning until the number of static neutralising particles is equal to the number of beam particles).

    There are several effects of neutralisation. One is that the ions stored in the beam modify the local pressure and, therefore, the life-time of stored beams. The most important effects come from the electric field of the ion (or electron) cloud. This induces a shift and spread of betatron oscillation frequencies and a coupling of horizontal and vertical motion. Finally, the ion cloud can interact as a whole with the beam and induce instabilities.

Bunched proton or positron beams do not suffer from neutralisation problems because the electrons are not stably trapped.

During the beam gap in the dog-bone damping ring, the trapping potential is interrupted. The duration is long enough that neutralisation problems will not be encountered.

20. Ion pump
A type of vacuum pump in which ionized gas molecules are attracted to a cathode by a high voltage where they remain trapped.

21. Kicker magnet
Very fast rise-time magnet used to divert bunches. A typical use is for extraction.

22. Luminosity

The luminosity of a machine is defined as the counting rate of events for a process of unit cross-section.

23. Momentum compaction factor

See dispersion.

24. Phase advance

See betatron function.

25. Phase space

A coordinate space. To completely describe the motion of a particle, we need six coordinates $(x, x', y, y', z, \Delta p/p)$ in the six-dimensional phase space, where $x' = dx/ds$, $y' = dy/ds$ are the slopes in the horizontal and vertical coordinates of the particle relative to the designed direction of motion (see 1). Instead of the relative momentum error of the particle, one can use alternately the energy deviation. The synchronous particle has all six coordinates equal to zero. The six-dimensional phase space can be decomposed into the two-dimensional longitudinal phase space $(z, \Delta p/p)$ and the four-dimensional transverse phase space. The transverse phase space can be split into two two-dimensional phase spaces: the horizontal (x, x') and the vertical (y, y').

26. Separate function magnets

In a separate function lattice, the functions of bending and focusing are handled by separate dipole and quadrupole magnets.

27. Space charge forces

The repulsive Coulomb forces in a bunch of particles of the same polarity, or the Coulomb forces interacting between bunches of colliding beams.

28. Spot size
The transverse size of a beam at a given point.

29. Storage ring
    A storage ring is a ring of magnets having the capability of storing particles from an accelerator for periods of up to many hours.

30. Strong focusing
    A system for focusing charged particles in which the particles pass alternately through non-uniform electric or magnetic fields having gradients of opposite sign.

31. Synchrotron frequency
    Frequency of longitudinal oscillations of the bunches.

32. Synchrotron oscillation
    Synchrotron oscillation is the longitudinal oscillation of particles in an accelerator about an equilibrium of the phase of the accelerating voltage at the time the particles are crossing the accelerating gap.

33. Synchronous particle
    The hypothetical particle circulating in phase with the rf voltage about which other particles in the phase space bucket would oscillate.

34. Synchrotron radiation.
    Electromagnetic radiation generated by the transverse acceleration of the relativistic charged particles in a magnetic field.

35. Taper
    A taper is a part of the vacuum chamber which provides a gradual transition from one cross-section of the chamber to another.

36. Tune
    The number of betatron oscillations per revolution of the beam. There is a horizontal and vertical tune. Quite often only the fractional part of the quotient is referred to as the tune; the whole digit part of this quotient is called the betatron number.

Bibliography

[1] R. Brinkmann, G. Materlik, J. Rossbach, and A. Wagner (eds.), *Conceptual Design of a 500 GeV* e^+e^- *Linear Collider with Integrated X-ray Laser Facility*, DESY 1997-048 and ECFA-97-182 (1997)

[2] P. Emma, *The Stanford Linear Collider*, Proc. 16th IEEE Particle Acc. Conf. (PAC95), pp. 606-610, Dallas, Texas, 1-5 May 1995

[3] R. Brinkmann, *Linear Collider Projects at DESY*, Proc. 6th European Particle Acc. Conf. (EPAC98), pp. 53-57, Stockholm, 22-26 June 1998

[4] K. Yokoya, *Bunch Lengthening in TESLA Damping Ring*, DESY–TESLA 98-22 (1998)

[5] M. Sands, *The Physics of Electron Storage Rings. An Introduction*, SLAC-0121 (1970)

[6] B. Wiik, *The Status of HERA*, Proc. 2nd European Particle Acc. Conf. (EPAC90), pp. 351-355, Nice, 12-16 June 1990

[7] R. Byrns et al., *Status of the Superconducting Cavity Program for HERA*, Proc. 2nd European Particle Acc. Conf. (EPAC90), pp. 1073-1075 Nice, 12-16 June 1990

[8] J. Haissinski, *Exact Longitudinal Equilibrium Distribution of Stored Electrons in the Presence of Self-Fields*, Nuovo Cimento 18 B, pp. 72-82 (1973)

[9] A. Hofmann, *Kinetic Theory*, CERN Accelerator School Proceedings (Editor: S. Turner), CERN 95-06, pp. 259-274 (1995)

[10] A. Hofmann, *Beam Instabilities*, CERN Accelerator School Proceedings (Editor: S. Turner), CERN 95-06, pp. 307-330 (1995)

[11] R. L. Holtzapple, *Longitudinal Dynamics at the Stanford Linear Collider*, Ph.D. thesis, SLAC-R-487 (1996)

[12] R.P. Walker, *Radiation Damping*, CERN Accelerator School Proceedings (Editor: S. Turner), CERN 94-01, pp. 461-480 (1994)

[13] R.P. Walker, *Quantum Excitation and Equilibrium Beam Properties*, CERN Accelerator School Proceedings (Editor: S. Turner), CERN 94-01, pp. 481-498 (1994)

[14] K. Wille, *Physik der Teilchenbeschleuniger und Synchrotronstrahlungsquellen*, B.G. Teubner, Stuttgart, 1996

[15] K.L. Bane, P.B. Wilson, and T. Weiland, *Wake Fields and Wake Field Acceleration*, Physics of High Energy Particle Accelerators (BNL/SUNNY Summer School, 1983), AIP Conf. Proc. No 127, pp. 876-928, ed. by M. Month et al. (1984)

[16] T. Weiland and R. Wanzenberg, *Wake Fields and Impedances*, DESY M-91-06 (1991)

[17] A. Chao, *Physics of Collective Beam Instabilities in High Energy Accelerators*, John Wiley & Sons, Inc., New York, 1993

[18] P.B. Wilson, *High energy electron linacs; Application to storage ring rf systems and linear colliders*, Physics of High Energy Particle Accelerators (Fermilab Summer School, 1981), AIP Conf. Proc. No 87, pp. 450-563, ed. by M. Month et al. (1982)

[19] L. Palumbo, V.G. Vaccaro, and M. Zobov, *Wake Fields and Impedance*, CERN Accelerator School Proceedings (Editor: S. Turner), CERN 95-06, pp. 331-390 (1995)

[20] H. Schlarb, *Resistive Wall Wake Fields*, Diploma thesis, University of Hamburg, DESY–TESLA 97-22 (1997)

[21] T. Weiland, *Comment on Wake Field Computation in Time Domain*, Nucl. Instr. Meth. 216, pp. 31-34 (1983)

[22] R. Wanzenberg, *Longitudinale Strahldynamik im Resonanten Wake Field Beschleuniger*, Ph.D. thesis, University of Hamburg, DESY M-90-08,(1990)

[23] The MAFIA collaboration "User Guide", CST GmbH, Darmstadt, 1996

[24] T. Schilcher, *Vector Sum Control of Pulsed Accelerating Fields in Lorentz Force Detuned Superconducting Cavities*, Ph.D. thesis, University of Hamburg, DESY–TESLA 98-20 (1998)

[25] P.B. Wilson, *Fundamental-mode rf Design in* e^+e^- *Storage Ring Facilities*, Joint US-CERN Particle Accelerator School: Frontier of Particle Beams: Factories with e^+e^- Rings, 1992; SLAC-PUB-6062 (1993)

[26] H. Padamsee, J. Knobloch, and T. Hays, *RF Superconductivity for Accelerators*, John Wiley & Sons, Inc., New York, 1998

[27] S. Koscielniak, *Coherent and Incoherent Bucket for a Beam Loaded Rf System*, Particle Accelerators, Vol. 48, pp. 1-18 (1994)

[28] J. Buon, *Beam Phase Space and Emittance*, CERN Accelerator School Proceedings (Editor: S. Turner), CERN 94-01, pp. 89-116 (1994)

[29] J.-L. Laclare, *Bunched Beam Coherent Instabilities*, CERN Accelerator School Proceedings (Editor: S. Turner), CERN 87-03, pp. 264-326 (1987)

[30] K.L. Bane, *Bunch lengthening in the SLC Damping Rings*, SLAC-PUB-5177 (1990)

[31] T. Okugi et. al, *Impedance Measurement Utilizing Bunch Lengthening Effect in ATF Damping Ring*, ATF 97-23 (1997)

[32] S. Heifets et al., *Impedance Study for the PEP-II B-Factory*, SLAC/AP-99 (1995)

[33] V.D. Shiltsev, *TESLA Damping Ring Impedances: Preliminary Design Consideration*, DESY–TESLA 96-02 (1996)

[34] A. Ruggiero, *Bunched Electron and Proton Beams*, IEEE Trans. Nucl. Sci. NS-24, No 3, pp. 1205-1207 (1977)

[35] K.L.F. Bane and R.D. Ruth, *Bunch lengthening calculations for the SLC Damping Rings*, SLAC-PUB-4905 (1989)

[36] P. Germain and H.G. Hereward, *Longitudinal Equilibrium Shape for Electron Bunches with various Self-fields*, CERN/MPS/DL 75-5 and CERN/ISR-DI/75-31 (1975)

[37] T. Weiland, *On the quantitative prediction of bunch lengthening in high energy electron storage rings*, DESY 81-088 (1981)

[38] R. Brinkmann and T. Weiland, private communication

[39] D. Brandt, *Simulation of longitudinal single-bunch effects in LEP*, CERN-ISR-TH/82-09 (1982)

[40] D. Brandt, *SIMTRAC – A Simulation Program for Tracking Longitudinal and Transverse Single-Bunch Effects*, LEP Note 512 (1984)

[41] R. Siemann, *Computer Simulation of Bunch Lengthening in SPEAR*, Nucl. Instr. Meth. 203, pp. 57-62 and CNLS 82/524 (1982)

[42] R. Siemann, *Computer Models of Instabilities in Electron Storage Rings*, Physics of High Energy Particle Accelerators (BNL/SUNY Summer School 1983), AIP Conf. Proc. No 127, pp. 368-442, ed. by M. Month et al. (1983)

[43] V. Nys, *Computer Simulation of the Longitudinal Motion including the Wake-field Force, using a Hermite Polynomial Expansion*, CERN/LEP-TH/86-34 (1986)

[44] G. Sabbi, *Simulation of Single-Bunch Collective Effects in LEP by Linear Expansion of the Distribution Moments*, CERN SL/95-25 (AP) (1995)

[45] K. Bane and K. Oide, *Simulations of the longitudinal instability in the SLC damping rings*, SLAC-PUB-6216 (1993)

[46] Mauro Migliorati, *Effetti Collettivi Nella Dinamica Dei Fasci In Una Macchina Acceleratrice Circolare Con Applicazioni Al Progetto DAΦNE*, Ph.D. thesis, La Sapienza, Rome (1996)

[47] M. Bassetti, A. Ghigo, M. Migliorati, L. Palumbo, and M. Serio, *A time simulation code of the longitudinal multibunch instabilities*, DAΦNE Technical Note G-19 (1993)

[48] S. Heifets, *Broad Band Impedance of the B-Factory*, SLAC/AP-93 (1992)

[49] K. Bane, *The calculated longitudinal impedance of the SLC Damping Rings*, SLAC-PUB-4618 (1988)

[50] *An Asymmetric B-Factory. Conceptual Design Report*, LBL-PUB-5379 and SLAC-418 (1993)

[51] G. Vignola, *D.A.Φ.N.E. Design Criteria and Project Overview*, LNF-91/037-R (1991)

[52] K. Bane and M. Sands, *Wakefields of Very Short Bunches in an Accelerating Cavity*, SLAC-PUB-4441 (1987)

[53] A. Novokhatski, M. Timm, and T. Weiland, *The Surface Roughness Wake Field Effect*, Proc. 5th International Computational Acc. Physics Conf. (ICAP98), Monterey Ca., USA; DESY–TESLA 99-17 (1998)

[54] A. Novokhatski, private communication

[55] K. Yokoya, *Resistive Wall Impedance of Beam Pipes of General Cross Section*, Particle Accelerators, Vol. 41, pp. 221-248 (1993)

[56] R. Gluckstern, J. van Zeijts, and B. Zotter, *Coupling Impedance of Beam Pipes of General Cross Section*, CERN SL/AP 92-25 (1992)

[57] O. Henry and O. Napoly, *The Resistive-Pipe Wake Potentials for Short Bunches*, Particle Accelerators, Vol. 35, pp. 235-247 (1991)

[58] B.I. Grishanov, F.V. Podgorny, J. Rümmler, and V.D. Shiltsev, *Very Fast Kicker for Accelerator Applications*, DESY–TESLA 96-11 (1996)

[59] M. Marx, private communication

[60] N. Kurita, D. Martin, C.-K. Ng, S. Smith, and T. Weiland, *Numerical Simulation of the PEP-II Beam Position Monitor*, SLAC-PUB-95-7006 (1995)

[61] C. Burnton, *Tracking Studies in the Longitudinal Phase Space for the TESLA Damping Ring Design*, DESY–TESLA 98-15 (1998)

[62] K.A. Thompson, *Simulation of Longitudinal Coupled-Bunch Instabilities*, ABC-24 (1991)

[63] K. Oide and K. Yokoya, *Longitudinal Single-Bunch Instability in Electron Storage Rings*, KEK Preprint 90-10 (1990)

[64] R. Brinkmann, C. Burnton, R. Wanzenberg, and T. Weiland, *Tracking Studies in the Longitudinal Phase Space for the Tesla Damping Ring Design*, Proc. 6th European Particle Acc. Conf. (EPAC98), pp. 948-950, Stockholm, 22-26 June 1998

[65] M. Ebert et al., *Transverse and Longitudinal Multi-Bunch Feedback Systems for PETRA*, DESY-91-036 (1991)

[66] W. Fischer and I. Lieb, *Funktionentheorie*, Verlag Vieweg, Wiesbaden, 1992

[67] A. Piwinski, *Wake Fields and Ohmic Losses in Round Vacuum Chambers*, DESY–HERA 92-11 (1992)

[68] I.S. Gradshteyn and I.M. Ryzhik, *Table of Integrals, Series, and Products*, 4th edition, Academic Press Inc., New York, 1965

[69] R.H. Siemann, *Spectral Analysis of Relativistic Bunched Beams*, SLAC-PUB-7159 (1996)

[70] B. Zotter, *A review of Self-consistent Integral Equations for the Stationary Distribution in Electron Bunches*, KEK-Report 90-21 (1991)

[71] Fermilab Operations Department,
http://www-bd.fnal.gov/operations/accgloss/gindex.html

[72] http://www.slac.stanford.edu/find/slacspeak

[73] B. Zotter and S. Kheifets, *Impedances and Wakes in High-Energy Particle Accelerators*, World Scientific Publishing Co. Ptc. Ltd., Singapore, 1998

[74] J. Rossbach and P. Schmüser, *Basic course on accelerator optics*, CERN Accelerator School Proceedings (Editor: S. Turner), CERN 94-01, pp. 17-88 (1994)

[75] W. Weng and S. Mane, *Fundamentals of Particle Beam Dynamics and Phase Space*, Physics of Particle Accelerators, AIP Conf. Proc. No 249, pp. 3-45, ed. by M. Month et al. (1992)

[76] Y. Baconnier, A. Poncet, and P.F. Taveres, *Neutralisation of accelerator beams by ionisation of the residual gas*, CERN Accelerator School Proceedings (Editor: S. Turner), CERN 94-01, pp. 525-564 (1994)

Acknowledgements

To begin with, I would like to thank DESY for the opportunity to work in the field of accelerator physics, and Prof. Dr. Thomas Weiland for suggesting the interesting topic of my thesis as well as for his scientific guidance.
I am greatly indebted to Dr. Reinhard Brinkmann and my tutor Dr. Rainer Wanzenberg for sharing their knowledge and expertise in accelerator physics, and being patient in the process of helping me to grasp and utilize what they shared with me. I also owe them thanks for the reading of my drafts and their consequent suggestions.
I would like to thank Dr. Kathleen Thompson, Dr. Karl Bane, and Dr. V. Shiltsev for their quick responses to my questions considering their work; Dr. Karl Bane deserves a special thanks for kindly supplying the quasi-Green's function for the SLC damping ring.
My gratitude is also directed towards Dr. Mauro Migliorati for the time he took one afternoon to tell me about his thesis and answer my questions.
I am deeply honoured by Dr. Alexandre Novohatski's interest in my work and the time he has taken to enlighten me on his view of physics.
Gratitude is also due to Dr. Kaoru Yokoya, who, during his visit at DESY in the summer of 1998, not only applied his code to the TESLA damping ring, but also stimulated many productive discussions.
A thank you is also due to Dr. Martin Dohlus for his advice.
I would like to thank Michaela Marx for her help with MAFIA over the past years and Martin Timm and Nicoleta Baboi for their help on various occasions in a number of different matters.
I would like to express my thanks to Susan Wipf and Dr. Nicholas Walker for their reading of thesis with respect to my use of English. I am especially obliged to Ruth Burnton and Rachel Unkefer, who, without any knowledge of accelerator physics, went about tracking language errors; many of their suggestions for rephrasing entered this thesis. Last but not least, I would like to thank Boris Wagner for checking some of the mathematical calculations.